

Institut National de la Recherche Scientifique  
Énergie, Matériaux et Télécommunications

# **STRUCTURAL EFFECT OF LOW-DIMENSIONAL NANOCARBON ON EFFICIENCY AND STABILITY OF SOLAR ENERGY CONVERSION DEVICES**

Par  
Rusoma Akilimali

Thèse présenté(e) pour l'obtention du grade de  
Philosophiae Doctor (Ph.D.)  
en Sciences de l'Énergie et Matériaux

## **Jury d'évaluation**

Président du jury et  
examineur interne

Fiorenzo Vetrone  
Professor, INRS-EMT

Examineur externe

Mohamed Siaj  
Professor, UQAM

Examineur externe

Rafik Naccache  
Assistant Professor, Université Concordia

Directeur de recherche

Federico Rosei  
Professor, INRS-EMT

## REMERCIEMENTS

I would like to express my sincere gratitude to my supervisor Prof. Federico Rosei, for accepting me as a student and directing my Ph.D. research program. His guidance, encouragement, and support helped me a lot in the pursuit of my Ph.D. study. I also want to thank Dr. Haiguang and Dr. Selopal, my co-supervisors, for their care, guidance, and support throughout my Ph.D. study.

I want to thank Dr. Selopal for the scientific discussions, the valuable suggestions on this thesis organization, as well as his help and support during my Ph.D. studies.

Thanks to my colleagues in professor Rosei's research group for their collaboration and support. Special thanks to Dr. Fabiola Navarro-Pardo, Dr. Adhikari Rajesh, Dr. Lei Jin, Dr. Yufeng Zhou, Dr. Kaustubh Basu, Dr. Wei Huang, Jiabin Liu, Dr. Daling Cui, Dr. Joyprokash Chakrabarty, Kanghong Wang, Dr. Daniel Benetti, and other colleagues for their help and suggestions.

I am also indebted to many of my colleagues and friends from whom I received friendship and unconditional support over the years. Specifically, I want to thank Ivy Asuo, Charlotte Boukandou, and Dr. Ifeanyichukwu Amaechi. I would also like to thank all members of staff at INRS-EMT including particularly Louise Hudon, Christophe Chabanier, Georges Lamoureux and H  l  ne Sabourin. Besides, I am grateful to Jean-Philippe Masse for TEM measurements, for his direct and indirect support.

Thanks to Dr. Ibrahima Ka for providing important technical knowledge in Raman measurements.

I am indebted to some of my colleagues (officemates) including Dr. Jonathan Claustre, Dr. Laura Cacot and Dr. Nathanael Komba, from whom I got unconditional support during the frustrating period of my studies.

Last, but not the least, I am grateful to my family, my ancestors and all the brothers and sisters that helped me throughout these years.

七轉八起



## RÉSUMÉ

La population humaine mondiale est actuellement de 7,8 milliards. Ces chiffres représentent un nombre record depuis la formation de la Terre et il est prévu d'augmenter de 3 milliards supplémentaires au cours des 30 prochaines années. Avec, la recherche de la prospérité induira une poussée pour une demande énergétique plus élevée dans le monde entier.

Cependant, la consommation d'énergie du siècle dernier nous a déjà montré comment elle a provoqué la pollution des écosystèmes terrestres et le changement climatique. En fait, les historiens tiennent cela au fait que nous vivons maintenant l'Anthropocène, l'ère géologique pendant laquelle l'activité humaine a un impact dominant sur le climat et l'environnement. Cette situation remet en cause nos modes de conversion et de consommation d'énergie à base de combustibles fossiles. On s'attend donc à ce qu'un changement structurel significatif du système énergétique soit le moteur de l'avenir des activités industrielles et économiques.

Au fur et à mesure que nous nous dirigeons vers des systèmes de conversion d'énergie plus durables, le développement des nouvelles technologies devrait s'envoler dans la communauté scientifique afin d'atténuer les externalités négatives des technologies actuelles. Parmi les énergies renouvelables, les technologies solaires promettent d'exploiter une plus grande part de l'énergie solaire en la convertissant directement en électricité ou en la stockant dans de nouveaux carburants propres tels que les batteries et les piles à hydrogène.

Alors que les technologies photovoltaïques sont déjà entrées sur le marché, de nouveaux types de technologies avec une meilleure empreinte environnementale sont en cours de développement et de recherche. La production d'hydrogène renouvelable ( $H_2$ ) induite par la division de l'eau par photoélectrochimie solaire (PEC) a également un grand potentiel pour les applications de stockage, mais la production de  $H_2$  est confrontée au défi d'atteindre des performances plus élevées et nécessite donc de nouvelles avancées pour être commercialement viable.

Pour améliorer leur efficacité globale, une compréhension précise du mécanisme de ces dispositifs photoélectriques est nécessaire. Dans cette thèse, l'efficacité de collecte de charge représente l'un des processus clés dans le développement de dispositifs nanostructurés efficaces qui fonctionnent plus près de leur capacité théorique. En effet, les dispositifs photovoltaïques de 3ème génération comme les Cellules solaire à pigment photosensible (Cellules de Grätzel) sont capables de dépasser la limite fondamentale de Shockley-Queisser de 30% rendement de



conversion énergétique (RE). Bien que l'utilisation de l'oxyde métallique  $\text{TiO}_2$  ait représenté une avancée historique dans le domaine de la photocatalyse, elle a eu le plus d'influence sur le développement des Cellules de Grätzel et des efforts pour réorganiser son utilisation doivent encore être menés.

En tant que composant principal du dispositif, le semi-conducteur fournit des sites d'ancrage pour l'absorption de colorant ainsi qu'une large bande interdite favorisant la séparation des charges ainsi que le transport d'électrons. Cependant, l'un de ses inconvénients les plus importants est sa très faible mobilité de charge, qui finit par provoquer la recombinaison des charges après un certain temps.

Pour augmenter la durée de vie des charges photogénérées et améliorer l'efficacité du transport de charge dans les dispositifs de Cellules de Grätzel et PEC, un nanoruban de graphène (GNR) incorporé dans un semi-conducteur à large bande interdite et un nanocomposite basé sur GNR a été développé dans cette thèse. Ce ruban de graphène de faible dimension et hautement anisotrope est une couche unique d'atomes de carbone et présente d'excellentes propriétés de transport de charge. Ce qui en fait un bon candidat pour prendre en charge des voies avantageuses pour les électrons à collecter par le dispositif.

À ce jour, le RE le plus élevée des Cellules de Grätzel à jonction liquide s'élève à 14,3%. C'est encore insuffisant par rapport aux cellules solaires de silicium monocristallin atteignant 26.1%. Des travaux récents sur la conception des photoanodes ont proposé d'améliorer le transport des porteurs au sein des photoanodes soit en modifiant les morphologies des semi-conducteurs à large bande interdite, soit par incorporation des allotropes de carbone tels que les nanotubes de carbone (CNT), les feuilles de graphène, l'oxyde de graphène, etc.

Dans cette thèse, pour la première fois, nous avons appliqué le GNR en tant qu'additif à la photoanode d'oxyde pour améliorer les performances des dispositifs de conversion d'énergie solaire. Dans une première phase, nous avons étudié l'effet de l'incorporation de différentes charges de GNR dans la photoanode  $\text{TiO}_2$  sur le rendement des Cellules de Grätzel. Nos résultats soulignent qu'une charge optimale de 0,005% en poids de GNR augmente le PCE des DSSC, ce qui est 20% plus élevé que le PCE des appareils basés sur du  $\text{TiO}_2$  de référence. Ce rendement amélioré est principalement attribué à une meilleure charge de colorant, à une durée de vie des électrons améliorée et à une recombinaison réduite des porteurs. En outre, la quantité optimisée de GNR rapportée dans cette étude est de 0,005% qui est beaucoup plus faible que celle des autres Cellules de Grätzel à base d'allotropes de carbone- $\text{TiO}_2$  hybrides. Nous pensons qu'il s'agit

d'une approche rapide, peu coûteuse et hautement reproductible pour augmenter le rendement des Cellules de Grätzel.

Dans une seconde phase, nous avons étudié l'effet de l'incorporation de charges optimales précédemment obtenues de multifeuillets de Graphène (FLG) et de GNR dans la photoanode  $\text{TiO}_2$  pour stabiliser les performances du DSSC en dirigeant les charges photogénérées vers le circuit externe du dispositif. Nos résultats mettent en évidence que, la présence de GNR dans la couche active  $\text{TiO}_2$ , fonctionne mieux que le graphène en modifiant la stabilité à long terme des paramètres fonctionnels des appareils de 6%, 31,12% et 38% de taux décroissant pour GNR- $\text{TiO}_2$ , graphène-  $\text{TiO}_2$  et pour les échantillons de référence respectivement. Cet avantage par rapport aux photoanodes de référence et à base de FLG est principalement dû à l'amélioration de la densité de photocourant ( $J_{\text{SC}}$ ), qui peut être attribuée au transport d'électrons fortement amélioré (réduction de la résistance au transport de charge) dans les anodes hybrides GNR- $\text{TiO}_2$  malgré la réduction résistance au transfert de charge ( $R_{\text{CT}}$ ) et l'augmentation du taux de recombinaison ( $k_{\text{eff}}$ ) lié à  $\omega_{\text{max}}$ . En outre, une description structurale de la morphologie intégrée des films hybrides par spectroscopie Raman montre que le GNR peut réaliser un échafaudage supérieur du film  $\text{TiO}_2$  avec moins de contenu carboné que FLG du fait de leur fort aspect anisotropique.

Dans la troisième phase, nous avons étudié l'effet de l'incorporation de différentes charges de GNR dans la photoanode  $\text{TiO}_2$  pour augmenter les performances du dispositif PEC pour la génération d'hydrogène. Nos résultats ont démontré qu'une charge optimale de 0,02% en poids de GNR augmente la densité de photocourant (à 0,8 V vs RHE) du dispositif PEC jusqu'à 5,51 mA / cm<sup>2</sup>, ce qui est 30% plus élevé que celui du dispositif de contrôle. Cette amélioration de la densité de photocourant peut être attribuée à un transport d'électrons amélioré (résistance au transport de charge réduite) dans les anodes hybrides GNR- $\text{TiO}_2$  comme confirmé par spectroscopie d'impédance électrochimique. De plus, la cellule PEC basée sur la photoanode hybride GNRs- $\text{TiO}_2$  / QDs maintient ~65% de la densité photocourante initiale après 7200 secondes d'illumination continue du soleil, ce qui est 15% meilleur que la cellule PEC basée sur la photoanode  $\text{TiO}_2$  / QDs. Nos résultats offrent une approche simple, évolutive et peu coûteuse pour fabriquer des photoanodes pour les dispositifs optoélectroniques hautes performances, comme l'amélioration des performances des cellules PEC pour la génération  $\text{H}_2$ .

Les résultats de la thèse démontrent comment l'effet synergique du nouveau nanocarbone de faible dimension, appelé GNR, associé au  $\text{TiO}_2$  a le potentiel d'exploiter de meilleures propriétés mécaniques et électriques dans les semi-conducteurs hybrides à oxyde métallique. On obtient

ainsi des performances et une stabilité améliorées, avec une teneur en carbone plus faible, grâce à des additifs à base de carbone aux propriétés interfaciales exceptionnelles qui améliorent la conductivité des photoanodes et limite les effets de la recombinaison dans les cellules de Grätzel et les dispositifs PEC. Cela ouvre la porte à une nouvelle dimension dans le domaine de la science des matériaux pour une conversion d'énergie à grande échelle, rentable et respectueuse de l'environnement.

**Mots-clés** : Nanoruban de Graphène ; Microfeuille de Graphène ; GNR-TiO<sub>2</sub> ; FLG-TiO<sub>2</sub> ; Transport d' Electron ; Recombinaison des Charges ; Stabilité à Long-terme ; Photoelectrochimie ; Génération d'Hydrogen ; Spectroscopie Raman.

## ABSTRACT

The world's population is currently at 7.8 billion, representing an all-time high number since Earth's formation; it is projected to increase with a supplementary 3 billion in the next 30 years. With it, the pursuit of prosperity will induce a push for higher energy demand around the world.

However, the last century's energy consumption has shown us already how it triggered the pollution of the earth's ecosystems and climate change. In fact, historians refer to the present era as the Anthropocene, the geological age during which human activity has a dominant impact on climate and the environment. This situation calls into question our fossil fuel-based energy conversion and consumption methods. Significant structural changes in the energy system are thus expected to drive the future of industrial and economic activities.

The development of new sustainable energy technologies holds the promise of mitigating the drawbacks of fossil fuels. Among the renewables, solar energy-based technologies are expected to harness a higher share of sunlight energy by either directly converting it into electricity or by storing it into clean fuels such as hydrogen.

Whilst photovoltaic technologies have already entered the market, a novel type of technologies with lower environmental footprint are being investigated. Renewable hydrogen ( $H_2$ ) production driven by solar photoelectrochemical (PEC) water splitting also has great potential for storage applications, but  $H_2$  generation faces the challenge of achieving higher performances and therefore require further advances to be commercially viable.

To improve their overall efficiencies, a thorough understanding of the mechanism of these photoelectric devices is required. In it, the charge collection efficiency represents one of the key processes in developing efficient an optoelectronic device that work closer to their theoretical capacity. In fact, 3rd generation photovoltaic devices such as dye-sensitized solar cells (DSSCs) are capable of overcoming the 30% PCE fundamental Shockley-Queisser limit.

Wide band gap semiconductor is considered as the main component of the photoanode, which provides anchoring sites for dye absorption, promoting charge separation and transport. However, the most important setback, is the low charge carrier mobilities, which eventually causes the charges to recombine. While the use of the metal oxide  $TiO_2$  has represented a historical advance in the field of photocatalysis, it has had the most influence in the development of DSSCs.

To enhance the lifetime of photogenerated charges and to improve the charge transport efficiencies in both DSSC devices and PEC devices, in this thesis we developed a hybrid nanocomposite photoanode consisting in graphene nanoribbons (GNR) incorporated in a wide band gap semiconductor. GNR is a low dimensional and highly anisotropic strip of graphene (with thickness of a single layer of carbon atoms) which exhibits excellent charge transport properties. We therefore hypothesized that it would create suitable pathways for electron transport and collection.

To date, the highest photoconversion efficiency (PCE) of liquid junction DSSCs is ~14.3%. This value (at laboratory scale) is still low compared with commercial single crystalline Silicon solar cell (26.7%). Recent work on the design of photoanodes proposed to improve carrier transport either by modifying the morphologies of the wide band gap semiconductors or by incorporation of carbon allotropes such as carbon nanotubes (CNT), graphene sheets, graphene oxide, etc.

In this thesis for the first time, we applied GNR as an additive to oxide photoanode to boost the performance of solar energy conversion devices. In the first phase, we studied the effect of incorporating different loadings of GNR into the  $\text{TiO}_2$  photoanode on the PCE of DSSCs. Our results highlight that an optimum loading of 0.005 wt% GNR boosts the PCE of DSSCs, which is 20% higher than the PCE of devices based on bare  $\text{TiO}_2$ . This enhanced PCE is mainly attributed to better dye loading, enhanced electron lifetime and reduced carrier recombination. In addition, the optimized amount of GNRs reported in this study is 0.005 wt% much lower than that of other carbon allotropes- $\text{TiO}_2$  hybrid photoanodes based DSSCs. We believe that this is a fast, low cost and highly reproducible approach to boost the PEC of DSSCs.

In the second phase, we studied the effect of incorporation of previously obtained optimal loadings of Graphene or few layer graphene (FLG) and of GNR into the  $\text{TiO}_2$  photoanode to stabilize the performance of DSSC by directing the photogenerated charges towards the external circuit of the device. Our results highlight that the presence of GNR in the  $\text{TiO}_2$  active layer performs better than FLG by altering the long-term stability of functional parameters of devices by 6%, 31% and 38% decreasing rate for GNR- $\text{TiO}_2$ , graphene- $\text{TiO}_2$  and for bare samples respectively. This advantage over both bare and FLG- $\text{TiO}_2$  photoanodes upon light soaking is mostly due to improvement in the photocurrent density ( $J_{\text{SC}}$ ), which can be attributed to highly enhanced electron transport (reduced charge transport resistance) in GNR- $\text{TiO}_2$  hybrid anodes despite the reduced charge transfer resistance ( $R_{\text{CT}}$ ) and increased rate of recombination ( $k_{\text{eff}}$ ) related with  $\omega_{\text{max}}$ . In addition, a structural description of the embedded morphology of hybrid films through

Raman spectroscopy shows that GNR can achieve a superior scaffolding of the  $\text{TiO}_2$  film with less carbonaceous content than FLG, due to their high aspect ratio.

In the third phase, we studied the effect of incorporating different loadings of GNR into the  $\text{TiO}_2$  photoanode to boost the performance of PEC devices for hydrogen generation. Our results demonstrated that an optimum loading of 0.02 wt% GNR increases the photocurrent density (at 0.8 V vs RHE) of PEC devices up to  $5.51 \text{ mA/cm}^2$ , which is 30% higher than that of the control device. This improvement in photocurrent density can be attributed to enhanced electron transport (reduced charge transport resistance) in GNR- $\text{TiO}_2$  hybrid anodes as confirmed by electrochemical impedance spectroscopy. In addition, PEC cells based on GNRs- $\text{TiO}_2$ /QDs hybrid photoanode maintains ~65% of the initial photocurrent density after 7200 seconds of continuous one sun illumination, which is 15% better than PEC cell based on  $\text{TiO}_2$ /QDs photoanode. Our findings offer a simple, large area scalable and low-cost approach to fabricate photoanode for high-performance optoelectronic devices, such as boosting the performance of PEC cells for  $\text{H}_2$  generation.

The thesis results demonstrate how the synergetic effect of the novel low dimensional nanocarbon, so-called GNR, within  $\text{TiO}_2$  has the potential to harness better mechanical and electric properties in hybrid metal oxide semiconductors. Thus, achieving improved performance and stability, with lower carbonaceous content, owing to carbon-based additives with exceptional interfacial properties, which can enhance the conductivity of photoanodes and limit the effects of non-radiative recombination in both DSSCs and PEC cells. This paves the way to new directions in materials science towards large scale, cost effective and environmentally friendly solar conversion technologies.

**Keywords :** Graphene nanoribbons; Graphene microplatelets; GNR- $\text{TiO}_2$ ; FLG- $\text{TiO}_2$ ; Electron transport; Carrier recombination; Long-term stability; Photoelectrochemical; Hydrogen generation; Raman spectroscopy.



# TABLE DES MATIÈRES

REMERCIEMENTS .....	III
RÉSUMÉ .....	V
ABSTRACT .....	IX
TABLE DES MATIÈRES .....	XIII
LIST OF FIGURES .....	XVI
LIST OF TABLES .....	XXI
LIST OF ABBREVIATIONS .....	XXIII
<b>1 CHAPTER 1 : INTRODUCTION.....</b>	<b>27</b>
1.1 MOTIVATION: ENERGY CRISIS .....	27
1.1.1 <i>Climate change</i> .....	27
1.1.2 <i>Government policy</i> .....	27
1.1.3 <i>Alternative fuels</i> .....	28
1.2 SOLAR ENERGY .....	29
1.2.1 <i>Harnessing Solar Energy</i> .....	30
1.2.2 <i>Solar spectrum and solar energy conversion</i> .....	30
1.3 PHOTOVOLTAIC TECHNOLOGY .....	31
1.3.1 <i>Environmental and economic impact of using Photovoltaics</i> .....	31
1.3.2 <i>The Beginning-Market and how PV cells work</i> .....	32
1.4 DYE SENSITIZED SOLAR CELLS (DSSC).....	33
1.4.1 <i>Background concepts</i> .....	33
1.4.2 <i>Excitonic solar cells</i> .....	34
1.4.3 <i>DSSC: Applications and practical limits</i> .....	35
1.4.4 <i>Theoretical Background</i> .....	39
1.4.5 <i>Composition and working principle of DSSC</i> .....	40
1.4.6 <i>Electron transport and recombination in TiO<sub>2</sub></i> .....	48
1.4.7 <i>Parameters and kinetic aspects of DSSC</i> .....	50



1.5	STRUCTURE AND WORKING PRINCIPLE OF PEC .....	54
1.5.1	<i>Hydrogen generation from PEC cells</i> .....	54
1.5.2	<i>Working principle</i> .....	55
1.5.3	<i>Quantum dot-based PEC cells</i> .....	56
1.6	OPTIMISATION OF TiO <sub>2</sub> NANOCRYSTAL PHOTOANODE BASED DEVICES .....	57
1.6.1	<i>TiO<sub>2</sub> Nanocrystal Photoanode and its various structures</i> .....	58
1.6.2	<i>Carbon nanomaterials and its composites</i> .....	60
1.6.3	<i>Lessons from TiO<sub>2</sub>-nanocarbons nanocomposites</i> .....	63
1.6.4	<i>GNR-TiO<sub>2</sub> nanocomposite's influence on the geometry of percolation networks</i> .....	66
1.7	OBJECTIVE AND AIM OF THE THESIS .....	70
1.8	THESIS ORGANIZATION.....	72
<b>2</b>	<b>CHAPTER 2 MATERIALS AND METHODS.....</b>	<b>73</b>
2.1	MATERIALS .....	73
2.2	METHODS .....	74
2.2.1	<i>Experimental details relevant to DSSC fabrication with TiO<sub>2</sub> photoanodes with GNR</i> .....	74
2.2.2	<i>Experimental details relevant to colloidal QD based PEC H<sub>2</sub> generation</i> .....	76
2.3	CHARACTERIZATIONS.....	78
2.3.1	<i>Film size characterization</i> .....	78
2.3.2	<i>Optical measurements</i> .....	78
2.3.3	<i>Photoelectrical Measurements</i> .....	78
2.3.4	<i>Materials characterization</i> .....	81
<b>3</b>	<b>CHAPITRE 3 HYBRID TiO<sub>2</sub>-GRAPHENE NANORIBBON PHOTOANODES TO BOOST THE PHOTOCONVERSION EFFICIENCY OF DYE SENSITIZED SOLAR CELLS.....</b>	<b>87</b>
3.1	INTRODUCTION .....	87
3.2	RESULTS AND DISCUSSION.....	88
3.2.1	<i>Structural characterization</i> .....	88
3.2.2	<i>Photovoltaic characterization</i> .....	92
3.3	CONCLUSIONS AND PERSPECTIVES.....	97

<b>4</b>	<b>CHAPITRE 4 STRUCTURAL EFFECT OF LOW-DIMENSION CARBON NANOSTRUCTURES ON LONG-TERM STABILITY OF DYE-SENSITIZED SOLAR CELLS</b>	<b>98</b>
4.1	INTRODUCTION .....	98
4.2	RESULTS AND DISCUSSIONS: .....	98
4.2.1	<i>Structural characterization</i> .....	98
4.2.2	<i>Photovoltaic characterization</i> .....	103
4.2.3	<i>3.2.3. EIS measurements</i> .....	107
4.3	CONCLUSIONS AND FUTURE ASPECTS .....	112
<b>5</b>	<b>CHAPITRE 5 GRAPHENE NANORIBBON-TIO<sub>2</sub>-QUANTUM DOTS HYBRID PHOTOANODE TO BOOST THE PERFORMANCE OF PHOTOELECTROCHEMICAL FOR HYDROGEN GENERATION</b>	<b>114</b>
5.1	INTRODUCTION .....	114
5.2	RESULTS AND DISCUSSION .....	115
5.2.1	<i>Structural and morphological characterization of GNR-TiO<sub>2</sub> hybrid anode</i> .....	115
5.2.2	<i>Structural and optical characterization of QDs</i> .....	119
5.2.3	<i>PEC measurements</i> .....	121
5.2.4	<i>Electrochemical impedance spectroscopy analysis</i> .....	123
5.2.5	<i>Long-term stability measurements</i> .....	124
5.3	CONCLUSIONS AND PERSPECTIVES .....	125
<b>6</b>	<b>CHAPTER 6: CONCLUSIONS AND PERSPECTIVES</b>	<b>126</b>
6.1	CONCLUSIONS .....	126
6.2	PERSPECTIVES .....	129
<b>7</b>	<b>REFERENCES</b>	<b>130</b>
<b>8</b>	<b>LIST OF PUBLICATIONS</b>	<b>147</b>
<b>9</b>	<b>ANNEXE I : SOMMAIRE RÉCAPITULATIF</b>	<b>149</b>

# LIST OF FIGURES

<b>Figure 1-1</b> Energy information Administration projection of world energy growth in consumption by fuel type with historical data up to 2012. (2).....	28
<b>Figure 1-2</b> Global energy flow budget. Numbers in TW (3) .....	29
<b>Figure 1-3</b> Comparison of spectral irradiance: black body radiation (black) at 5800 K, AM0 irradiation in space (blue), AM1.5 irradiation in north American latitudes (red). The path length in air mass unit as a function of the zenith angle (5).....	31
<b>Figure 1-4</b> The different photovoltaic technologies divided into three generations followed by their highest efficiency.....	32
<b>Figure 1-5</b> Band diagram and main processes in excitonic solar cells (18).....	35
<b>Figure 1-6</b> The effect of using a mesoporous photoanode in DSSCs: IPCE as a function of the excitation wavelength; (a) Single crystal anatase TiO <sub>2</sub> , (b) Mesoporous anatase TiO <sub>2</sub> film (22) .....	36
<b>Figure 1-7</b> DSSC façade at the SwissTech convention center at École Polytechnique fédérale de Lausanne (30) Despite these good performances, their commercialization remains limited due to several disadvantages: .....	37
<b>Figure 1-8</b> Evolution of publications counts with "Dye sensitized solar cells" (31) .....	38
<b>Figure 1-9</b> Comparison between the most efficient single junction solar cells with the fundamental Shockley-Queisser limit (black line) (33) .....	39
<b>Figure 1-10</b> Working operation of DSSC (36) (37).....	40
<b>Figure 1-11</b> Energy band diagram for various semiconductors used in DSSC. ....	44
<b>Figure 1-12</b> (a) Dye adsorption as a function of particle size and (b) efficiency of DSSC as a function of dye adsorption (60).....	46
<b>Figure 1-13</b> Schematic of the structure of a dye sensitized solar cell.....	46
<b>Figure 1-14</b> Working principle of a DSSC and kinetics (28).....	50
<b>Figure 1-15</b> I-V photovoltaic characteristics (80) .....	51
<b>Figure 1-16</b> Examples of IPCE spectrum for of conventional electrode (Electrode 1), graphene-TiO <sub>2</sub> composite electrode (Electrode 2) and the CNT composite electrode (81) .....	52
<b>Figure 1-17</b> (a) Electrical circuit equivalent of a typical DSSC with Nyquist plot (38) (b) Impedance vs frequency and Bode plot, phase vs frequency (83).....	53

<b>Figure 1-18</b> Schematic diagram of the PEC cell used by Fujishima and Honda (21).....	55
<b>Figure 1-19</b> (a) Main processes for charge transport and recombination in photocatalytic water splitting. PEC based water splitting systems implementing (b) n-type semiconductor photoanode, and (c) p-type semiconductor photocathode (84). ....	56
<b>Figure 1-20</b> Band structure of different semiconductors with respect to the redox potentials of water splitting (88) .....	57
<b>Figure 1-21</b> Typical TiO <sub>2</sub> nanoarchitectures for improving DSSC performance .....	58
<b>Figure 1-22</b> (a) Photoanodes of nanoparticles with transport pathways;(b) bi-layer photoanode with light scattering layer; (c) directional electron transport in 1D nanowires and (d) hierarchical 1D nanowire architectures (90).....	59
<b>Figure 1-23</b> Different allotropes of graphene nanomaterials (107) .....	61
<b>Figure 1-24</b> Schematic of edge shape and nomenclature for armchair and zigzag GNRs and Different ways to unzip CNTs for production of GNRs: (a) Intercalation exfoliation, (b) chemical oxidation, (c) catalytic approach, (d) the electrical method, and (f) selective etching by Ar plasma (109).....	62
<b>Figure 1-25</b> Difference between a,c) 1D and b,d) 2D nanomaterials composite electrodes. In 2D nanomaterial composite electrodes (graphene bridges) (139), (e) the energy level diagram of TiO <sub>2</sub> -graphene based DSSCs. ....	65
<b>Figure 1-26</b> (a) Configuration off graphene at room temperature with intrinsic ripples (145), (b) Generation of wrinkles on substrate (146), (c) Schematic of simple ripple, standing collapsed wrinkle and folded wrinkle (147) .....	67
<b>Figure 1-27</b> (a) Percolation threshold with bonding strength and electrical conductivity evolution to filler content percentage (151) . I-V parameters of TiO <sub>2</sub> nanocomposite with (b) MWCNT (122) (c) F-MWCNT (142) (d) and Graphene (140).....	67
<b>Figure 2-1</b> Doctor blade TiO <sub>2</sub> film deposition .....	75
<b>Figure 2-2</b> Schematic of DSSC device fabrication steps. Image of an electrode after N719 dye sensitization (5) .....	75
<b>Figure 2-3</b> Schematic resuming the PEC cell formation (5).....	77
<b>Figure 2-4</b> Setting for PV measurement and device .....	79
<b>Figure 2-5</b> Schematic and picture of a PEC cell in a single compartment configuration, Image of the cell. Indicated are ports for the working electrode (WE), counter electrode (CE), and for inlet circulation for gas detection.....	80

<b>Figure 2-6</b> Gamry impedance analyzer (171) .....	81
<b>Figure 2-7</b> Schematic of SEM (172).....	82
<b>Figure 2-8</b> Model of the interaction pear and diagram of interaction between the primary electrons to produce the secondary particles (173).....	83
<b>Figure 2-9</b> Schematic of TEM (174) .....	84
<b>Figure 2-10</b> Differences in mechanisms in Raman and IR .....	85
<b>Figure 2-11</b> Raman spectrum for (a)-(b) graphene, graphite and (c) TiO <sub>2</sub> rutile, TiO <sub>2</sub> anatase (175, 176) .....	86
<b>Figure 2-12</b> (a) Raman spectrum of the graphene before being transferred onto the PET substrate. (b) Schematic diagram of Raman 2D peak position shift of graphene under strain-free tension and compression conditions (177).....	86
<b>Figure 3-1.</b> Schematic of DSSCs components with TiO <sub>2</sub> -GNR hybrid photoanodes highlighting preferred electrons transport through mesoporous film toward FTO.....	87
<b>Figure 3-2.</b> SEM images of the TiO <sub>2</sub> film with different concentrations (wt %) of GNR deposited on FTO: (a) 0.000%; (b) 0.005% of GNR; (c) 0.045% of GNRs, the dotted rectangle highlights the presence of cracks. (d) - (f) TEM of GNRs embedded inside the TiO <sub>2</sub> matrix at different magnification. ....	89
<b>Figure 3-3</b> Raman mapping of the composite photoanode filtered for: (a) TiO <sub>2</sub> ; (b) GNR respectively. (c) Raman spectra of bare TiO <sub>2</sub> mesoporous film (green line), TiO <sub>2</sub> -GNR hybrid mesoporous film (red line) and GNR powder (black line). ....	90
<b>Figure 3-4</b> Optical characterization: (a) Absorption spectra of GNR-TiO <sub>2</sub> mesoporous films at different concentration of GNR; (b) Absorption spectra of de-absorbed dye molecules solutions for different concentration of GNR; (c) Calculated average number of moles of dye molecules versus GNR concentration. ....	91
<b>Figure 3-5</b> (a) Current density–voltage curves of device with different concentrations of GNRs in TiO <sub>2</sub> under one sun illumination (AM1.5G irradiation (100 mW/cm <sup>2</sup> ), (b) Transient photovoltage decay measurements of corresponding devices. Normalized V <sub>oc</sub> decay with time; (c) Calculated electron life time values from V <sub>oc</sub> decay. ....	93
<b>Figure 3-6.</b> Variation of the functional parameters of the device under one sun illumination (AM1.5G irradiation, 100 mW cm <sup>-2</sup> ) with GNR concentration in TiO <sub>2</sub> : (a) J <sub>sc</sub> ; (b) PCE; (c) V <sub>oc</sub> ; (d) FF. ....	94
<b>Figure 3-7</b> EIS analysis of DSSCs at different GNR concentrations: (a) recombination resistance; (b) chemical capacitance from EIS measurements in the dark. ....	96

<b>Figure 4-1.</b> Schematic of DSSCs components with $\text{TiO}_2$ , $\text{TiO}_2$ -Graphene and $\text{TiO}_2$ -GNR hybrid photoanodes highlighting preferred electrons transport through FLG and GNR within mesoporous film toward FTO. ....	98
<b>Figure 4-2.</b> Raman spectra (a) of bare $\text{TiO}_2$ , Graphene- $\text{TiO}_2$ and GNR- $\text{TiO}_2$ (0.010 and 0.005 wt % respectively) deposited on FTO. SEM images (b) of 0.075 wt% of graphene and (c) of 0.075 wt% of GNR in $\text{TiO}_2$ , with dotted rectangle highlighting the presence of the nanocarbon structures. Raman maps of G-band (d)-(e) and D-band (f)-(g) intensities for the samples containing graphene, GNR respectively, and of (h) $E_{g2}$ band of $\text{TiO}_2$ . ....	99
<b>Figure 4-3.</b> Raman spectra of the D, G and D'-bands (a) and the 2D and D+D'-bands (b) of GNR- $\text{TiO}_2$ and FLG- $\text{TiO}_2$ compared with pristine GNR and FLG spectra, under 532 nm laser. (c) G band and 2D band evolution by FLG and GNR incorporation in $\text{TiO}_2$ , (d) schematic of compressive strain forces applied to FLG and GNR, (e) schematic of Fermi energy position of energy at the Dirac K point of FLG type structures after p-doping .....	101
<b>Figure 4-4</b> Schematic of the band alignment and carrier dynamics within hybrid photoanodes: (a) FLG- $\text{TiO}_2$ ; (b) GNR- $\text{TiO}_2$ . Photovoltaic characterizations of DSSCs based on hybrid photoanodes of FLG and GNR in $\text{TiO}_2$ and bare $\text{TiO}_2$ : (c) Current density-voltage curves under one sun illumination (AM1.5G irradiation (100 mW/cm <sup>2</sup> ). Transient photovoltage decay measurements of the corresponding devices: (d) $V_{oc}$ decay; (e) electron lifetime. ....	103
<b>Figure 4-5.</b> Normalized functional parameters of DSSCs with optimum concentration of FLG and GNR in $\text{TiO}_2$ and bare $\text{TiO}_2$ under a continuous light irradiation as a function of soaking time. (a) $J_{sc}$ ; (b) $V_{oc}$ ; (c) PCE; (d) FF.....	106
<b>Figure 4-6.</b> EIS analysis of bare DSSCs FLG- $\text{TiO}_2$ and GNR- $\text{TiO}_2$ hybrid DSSC before (lighter color) and after 270h (darker colours) simulated sun exposure under dark measurement: (a) Nyquist plot; (b) Bode plot at 750 mV and (c) $R_{ct}$ , (e) $\tau_n$ , (d) (f) histograms of changes in charge transfer resistance and electron lifetime after aging, at potentials between 0-850mV. ..	110
<b>Figure 5-1</b> (a) Schematic illustration of the working principle of PEC device for hydrogen generation. (b) Electron transport process in mesoporous $\text{TiO}_2$ film with and without GNR. The arrows indicate the electron transfer process. ....	114
<b>Figure 5-2</b> SEM images of GNR- $\text{TiO}_2$ hybrid mesoporous films with different concentration of GNR: (a-b) 0.00 wt %; (c-d) 0.02 wt% and (e-f) 0.05 wt% at different magnifications. The presence of deep cracks at higher concentration of the GNR is highlighted in white.....	116
<b>Figure 5-3</b> A comparison of absorption spectra of GNR- $\text{TiO}_2$ hybrid mesoporous films deposited on transparent conducting oxide glass with different concentration of GNR (wt %) .....	117

- Figure 5-4**(a)-(b) TEM images of GNRs (red-dotted) supported on Cu grid. Raman specter of the GNR (green), TiO<sub>2</sub> (blue), GNR-TiO<sub>2</sub> (red) composite photoanode with GNR = 0.02 wt% and GNR-TiO<sub>2</sub> (black) composite photoanode with GNR=0.05 wt% ..... 118
- Figure 5-5** (a) TEM image of CdSe/(CdS)<sub>6</sub> core/shell QDs, inset shows the HR-TEM image. Optical properties of QDs: (b) Absorption spectrum in UV-Visible region of as synthesized CdSe/(CdS)<sub>6</sub> core/shell QDs in toluene; (c) PL spectra of respective QDs in toluene. Transient PL curves of CdSe/(CdS)<sub>6</sub> core/shell QDs: (d) Deposited onto ZrO<sub>2</sub> mesoporous film; (b) Deposited onto and TiO<sub>2</sub> mesoporous film. at 444 nm excitation wavelength ..... 120
- Figure 5-6** Photocurrent density-potential curves of PEC devices based on QDs sensitized GNR-TiO<sub>2</sub> hybrid photoanodes under dark (black solid line), chopped (dotted blue line) and continuous illumination (AM 1.5 G, 100 mW/cm<sup>2</sup>) (red solid line) with different concentration of GNR: (a) 0.00 wt%; (b) 0.01 wt%; (c) 0.02 wt%; (d) 0.03 wt%; and (e) 0.05 wt%. (f) Variation of photocurrent density of PEC devices based on QDs sensitized GNR-TiO<sub>2</sub> hybrid photoanodes with different content of GNR at 0.8 V vs RHE under on sun illumination (AM 1.5 G, 100 mW/cm<sup>2</sup>). ..... 122
- Figure 5-7** The Nyquist plot of PEC devices based on GNR-TiO<sub>2</sub>/QDs hybrid photoanodes with different concentration of GNR: Black (0.0 wt%); Green (0.02 wt%) and Orange (0.05 wt%). Inset table displays the variation of charge transfer resistance with GNRs concentration ..... 123
- Figure 5-8** Comparison of normalized current density (mW·cm<sup>-2</sup>) versus time for PEC devices based on GNR-TiO<sub>2</sub>/QDs (red) and TiO<sub>2</sub>/QDs (green) photoanodes at 0.6 V (versus RHE) under one sun continuous illumination (AM 1.5 G, 100 mW·cm<sup>-2</sup>) for 7200 seconds ..... 124

## LIST OF TABLES

<b>Table 1-1:</b> Comparison between semiconductor based solar cell and the dye sensitized solar cell (24)	36
<b>Table 1-2</b> Power conversion efficiencies as a function of the metal oxide used in DSSCs	44
<b>Table 1-3</b> TiO <sub>2</sub> crystallographic characteristics and physical properties (51, 52)	45
<b>Table 3-1</b> Functional properties of DSSCs with different GNR content.	93
<b>Table 4-1</b> Functional properties of DSSCs with different FLG and GNR content.	104
<b>Table 4-2</b> EIS parameters evolution at 600mV before and after (bold) 273h light soaking time for bare TiO <sub>2</sub> , FLG-TiO <sub>2</sub> and GNR-TiO <sub>2</sub> samples	111
<b>Table 5-1</b> Comparison of photocurrent density at 0.8V vs RHE under one sun illumination (AM 1.5 G, 100 mW·cm <sup>-2</sup> ) of PEC devices based on GNR-TiO <sub>2</sub> /QDs hybrid photoanodes with different concentration of GNR (wt%).	123





## LIST OF ABBREVIATIONS

### Chemical compounds

<b>1D</b>	One dimension
<b>2D</b>	Two dimension
<b>3D</b>	Three dimension
<b>AM</b>	Air mass
<b>BL</b>	Blocking layer
<b>CB</b>	Conduction band
<b>CdTe</b>	Cadmium telluride
<b>CE</b>	Counter electrode
<b>CNT</b>	Carbon nanotube
<b>CT</b>	Charge transfer
<b>CO<sub>2</sub></b>	Carbon dioxide
<b>CIGS</b>	Copper indium gallium selenide
<b>DSSC</b>	Dye sensitized solar cell
<b>EDS</b>	Energy dispersive x ray spectroscopy
<b>EPD</b>	Electrophoretic deposition
<b>EIS</b>	Electrochemical impedance spectroscopy
<b>EPFL</b>	École polytechnique fédérale de Lausanne
<b>FF</b>	Fill factor
<b>FLG</b>	Few layer graphene
<b>FTO</b>	Fluorine doped tin oxide
<b>FWHM</b>	Full width at half maximum
<b>GD</b>	Graphdiyne
<b>GHG</b>	Green house gas
<b>GQD</b>	Graphene quantum dot
<b>GNR</b>	Graphene nanoribbon
<b>GO</b>	Graphene Oxide
<b>HER</b>	Hydrogen evolution reaction
<b>HOMO</b>	Highest occupied molecular orbital
<b>HRTEM</b>	High resolution transmission electron microscope
<b>INRS</b>	Institut national de la recherche scientifique
<b>IPCE</b>	Incident photon to current conversion efficiency
<b>IR</b>	Infrared
<b>LHE</b>	Light harvesting efficiency
<b>LUMO</b>	Lowest unoccupied molecular orbital
<b>MWCNT</b>	Multi walled carbon nanotube
<b>NHE</b>	Normal hydrogen electrode
<b>NIR</b>	Near infrared
<b>OER</b>	Oxygen evolution reaction
<b>PCE</b>	Power/photo conversion efficiency
<b>PEC</b>	Photoelectrochemical
<b>PV</b>	Photovoltaic
<b>QD</b>	Quantum dot
<b>RHE</b>	Reversible hydrogen electrode
<b>RPM</b>	Revolutions per minute
<b>Ru</b>	Ruthenium

<b>SEM</b>	Scanning electron microscopy
<b>SILAR</b>	Successive ionic layer adsorption and reaction
<b>SWCNT</b>	Single walled carbon nanotube
<b>TCO</b>	Transparent conducting oxide
<b>TEM</b>	Transmission electron microscope
<b>UV.VIS</b>	Ultraviolet visible
<b>UV</b>	Ultraviolet
<b>VB</b>	Valence band

## Symbols

<b>H</b>	Hour
<b>Min</b>	Minute
<b>μs</b>	Microsecond
<b>ms</b>	Millisecond
<b>ns</b>	Nanosecond
<b>fs</b>	Femtosecond
<b>ps</b>	Picosecond
<b>M</b>	Molar
<b>mM</b>	Millimolar
<b>Eqn</b>	Equation
<b>C<sub>μ</sub></b>	Chemical capacitance
<b>E<sub>g</sub></b>	Bandgap
<b>I<sub>sc</sub></b>	Short circuit current
<b>I<sub>max</sub></b>	Current at maximum power output
<b>J<sub>sc</sub></b>	Short circuit current density
<b>P<sub>in</sub></b>	Input light power
<b>P<sub>max</sub></b>	Maximum power output
<b>V<sub>oc</sub></b>	Open circuit voltage
<b>V<sub>max</sub></b>	Voltage at maximum power output
<b>J<sub>max</sub></b>	Current density at maximum power output
<b>η</b>	Power conversion efficiency
<b>Ω/□</b>	Ohm per square
<b>eV</b>	Electron volt
<b>kV</b>	Kilovolt
<b>TW</b>	Tera watt
<b>c</b>	Speed of light in vacuum
<b>k</b>	Boltzmann constant
<b>h</b>	Planck constant
<b>km</b>	Kilometer
<b>m</b>	Meter
<b>cm</b>	Centimeter
<b>mm</b>	Millimeter
<b>μm</b>	Micrometer
<b>nm</b>	Nanometer
<b>W</b>	Watt
<b>kW</b>	Kilowatt
<b>l</b>	Liter
<b>ml</b>	Milliliter
<b>g</b>	Gram
<b>mg</b>	Milligram

$\lambda$	Lambda
$^{\circ}\text{C}$	Degree Celsius
K	Kelvin
J	Joule
Ppm	Parts per million
MPa	Megapascal



# 1 CHAPTER 1 INTRODUCTION

---

## 1.1 Motivation: Energy crisis

### 1.1.1 Climate change

Human civilisation lives in a critical period coinciding with a great acceleration in wealth creation and an all-time high human population. This acceleration has been possible thanks to scientific and technological progress that helped harness the potential of new energy sources like coal, oil, and natural gas since the industrial revolution and nuclear energy since the second half of the 20<sup>th</sup> century. The share of fossil fuels, represents up to 84% of the world's energy consumption and its trade have driven the need of the world economy towards a path of sustainable development (1). The supply of fossil fuels is considered strategic for the well-being of developed nations and thus has accelerated their demand and limited their availability.

However, the impact of this growth in energy conversion and transmission methods has staggeringly increased the level of pollution which consequently caused public health issues, glaciers to melt, sea levels to rise, the cloud forest to die, wild life to scramble and indigenous communities to disintegrate (migration).

Nevertheless, global energy demand is expected to more than double from 13 TW today to 30 TW by 2050. And the yearly increase will result in the rise of demand towards finite fossil fuels which in turn will also deplete these natural resources that have taken millions of years to form.

It is today realistic to say that our energy generation and transmission method affects our environment, and has the potential of endangering our lives on Earth.

Nowadays fossil fuels, such as coal, oil and natural gas represent the main global primary energy resources. Nuclear 'fuels' ( $^{238}\text{U}$ ), although not been considered a traditional source, have within the last couple of decades considerably increased their role in meeting the energy needs globally (2).

### 1.1.2 Government policy

In 1997, the Kyoto protocol, an international agreement between industrialized nations, aimed to reduce carbon dioxide ( $\text{CO}_2$ ) emissions and greenhouse gases (GHG) in the atmosphere. Some of the gases among the main contributors to the build-up of GHGs are clearly caused by human activities. Since the Kyoto agreement, policy makers and governments around the world have variably pledged to implement wider actions to tackle the climate change issues and modify their economies towards environmentally sustainable growth.

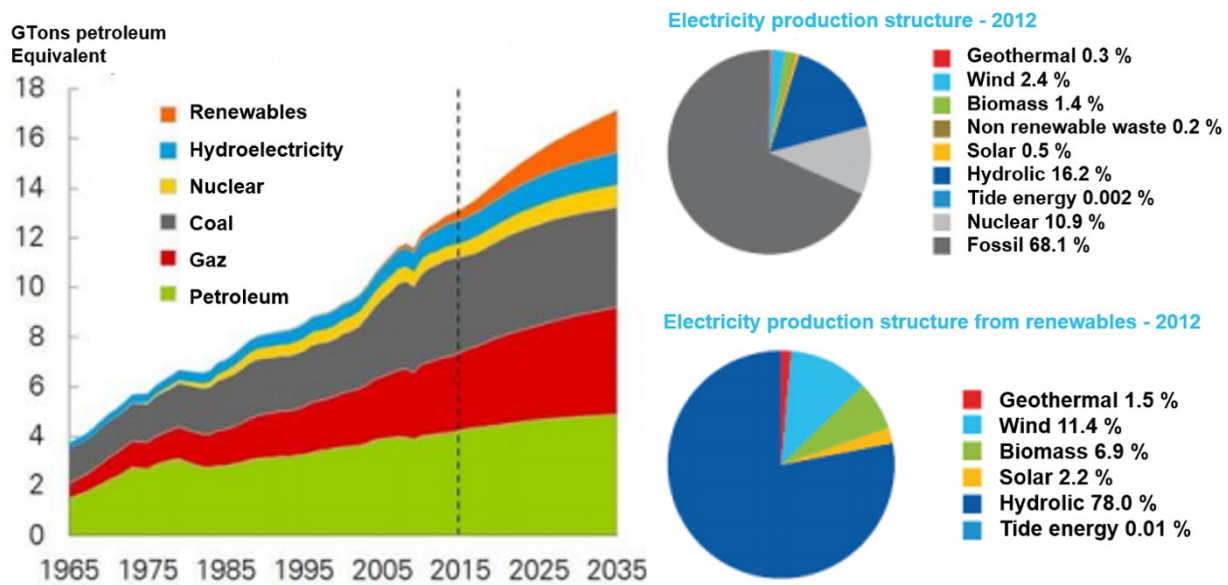


Figure 1-1 Energy information Administration projection of world energy growth in consumption by fuel type with historical data up to 2012. (2)

### 1.1.3 Alternative fuels

Therefore, to meet the needs of an ever-growing world population and an increasing energy demand, mounting reliance on alternative and sustainable technologies need to be assumed. As a result, renewable energy supplies generated from solar, wind, biomass, geothermal, hydropower and ocean resources, need to be harnessed.

Wind energy ( $P_{kinet: air} = 400$  TW) and biomass ( $P_{biosphere} = 100$  TW) (3), are still strong candidates for renewable energy utilization; in comparison, the theoretical potential of hydraulic power is relatively small ( $P_{hydro} = 5$  TW) (see **Figure 1-1** for details). Of course, for each of these theoretical values, the so-called technically usable part amounts to a substantially smaller fraction only.

This is also the case for hydrogen. Although its utilisation generates almost no ecological footprint (its by-product when combusted in a fuel cell is water), and the highest energy per mass of any fuel (120 MJ/kg versus 44 MJ/kg for gasoline), currently hydrogen is mostly extracted from methane (natural gas), which is a non-renewable source.

Depending on the source of electricity used, the once promising pathway of electrolysis is considered costly and to be highly damaging for the environment as it still relies on grids which release GHS and on fossil fuel-based resources. Moreover, biomass-derived liquids are

composed of larger molecules with more carbon atoms than natural gas, making them more difficult to reform.

More sustainable sources of Hydrogen have to be developed from renewable energies themselves to make it relevant for the future of storable and transportable fuels. Fortunately, such source of energy can come from the sun. Solar energy can therefore be considered as a potential energy source to split water into its constituents  $O_2$  and  $H_2$  with long-term potential for sustainable hydrogen conversion with low environmental impact (4).

## 1.2 Solar Energy

Almost all alternative energy sources lag behind solar radiation with  $P_{rad\ surf} = 89,000$  TW.

Solar energy is at the forefront of almost all types of 'renewable energy'. It has one of the lowest environmental/carbon footprints. 175,000 TW of energy comes in from the outer atmosphere. This amount (see **Figure. 1-2**) outweigh the present global primary energy requirement per unit time of about 15 TW by four orders of magnitude.

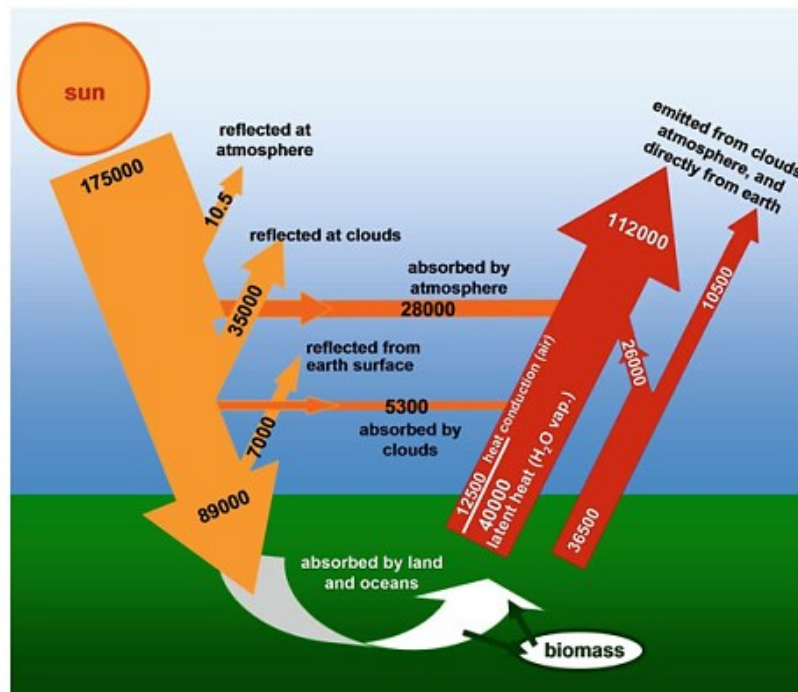


Figure 1-2 Global energy flow budget. Numbers in TW (3)

Although only 1 % is assumed to be technically available, a hypothetical overall conversion efficiency of solar light ( $\eta_{solar\ light}$ ) of that same percentage, would theoretically place solar radiation



as our only primary energy supplier for the world's needs, even with further population growth. However, the challenge still lies in harvesting the solar resource.

### 1.2.1 Harnessing Solar Energy

The role of scientists and engineers is to increase the technically usable share of solar energy. The technology that directly converts light into electricity is Photovoltaics (PV). Many Photovoltaic technologies are currently being developed, and Research and development efforts in the field of solar generation are growing significantly.

### 1.2.2 Solar spectrum and solar energy conversion

The energy radiated by the sun reaches the earth in the form of electromagnetic waves, all of which can be approximately modeled as a black body emitting at the temperature of 5800 K. Planck's radiation law (shown in Eqn.1-1) describes the spectral irradiance of a black body.

$$F(\lambda) = \frac{2\pi hc^2}{\lambda^5 (\exp(\frac{hc}{k\lambda T}) - 1)} \quad (1-1)$$

Where  $\lambda$  is the wavelength of light, T is the temperature of the blackbody in Kelvin (K), F is the spectral irradiance in  $\text{Wm}^{-2}\mu\text{m}^{-1}$ ; and h is Planck's constant, c is the speed of light in vacuum and k is Boltzmann's constant.

Solar radiation is reflected and absorbed by the earth's atmosphere and its clouds and also eventually reflected from the earth's surface. The AM (shown in Eqn.1-2) is a parameter defined as the path length which sunlight travels through the atmosphere normalized to the shortest path length, i.e. when the sun is directly overhead.

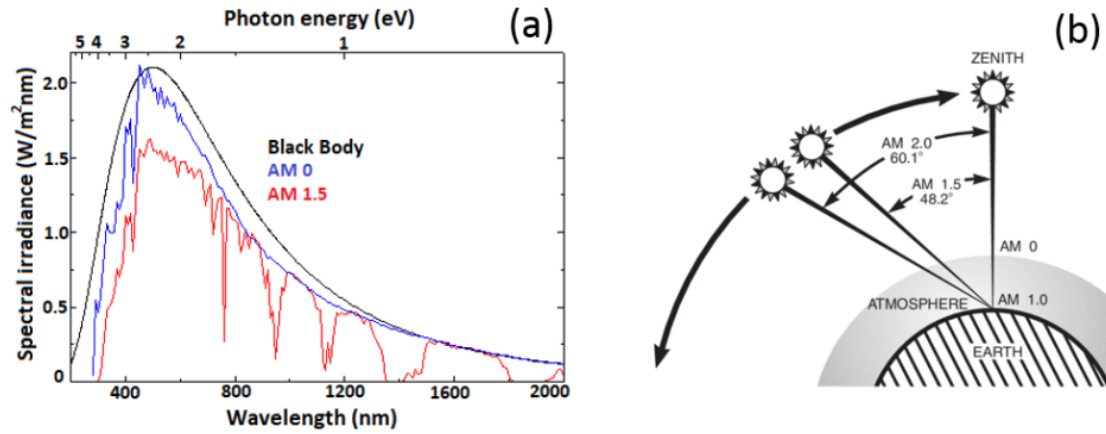


Figure 1-3 Comparison of spectral irradiance: black body radiation (black) at 5800 K, AM0 irradiation in space (blue), AM1.5 irradiation in north American latitudes (red). The path length in air mass unit as a function of the zenith angle (5)

AM is defined as:

$$AM = \frac{L}{L_0} \approx \frac{1}{\cos \theta} \quad (1-2)$$

Where  $\theta$  is the angle of elevation of the sun,  $L$  is the path length of light, and  $L_0$  is the thickness of the atmosphere's layer.

In 1961, studies have suggested the fundamental limitations that govern the performance of solar cells to be for an optimum photoconversion (6) at around 33% of the solar energy with a bandgap of 1.4 eV. The rest of the solar energy, 47% is converted to heat (phonons), 18% of the photons is transmitted unabsorbed, and around 2% is lost from recombination of newly generated electrons and holes (7).

## 1.3 Photovoltaic Technology

### 1.3.1 Environmental and economic impact of using Photovoltaics

Solar energy technologies provide advantageous environmental benefits compared to conventional and other alternative energy sources. Their main advantage is related to the reduced CO<sub>2</sub> emissions and absence of air emissions and waste products during their operation. Since they do not require transmission lines, due to their on-site energy conversion and use, they reduce the necessity of electric grids and improve the quality of water resources (8).

Additionally in regards to socio-economic perspectives, they contribute to an increased energy independence both locally and regionally, in the provision of significant work opportunities, in the

support of the deregulation of energy markets and in the acceleration of the rural electrification in developing countries (9).

### 1.3.2 The Beginning-Market and how PV cells work

Various technologies are being developed to establish photovoltaic cells. The degrees of maturity, performance and lifespan are very different from one technology to another. Current research and development efforts are leading to rapid progress, making photovoltaics a sector in constant evolution.

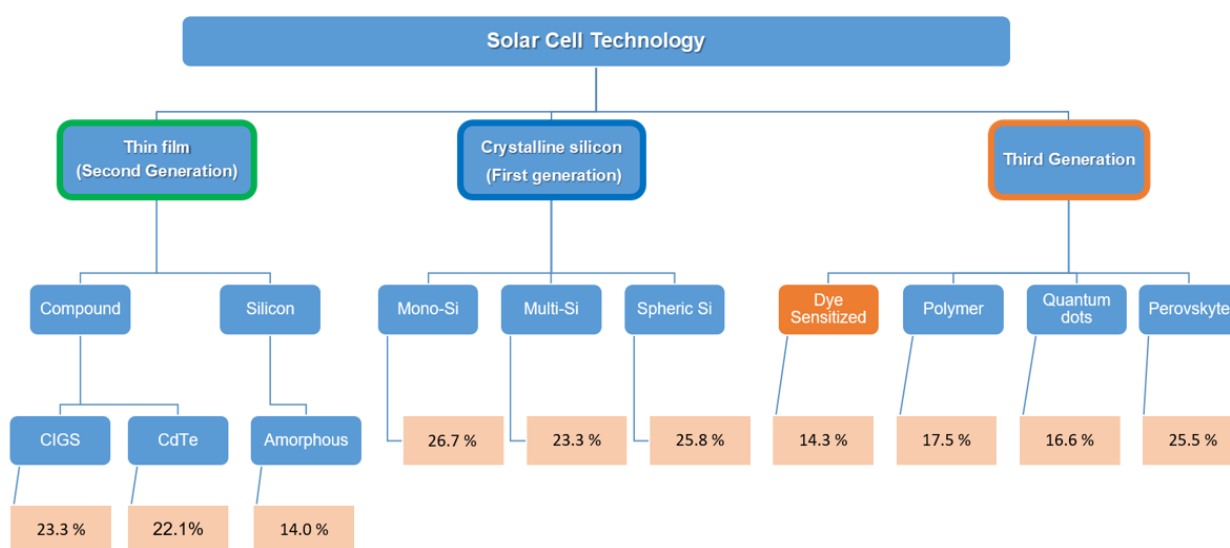


**Figure 1-4 The different photovoltaic technologies divided into three generations followed by their highest efficiency**

The photovoltaic effect is a process in which two dissimilar materials in close contact produce an electrical voltage (from pioneering work of Alessandro Volta) when struck by light (photo in Greek) or other radiant energy (10).

A classification for all the available technologies has since been developed. A general division of three basic technologies can be established:

- the **first generation** consists essentially in monocrystalline and polycrystalline silicon based solar cells (11). The manufacturing process of crystalline silicon requires high purity that induces expensive production cost. Currently, 90% of commercial photovoltaic devices are from the first generation. Nevertheless, their cost, high weight, lack of flexibility and mostly their energy

consuming manufacturing methods represent major disadvantages. (See schematics for their efficiencies)

- the **second generation** consists in copper-indium-gallium-selenide (CIGS), cadmium telluride (CdTe) and amorphous silicon (a-Si) and is based on thin-film technologies. As such, their thickness allows reducing the production cost to about \$1/W and reaching a wide range of applications. (See schematics for their efficiencies).

## 1.4 Dye Sensitized Solar Cells (DSSC)

This section will develop on the aspects of **3<sup>rd</sup> generation** solar cells (12) and focus on a specific one that we have used in this thesis.

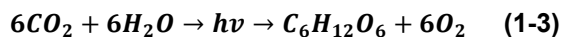
- **Multi-junction solar cells** are used in aerospace applications and consist in different semiconductor layers, converting sunlight into electricity. They are a type of tandem solar cell and exhibit PCEs up to 37% in laboratories (13). They are not yet commercially available due to their complicated and difficult production process which uses expensive materials.
- **-Organic solar cells** or OPVs are constituted by  $\pi$ -conjugated polymers or small organic molecules (14). Because these materials are soluble in common solvents, they can be deposited onto various substrates, such as flexible substrates, using roll to roll techniques or other printing techniques that are considerably less costly. Their main drawback relates to their susceptibility to degradation. Improvements are still required before this promising technology can be commercialized.

The three other technologies, DSSC, quantum dot solar cells (QDSC) and perovskite solar cells have been widely studied by the research and development community due to their ability to grow fast and their heavy reliance on nanomaterials.

We will now focus on the specific technology selected for this thesis: Dye Sensitized Solar Cells.

### 1.4.1 Background concepts

Biomimetics has been used for many innovations in materials science and will continue to be the path for future technological developments. DSSC are no exception to this trend. The well-known photosynthesis phenomena in plants in which solar energy is converted into biochemical energy has been imitated by scientists (15) since the 1970s (as shown in Eqn.1-3) (16).



The possibility to develop artificial photosynthesis rapidly stirred interest in the field of solar energy.

#### 1.4.2 Excitonic solar cells

The nanometer scale structural organization of the architectures of third generation solar cells is a crucial factor in their ability to convert incident light into electricity. Like all other solar cells, DSSC are grouped in a specific class of devices which requires an effective sequential task for solar energy harvesting:

1. photoexcitation of charge carriers in light absorbing material, and
2. the separation and extraction of the free charge carriers to external electrodes.

However, details in the process sets 3<sup>rd</sup> generation solar cells aside from others. Firstly, unlike the other inorganic solar cells that exhibit high charge mobility ( $450 \text{ cm}^2 \text{ V}^{-1} \text{ s}^{-1}$  for silicon), DSSC, along with OPVs, have lower charge transport mobilities (17) which causes to reduce the effective thickness of the active single layer (100 nm compared to  $\sim 100 \text{ }\mu\text{m}$ ) dependent on the absorption cross section of the material, to absorb a significant fraction of incident light. In fact, excitonic SC have the strong tendency for the exciton to recombine before it reaches the interface or when it encounters defects. Secondly, and most importantly the nature of electronic excitation following photon absorption sets them aside. In fact, after absorption the excited electron remains in a bound state with its conjugate hole, thus creating electron-hole pairs called excitons.

Excitonic states arise from the Coulomb attraction of electron-hole pairs. Due to the lack of ordered crystallinity and weak intermolecular forces, DSSCs do not exhibit delocalized electronic band structure allowing electrons to freely move throughout the structure. Moreover, the absence of strong dielectric screening induces stronger exciton binding at room temperature (binding energy smaller than  $kT$ ). Thus, the generation of free charge carriers does not coincide with light absorption as in conventional cells.

Therefore, for an effective photovoltaic effect to take place, they need to generate and simultaneously dissociate the exciton at a donor-acceptor interface. To this end, we need to constitute a hybrid system known as a heterojunction. For this purpose, the interface must have a strong interfacial interaction energy between the two junctions. This is possible through molecular or band energy levels that are energetically favourable for forward charge transfer of an electron or hole across the interface.

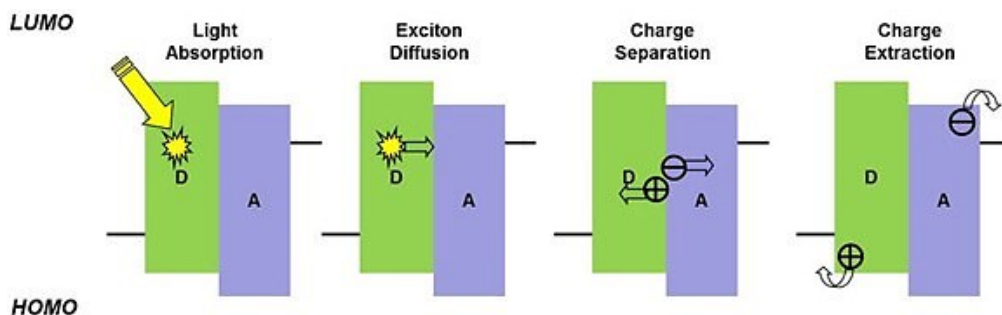


**Figure 1-5 Band diagram and main processes in excitonic solar cells (18)**

Typically, the nanostructured material should be small enough (10 nm) to produce and dissociate excitons at or close to the interface and thick enough (100 nm) to absorb sufficient light. Therefore, when these devices are not well fabricated, they can exhibit smaller performances and shorter lifetimes. Among the many applications that have been developed from hybrid systems for the conversion of light energy we can cite:

- i. Water splitting: the dissociation of water that has the objective of producing hydrogen and oxygen from water (19). This will be developed in the following section.
- ii. CO<sub>2</sub> photoreduction through homogeneous catalysis (20) that can potentially be useful for tackling greenhouse gases.
- iii. DSSC that we will develop further in the next section.

### 1.4.3 DSSC: Applications and practical limits

Following the work of Fujishima and Honda in 1972, that discovered photocatalytic decomposition of water on top of a monocrystalline titania dioxide electrode (TiO<sub>2</sub>) (21), Grätzel and O'Regan developed the first Dye sensitized solar Cell in 1991 by combining the electrode with an efficient charge injection dye (22). By using thin nanocrystalline mesoporous TiO<sub>2</sub> films and increasing light absorption with a porous structure, they opened new perspectives by increasing 10 fold to up to 7.9% the performances of photoelectrochemical devices (23) (see **Figure 1-6**).

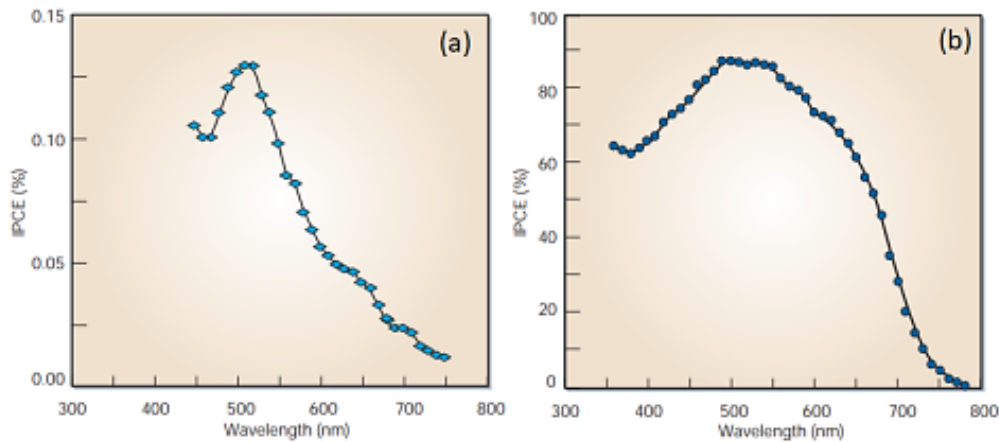


**Figure 1-6 The effect of using a mesoporous photoanode in DSSCs: IPCE as a function of the excitation wavelength; (a) Single crystal anatase TiO<sub>2</sub>, (b) Mesoporous anatase TiO<sub>2</sub> film (22)**

DSSCs are produced by a less energy intensive manufacturing process than silicon-based solar cells, they can be fabricated on flexible substrates and their performances are not affected by temperature increase (24). With a good energy payback time (months vs years for conventional silicon-based solar cells (25)), they have reached up to 14% and 10% PCE in laboratory and in modules respectively (26).

**Table 1-1: Comparison between semiconductor based solar cell and the dye sensitized solar cell (27)**

	<b>Semiconductor Solar Cells</b>	<b>Dye sensitized Solar Cells</b>
<b>Transparency</b>	Opaque	Transparent
<b>Pro-environment (material and process)</b>	Normal	Great
<b>Power generation cost</b>	High	Low
<b>Power generation efficiency</b>	High	Normal
<b>Color</b>	Limited	Various

Due to their specific hybrid architecture, DSSCs can only capture light through very thin films of dye which can be deposited with solution processable techniques. This also means that we can manufacture simple and low cost large-scale devices compatible with industrial production

methods such as spin coating, roll to roll processing, inkjet or screen printing. Hence, unlike inorganic solar cells, DSSC devices can be both flexible and light-weight and can be more easily incorporated into consumer goods, such as backpacks (28).

Another advantage comes from the strong absorption properties under low or diffuse light conditions. Due to this, DSSC outperform conventional silicon solar cells in low indoor light and diffused (cloudy) outdoor sunlight. Along with the fact that these cells are also often highly coloured, they can absorb from both sides which is excellent for decorative uses such as building façades (see **Figure 1-7**) and in building integrated photovoltaics (BIPV) (29). Overall the return on investment is faster for DSSCs than conventional solar cells.



**Figure 1-7 DSSC façade at the SwissTech convention center at École Polytechnique fédérale de Lausanne (30)**

Despite these advantages, their commercialization remains limited due to several drawbacks:

- i) some liquid electrolytes can be corrosive and dissolve many commonly used sealants and metal interconnects in devices;
- ii) the production cost is still fairly high; it can be reduced by replacing expensive sensitizing dyes;
- iii) the performance and long-term stability still to be improved.

Since 2015 a decrease in the number of publications on DSSC can be observed due to the number of research groups that have reoriented their focus on perovskite solar cells. This emerging technology that uses perovskite films instead of dyes for photon absorption, has in fact reached up to 25.5% PCE in less than a decade, making them the fastest growing solar technology to date despite their unproven long-term stability and their sensitivity to moisture (31).



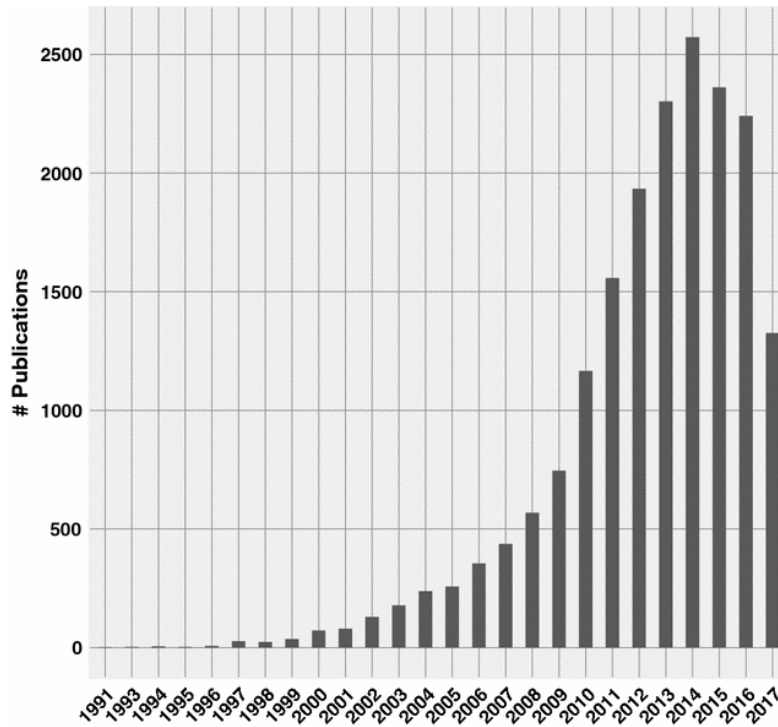
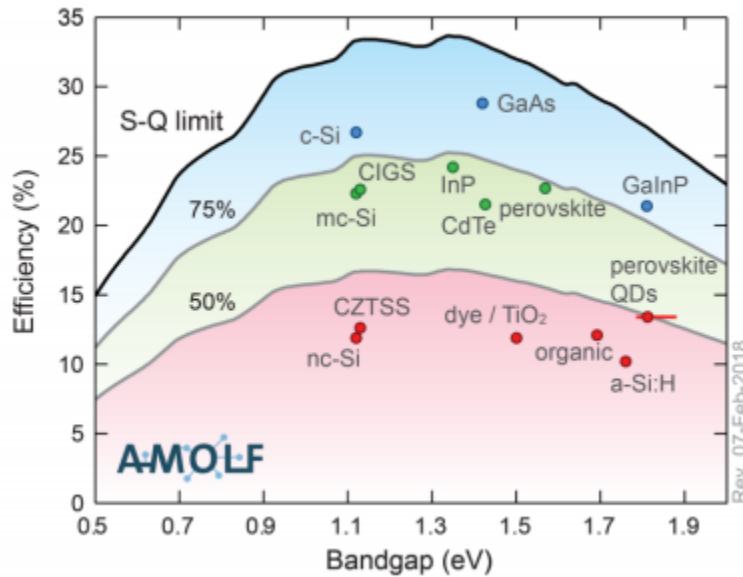


Figure 1-8 Evolution of publications counts with "Dye sensitized solar cells" (32)

The current PCE of DSSC amounts to 14% with low cost materials, and easy production methods (33). However their performances are still distant from their Shockley Queisser limit (6).



**Figure 1-9 Comparison between the most efficient single junction solar cells with the fundamental Shockley-Queisser limit (black line) (34)**

Another technology developed in this thesis, is that of quantum dot solar cells (QDSC), in which inorganic Quantum Dots replace the Dye molecules used in DSSCs and act as sensitizers. By changing their size, nanocrystals can exhibit tunable bandgaps across a wide range of energy levels, which, enables effective light-harvesting in the NIR region. QDSCs yield PCEs up to 16.6% (35).

#### 1.4.4 Theoretical Background

In this section we will describe in greater detail the structure and working principle of DSSCs.

Considering that the wideband gap of usual metal oxide semiconductors (above 3 eV) can only absorb ultraviolet light (around 380 nm), DSSC have to use a dye molecule layer responsive to visible and infrared radiation, which represent most of the photons of the solar spectrum.

The following equations (36) summarize the overall reactions that take place in DSSCs:



A potential also appears within the system due to the difference in the chemical potential between the redox couple and the semiconductor (see **Figure 1-10**). The injected electrons travelling from the dye through the semiconductor are responsible for the elevation of the Fermi level which in turn creates the photovoltage.

To place this in perspective, it is important to describe with more precision the key processes linking the functioning DSSC with different kinetics of the reactions at each component of the device:

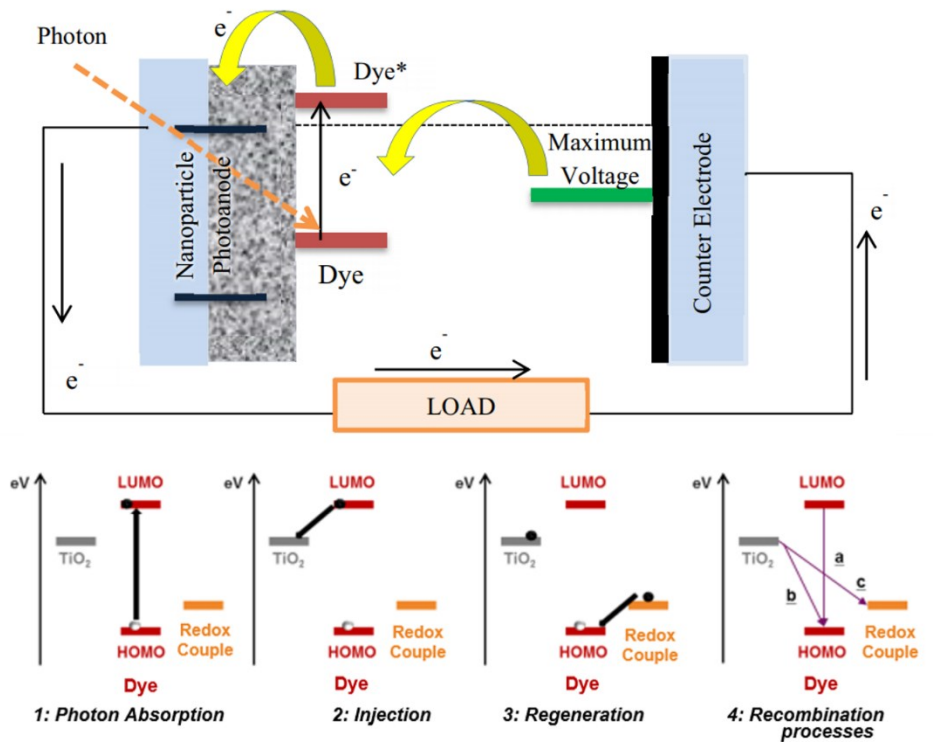


Figure 1-10 Working operation of DSSC (37) (38)

#### 1.4.5 Composition and working principle of DSSC

The basic mechanism, in **Figure 1-10**, is as follows:

- (1) Under illumination, absorption of the energy of light by the dye molecules, which generates an excited state. (1-4)
- (2) The photoexcited electrons are not stable and thus are captured by the conduction band of the semiconductor (from the LUMO of the dye), realizing the separation of holes and electrons. (1-5)
- (3) The separated carriers are then transferred to their respective electrodes, anode for the electron and
- (4) The counter electrode for the hole.
- (5) The electron-deficient electrolyte will get the electron from the counter electrode, completing the circle (1-7)

The electrons in the semiconductor are not driven by an electrical field like in Si solar cells. In fact, the size of the nanocrystal semiconductor (around 20 nm) is too small for any electrical field to form (39). The electrolyte is not able to create an electrical field due to the high concentration of charged species which screen the loads that can generate this field.

The composition of the cell comprises five parts: Transparent conducting substrate, porous nanocrystal semiconductor film, the photosensitizer (dye), electrolyte and the counter electrode. DSSCs is a kind of heterojunction solar cell with electrons and holes that are separated by two chemicals.

#### **1.4.5.1 Transparent Conducting Oxide**

The substrate used for the outside circuit must be highly transparent to allow the maximum passage of light towards the active area of the cell. Its electrical conductivity must also be high to reduce ohmic losses (dissipative) (40). Typically, a glass substrate covered with a layer of FTO (fluorine-doped tin oxide,  $\text{SnO}_2$ : F) or ITO (indium tin-doped oxide,  $\text{In}_2\text{O}_3$ :  $\text{SnO}_2$ ) is used.

The FTO layer has about 80% transmittance in the visible region and a square resistance of about  $10 \Omega/\square$  while the transmission of the ITO layer can approach 85% for the same square resistance (41). In contrast, after annealing at  $450^\circ\text{C}$  in oxygen atmosphere for two hours, the square resistance of the FTO substrate did not change (41), while that of ITO substrate increased beyond  $50 \Omega/\square$ . This thermal stability of FTO substrates leads to their use mainly for DSSC cells, which require in most cases annealing at these temperatures to obtain a porous metal oxide layer that allows for electrons to percolate (see following sections).

Due to their flexibility and low production cost, polymeric substrates such as Polyethylene naphtalate (PEN) (42) or polyethylene terephthalate (PET) (43) can also be used but cannot sustain more than  $150^\circ\text{C}$  heat treatments.

In this work, we use classical FTO substrates and most often, a 100 nm thin blocking layer of  $\text{TiO}_2$  is deposited on the transparent electrode before the porous layer (44), to prevent holes direct contact with the FTO/electrolyte interface, as this could generate current leaks in the cell.

#### **1.4.5.2 Photosensitizer**

The photosensitizer or dye is a component that can absorb visible light and is actively involved in light harvesting forming excited electrons or exciton (1-4), in charge separation and in the electron and hole injection into the oxide semiconductor (1-5) and into the hole conducting material (1-6)

respectively. It is grafted on the surface of the metal oxide with which the energy level needs to be matched for the electrons to be injected into the conduction band of the semiconductor. The oxidized photosensitizer has oxidation ability, while the semiconductor shows a reduction ability because of the injection of electrons in the conduction band.

The dye must meet the following requirements: (28, 45)

(1) An anchor group (-COOH, H<sub>2</sub>PO<sub>3</sub>, -SO<sub>3</sub>H, etc) must exist in dye molecules, for strong adsorption on the metal oxide (46, 47)

(2) The latter point requires the absorption from a single layer to ensure an efficient charge transfer of the electrons to the metal oxide. This means that the aggregation of dyes on the semiconductor surface is detrimental.

(3) Absorb all wavelengths extending from visible to even the near infrared (NIR) region, as 40% of solar light is emissive in this region. It must thus possess a high molar extinction coefficient ( $\epsilon > 10^4 \text{ mol}^{-1} \cdot \text{L} \cdot \text{cm}^{-1}$ ). This step helps to promote electrons from a lower to a higher energy level, through excitation. The electron lifetime of the photoexcited dye is about  $10^{-9}$  -  $10^{-8}$  for metal complex dyes (48)

(4) The LUMO level of the dye must have a potential more negative than the CB of the metal oxide semiconductor (higher than -4,0 eV for TiO<sub>2</sub> and -3,9 eV for ZnO) for an efficient charge transfer. This electron injection, at the dye/metal oxide interface, usually occurs at surprising fast speed ranging from femtosecond to picosecond (49), while the relaxation time from the excited state to the ground state is about 1000 times slower, at 20-60 ns (Ruthenium dye). This kinetic gap is a fundamental guarantee for electron injection in DSSC.. Typically the electron injection is faster for organic dyes than that for metal complex dye (49).

(5) For the dye regeneration process, electrons from the redox mediator reduce the dye cation in a microsecond period hence the lifetime of the oxidized dye should be higher than 100s (49). In the case of liquid electrolyte, the redox potential ( $E_{redox}$ ) closely linked to the HOMO level, and more precisely its oxidized state energy level, which must be at more positive potential with respect to the energy level of the hole conducting material for efficient regeneration.

The electrochemical potential of the redox mediator is given by Nernst's expression (shown in Eqn. 1-8) in:

$$E_{redox} = E^0 - \frac{RT}{nF} \times \ln \left( \frac{[Red]}{[Ox]} \right) \quad (1-8)$$

With  $E^0$  is the standard potential,  $R$  is the universal gas constant,  $T$  is the temperature,  $F$  is Faraday's constant.  $[Red]$  is the concentration of the reduced species and  $[Ox]$  is the concentration of the oxidized species.

The widely used Ru dye can be efficiently excited and regenerated with  $10^8$  circles (20 years stability).

Another important point is the holes produced by  $TiO_2$ , which would oxidize the absorbed dye, changing the property of the interface, and decreasing the efficiency of the solar cell as a result. Hence, we would want to reduce UV light absorption.

(6) The dye should be light, electrically and thermally stable under light for at least 20 years.

Based on these requirements, many different sensitizers have been studied and significant advances in design and synthesis for DSSC applications has been reported.

Dyes can be classified into three main categories:

**Metal complexes**, in which the Ruthenium (Ru) metal organic complex is excited by absorption of a photon. In general it is composed of a metal center and ligands containing anchor groups. The metal-ligand structure contributes in the absorption and the charge transfer mechanism before the excited electron is transferred to the conduction band of the metal oxide through an anchor group (48).

**Porphyrin, phtalocyanine**, serves as remarkable candidates of dye for DSSC due to their good photoelectric response in the NIR. They also exhibit good resistance to heat, light and chemical agents.

Over the last years scientists have synthesized many dye molecules and due to the high price of Ru, metal free dyes have also been reported (50).

**Several nanocomposite materials using QD** such as  $CdS/TiO_2$ ,  $CdSe/CdS/TiO_2$  etc have been recently reported (51), and will be discussed further in this thesis (Chapter 5). Instead of using a dye photosensitizer, these narrower bandgap QD semiconductors exhibit quantum confinement that allows them to tune their bandgap to harvest more photons. Moreover, they can promote the separation of photogenerated excitons, effectively prolonging the carrier lifetime and promoting electron transfer from the interface to the adsorbed species.

### 1.4.5.3 Semiconductor

The nanocrystalline semiconductor represents the central component in DSSCs. Together with the photosensitizer, they are called the photoanode. . It separates the charges via its electronic configuration and assures the diffusion of charges through transport and recombination networks of percolating particles.

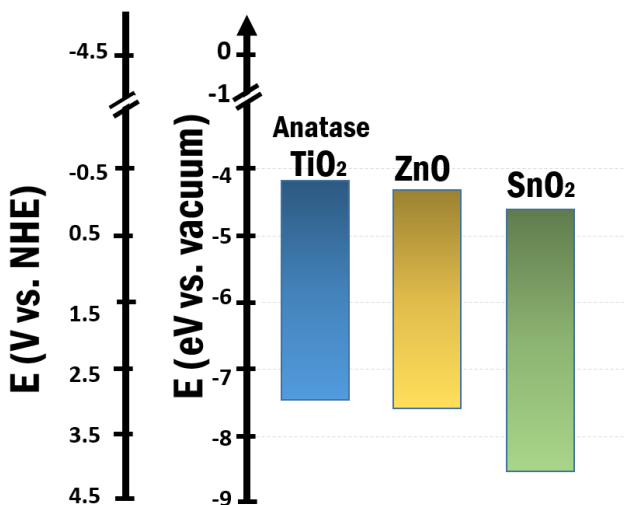


Figure 1-11 Energy band diagram for various semiconductors used in DSSC.

The photoanode should first be a wide band gap metal oxide layer deposited on top of a conductive TCO substrate (52). A large surface area is needed to enable high dye loading and a fast charge transport rate is needed to ensure high electron collection efficiency ( $\eta_{\text{coll}}$ ).

Metal oxide semiconductors have a large bandgap (around 3 eV) (see **Figure 1-11**), and thereby avoid absorption and scattering in the visible region. They must have an appropriate energy level gap which matches with the excited state of the dye to allow fast electron injection within the conduction band without degrading the open circuit voltage ( $V_{\text{OC}}$ ).

Although other metal oxides have been tested such as ZnO, SnO<sub>2</sub>, etc, TiO<sub>2</sub> nanocrystalline despite its low electron mobility ( $0.5 \text{ cm}^2 \text{ V}^{-1} \text{ s}^{-1}$ ) has been used to obtain the highest PCEs and thus still represents the conventional layer of choice.

Table 1-2 Power conversion efficiencies as a function of the metal oxide used in DSSCs

Metal oxide	PCE (%)	Dye	Electrolyte
-------------	---------	-----	-------------

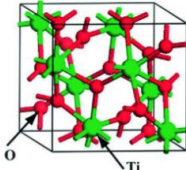
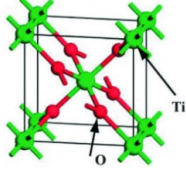
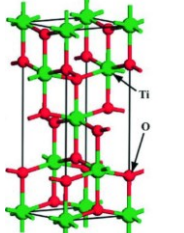
<b>TiO<sub>2</sub> (26)</b>	14.5	N719	I <sup>-3</sup> /I <sup>-</sup>
<b>ZnO (53)</b>	7.5	N719	I <sup>-3</sup> /I <sup>-</sup>
<b>SnO<sub>2</sub> (54)</b>	4.4	N719	I <sup>-3</sup> /I <sup>-</sup>

We will therefore focus on TiO<sub>2</sub>. Pure TiO<sub>2</sub> is a colorless and non-toxic oxide with a high refractive index and brightness. It is an ionic compound and exhibits strong electron–phonon coupling, known as polarons. Titania is the ninth most abundant element (55) on Earth and has almost 7 million tons/year of production capacity, among which 0.7% is dedicated for TiO<sub>2</sub> nanostructures. At the nanoscale, it gives rise to a variety of applications such as white pigments in surface coating, toothpaste, food coloring and cosmetics or as self-cleaning function, as anti-fogging function and as photocatalyst (56).

It is widely known to possess three different crystallographic structures: Rutile, Anatase and Brookite. Their crystallographic parameters are described in **Table 1-3**:

For an efficient DSSC, nanoparticles of 20 nm are required and among these three crystallographic phases, anatase represents the one which has a suitable structure for dye adsorption (see **Figure 1-12**). This is obtained by transitioning from the stable (57) rutile surface to mesoporous anatase which provides energetically favorable phase for small (below 40 nm) nanoparticles to adsorb more dye on their surface.

**Table 1-3 TiO<sub>2</sub> crystallographic characteristics and physical properties (58–60)**

TiO <sub>2</sub> forms	Brookite	Rutile	Anatase
<b>Crystalline structure</b>	Orthorhombic 	Tetragonal 	Tetragonal 
<b>Space group</b>	Pbca	P42/mmm	I41/amd
<b>Lattice parameters</b>	a = 9.16 Å, b=5.43 Å c = 5.13 Å	a = b = 4.58 Å c =2.96 Å	a = b = 3.78 Å c = 9.51 Å
<b>Bandgap</b>	3.4 eV	3.0 eV	3.2 eV
<b>Refractive index</b>	2.66	2.70	2.52
<b>Electrical Conductivity</b>			10 <sup>5</sup> S.m <sup>-1</sup> (at 300K)



Electron mobility		$0.1 \text{ cm}^2 \cdot \text{V}^{-1} \cdot \text{s}^{-1}$	$0.5 \text{ cm}^2 \cdot \text{V}^{-1} \cdot \text{s}^{-1}$
-------------------	--	--	--

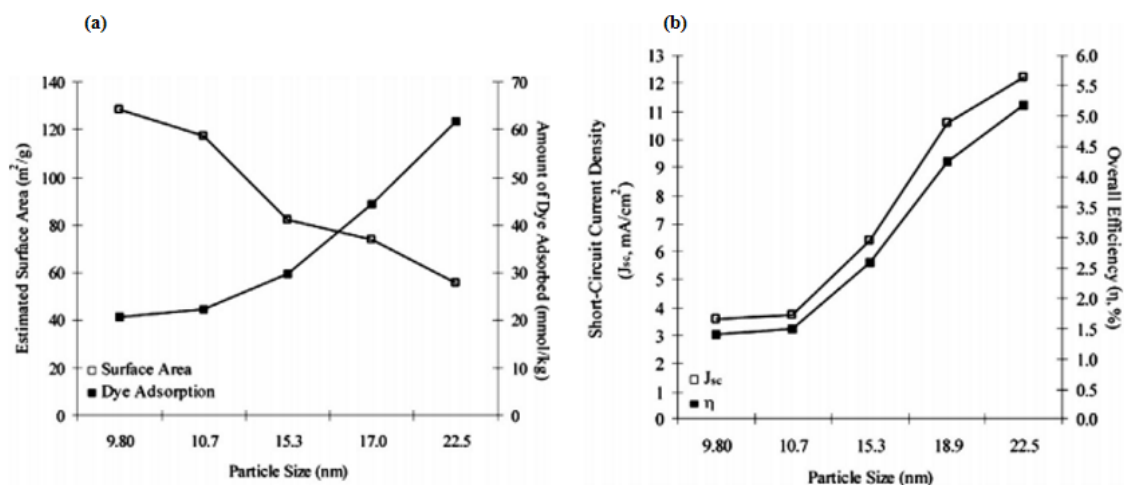


Figure 1-12 (a) Dye adsorption as a function of particle size and (b) efficiency of DSSC as a function of dye adsorption (61)

Nanoparticles are used to fabricate the photoanode using different techniques such as doctor-blading, screen printing, etc. (62), which can provide a large surface area for dye absorption as well as relatively high porosity for efficient dye / electrolyte penetration.

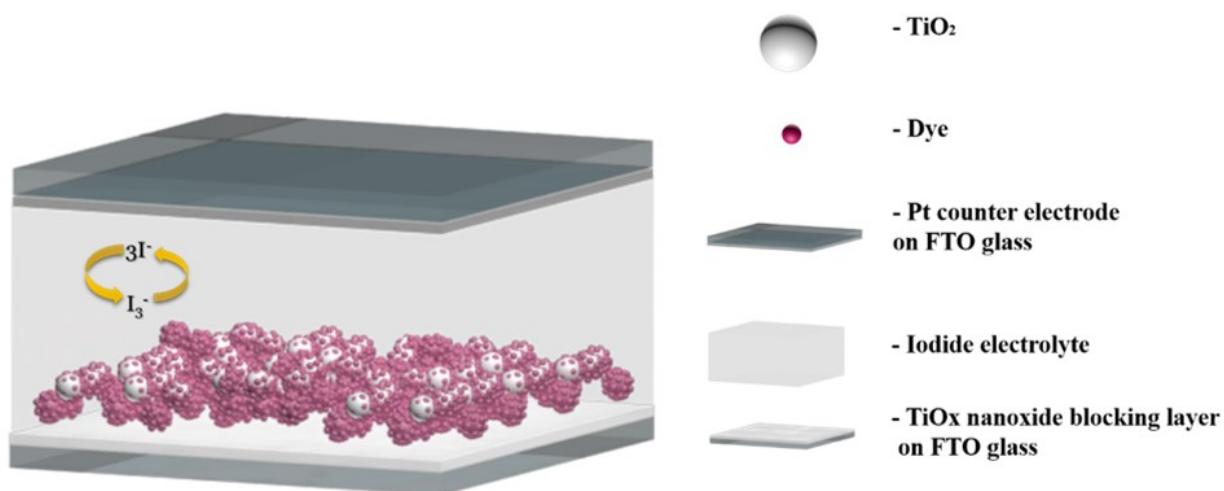


Figure 1-13 Schematic of the structure of a dye sensitized solar cell

Due to the large bandgap of  $\text{TiO}_2$ , it is only able to absorb UV light below 380 nm and so has low conversion efficiencies. Subsequently, the photogenerated charge is injected into the semiconductor with a wide band gap after this one goes into sensitization..

#### 1.4.5.4 Electrolyte

The main function of the electrolyte is to regenerate the reduced dye following the injection of electrons to the conduction band of the semiconductor. This regeneration is rather easy in the presence of catalyst. In liquid electrolytes, diffusion is the transport mechanism of the oxidized species toward the counter electrode (1-10).

Modifying the electrolyte affects directly dye regeneration, the diffusion kinetics within the electrolyte, recombination phenomena and charge transfer kinetics (63). It is thus important to note that, long-term stability of DSSCs depends in part on the properties of the electrolyte.

A good electrolyte must (64):

- i) have a high electrical conductivity for rapid diffusion of charges,
- ii) have a unique contact interface with the sensitized semiconductor and the counter electrode,
- iii) not cause desorption or degradation of the dye,
- iv) not present any absorption in the visible range which would risk screening the absorption of the dye,
- v) be chemically stable and viscous to facilitate charge transport,
- vi) possess a high boiling point, over 80°C.

Although liquid, quasi-solid and solid-state electrolytes have been developed, liquid cells still display the highest PCEs (after perovskite cells) (65), thanks to the great ease in infiltration of mesoporous layers.

With a thickness of the porous layer reaching about 15  $\mu\text{m}$ , a large amount of dye is rapidly available for regeneration of the oxidized dye (66).

The conventional redox mediator is the triiodide/iodide ( $\text{I}_3^-/\text{I}^-$ ) redox couple (22) its oxidation potential ( $E^0_{\text{ox}} = 0.35\text{V}$  vs NHE and  $E^0_{\text{ox}} = 0.53\text{V}$  vs NHE) in Acetonitrile (ACN) and in water respectively is suitable with respect to the HOMO level of most dyes, it has a good solubility. Most importantly, it has a fast dye regeneration and its recombination kinetics is slow with  $\text{TiO}_2$  which is the reason why the ( $\text{I}_3^-/\text{I}^-$ ) redox couple is the basis of the most widely used liquid electrolytes with the highest reported PCE of 14.3% (26).

Despite the good performances, this redox couple displays several disadvantages (67):

- i) it is highly corrosive and dissolves many of the commonly used sealants and metal interconnects;
- ii) the dye regeneration by the couple results in a low oxidation potential representing a large internal loss (600 mV) in potential;
- iii) it absorbs a portion of the solar spectrum under 500 nm.

Other alternatives have been studied to avoid these shortcomings. To date, the cobalt electrolyte has one of the best performances (68) and additives within the electrolyte are able to play a very important role in determining the photovoltaic performance.

#### 1.4.5.5 Counter electrode

Counter electrode (CE), also known as the photocathode, is the electrode that has to regenerate the electrolyte (69). The nature of the CE may vary depending on the type of electrolyte being used. Due to their role, CEs must be highly conductive and stable.

For liquid DSSCs, the most commonly used material is platinum deposited on a FTO based conductive glass. Platinum is generally used due to its excellent chemical and thermal stabilities and its good conductivity (70). Pt is either used in its bulk, nanostructures or nanocomposited form. The deposition methods include electrodeposition, sputtering, vapor deposition method, spray pyrolysis, etc. (71). However, for CEs to exhibit a good electrocatalytic activity, the most effective way is by thermal decomposition of chloroplatinic acid with charge transfer resistance of less than  $1 \Omega \cdot \text{cm}^{-2}$  (72).

Nevertheless, due to its elevated cost, less expensive alternatives to platinum-based CE have been developed. Activated carbon, carbon black, graphite, carbon nanotubes, graphene (73) have been reported as these carbon material also exhibit excellent electrical conductivity, catalytic ability and lower prices.

#### 1.4.6 Electron transport and recombination in $\text{TiO}_2$

A crystalline structure is required in  $\text{TiO}_2$  films in order for dyes to benefit from the leftover spaces that mesoporous structure create when phase transitioning from rutile to anatase crystalline structure. Moreover absorption of dye molecules occupy spaces much smaller than the optical cross section required for effective light capture. In fact, compared to a flat semiconductor surface, typically a 15  $\mu\text{m}$  thick anatase mesoporous layer enhances more than 1000-fold the internal

surface area which provides higher number of dyes for absorption and respectable electron  $\eta_{\text{coll}}$  to DSSC.

However, while the particle size decreases to 20 nm, the diffusion coefficient of single crystal anatase which was  $0.5 \text{ cm}^2 \cdot \text{V}^{-1} \cdot \text{s}^{-1}$ , (58) is reduced to  $0.1 \text{ cm}^2 \cdot \text{V}^{-1} \cdot \text{s}^{-1}$  for crystalline thin films (see **Table 1-3**). This diffusion coefficient of nanoparticles is about four orders of magnitude lower than that of the single crystals which shows how nanostructures greatly affects charge mobility and lifetime of charges which are an important parameter in  $\text{TiO}_2$ -based devices. Electron transport through any bulk semiconductor materials is controlled by its coupling strength that exhibits band-type behavior (i.e. weak electron–phonon interaction with large polarons boasting spatially extended wave functions); and therefore, is inevitably linked to the bonding characteristics (74). Moreover, the anatase phase has a wide band gap leading to quasi Fermi level much more elevated and thus more favorable for high  $V_{\text{oc}}$  (61). Thus, the transport of electrons in the semiconductor takes place by diffusion under the effect of the electron density gradient.

It is therefore not only the particle size, but also the thickness, the pore size, the roughness, and the surface area altogether that make anatase  $\text{TiO}_2$  the preferred phase for DSSC. Electronic transport in a mesoporous structure pass through  $\sim 10^7$  trapping events in nanocrystalline materials which ultimately reduces the diffusion coefficient (75). The density of trap states (76) induces poor diffusion coefficient which transport can be best described as of multiple trapping mechanism. These energy states of surface atoms induced carrier drift lengths ( $\sim 100 \text{ nm}$ ) and charge screening lengths much larger than the particle size thereby indicating that the electrons move through the mesoporous network by trap filling, i.e., trapping and detrapping events (76, 77). This in turn affects electron lifetimes by reducing the diffusion length and increasing recombination (78).

To obtain an excellent  $\eta_{\text{coll}}$  the electron diffusion length ( $L_n$ ) must be greater than the semiconductor film thickness ( $d$ ) (79), in other words, the electron transport life time ( $\tau_n$ ) must be larger than the electron transport time ( $\tau_{\text{tr}}$ ).

The key processes of the operating principle and its kinetic characteristics within each component described in **Figure 1-14**, help understand the influence of kinetic mechanisms within layers.

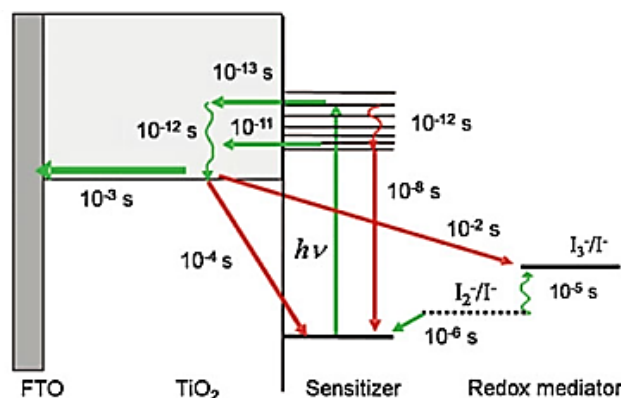


**Figure 1-14 Working principle of a DSSC and kinetics (28)**

The electron transport in DSSCs through the mesoporous electrode is coupled with the electrolyte as there is a junction capacitor in the metal oxide–electrolyte interface (**Figure 1-14**). The capacitive charging at this junction further delays the electron diffusion that is coupled with the ion movement in the electrolyte.

The recapture of the electrons from the conduction band of the semiconductor to the oxidized dye and the one to the oxidant of the electrolyte redox couple are the two main parasitic processes that reduce the efficiency of DSSC. However, the kinetics of regeneration of the oxidized dye by the electrolyte reducer is in general faster than the recapture (100 times higher). This means that the loss of efficiency through this mechanism affects only minimally the overall efficiency.

Thus, recombination reaction to the redox couple is the real factor which reduces the efficiency due to the fact that the lifetime of excited electrons is always related to this recombination process. This process is the main pathway of electron loss (80) and the section on the optimisation of the  $\text{TiO}_2$  nanocrystal photoanode based devices will further describe how to maintain these properties.

#### 1.4.7 Parameters and kinetic aspects of DSSC

The basic principle of the main characterization techniques used in this thesis for the cell performance and functioning are described here. Firstly, we will include current-voltage density (I-V) curve measurement and secondly we will present electrochemical impedance spectroscopy (EIS).

### 1.4.7.1 I-V measurement

This is the most widely and directly used measurement, and is performed by applying a series of voltages to the device. With these measurements we can determine the total cell Power Conversion Efficiency (PCE or  $\eta$ ) (shown in Eqn.1-13) by:

$$\eta = \frac{|J_{\max} \times V_{\max}|}{P_{\text{in}}} = \frac{J_{\text{sc}} \times V_{\text{oc}} \times FF}{P_{\text{in}}} \quad (1-9)$$

with,  $FF = \frac{|J_{\max} \times V_{\max}|}{J_{\text{sc}} \times V_{\text{oc}}}$

Where  $P_{\text{in}}$  refers to the power density of the solar irradiation; FF is a value ranging between 0 and less than 1, called fill factor;  $J_{\text{MAX}}$  and  $V_{\text{MAX}}$  are the value of current and voltage respectively when P cell reaches the maximum value;  $J_{\text{SC}}$  is the short circuit current determined at 0 voltage;  $V_{\text{OC}}$  is the open circuit voltage when the current is 0. The maximum value of the product by current and voltage is named the output efficiency.

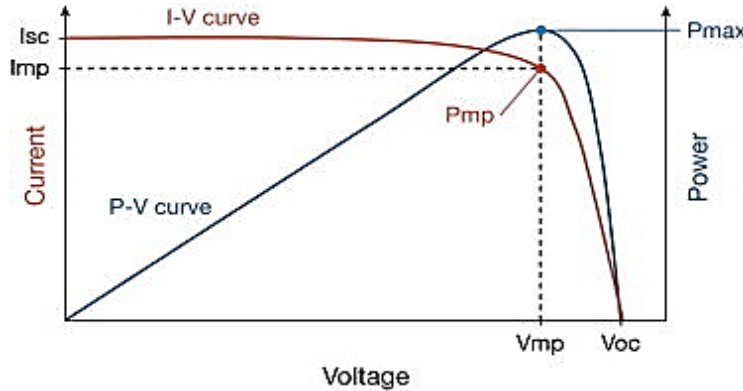


Figure 1-15 I-V photovoltaic characteristics (81)

The value of FF is affected by the internal series resistance of the device that appears at different interfaces, by the intrinsic resistance of materials or the presence of defects in the cell.  $V_{\text{OC}}$  is determined by the difference between the Fermi level and the electrolytes' Nernst potential of the redox pair. So far there are no dye, which can be excited by the whole light spectrum, although, the number of electrons injected into  $\text{TiO}_2$  and the electron transmission efficiency can be originating from dyes excited by different wavelength. .

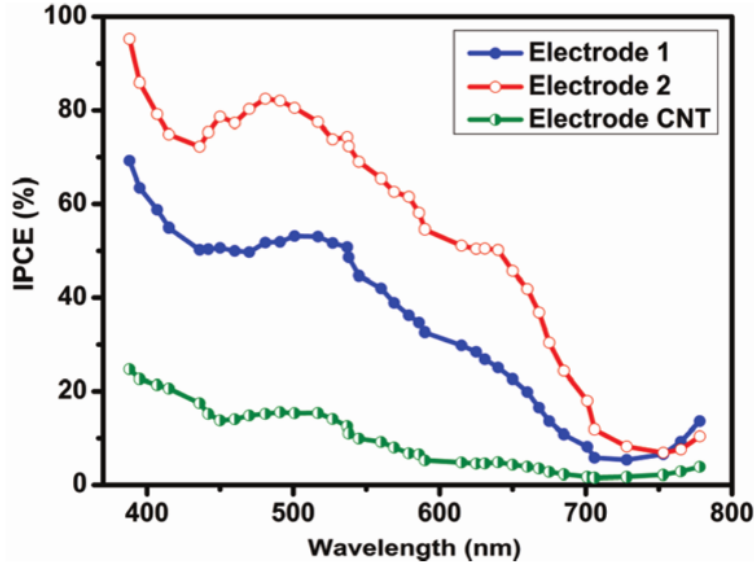


Figure 1-16 Examples of IPCE spectrum for of conventional electrode (Electrode 1), graphene-TiO<sub>2</sub> composite electrode (Electrode 2) and the CNT composite electrode (82)

$J_{SC}$  can be determined via the following equation (1-10):

$$J_{SC} = q \int_{\lambda_{min}}^{\lambda_{max}} I_0(\lambda) IPCE(\lambda) d\lambda \quad (1-10)$$

Where, IPCE (shown in Eqn. 1-11) is the Incident photon to electron conversion efficiency, and represents the number of electrons collected in the cell for a given number of incident monochromatic photons.

$$IPCE(\lambda) = \frac{n_{electrons}(\lambda)}{n_{photons}(\lambda)} = \frac{I(\lambda)hc}{P_{in}(\lambda)e\lambda} \quad (1-11)$$

Here  $J_{SC}(\lambda)$  is the measured current (mA.cm<sup>-2</sup>),  $P_{in}(\lambda)$  is the input power (W.m<sup>-2</sup>),  $\lambda$  is the wavelength of irradiation (nm). The IPCE (shown in Eqn.1-12) is also defined as the product of four fundamental efficiencies:

$$IPCE(\lambda) = LHE(\lambda) \cdot \Phi_{inj} \eta_{coll} \eta_{reg} \quad (1-12)$$

with  $LHE(\lambda)$  is the light harvesting efficiency of the sensitizer,  $\Phi_{inj}$  is the electron injection efficiency from the excited dye to the semiconductor,  $\eta_{coll}$  is the charge collection efficiency at the contact and  $\eta_{reg}$  is the efficiency of dye regeneration.

One way to increase  $J_{SC}$  is to improve the absorption efficiency LHE ( $\lambda$ ) ( $\eta_{abs}$ ). The solar standard (AM 1.5G) unleashes maximum energy for 500 nm, the maximum photon flux is obtained at 670 nm. To obtain the best performances from the active material, it should not only absorb photons of wavelength corresponding to the maximum irradiation, but must also have a broad absorption spectrum and a high absorption coefficient.

#### 1.4.7.2 Electrochemical impedance spectroscopy (EIS)

EIS is a useful tool to study the kinetics of electrical transport in the counter electrode, in the electrolyte and in photoanode of DSSC. It tests the response of cell in amplitude and phase by applying a small sine wave disturbance that reveals the charge transport property induced by fitting the resistors (R), capacitors (C), inductors (L) elements, and other parameters at different frequencies. **Figure 1-17** (a), shows a typical impedance spectrum of a DSSC together with its electrical equivalent model (83) and the Nyquist plot. The diameter of these semicircles corresponds to the bulk resistivity of the composites at different  $V_{OC}$  levels.

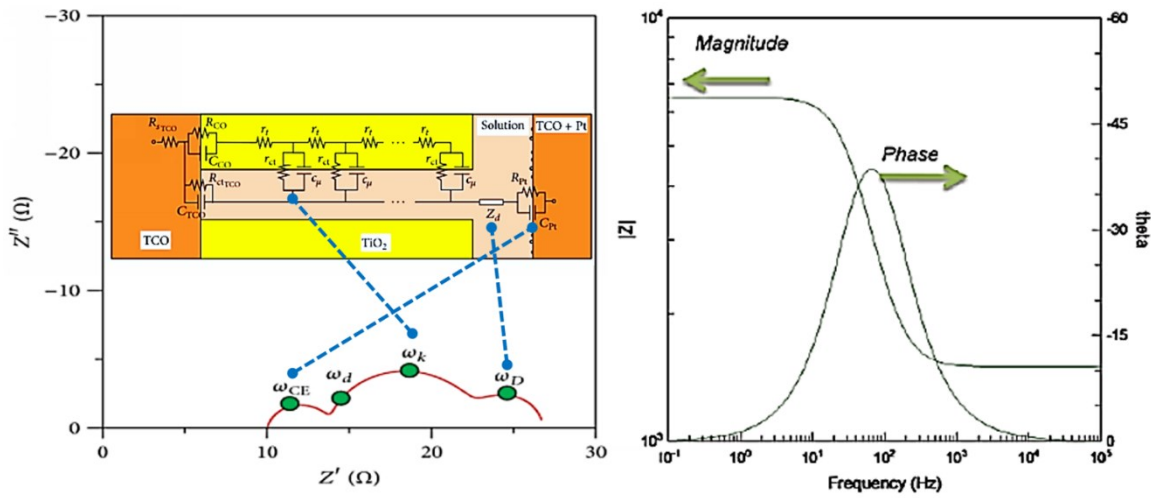


**Figure 1-17** (a) Electrical circuit equivalent of a typical DSSC with Nyquist plot (39) (b) Impedance vs frequency and Bode plot, phase vs frequency (84)

In the equivalent circuit model, the charge transfer resistance of the charge recombination process  $R_{CT}$  (or  $R_{REC}$ ) between electrons in the mesoporous  $TiO_2$  layer and ions in the electrolyte are measured by adapting the model of components.  $C_\mu$  (or  $C_{REC}$ ) is the chemical capacitance of the mesoporous metal oxide film. A constant phase elements (CPEs) are generally used to simulate the impedance data instead of the ideal capacitor.

The lifetime of electrons in DSSCs is a strong function of the open-circuit voltage,  $V_{OC}$ .



The effective electron lifetime  $T_{\text{REC}}$  (or  $T_n$ ), is a quantity that contains information on charge transfer and also the distribution of electronic states and electronic transitions that intervene in the operation of DSSCs. Generally,  $T_{\text{REC}} = R_{\text{REC}} C_{\mu}$ , and are the time constant of circuits. Another electrochemical parameter can be obtained through the phase of the Bode plot. In fact,  $k_{\text{eff}}$ , the effective rate constant for recombination at the photoanode and electrolyte interface can be estimated from the peak frequency  $\omega_{\text{MAX}}$  of the central arc. Here  $\omega_{\text{max}} \approx k_{\text{eff}} = 1/T_{\text{REC}}$ .

Among other terms in **Figure 1-17.(a)**,  $t$  is the transport resistance of the electrons in the semiconductor,  $R_s$  is the series resistance including the sheet resistance of the TCO glass and the contact resistance of the cell, and  $Z_d$  is the impedance parameter designating the diffusion of  $\text{I}_3^-$  in the electrolyte. The subscripts Pt, TCO and CO denote the charge transfer resistance and capacitance parameters at the cathode, TCO-electrolyte interface and TCO- $\text{TiO}_2$  interface respectively.

## 1.5 Structure and working principle of PEC

Among all the technologies which convert solar energy, solar cells and  $\text{H}_2$  generation by PEC cells are considered the most promising ones for renewable and sustainable applications. To tackle the main challenges of environmental degradation and energy supply, Hydrogen has to be produced from water using renewable forms of energy such as sunlight.

There are several ways for hydrogen conversion from renewables. (i) Electrolysis of water using a solar cell, hydroelectric power generation, etc. (ii) Thermochemical processes of reforming of biomass. (iii) Photocatalytic or photoelectrochemical water splitting (artificial photosynthesis).

### 1.5.1 Hydrogen generation from PEC cells

PEC water splitting is one the most prominent processes for solar-fuel conversion providing clean, storable and sustainable energy vectors such as hydrogen directly from sunlight, water and  $\text{CO}_2$ .

The first cell was constructed by scientists Fujishima and Honda in 1972 with the use of a water immersed  $\text{TiO}_2$  photoanode and platinum as cathode illuminated by UV light (21). Water was subsequently decomposed into oxygen evolution at the photoanode and  $\text{H}_2$  at the cathode (85).

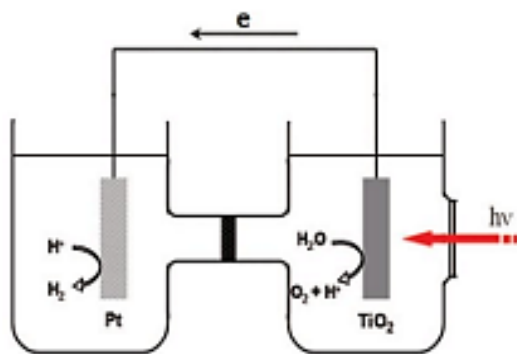
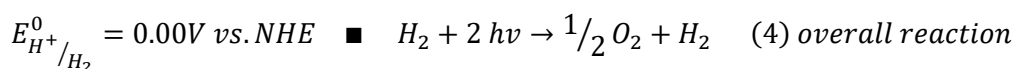
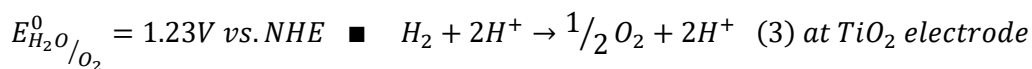
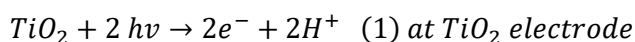


Figure 1-18 Schematic diagram of the PEC cell used by Fujishima and Honda (21)



### 1.5.2 Working principle

The overall PEC water splitting process consists of four steps (see **Figure 1-19**):

- (i) Upon excitation by a simulated sunlight source, the  $TiO_2$  photocatalyst absorbs light irradiation and generates an exciton that promotes the electron to the conduction band and leaves a hole in the valence band.
- (ii) The holes migrate to the photocatalyst surface where they oxidize water to produce oxygen (OER), and
- (iii) The electrons are conducted to a metal electrode (typically Pt) where they reduce  $H^+$  ions in the electrolyte solution to make  $H_2$  (HER)
- (iv) The transport of  $H^+$  from the anode to the cathode through the electrolyte completes the electrochemical circuit.

Under normal conditions, to achieve PEC water splitting, an incident energy of  $\Delta G = 237.1 \text{ kJ/mol}$  is required which corresponds to a thermodynamic electrochemical potential of  $1.23 \text{ V}$  (86). Therefore, for efficient PEC water splitting, the band gap energy ( $E_g$ ) of the photocatalyst must be higher than  $1.23 \text{ eV}$ . In practice, due to various energy losses the bandgap should be at least  $1.8 \text{ eV}$ . The water splitting reaction is shown in Eq. (4).

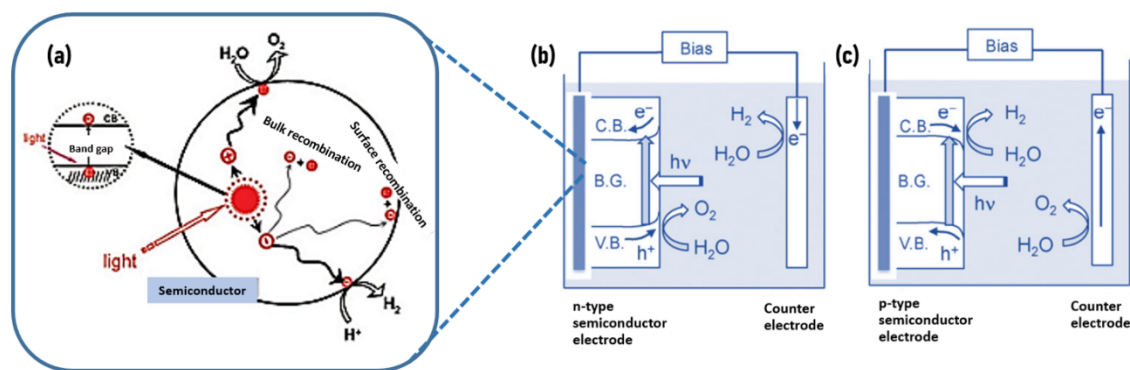


**Figure 1-19 (a) Main processes for charge transport and recombination in photocatalytic water splitting. PEC based water splitting systems implementing (b) n-type semiconductor photoanode, and (c) p-type semiconductor photocathode (85).**

Additionally, the conduction band minima of the photocatalyst must be more negative than the reduction potential of  $H^+/H_2$  (0 V vs NHE), whereas the valence band maxima must be more positive than the oxidation potential of  $O_2/H_2O$  (1.23 V vs NHE).

Since the beginning of PEC water-splitting, whose setup is illustrated in **Figure 1-18**, there has been a significant interest in developing semiconductor materials for efficient photoelectrodes (85).

On a large scale, its application requires low cost, abundant, stable, and nontoxic photoelectrode materials.  $TiO_2$  remains to date, a good candidate to play this role, due to its exceptional stability against corrosion (56).

On the other hand, modifying a photocatalyst with a suitable band width material can improve the overall solar-to-hydrogen (STH) energy conversion efficiency.

### 1.5.3 Quantum dot-based PEC cells

Owing to their capacity of splitting of its electronic band into discrete electronic levels, Quantum dots (QD) have been proposed as promising nanomaterials that can tune their band width by controlling the size, composition and morphology. The exciton Bohr diameter of  $TiO_2$  is 1.5 nm, below which  $TiO_2$  exhibit quantum size effects. The  $TiO_2$  particles considered for DSSC is typically above 20 nm range i.e., much higher than its exciton Bohr radius of 1.5 nm. They are therefore considered as a network of bulk nanocrystals absorbing light only in the UV range. To overcome this drawback, QD sensitized photoanodes have since been promoted to expand the absorption range of light and thus improve the efficiencies of  $H_2$  generation (87, 88).

In this thesis a new kind of CdSe/CdS core-shell structure with a ZnS capping QD with adequate band structure (see **Figure 1-20**) has been used.

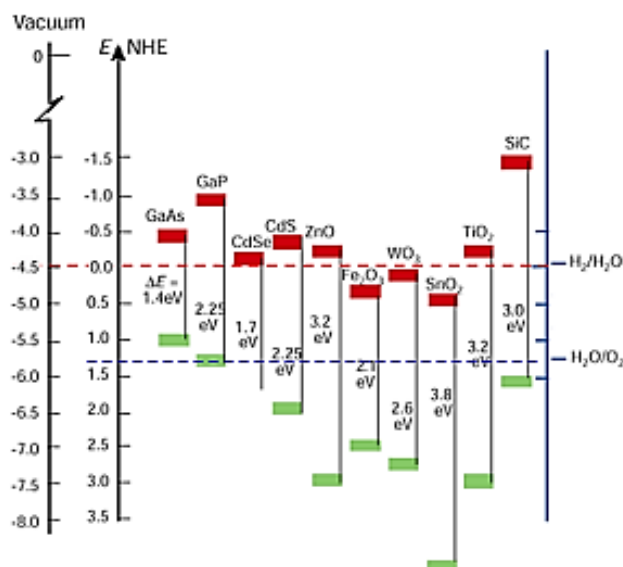


**Figure 1-20 Band structure of different semiconductors with respect to the redox potentials of water splitting (89)**

However, the low conductivity (transportation), the short hole diffusion length (typically 2–4 nm), and the fast electron-hole recombination (charge separation) still limits the performance of PEC water splitting. While this major challenge still has to be overcome before commercialization can be achieved, many studies have since highlighted the importance of nanostructured materials, their morphological and crystalline effects in water splitting (90).

## 1.6 Optimisation of TiO<sub>2</sub> nanocrystal photoanode based devices

One of the major bottlenecks in TiO<sub>2</sub> photoanodes is the transport of the photogenerated electrons across the TiO<sub>2</sub> network. This process competes with charge recombination.

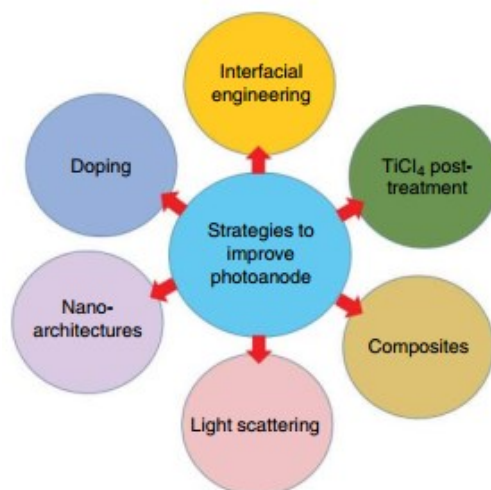


**Figure 1-21 Typical TiO<sub>2</sub> nanoarchitectures for improving DSSC performance**

The main strategies to suppress this recombination and improve electron transport are shown in **Figure 1-21**. We will discuss these approaches that investigate how the modification of TiO<sub>2</sub> photoanode morphologies, the light scattering, the synthesis of suitable architecture and the elaboration of composites have guided choices to improving the performances in this thesis.

### 1.6.1 TiO<sub>2</sub> Nanocrystal Photoanode and its various structures

Although this photoanode consisting of small sized (20 nm) nanoparticles is effective for dye sensitization, there is no scattering for the incoming light since they are transparent to the visible spectrum, thereby hindering light harvesting. To scatter the incident light back to the photoanode, which would typically pass through un-absorbed in a traditional photoanode, a bilayer structure was implemented. The second layer of large nanoparticle, usually 200-500 nm in size are also sdoctor bladed on top of the transparent film. These large nanoparticles trap the incoming light radiation within the photoanode, thereby increasing the light harvesting efficiency (91).

Studies on the morphology of TiO<sub>2</sub> electrodes have sought to replace the mesoporous structure by 1D nanostructures to avoid grain boundaries and defects that increase recombination probability. These 1D structures constitute a direct path for electron transfer and comprise nanostructures such as TiO<sub>2</sub> nanotubes (92). This particular structure exhibits electron scattering coefficients higher than that of nanoparticles. Some photoanodes using TiO<sub>2</sub> nanotubes (6 to 15 µm in length and 295 nm in external diameter for 21-41 nm internal diameter) (93) have shown a yield of 3.5% compared to reference cell. This low yield was attributed to the low specific surface area of this 1D system. Nevertheless, a variety of TiO<sub>2</sub> nanotubes for the formation of a space

charge layer, which can promote electron transport and reduce interfacial recombination (91, 94) have been developed. They show how tube thickness, length, diameter and tube tops influence the performance of DSSCs: (95–98)

- The length of the tube affects the overall PCE of DSSCs. The longer the length the more dye will be adsorbed and thus the higher will be the current density. For high charge collection efficiency, the length of the tube must be less than the electron diffusion length. This is because the current density depends on the charge collection efficiency of the photoanode.
- Adsorption of the dye depends on the inner diameter or pore size of the tube. The larger the pore size the lower will be the surface area for dye adsorption. Spacing between tube will also influence proportionally the high rate of dye adsorption.
- Well-defined and open  $\text{TiO}_2$  nanotube tops can significantly enhance their performance when used in DSSCs.

Moreover, the internal electric field present in 1D nanostructures drives the transport of photoinjected electrons (91) and can extend the diffusion length to be as long as  $100\ \mu\text{m}$  (96). Other photoanode 1D morphologies such as nanofibers (NF) show intense light absorption in the visible range due to high crystallinity and low surface defects. This is partly due to the derived optical path length extending from the wavelength of incident light caused by scattering of light in a layer of  $\text{TiO}_2$  nanofibers (99, 100). Nanowires (NWs) have increased their performance with 9.3% PCE, with the use of oriented attachment network structure to improve the energy barrier at the interface of the semiconductor/electrolyte, reduce the electron transfer to the electrolyte and decrease the density of surface traps have been reported (101).

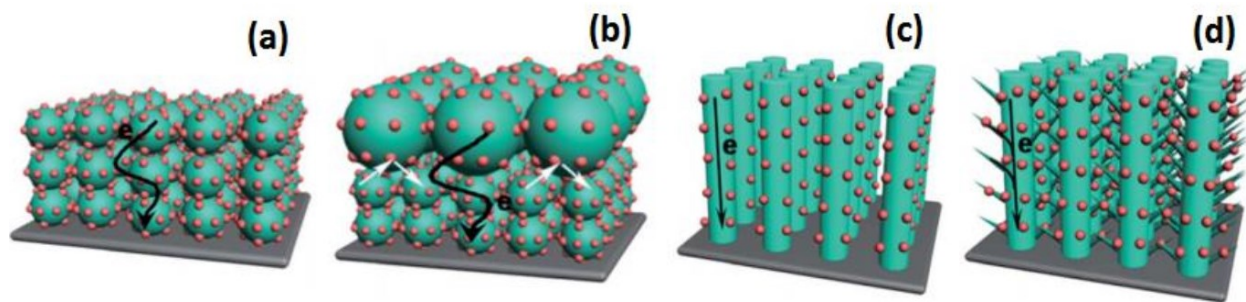


**Figure 1-22 (a) Photoanodes of nanoparticles with transport pathways; (b) bi-layer photoanode with light scattering layer; (c) directional electron transport in 1D nanowires and (d) hierarchical 1D nanowire architectures (91)**

Other nanoscale architectures such as branched nanowires (NW) (102), have been implemented and led to higher performances than bare TiO<sub>2</sub> nanoparticles due to improved dye absorption, electron transport and light scattering ability (103).

Generally, 1D structures must have a high surface area which will lead to sufficient dye loading, higher light absorption. However, electron recombination is also proportional to the photoanode's surface area and thus one-dimensional structures and branched structures may have grain boundaries that limit their conductivity, thus limiting their application in DSSCs. However, to date, films made of TiO<sub>2</sub> mesoporous anatase spherical shape are the most successful structure and morphology due to their porosity, dye absorption, charge transfer, and electron transport with a maximum efficiency over 14% (26). Therefore, this structure has been chosen as semiconducting material in this thesis.

### 1.6.2 Carbon nanomaterials and its composites

The synthesis of TiO<sub>2</sub> of different morphologies require complex processes involving reaction methods for controlling the length, diameter and thickness of nanotubes and the branches of nanowires. Therefore, another approach implicating the use of composites to improve conduction pathways and increase the  $J_{SC}$  have been developed. The addition of 1D nanostructured charge carriers to direct the photogenerated electrons has been proposed. They usually have good electrical conductivity, high electron mobility, and good stability against electrolytes. These materials include nano-objects such as carbon nanotubes and graphene, which are adopted as conducting scaffolds in TiO<sub>2</sub> based DSSC and PEC cell (104).

In 2004, Andre Geim and Konstantin Novoselov (105) reported the isolation of 2D atomic crystal made from sp<sup>2</sup> hybridized carbon atoms, graphene, which is composed of benzene rings. Graphene is the thinnest 2D material to date with a thickness of only 0.35 nm, exhibiting many excellent properties. For example, its tensile strength reaches 130 GPa, the highest among known materials and more than 100 times stronger than steel; its carrier mobility is as high as 15 000 cm<sup>2</sup> V<sup>-1</sup> s<sup>-1</sup>, twice as that of indium antimonide which was previously known to have the highest carrier mobility, and more than 10 times higher than the commercial silicon wafer and under certain conditions (fast cooling ) the carrier mobility can reach 25 000 cm<sup>2</sup> V<sup>-1</sup> s<sup>-1</sup> its thermal conductivity is three times larger than that of diamond, achieving 5000 W m<sup>-1</sup> .K<sup>-1</sup>. Small amounts of graphene in the photoanode does not affect the transparency (106) but creates an electron percolating network, thus not only offering faster electron transport within the photoanode, but also facilitating fast collection of electrons towards the FTO (107).

### 1.6.2.1 Graphene allotropes

The isolation of graphene triggered the emergence of the new graphene nanocarbons family, and with it a reference for building block of low dimensional materials: From 0D graphene quantum dots (GQD), to 1D SWCNT, MWCNT and GNR, 2D graphene, up to three-dimensional diamond and graphite, forming a complete system.

While CNT face challenges such as the control of chirality, separation of metal and semiconductor-type, impurities in catalysts, etc., delaying their use in applications , graphene in comparison avoided many difficulties and has been widely used due to the fact that the major properties of graphene are comparable and even better than those of CNTs.

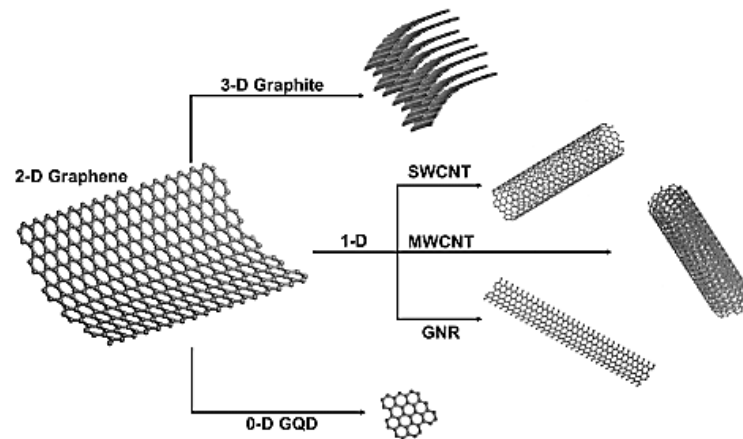


**Figure 1-23 Different allotropes of graphene nanomaterials (108)**

Moreover, planar graphene is suitable for direct fabrication of various semiconductor devices and interconnectors, leading to highly valuable full-carbon integrated circuits. Due to its outstanding mechanical and electrical properties it is possible to synthesize graphene-based flexible electronics and functional composites. With the many advantages including outstanding properties, low cost and good processability, graphene is predicted to have great application potential in fields like electronics, information, clean energy, materials innovation and biomedicine (109).



### 1.6.2.2 Graphene Nanoribbons

Discovered alongside the development of bottom-up and top down synthesis methods, GNRs corresponds to rather a newcomer in the family and is rapidly growing as a fascinating material. Made of a thin and planar elongated strip, GNR are considered a quasi-one-dimensional graphene structure. They possess abundant edges, which help them categorise as armchair, zigzag or intermediate in nature. This edge structure provide them with unique electronic properties from semiconductor to semimetals as their width is increased, and which comes in principle from the boundary conditions.

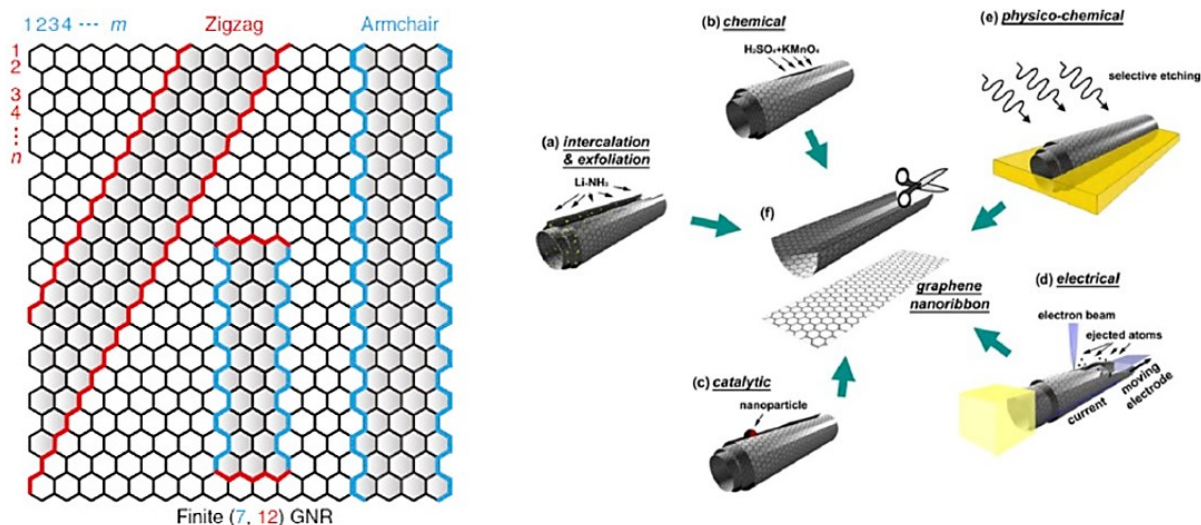


**Figure 1-24** Schematic of edge shape and nomenclature for armchair and zigzag GNRs and Different ways to unzip CNTs for production of GNRs: (a) Intercalation exfoliation, (b) chemical oxidation, (c) catalytic approach, (d) the electrical method, and (f) selective etching by Ar plasma (110)

In fact, GNRs possess bandgaps that distinguish them from extended, two-dimensional graphene together with a high charge carrier mobility (111). **Figure 1-24** shows two basic edge types, namely zigzag (blue) and armchair edges (red).

In comparison to other 1D carbon nanomaterials such as carbon nanotube, GNRs have less reduce surface exposure, inevitably reducing both positive and negative van der Waals forces based interactions that can be highly detrimental. This feature comes from the rolled-up nature of carbon nanotubes exposing its  $\pi$  bonds and causing agglomeration of carbon nanotubes that reduces their ability to use their properties.

However, some GNR may have reduced quality more related to its burgeoning top-down synthesis method. In fact, there are different ways to unzip lengthwise MWCNTs to synthesize

GNRs (see **Figure 1-24**). These procedures are very attractive since they are not only simple and inexpensive but also lead to GNRs with defined shape.

Kosynkin et al (111) developed a wet chemical approach by oxidation to produce in a simple, efficient, and scalable way GNR in solution, however leaving some oxidized edges in the process. Another approach developed by Jiao et al (112) helped produce controlled GNRs with defect-poor structures and good electric performance (with a charge carrier mobility of up to  $15\,000\text{ cm}^2\text{V}^{-1}\text{s}^{-1}$ ) by unzipping PMMA-MWCNT film by oxygen selective etching by Ar plasma.

Although defects are present in any material, some are unavoidably formed during processing of GNR and GNR nanocomposites. They ultimately deteriorate the properties of GNR and other graphene type material and limit their application.

Gentle and environmentally friendly, exfoliation and dispersion techniques contribute nevertheless to form GNRs and make them suitable for various technological applications.

### 1.6.3 Lessons from $\text{TiO}_2$ -nanocarbons nanocomposites

While the kinetics tells us what we can do to increase the efficiency of DSSC, it is by understanding the energy level matching of materials used at each step that we can optimise their performance.

In addition to the quest for higher efficiency, improving stability is also of great importance. One of the major setbacks for both PEC and DSSC cells is the long-term stability of its components. Although DSSCs have issues related with liquid electrolyte evaporation and corrosive power (113), the main issue related with  $\text{TiO}_2$  metal oxides originates from the formation of UV induced deep traps (114), which promotes the formation of excess holes in  $\text{TiO}_2$ . Over time, these holes become recombination centers themselves and induce structural defects and low mobility of charges (114).

In this thesis we introduce GNR- $\text{TiO}_2$  photoanodes to address this issue. Up to now, only few GNR-metal oxide nanocomposites have been studied. These studies are mainly related to their applications in Lithium ion Batteries (115). Nevertheless, owing to their high electron mobility and effective transport path for injected electrons (116, 117), graphene and carbon nanotubes have been widely used to create  $\text{TiO}_2$ -nanocarbon hybrid that were applied in optoelectronics and photocatalysis. Findings from these studies allow us to draw useful information to develop research and development routes on GNRs applications.

### 1.6.3.1 Carbon nanotubes-TiO<sub>2</sub> nanocomposite

Among the carbon allotrope additives, the high conductivity of CNT have been most intensively studied as their large aspect ratio coupled with high conductivity play a crucial role in the high performance of DSCCs (118, 119).

Recent studies show that nanocomposite synthesis methods and the material properties lead to a wide variety of optimal concentration of carbon nanotubes in the active layer of DSSCs. In all cases, once the optimum concentration of carbon nanotubes has been reached, the efficiency of the cell increases compared to the reference cell. For example, Dembele et al. (118) have shown that the efficiency of their liquid cell increases from 7% to 9% when 0.01% carbon nanotube is added within the porous layer. This increase is mainly attributed to improved charge collection and reduced recombination (118).

However, a slight decrease in the open circuit voltage  $V_{OC}$  was also observed, as has also reported by other authors (120–123). This was attributed to the apparent downward shift in the Fermi level of CNT-TiO<sub>2</sub> hybrids towards more positive potentials, affected by the weaker edge of the conduction band of CNTs than that of TiO<sub>2</sub> (120, 122). The shifting towards more positive potentials depends on the carbon nanotubes content. The larger the CNT content, the larger the expected  $V_{OC}$  decrease. Furthermore, the positive shift, owing to the mixing of CNTs, provides a significant driving force to accelerate the electron transport from the dye to the conduction band of the composite, thus improving the charge injection efficiency (124, 125).

The alignment of CNTs exhibit a great isotropic behavior in the two directions. The conductivity in the parallel direction has therefore been demonstrated to be higher than that in the perpendicular direction (126–128).

Guai et al. (129), observed that the semiconducting SWCNTs provide better PCE compared to metallic SWCNT. This could be attributed to the non-continuous band structure of s-SWCNTs, while metallic based SWCNTs possess a zero band-gap (130, 131).

However, due decrease in transparency and to the poor point contact between the round TiO<sub>2</sub> and straight nanotubes, the addition of carbon nanotubes only enables small increases in the overall cell efficiency (132).

### 1.6.3.2 FLG-TiO<sub>2</sub> nanocomposite

Due to their tunable bandgap, high surface area, and high electron mobility, graphene and graphene-based sheets have been reported as efficient components for various parts of DSSCs (133–135). Introduced as additive into nanocrystalline photoanode of DSSCs the 2D structure benefits on the charge separation as it has not only excellent conductivity but has also good area to area contact with the TiO<sub>2</sub>, compared to the point to point contact exhibited by CNTs embedded in the nanocomposite (136).

Many studies show that the FLG-based TiO<sub>2</sub> hybrid photoanodes provide better PCE as compared to CNTs (137–140). In fact, in contrast to its 1D counterpart, a single sheet of graphene provides better contact with the spherical TiO<sub>2</sub> nanoparticles on the nanoscale, thus bridging the mesoporous structure more efficiently. This impacts the overall efficiency of DSSCs owing to lower charge recombination with the electrolyte compared to CNTs.

In addition graphene has a work function (-4.42 eV) (138) which lies precisely between the E<sub>CB</sub> of the TiO<sub>2</sub> (-4.4 eV) (28) and FTO conductive glass substrate (-4.7 eV) (28). This suitable band alignment in turn facilitates the scaffolded transport of photo-injected electrons from the TiO<sub>2</sub>'s conduction band to FTO substrate (140, 141).

Moreover, several factors such as the ratio of the graphene, the size and thickness of the graphene film further determines the efficiency of the solar cell. Small quantities (0.6 %wt) of graphene led to a faster electron transport and a lower recombination, together with higher light scattering. However, excessive graphene content increased recombination processes.

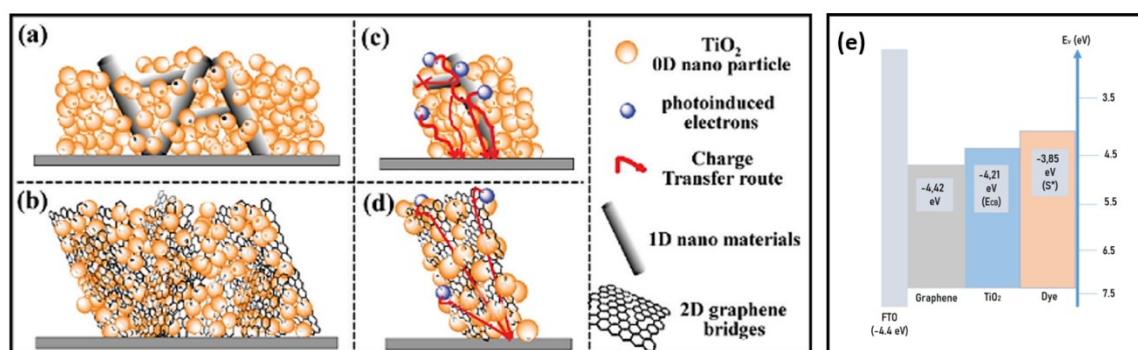


Figure 1-25 Difference between a,c) 1D and b,d) 2D nanomaterials composite electrodes. In 2D nanomaterial composite electrodes (graphene bridges) (140), (e) the energy level diagram of TiO<sub>2</sub>-graphene based DSSCs.

#### 1.6.4 GNR-TiO<sub>2</sub> nanocomposite's influence on the geometry of percolation networks

The following features are more or less common for both CNT and graphene additives.

1) increasing the surface area of hybrid anode and, thus, more dye loading; 2) improving the electron injection efficiency of the electrons due to the increased positive potential; and 3) increasing the electrical conductivity.

Additionally, at high concentrations, most of the beneficial features tend to disappear, limiting further improvement in the PCE of composite photoanodes. This limit is related to a percolation threshold in nanocomposites (142) but also in the intrinsic properties of CNTs and graphene structures.

For CNTs, when the concentration was much larger, the photoanode was essentially composed of CNTs covered by TiO<sub>2</sub> nanoparticles. Therefore, as **Figure 1-27** shows, not only the absorption was affected but the  $V_{OC}$  decrease was much more pronounced and led to a strong decrease of PCE (118, 123). Additionally, at high MWCNT concentrations the partial coverage of the surface of the MWCNTs by the TiO<sub>2</sub> nanoparticles leaves CNTs in direct contact with the electrolyte (143). This creates a preferential path for charge recombination, which results in charge loss and a decrease in  $V_{OC}$ . Besides these drawbacks, the tendency for CNTs to agglomerate with each other at a high concentrations, create detrimental bundles that reduces their practical utilisation for electronic devices (143).

Although van der Waals forces do not have the same effect on graphene flakes, there are drawbacks intrinsic to graphene structures. Free-standing 2D graphene always vibrates to form ripples on the graphene surface, highly conduces to transform the nanomaterial from 2D to 3D nanostructures. As a consequence, while the electrical conductivity of graphene sheet should be ballistic (144, 145) the presence of defects and ripples affect the prediction in experimental situations. These ripples and wrinkles are mainly due to distortions in the structure related to thermal fluctuations or interaction with the host material.

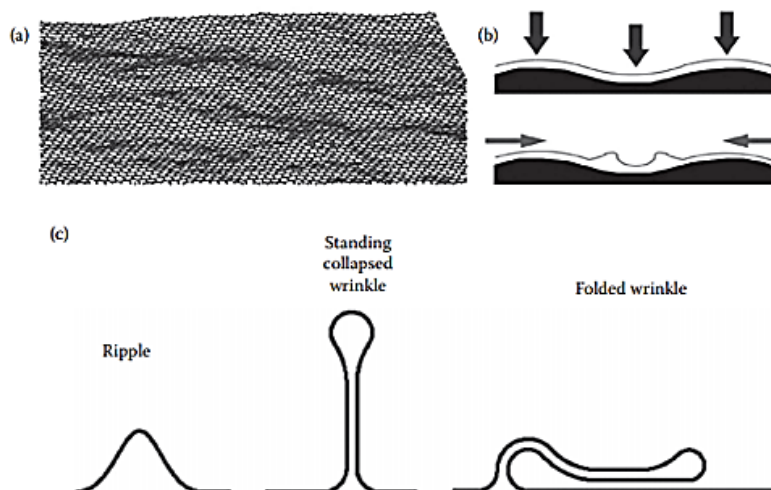


**Figure 1-26** (a) Configuration of graphene at room temperature with intrinsic ripples (146), (b) Generation of wrinkles on substrate (147), (c) Schematic of simple ripple, standing collapsed wrinkle and folded wrinkle (148)

Bending can also come from the chemical and physical environment, like thermal stress, which causes additional scattering and resistivity due to a coupling between geometry and electron propagation (146, 147, 149–151). All of this results in affecting the physical and chemical properties of graphene and of its potential device applications in particular. Owing to their narrow width morphologies, GNR reduce the occurrence of these drawbacks.

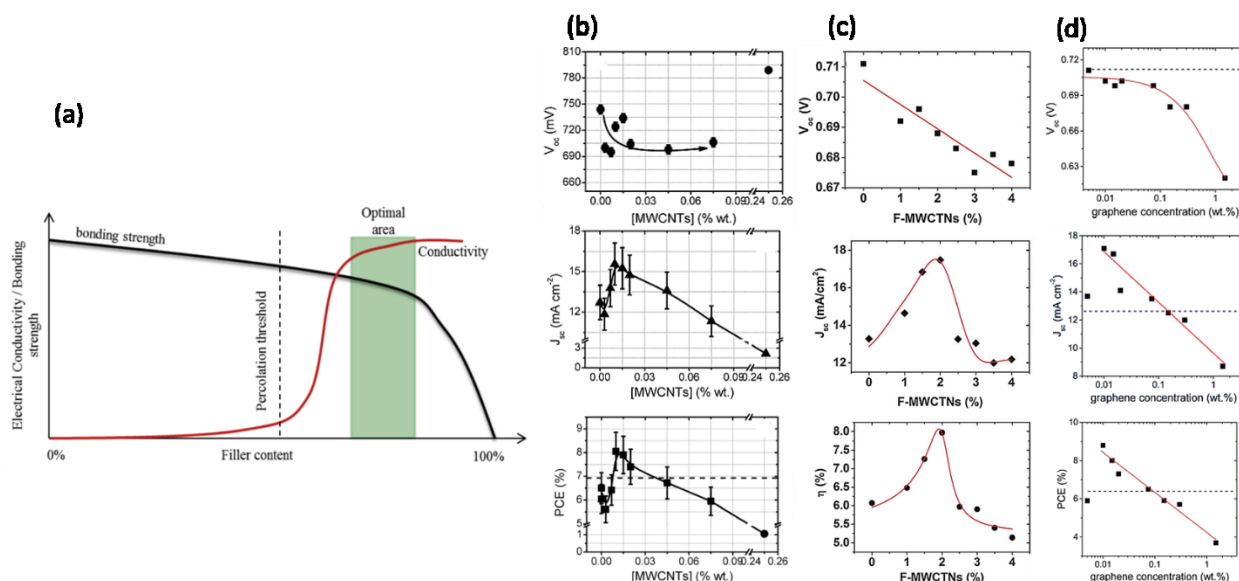


**Figure 1-27** (a) Percolation threshold with bonding strength and electrical conductivity evolution to filler content percentage (152). I-V parameters of TiO<sub>2</sub> nanocomposite with (b) MWCNT (123) (c) F-MWCNT (143) (d) and Graphene (141)



Although GNR exhibit the same anisotropic features as their original CNTs counterpart, they tend however to behave chemically like graphene sheets, including enhanced dispersion in solvent. As shown in **Figure 1-27**, overall as additives, nanocarbons describe a percolation threshold after a linear increase, then followed by a decrease in performance. The same trend should therefore be observed for GNR.

Moreover, according to the percolation theory (75), the higher aspect ratio of GNR compared to graphene sheets should lower the percolation threshold for both toughening and electrical conductivity.

#### **1.6.4.1 Toughening mechanism: Stability and integrity**

Since the intensity of reinforcement effects significantly depends on interfacial bonding of the host material and GNRs dispersion throughout matrix, toughening mechanisms are likely to positively contribute to the issues of TiO<sub>2</sub> film degradation by bridging cracks formed through ageing and graphene pullouts. They could thus be used to achieve higher mechanical strengths, favoring higher bending strength and elasticity (153–156), and increase the long-term stability of DSSCs.

#### **1.6.4.2 Percolation pathways**

The sp<sup>2</sup>-bonded plane carbon atoms with high monolayer transparency (97.3%), the high specific surface area (2630 m<sup>2</sup>/g), the high electrical conductivity of 10<sup>6</sup> S/m, and the thermal conductivity of 5300 W/mK (157) of low dimensional nanocarbons such as graphene and GNR motivated our study to enable higher electrical conductivities of novel nanocarbon composite films for optoelectronic devices.

Percolation theory (158) referring to critical filler loading consists in increasing the electrical conductivity behavior of films by several orders of magnitude because of the formation of continuous conducting paths. The concentration of GNR must be above the percolation threshold so that a conducting network can be achieved in the photoanode.

Even at low additive concentrations, GNR may take advantage of their high aspect ratios to be in intimate contact with TiO<sub>2</sub> and reaching closer to each ribbon flakes building conductive pathways through the bulk (141, 153, 159).

Percolation theory predicts that the onset of percolation threshold should decrease with increasing aspect ratio [length/width (L/W)] of graphene.

To achieve optimum values for reinforcements and film conductivity, good-quality GNR and GNR-TiO<sub>2</sub> nanocomposite with lower defect concentration should be elaborated. These critical features depend on the processing routes and conditions (153). Thus, the functionality of GNR plays a critical role in lowering filler loading rate, dispersion, and organization of sheets within the host matrix to improve the overall performance of composites. In fact, the PCE of DSSCs is strongly affected by the dispersion of nanocarbons in the base fluid (75, 159–161), such as water, ethanol etc., due to lack of hydrophilic groups (119, 162).

Therefore, in this thesis facile, low-cost and unaggressive production methods have been privileged.



## 1.7 Objective and aim of the thesis

In past few decades, the worldwide energy demand increased significantly due to the rapid development of industrialization and globalization. Thus, there is a great need for the design and synthesis of novel materials and incorporate them in the fabrication of high performance solar energy conversion devices. The use of solar energy in this thesis focuses on DSSC and PEC devices.

The key factor which restricts the efficiency of photoconversion systems is the non-radiative recombination of photoinduced electrons and holes. To suppress these non-radiative recombination events, we have chosen to introduce low dimensional carbon nanomaterials with small size and large surface area, so called “GNR”, into the wide band-gap semiconductor (i.e.  $\text{TiO}_2$ ). GNRs have great advantages such as high transparency, high conductivity, high surface area and strong mechanical strength, which provide a new opportunity to upgrade traditional energy conversion and storage devices.

Currently, Si solar cells constitute the most widespread commercial product because of their high conversion efficiency and relative long-term stability as compared to other solar cell technologies; however, their high production cost and environmental impacts are restricted to the terrestrial PV market. Therefore, in recent years, DSSCs, which belong to third generation PV devices, have been explored as alternative to Si solar cells. DSSCs are considered as a promising future technology due to their appealing features including a simple fabrication process, eco-friendly materials and colour choice and transparency.

The aim of this thesis is to develop low cost, simple processable and environmentally friendly DSSCs and PECs with GNR- $\text{TiO}_2$  based composite photoanode, to improve the PEC in solar cells, the hydrogen generation in PECs and long-term stability of these devices.

Due to the exceptional morphological, electrical and mechanical properties of GNRs, we can form by a simple blending method an attractive interfacial interaction at the nanoscale that can effectively improve electron flow direction and combat  $\text{TiO}_2$  to agglomerate over time by toughening grains through van der Waals forces and improve the charge collection efficiency of photogenerated electrons through its one-dimensional higher aspect ratio.

Specifically, the objectives of this thesis are:

(1) Elaborate DSSCs with efficient GNR- $\text{TiO}_2$  composite photoanode to achieve higher  $J_{sc}$  and PCE with lower carbonaceous content, by current-density-voltage (J-V), transient photovoltage decay and EIS.

(2) Compare the effect of GNR higher aspect-ratio on the percolation threshold of GNR-TiO<sub>2</sub> vs graphene-TiO<sub>2</sub> through the photoelectric performance and long-term stability of DSSCs, by using Raman spectroscopy and EIS to investigate the effect of comparative morphologies on transport mechanisms.

(3) Fabricate highly efficient and durable PEC device with Quantum dot sensitized GNR-TiO<sub>2</sub> photoanode to improve hydrogen generation efficiency, by using UV-visible to monitor the negative effects of the nanocomposite over the absorption, SEM and Raman spectroscopy and for optimizing the concentration of GNR in the device for high J<sub>SC</sub>.

## 1.8 Thesis organization

This document is divided into six chapters which are organized as follows:

**Chapter 1** Introduction of fundamental concepts of the background are briefly introduced here, followed by the presentation of the objective and aim of the thesis.

**Chapter 2** Materials and Methods. In this Chapter, we present the description of fabrication and characterization techniques used throughout this work.

**Chapter 3** Hybrid  $\text{TiO}_2$ -Graphene Nanoribbon photoanodes to boost the photoconversion efficiency of dye sensitized solar cells. We demonstrate the fabrication of DSSC with optimal concentrations of GNR in the photoanode and how it improves the overall efficiency.

**Chapter 4** Structural effect of low-dimension carbon nanostructures on long-term stability of Dye-sensitized solar cells. We discuss and compare the effect of incorporation of graphene sheets with different aspect ratios on the evolution on J-V parameters and impedance parameters, and the ability for these materials to stabilize effectively the devices.

**Chapter 5** Graphene Nanoribbon- $\text{TiO}_2$ -quantum Dots Hybrid Photoanode to Boost the Performance of Photoelectrochemical cells for Hydrogen Generation. We demonstrate how the fabrication of PEC cells with optimal concentrations of GNR in the photoanode can improve the overall hydrogen generation efficiency

**Chapter 6** Conclusions and recommendations based on the analysis of the results and the proposition of supplementary studies.

This thesis involved using novel hybrid nanocomposite into DSSC and PEC. The general conclusion will summarize the main results that are presented in this document and will open up with scientific and technological perspectives related to DSSC and PEC.

## 2 CHAPTER 2 MATERIALS AND METHODS

---

In this chapter, the experimental details of the preparation of the GNR dispersion, preparation of GNR-TiO<sub>2</sub> photoanode, fabrication and characterization of the photoanode structure and the entire PEC cells, namely the DSSC, and PEC cell for H<sub>2</sub> generation are reported. The first section mainly introduces the preparation of the photoanode, the GNR-TiO<sub>2</sub> photoanode and the fabrication and characterization of the entire DSSC. The second section focuses on the fabrication and characterization of the PEC cell for application in H<sub>2</sub> generation. To fabricate the GNR-TiO<sub>2</sub> photoanode and the graphene-TiO<sub>2</sub> photoanode, different concentrations of GNR (dispersed in dimethylformamide) and of graphene (dispersed in ethanol) were systematically introduced and the photoanodes were sensitized by dye via dip coating. To fabricate the photoanodes for PEC based H<sub>2</sub> generation, similar approach was undertaken, here the photoanodes were sensitized by colloidal core-shell quantum dots (QDs) using Electrophoretic deposition (EPD).

### 2.1 Materials

FTO conducting substrates with sheet resistance 15  $\Omega/\square$  were supplied by Xop Glass (Spain). TiO<sub>2</sub> nano-oxide blocking layer solution was bought from Solaronix. The transparent mesoporous TiO<sub>2</sub> paste composed of 20 nm sized anatase particles (Code 18 NR-T) and scattering paste of 150-200 nm sized anatase particles (Code 18 NR-AO) were supplied by Dyesol, Australia. Redox couple electrolyte which consists of iodine and tri-iodide ( $I^-/I_3^-$ ), Ruthenium based N719 dye (Ruthenizer 535-bisTBA) and Meltronix spacers were bought from Solaronix. Sulfur (100%), oleylamine (OLA) (technical grade, 70%), cadmium oxide (99%), cadmium nitrate tetra hydrate ( $\geq 99\%$ ), oleic acid (OA), Rhodamine 6G and octadecene (ODE), selenium pellet ( $\geq 99.999\%$ ), trioctyl phosphine oxide (TOPO), trioctyl phosphine (TOP) (97%), hexane, zinc acetate dihydrate (98%), sodium sulfide nonahydrate ( $\geq 99.9\%$ ), sodiumsulfide (Na<sub>2</sub>S), sodium hydroxide (NaOH), sodium sulfite (Na<sub>2</sub>SO<sub>3</sub>), toluene, methanol, acetone, ethanol, dimethylformamide (DMF), Titanium(IV) chloride (TiCl<sub>4</sub> 0.09 M in 20% HCl) for TiO<sub>x</sub>, titanium isopropoxide (99.999%), hydrochloric acid (37%), etyl cellulose and isopropanol (IPA) were obtained from Sigma-Aldrich Inc. Graphene microplatelets were purchased from Raymor Inc. and GNR were purchased at Sigma Aldrich.

## 2.2 Method

### 2.2.1 Experimental details relevant to DSSC fabrication with TiO<sub>2</sub> photoanodes with GNR

#### 2.2.1.1 Preparation of GNR dispersion

The homogeneous dispersion of GNR was prepared through bath sonication in DMF for 12h in order for the exfoliation of carbon nanomaterials to take place (163). After that, direct mechanical mixing of the GNR suspension with 20 nm sized TiO<sub>2</sub> nanoparticulate was performed to obtain various concentrations of the precursor of GNR-TiO<sub>2</sub> composite. TiO<sub>2</sub> paste was used without any pre-treatment.

#### 2.2.1.2 Pre- and post-treatment of the photoanode

The pre-treatment of the TiO<sub>2</sub> photoanode corresponds to the deposition of the blocking layer of TiO<sub>2</sub>. It was carried out by spin coating, and used precursor solution of TiO<sub>x</sub> film at 2,000 r.p.m. for 60 s and followed by annealing at 500 °C for 30 min (164). Alternatively, this pre-treatment can be achieved by soaking the FTO substrates in 50 mM TiCl<sub>4</sub> aqueous solution and 90 mM TiCl<sub>4</sub> aqueous solution, for 30 min at 70 °C. After that they were flushed with deionized water and sintered at 500 °C for 30 min (164). For post treatment of the TiO<sub>2</sub> film, the same procedure as pre-treatment was followed with the TiO<sub>x</sub> and TiCl<sub>4</sub> precursor solutions.

#### 2.2.1.3 DSSC Fabrication of DSSC TiO<sub>2</sub> nanoparticles-GNR hybrid photoanodes

For the removal of traces of glue from packaging, the FTO substrates were sonicated for 30 min with 2% Triton X-100 in deionized water, followed by 30 min sonication in isopropyl alcohol, then washed with ethanol and then thoroughly rinsed with deionized water, dried in a filtered air stream and finally exposed to UV light for 30 min. Subsequently using the techniques described above, a blocking layer of TiO<sub>2</sub> was deposited on the substrate.

Different concentrations of GNR added to TiO<sub>2</sub> nanoparticles pastes (as mentioned above) have to be prepared to fabricate photoanodes with different concentrations of GNRs. After this washing process the GNR-TiO<sub>2</sub> hybrid nanocomposite is deposited by doctor blade technique by using a scotch tape as spacer and mask on the two lateral sides of the substrate. The prepared paste was printed onto the substrate by tip coating, left to dry in air during 15 min; the scotch tape was removed and the samples were placed on a hot plate at 150°C during 6 min. This operation was repeated by doubling the spacer (two layers of scotch at each corner) during the printing process,

to obtain a double layer. Thereafter we need to sinter the deposited film for 30 min at 500°C. Anneal the prepared samples at 500°C during 30min in the furnace, let them cool down.

Subsequently (for DSSCs) a passivating layer of  $\text{TiO}_2$  along with the  $\text{TiO}_2$  film was coated using the methods which are already described in the experimental methods section entitled “Pre- and Post-Treatment of the  $\text{TiO}_2$  Photoanode”

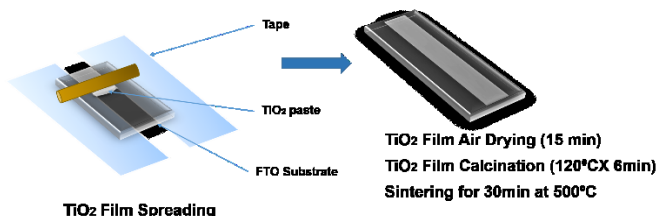


Figure 2-1 Doctor blade  $\text{TiO}_2$  film deposition

#### 2.2.1.4 DSSCs device fabrication

After the hybrid nanocomposite films were cooled down close to room temperature, the films were then immersed in a 0.5 mM ethanolic solution of the commercial N719 dye for 18 hours, and subsequently rinsed with ethanol to remove the unabsorbed dye molecules (165).

**DSSC cell assembly** is constructed by sandwiching the dye sensitized  $\text{TiO}_2$  hybrid photoanode and at the counter electrode made with 10 nm thick Pt deposited FTO glass substrate. To prevent the DSSCs from short circuiting when the photoanode and counter electrode are clamped together, a 60  $\mu\text{m}$  thick thermoplastic spacer was used. An iodide/tri-iodide redox couple electrolyte was injected through the spacers, which act as the hole transporting medium.

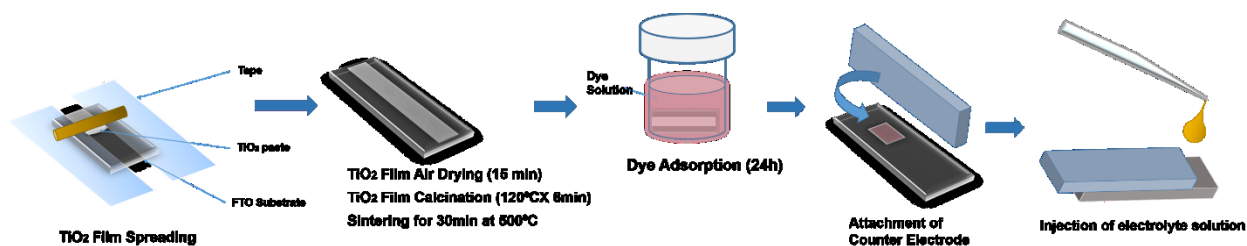


Figure 2-2 Schematic of DSSC device fabrication steps. Image of an electrode after N719 dye sensitization (5)

## 2.2.2 Experimental details relevant to colloidal QD based PEC H<sub>2</sub> generation

### 2.2.2.1 Synthesis of CdSe QDs

Using the hot-injection approach, synthesis of CdSe QDs of diameter 1.65 nm were carried out.<sup>(166, 167)</sup> Typically, at room temperature, TOPO (1 g) and Cd-oleate (0.38 mM, 1 mL) in 8 mL of ODE were purged in N<sub>2</sub> atmosphere for 30 min. The reaction system was evacuated for 30 min at 100 °C, then the temperature was raised to 300 °C. The mixture of 3 mL of OLA, TOP-Se (4 mM, 4 mL) and 1 mL of ODE at room temperature was injected rapidly into the Cd-oleate suspension while stirring the mixture vigorously. After injection, the reaction cell was quenched with cold water. After that 20 mL of ethanol was added and then the suspension was centrifuged. Finally, the supernatant was removed and the QDs were dispersed in toluene.

### 2.2.2.2 Synthesis of CdSe/CdS QDs

According to the procedure described in Ghosh et al.<sup>(168, 169)</sup>, the deposition of CdS layers on CdSe QDs was obtained by successive ionic layer adsorption and reaction (SILAR). The synthesis of the CdSe/CdS QDs was obtained by growing CdS monolayers over the CdSe core. Typically, in a 100 mL round-bottom flask, 5 mL of ODE, 5 mL of OLA and CdSe QDs ( $\sim 2 \times 10^{-7}$  M in hexane) were degassed at 110 °C for 30 min. While re-storing the reaction flask in N<sub>2</sub>, the temperature was increased to 240 °C with stirring. Subsequently, the Cd(OA)<sub>2</sub> which was dispersed in ODE (0.25 mL, 0.2 M) was added drop by drop in the mixture and was allowed to react for 2.5 h, followed by, 0.2 M sulfur in ODE was added dropwise with the same volume. All subsequent shells were annealed at 240 °C for  $\sim 10$  min succeeding the injection of sulfur, and  $\sim 2.5$  h following drop by drop addition of the Cd(OA)<sub>2</sub> in ODE. Sulfur/Cd(OA)<sub>2</sub> addition volumes for shell addition cycles 1-13 were as follows: 0.25, 0.36, 0.49, 0.63, 0.8, 0.98, 1.18, 1.41, 1.66, 1.92, 2.2, 2.51 and 2.8 mL, respectively <sup>(167)</sup>. Using cold water, the reaction was cooled down to room temperature. Ethanol was added to the mixture which was then centrifuged and the supernatant was removed. The QDs were then dispersed in toluene for further characterization.

### 2.2.2.3 Sensitization of the TiO<sub>2</sub>/GNR with CdSe/CdS QDs

GNR-TiO<sub>2</sub> hybrid and TiO<sub>2</sub> films on FTO substrate were vertically immersed in the QDs toluene solution in such a way that the deposited films were facing each other. The distance between them was adjusted at around 1 cm and a direct current bias of 200 V was applied for 120 min. To

wash off unabsorbed QDs after EPD, the samples were rinsed several times with toluene and dried with N<sub>2</sub> flow at room temperature. Prior to ZnS capping, photoanodes went through ligand exchange by applying 3 SILAR cycles of methanolic solution cetyl-trimethyl ammonium bromide (CTAB) and toluene for 1 min dipping. After CTAB capping, 1 min dipping in methanol was applied to wash and remove the chemical residuals from the surface and then dried with N<sub>2</sub>, finally 1 min dipping in toluene and dried with N<sub>2</sub> for one SILAR cycle.

#### 2.2.2.4 ZnS capping layer

The ZnS capping layer was formed using the SILAR process as follows. In a typical SILAR deposition cycle, Zn<sup>2+</sup> ions were deposited from a methanolic 0.1 M solution of Zn(OAc)<sub>2</sub>. The sulfide precursor was 0.1 M solution of Na<sub>2</sub>S in the mixture of methanol/water (1/1 v/v). A single SILAR cycle consisted of 1 min of dip-coating the TiO<sub>2</sub> working electrode into the cation precursors (Zn<sup>2+</sup>), and subsequently into the anion solutions (S<sup>2-</sup>). After each bath, the photoanode was thoroughly rinsed by immersing it in the corresponding solvent (methanol or mixed solution), respectively, to remove the chemical residuals from the surface and then drying with a N<sub>2</sub> gun. Two SILAR cycles were applied to form the capping ZnS layer.

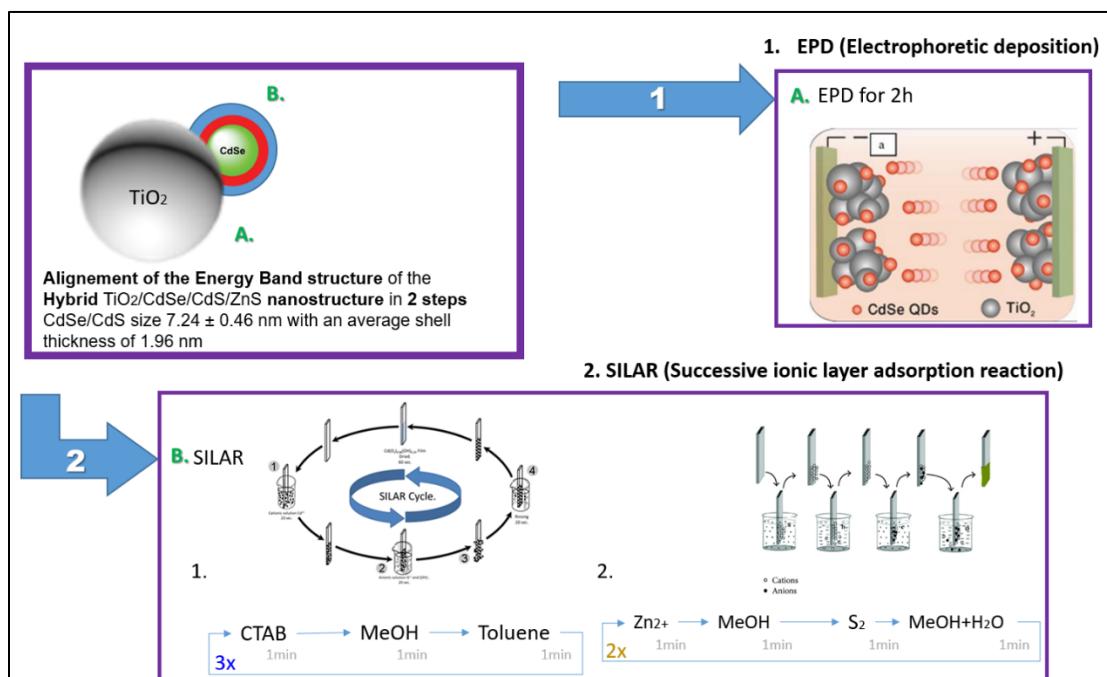


Figure 2-3 Schematic resuming the PEC cell formation (5)



## 2.3 Characterizations

### 2.3.1 Film size characterization

The thickness of the hybrid GNR-TiO<sub>2</sub> photoanodes is measured either by surface profilometer using Dektak or by cross sectional measurements by SEM. The hybrid GNR-TiO<sub>2</sub> photoanode is then immersed in dye molecules for 24h then washed with the corresponding solvent (ethanol).

### 2.3.2 Optical measurements

UV-visible spectroscopy refers to absorption spectroscopy or reflectance spectroscopy in the ultraviolet-visible spectral region using light in the visible and adjacent (near - UV and NIR) ranges. Ultraviolet (190 - 380 nm) and visible (380 – 750 nm) radiation interacts with matter may cause promotion of electrons from the ground state to a high energy state, which are also called electronic transitions. The UV-visible absorption spectrum was measured to investigate the optical properties of GNR-TiO<sub>2</sub> mesoporous films at different concentrations of GNR. A Cary 5000 UV-visible-NIR spectrophotometer (Varian) with a scan speed of 600 nm/minute was used. All experimental data were corrected for background absorption.

Dye loading measurements of all photoanodes were measured by UV-Vis spectroscopy. Dye molecules were removed from the photoanodes by washing with 0.1M NaOH aqueous solution. Optical absorption spectra of the removed dye molecules solutions were collected. Here cubic centimeter quartz cuvettes were used for liquid samples.

### 2.3.3 Photoelectrical Measurements

#### 2.3.3.1 PV measurements

The steady-state I–V characteristic of DSSCs provide the performance parameters of the cell, such as the short-circuit current ( $J_{SC}$ ), open-circuit potential ( $V_{OC}$ ), fill factor (FF) and photocurrent efficiency ( $\eta$ ). The current-voltage characteristics of the fabricated cells were measured by using a Class AAA Solar Simulator from Photo Emission Tech (SS50AAA) coupled with a Keysight 2900A Sourcemeter under simulated sunlight of 1 sun AM 1.5G irradiation (100 mW/cm<sup>2</sup>).

Open-circuit voltage decay (OCVD) measurements were conducted by stopping the illumination of the cells under open-circuit conditions and using the Keysight to monitor the resulting decline of  $V_{OC}$  (170). The electron lifetime ( $\tau_n$ ) was then determined by the reciprocal of the derivative of the decay curves normalized by the thermal voltage, using the following equation

(171):  $T_n = -k_B T/e * (dV_{OC}/dt)^{-1}$ , where  $k_B$  is Boltzmann's constant,  $T$  is the absolute temperature,  $e$  is the positive elementary charge, and  $dV_{OC}/dt$  is the derivative of the transient open-circuit voltage.



Figure 2-4 Setting for PV measurement and device

The power intensity of the simulated sunlight was calibrated with a Si reference diode. The Keysight 2900A Sourcemeter was controlled with a computer software written using the TESTPOINT platform. The fill factor (FF) and the PCE were calculated using the following equations.

$$FF = \frac{P_{max}}{J_{sc} \times V_{oc}} = \frac{J_{max} \times V_{max}}{J_{sc} \times V_{oc}}$$

$$PCE(\%) = \frac{P_{max}}{P_{in}} \times 100\% = \frac{J_{sc} \times V_{oc} \times FF}{P_{in}} \times 100\%$$

Here,  $P_{max}$  is the maximum power output,  $J_{sc}$  is the short-circuit current density,  $V_{oc}$  is the open circuit voltage.  $J_{max}$  and  $V_{max}$  are the current density and the voltage at maximum power output in the J-V curves respectively.  $P_{in}$  is the incident light power.

### 2.3.3.2 PEC measurements

The basic PEC test setup consists of a light source, light filters, a chopper or shutter (optional), a photoelectrochemical cell, and an electrical measurement tool, as presented in **Figure 2-5**.

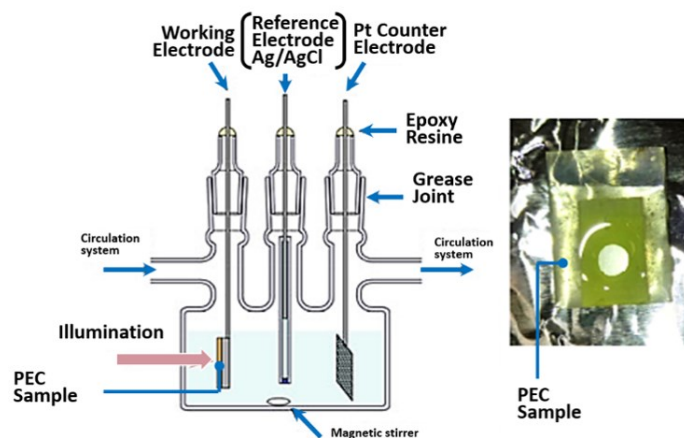


**Figure 2-5 Schematic and picture of a PEC cell in a single compartment configuration, Image of the cell. Indicated are ports for the working electrode (WE), counter electrode (CE), and for inlet circulation for gas detection.**

The PEC performance of the photoelectrodes was evaluated in a typical three-electrode configuration, consisting of a GNR-TiO<sub>2</sub>/QDs hybrid mesoporous film as a working electrode (WE), a Pt counter electrode (CE), and a KCl saturated reference electrode (RE). Insulating epoxy resin was used to cover the sample's surface except for the active area, to avoid any direct contact between the electrolyte and the conducting back-contact and/or the connecting wire. Subsequently the sample was fully immersed in the electrolyte containing 0.25 M Na<sub>2</sub>S and 0.35 M Na<sub>2</sub>SO<sub>3</sub> (pH~13) as the sacrificial hole scavenger. All potentials, measured with respect to the reference electrode of Ag/AgCl during the PEC measurements, were converted to scale according to the following equation  $V_{RHE} = V_{Ag/AgCl} + 0.197V + pH \times (0.059)$ . The photo response was measured by using a sun simulator (Sciencetech SLB-300A) under one sun simulated sunlight. The PEC test setup was mounted horizontally with the sample placed at a distance of two cm from the lamp case (seven cm far from actual bulb). Prior to each measurement, the light intensity was monitored using a silicon reference cell and adjusted to AM 1.5 G illumination, 100 mW/cm<sup>2</sup>. All the current versus potential measurements were carried out at a 20 mV/s sweep rate. The chopped characterization was performed by intermittently opening and closing the chopper.

### 2.3.3.3 Electrochemical impedance spectroscopy (EIS) measurements



Figure 2-6 Gamry impedance analyzer (172)

Electrochemical impedance spectroscopy (EIS) was carried under dark conditions by using a SOLARTRON 1260 A Impedance/Gain-Phase Analyzer by applying open circuit conditions with a test recorded at a frequency of 300 kHz to 1Hz, and the AC signal was 1 mV rms in amplitude. All the impedance measurements were analyzed using an appropriate equivalent circuit model with Gamry software (Version 7.5, Echem Analyst).

The impedance data, i.e. The Nyquist and Bode plots of the composites devices, are measured at different frequency increasing from right ( $10^{-3}$ ) to left ( $10^7$ ) by using Zview2 software.

### 2.3.4 Materials characterization

The morphology of the samples was studied using scanning electron microscopy (SEM), electron microscopy (TEM) and Raman spectroscopy with its 2D mapping image..

#### 2.3.4.1 Scanning Electron Microscopy (SEM)

SEM is an electron microscopy technique capable of producing high resolution images of the surface of a sample using the principle of electron-matter interaction. The detection of secondary electrons ejected by the incident electron beam provides information on the topography of the sample.

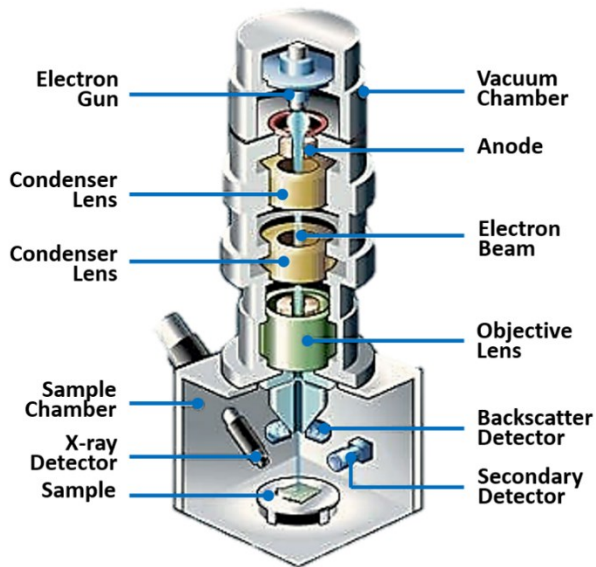


Figure 2-7 Schematic of SEM (173)

The detection of backscattered electrons originating from the interaction between the probing electrons and the atomic nuclei of the sample gives qualitative information on the phase (topographic analysis), the spent backscattered electrons (phase contrast imaging) or quantitative contrast on the atomic composition of the sample from the X-rays (EDX analysis of chemical composition).

First, at the top of **Figure 2-7**, the electron gun makes it possible to produce the beam of primary electrons. A sharp anode is placed in a strong electric field in a vacuum chamber to produce the primary electron beam via the peak effect. A system of electromagnetic lenses then makes it possible to accelerate the beam to voltages between 0 and 30 kvolts. Finally, the beam is redirected by a lens, to scan the surface of the sample. Following excitation by the primary beam, some particles are emitted by the sample and are collected by different detectors. To better understand the characteristics of the species detected, it is necessary to look at the model of the interaction pear (**Figure 2-8**), which describes the depth of emission of particles. At the surface of the sample, it is mainly the secondary and Auger electrons which are emitted while in depth, the backscattered electrons and the characteristic X-rays are in the majority.

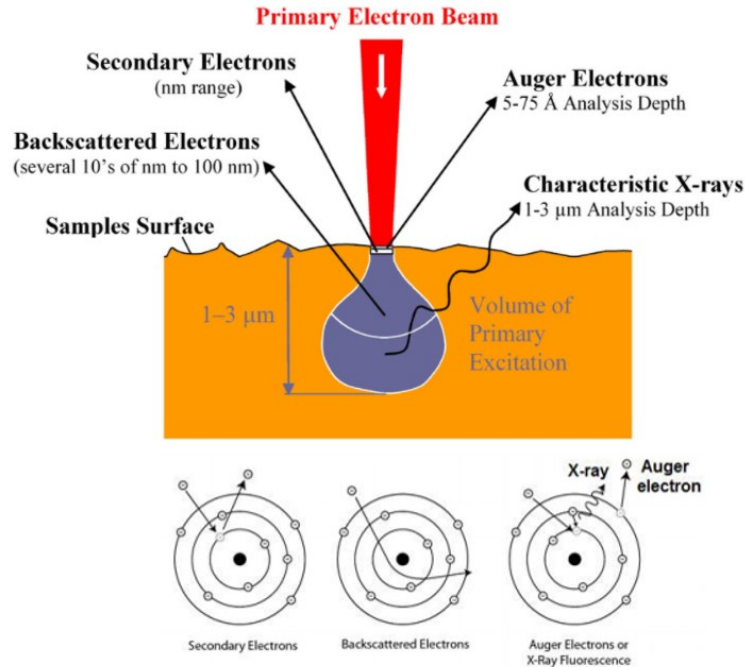


Figure 2-8 Model of the interaction pear and diagram of interaction between the primary electrons to produce the secondary particles (174)

**Secondary electrons** are produced as a result of ionization by primary electrons. These secondary electrons have low kinetic energy and are thus easily deflected by low voltages by a detector placed perpendicular to the primary electron beam. Since secondary electrons have low energy, they are emitted very near of the surface and therefore provide information on the surface topography of the sample.

**Backscattered electrons** are electrons which have lost some energy while interacting with atomic nuclei. As a result, the primary and spent back electrons have almost equal energy, making the backscattered electrons more difficult to deflect. This is why the detector is generally annular and placed around the primary beam with a higher electrical voltage than that of the secondary detector. The Backscattered electrons depend on the atomic number of the atoms in the sample and allow phase contrast to be obtained.

**Auger electrons and X-rays** are considered the "fingerprint" of emissive atoms because their signature corresponds to an energy difference typical of an atomic electronic transition. When a core electron is ejected by a primary electron, an electronic gap is created. This is then filled by an electron from the layers higher: the atom must then emit the excess energy in the form of an Auger electron or X-ray photon. In practice, most scanning electron microscopes can detect X-

rays with energy dispersive detectors (EDS). This type of detector is very useful for obtaining information on the chemical composition of a sample.

SEM images were recorded using a focused ion beam (FIB) integrated with a SEM Tescan LYRA 3XMH at an accelerating voltage of 20 kV.

#### 2.3.4.2 TEM

The principle of operation of TEM is very similar to that of SEM. A beam electron bombards scans the sample and secondary electrons are detected. The main difference is that the electron beam passes through the sample. It is then necessary to apply acceleration voltages about 10X more intense (about 200-300 kV) than with SEM (0 to 30 kV).

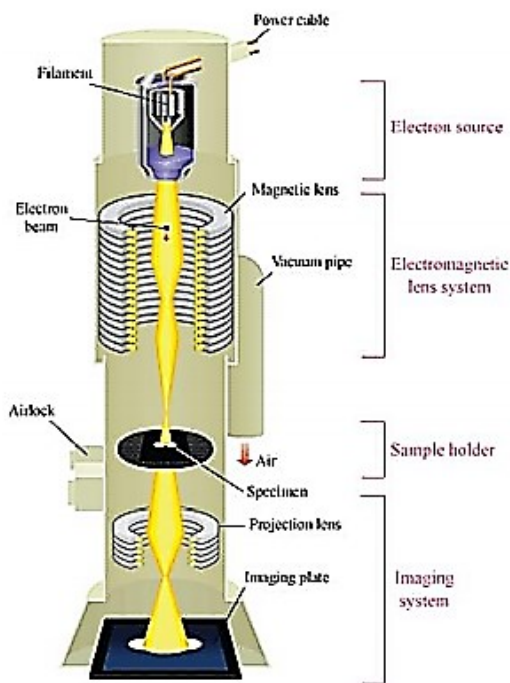


Figure 2-9 Schematic of TEM (175)

Transmission Electron Microscopy allows images of the sample to be obtained with a resolution of 0.3 nm by the transmission of an electron beam through the material observed and electron diffraction figures to study the crystallinity of materials.

### 2.3.4.3 Raman spectroscopy

Raman spectroscopy is, together with infrared (IR) spectroscopy and inelastic scattering neutron or x-ray, a vibrational spectroscopic technique. The underlying principle is based on the inelastic diffusion of light by matter. During the interaction of photons with matter, an incident photon can be scattered, with the simultaneous creation or annihilation of a vibration (phonon in a crystal). This process is called Stokes scattering if the frequency of the scattered photon is lower than that of the incident photon and anti-Stokes scattering otherwise. This effect is very small, typically a million times less intense than elastic scattering, so it is very difficult to observe. Raman spectroscopy is a non-destructive technique. It only requires very small amounts of sample in the case of micro-Raman spectroscopy (a few  $\mu\text{m}^3$ ) and no special preparation is necessary. The spectrum is characteristic of the sample and can be obtained from any state of matter: gaseous, liquid or solid (amorphous or crystalline).

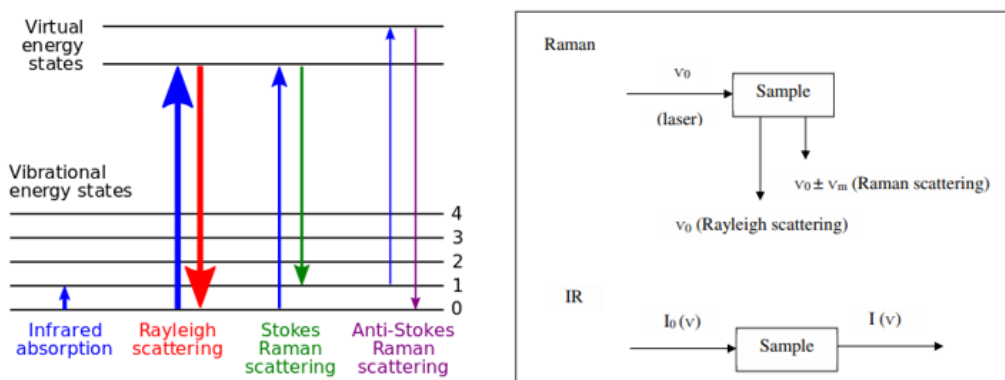
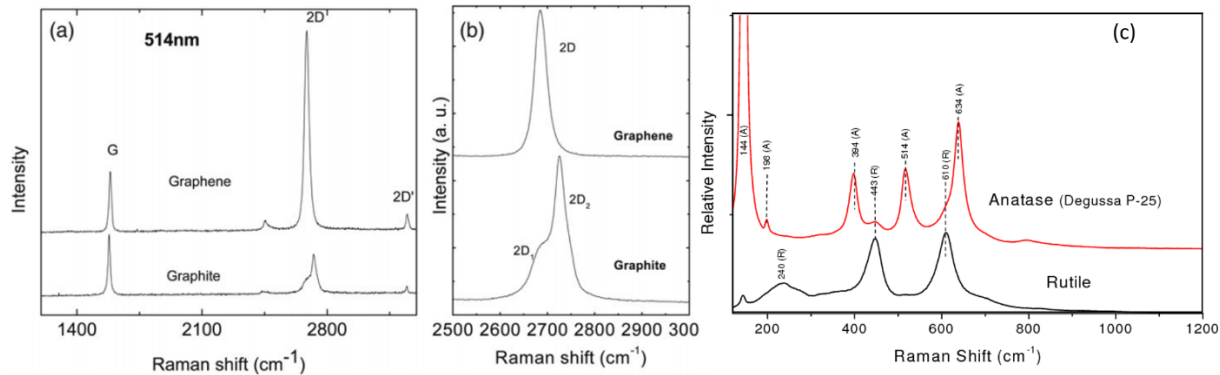


Figure 2-10 Differences in mechanisms in Raman and IR

The Raman spectroscopy laser wavelength used for this study is 514 nm. Samples were analyzed using a WITec alpha 300 micro Raman, which uses a 514 nm fiber coupled laser for excitation. The laser beam falls on the filter and then it passes to the objective and collides with the sample. The light will be scattered in all directions and will be reflected to the objective again. After the reflected light reaches the objective it falls down on the spectrometer system and finally to the Charge Coupled Device (CCD)





**Figure 2-11 Raman spectrum for (a)-(b) graphene, graphite and (c) TiO<sub>2</sub> rutile, TiO<sub>2</sub> anatase (176, 177)**

Raman spectroscopy is a proven technique to probe selected phonons in graphene based structures. The number of layers, the density of defects, the electronic properties and much more can be determined through it. The Raman spectrum of graphene based structures is characterized by four major peaks, namely D, G, D', and 2D peak seen in **Figure 2-11**. It represents the measurement of the Raman spectrum of two crystalline forms of TiO<sub>2</sub>: anatase and rutile, and two graphene based structure highlighting the effect of graphene layer stacking.

Two main peaks are related to mechanical information: the G peak and the 2D peak. The G peak corresponds to the stretching vibration between the sp<sup>2</sup> carbon atoms. The 2D peak corresponds to the double resonance transition of two phonons with reverse momentum in carbon atoms. The D peak will appear in the Raman spectrum if the graphene structure has defects or is near the fringe of graphene.

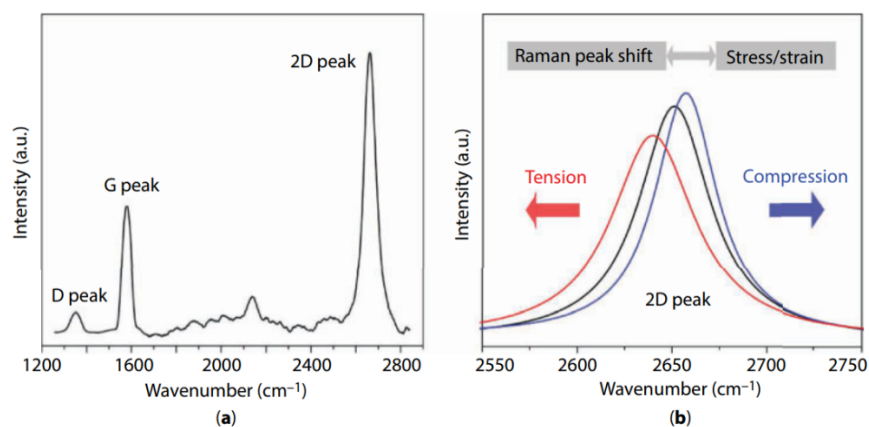


**Figure 2-12 (a) Raman spectrum of the graphene before being transferred onto the PET substrate. (b) Schematic diagram of Raman 2D peak position shift of graphene under strain-free tension and compression conditions (178).**

### 3 CHAPTER 3 HYBRID $\text{TiO}_2$ -GRAPHENE NANORIBBON PHOTOANODES TO BOOST THE PHOTOCONVERSION EFFICIENCY OF DYE SENSITIZED SOLAR CELLS

#### 3.1 Introduction

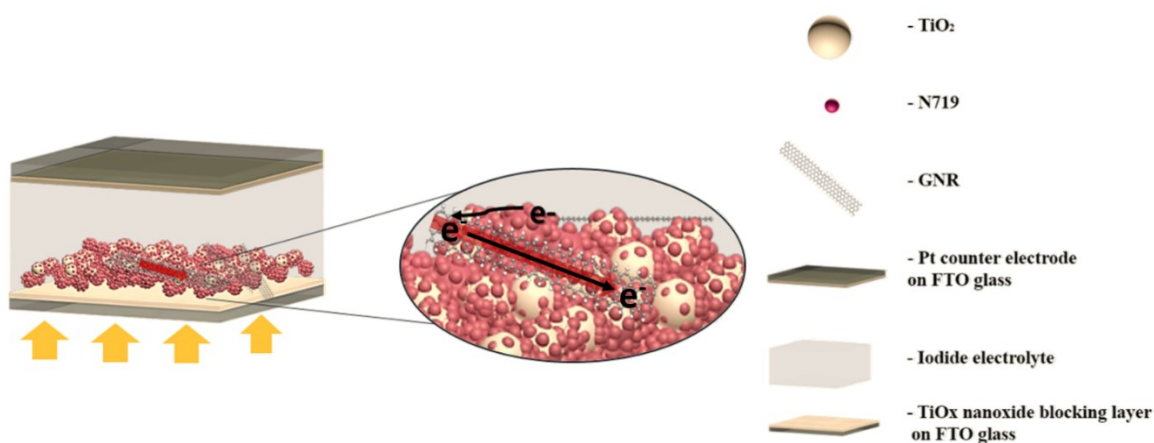


**Figure 3-1. Schematic of DSSCs components with  $\text{TiO}_2$ -GNR hybrid photoanodes highlighting preferred electrons transport through mesoporous film toward FTO.**

Herein, we describe the incorporation of small amounts of GNR in  $\text{TiO}_2$  mesoporous film and demonstrate that this procedure significantly enhances the electrons transport in DSSCs. The  $\text{TiO}_2$ -GNR hybrid photoanodes with different GNR (wt. %) concentration were prepared using the doctor-blade method. The device functional performance initially improved, but then decreased with further increase in GNR concentration inside the  $\text{TiO}_2$  active layer. At the optimum GNR concentration (0.005 wt. %), DSSC yields the highest PCE of 7.18%, under one simulated sunlight at AM 1.5G ( $100 \text{ mW/cm}^2$ ), which is 20% higher than the PCE of the control device made of a

bare  $\text{TiO}_2$  photoanode. This enhanced PV performance is systematically investigated by quantitative dye loading, transient photovoltage decay and electrochemical impedance spectroscopy (EIS) measurements. In addition, the optimized amount of GNRs reported in this study is much lower than that of other carbon allotropes- $\text{TiO}_2$  hybrid photoanodes based DSSCs (141, 179–181).

## 3.2 Results and discussion

### 3.2.1 Structural characterization

**Figure 3-2** (a)-(c) shows SEM images of the bare and GNR- $\text{TiO}_2$  hybrid photoanodes with different concentrations of GNRs. It is very difficult to see the GNRs in the GNR- $\text{TiO}_2$  hybrid photoanodes due to the complete coverage of GNR by  $\text{TiO}_2$  nanoparticles. SEM images of highly concentrated GNR- $\text{TiO}_2$  hybrid photoanodes show deep cracks (see **Figure 3-2** (c)), which are absent in bare and optimized amount of GNR- $\text{TiO}_2$  hybrid photoanodes (**Figure 3-2** (a)-(b)). These cracks and holes are responsible for electron trapping inside the photoanodes, which hinders efficient electron transport within the photoanode and also provides potential recombination sites for the electrolyte and back transfer electrons (electrolyte/FTO). This reduces the overall device functional performance, as confirmed also by J-V measurements.

TEM imaging on selected areas of GNR- $\text{TiO}_2$  hybrid photoanodes indicates the presence of GNRs embedded inside of  $\text{TiO}_2$  matrix. In general the length-to-width ratio and size of GNR produced by splitting CNTs is more homogeneous as compared to the most commonly used GO produced by Hummers' method (182). **Figure 3-2** (d)-(f) displays the presence of GNR embedded in the  $\text{TiO}_2$  matrix at different magnification levels. The GNRs in the  $\text{TiO}_2$  matrix offer oriented pathways for electrons, and contribute to reducing the influence of potential grain boundaries. In addition, 2-dimensional (2D) Raman spectroscopy was used to characterize the GNR embedded inside the mesoporous  $\text{TiO}_2$  film.

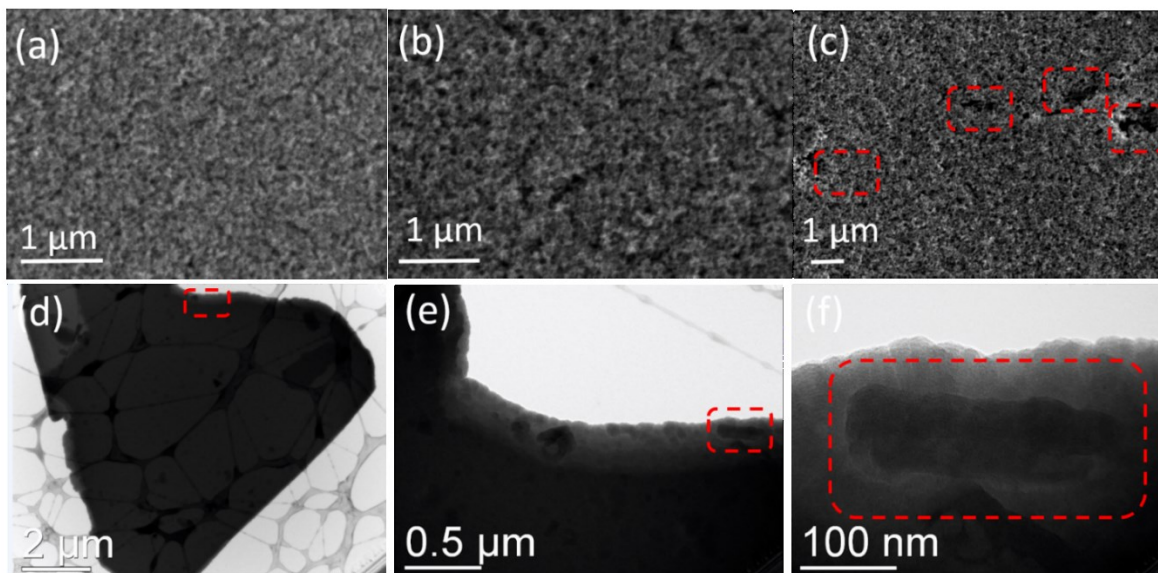


**Figure 3-2.** SEM images of the TiO<sub>2</sub> film with different concentrations (wt %) of GNR deposited on FTO: (a) 0.000%; (b) 0.005% of GNR; (c) 0.045% of GNRs, the dotted rectangle highlights the presence of cracks. (d) - (f) TEM of GNRs embedded inside the TiO<sub>2</sub> matrix at different magnification.

**Figure 3-3** displays the Raman images and spectra of the GNR-TiO<sub>2</sub> hybrid mesoporous film. Raman mapping images were obtained after filtering for the TiO<sub>2</sub> E<sub>g</sub> (2) peak (642 cm<sup>-1</sup>) (see **Figure 3-3** (a)) and GNR's G'-band (2683 cm<sup>-1</sup>) (see **Figure 3-3** (b)) separately to highlight the presence of GNR in TiO<sub>2</sub>. The majority of small and elongated black spots in **Figure 3-3** (a) are revealed in **Figure 3-3** (b) as being caused by the presence of GNR. Raman spectrum of the GNRs in **Figure 3-3** (c), contains a weak D-band (1347 cm<sup>-1</sup>) signal, originating from the high crystallinity of the parent MWCNTs.

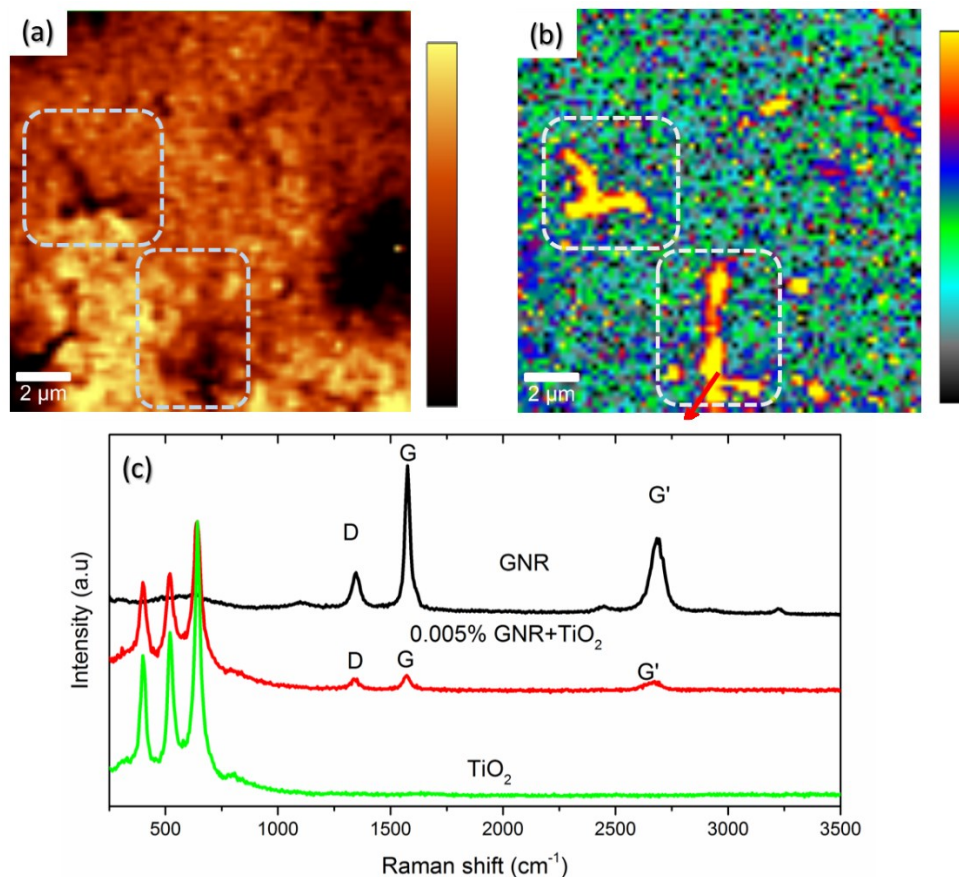


**Figure 3-3** Raman mapping of the composite photoanode filtered for: (a)  $\text{TiO}_2$ ; (b) GNR respectively. (c) Raman spectra of bare  $\text{TiO}_2$  mesoporous film (green line),  $\text{TiO}_2$ -GNR hybrid mesoporous film (red line) and GNR powder (black line).

The Raman spectra of GNR displays the presence of the D, G and  $G'$ -bands at  $1343\text{ cm}^{-1}$ ,  $1580\text{ cm}^{-1}$  and  $2682\text{ cm}^{-1}$  respectively (see **Figure 3-3** (c)), which are specific of carbonaceous materials (183). The Raman spectrum of the GNR- $\text{TiO}_2$  hybrid mesoporous film also shows the same D, G and  $G'$ -bands, confirming the presence of GNRs in the  $\text{TiO}_2$  mesoporous film after annealing at  $500\text{ }^\circ\text{C}$  for 30 min in ambient conditions. However, the relative intensity of the G-band decreases drastically when GNRs are embedded in the  $\text{TiO}_2$  mesoporous layer. The  $I_D/I_G$  ratio significantly increases from the initial GNR ( $I_D/I_G = 0.25$ ) to the embedded GNR ( $I_D/I_G = 0.69$ ), whereas the  $I_{G'}/I_G$  ratio increases slightly from the initial GNR ( $I_{G'}/I_G = 0.52$ ) to the embedded GNR ( $I_{G'}/I_G = 0.59$ ) (see **Figure 3-3** (c)). These results reveal the presence of GNR inside the  $\text{TiO}_2$  mesoporous film and are complementary with SEM and TEM images of hybrid  $\text{TiO}_2$ -GNR film.

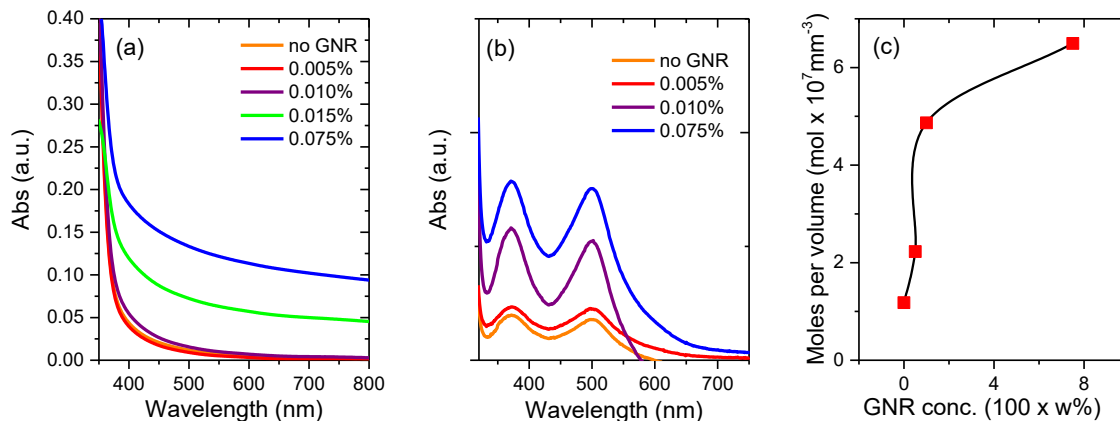


**Figure 3-4 Optical characterization: (a) Absorption spectra of GNR-TiO<sub>2</sub> mesoporous films at different concentration of GNR; (b) Absorption spectra of de-absorbed dye molecules solutions for different concentration of GNR; (c) Calculated average number of moles of dye molecules versus GNR concentration.**

The GNR-TiO<sub>2</sub> hybrid mesoporous film transparency in the UV-Visible region with increased GNR content is shown in **Figure 3-4** (a). The results show that film transparency is not affected by GNR content below 0.01 wt% and the wavelength position of the absorption peak of TiO<sub>2</sub> remains unaltered. For high content of GNR, above 0.015 wt%, GNR starts absorbing the light in the UV-Visible range, and reducing the transparency of the hybrid photoanodes. For the sample with 0.015 wt%, the absorption is almost two times higher than that of the bare sample and sample with 0.005 wt% GNR content, which may be due to the aggregation effect of GNR in TiO<sub>2</sub>. Therefore the direct light absorption by the GNRs is a loss of part of the radiation available for exciton generation, which in turn reduces the overall functional performance. The quantum confinement effect theoretically allows graphene with the structure of a GNR to have a tunable band gap covering the whole solar light spectrum (135), however as shown by **Figure 3-4** this feature cannot be highlighted with GNRs used in this study.

**Figure 3-4** (b) displays the absorption spectra of dye molecules solution after the removal from GNR-TiO<sub>2</sub> hybrid photoanodes with different content of GNR. As the percentage of GNR increases in the TiO<sub>2</sub> mesoporous film, dye loading amount starts increasing slightly for samples with GNR concentration below 0.010 wt%, whereas above 0.010% the dye loading is significantly enhanced. The calculated average number of dye mole per volume units is shown in **Figure 3-4** (c). The results show that at higher concentrations of GNRs, for instance 0.075 wt% amount of dye loading is 3 times higher compared to the bare TiO<sub>2</sub> mesoporous film. This higher dye loading may be due to the chemisorption of multilayered dye, which reduces the overall PCE of the device, because it is well known that the best performance can be obtained when dye molecules are



chemisorbed in a closely packed monolayer (184). On the other hand, previous studies using CNT-TiO<sub>2</sub> composites (123) may suggest that this can also result from the aggregation of GNRs excessively covering the surface of TiO<sub>2</sub>, thus contributing to a smaller photoactive surface area and an increased concentration of electron trap sites. These findings highlight that higher loading of GNRs have a negative effect on the device functional performance, which is further confirmed by the J-V measurements.

### 3.2.2 Photovoltaic characterization

The J-V curves of DSSCs under AM 1.5 G irradiation (100 mW cm<sup>-2</sup>) are shown in **Figure 3-5** (a) and the corresponding functional parameters including the open circuit voltage ( $V_{oc}$ ), current density ( $J_{sc}$ ), fill factor (FF) and the PCE are reported in Table 1. The GNR-TiO<sub>2</sub> hybrid photoanode based DSSC shows better functional performance compared to the control device. This trend is valid only up to a threshold of optimum GNR concentration of 0.005wt %, holding the highest  $J_{sc}$  of 14,22 mA/cm<sup>2</sup> and the highest PCE of 7.18 %, which corresponds to approximately 20% enhancement with respect to bare TiO<sub>2</sub> (5.99 %). This improvement in the PCE of DSSCs based on GNR-TiO<sub>2</sub> hybrid photoanode is mainly related to the enhanced  $J_{sc}$ , which can be attributed to a better generation and transport of light-generated carriers, and also an enhanced dye loading with small content of GNR in TiO<sub>2</sub>. This small content does not affect the structural and optical properties of the photoanodes such as morphology and transparency, as discussed previously.

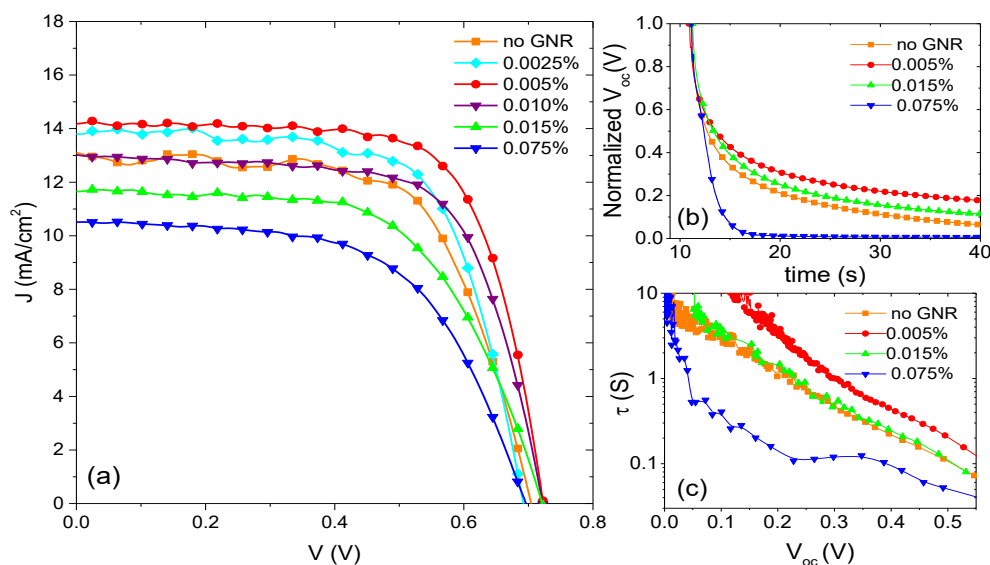


**Figure 3-5 (a) Current density–voltage curves of device with different concentrations of GNRs in TiO<sub>2</sub> under one sun illumination (AM1.5G irradiation (100 mW/cm<sup>2</sup>), (b) Transient photovoltage decay measurements of corresponding devices. Normalized V<sub>oc</sub> decay with time; (c) Calculated electron life time values from V<sub>oc</sub> decay.**

A further increase in GNR concentration from 0.005 to 0.075 wt% reduces the PCE as shown in **Figure 3-5** (a), which is consistent with the structural and optical properties of GNR-TiO<sub>2</sub> hybrid photoanodes of higher GNR content. These obtained PV performance results of DSSCs based on GNR-TiO<sub>2</sub> hybrid photoanodes with different concentration of GNR are further confirmed from transient photovoltage decay and electrochemical impedance spectroscopy (EIS) measurements as discussed in later sections.

**Table 3-1 Functional properties of DSSCs with different GNR content.**

GNR ( wt %)	V <sub>oc</sub> (V)	J <sub>sc</sub> (mA/cm <sup>2</sup> )	FF (%)	PCE (%)
<b>0</b>	0.705	13.13	65	5.99
<b>0.0025</b>	0.692	13.60	69	6.49
<b>0.0050</b>	0.724	14.22	70	7.18
<b>0.010</b>	0.724	13.01	68	6.39
<b>0.015</b>	0.726	11.59	60	5.07
<b>0.075</b>	0.696	10.50	68	4.99

**Figure 3-6** displays the variation of all functional parameters (PCE, J<sub>sc</sub>, V<sub>oc</sub>, and FF) of the DSSCs as a function of the GNR content in the TiO<sub>2</sub> mesoporous film. With an increase of GNR content from 0.0025 to 0.005 wt %, the functional parameters improved compared to DSSCs using bare TiO<sub>2</sub> photoanodes. The J<sub>sc</sub> increases from 13.13 to 14.22 mA/cm<sup>2</sup> (see **Figure 3-6** (a)), V<sub>oc</sub> increases from 0.705 to 0.724 V (see **Figure 3-6** (c) and the FF increases from 65 to 70% (see **Figure 3-6** (d)), hence the overall PCE increases from 5.99 to 7.18% (see **Figure 3-6** (b)). However, when further increasing of the GNR content from 0.005 to 0.075 wt%, all the functional parameters decrease as shown in **Figure 3-6**. For instance, at 0.075 wt % GNR content, there is a drastic reduction in the functional parameters with respect to DSSCs based on bare TiO<sub>2</sub> photoanodes: J<sub>sc</sub> decreases from 13.13 to 10.50 mA/cm<sup>2</sup>, V<sub>oc</sub> decreases from 0.705 to 0.696 V and FF increases from 65 to 68% (see **Figure 3-6** (d)), hence the overall PCE decrease from 5.99



to 4.99%. This trend of variation of functional parameters with the GNR content in the TiO<sub>2</sub> mesoporous film is consistent with the structural and optical properties of the GNR-TiO<sub>2</sub> hybrid and bare TiO<sub>2</sub> photoanodes as discussed above.

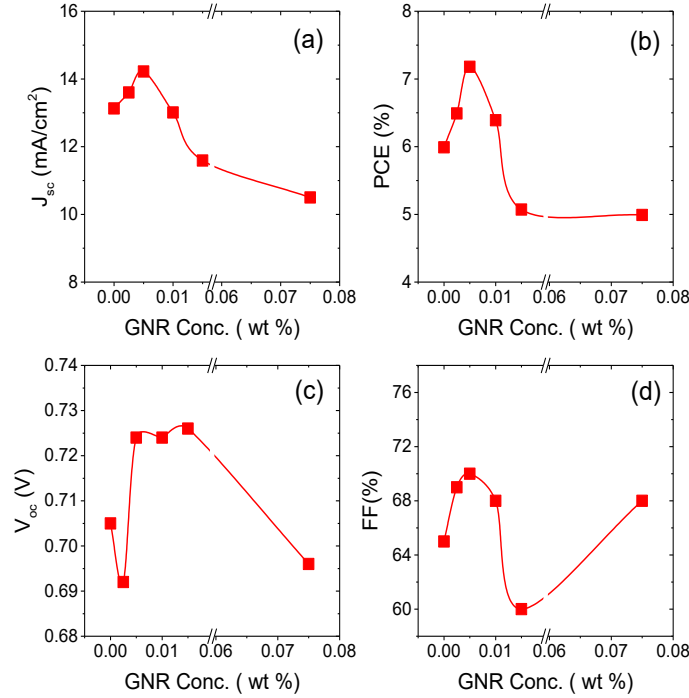


**Figure 3-6. Variation of the functional parameters of the device under one sun illumination (AM1.5G irradiation, 100 mW cm<sup>-2</sup>) with GNR concentration in TiO<sub>2</sub>: (a) J<sub>sc</sub>; (b) PCE; (c) V<sub>oc</sub>; (d) FF.**

Transient photovoltage decay measurement was applied to understand the effect of different GNR content on the carrier dynamic of the device. The results of this measurement provide information about the carrier recombination occurring at the TiO<sub>2</sub>/Dye/electrolyte interface. **Figure 3-5 (b)** displays the V<sub>oc</sub> decay curves versus time for all DSSCs based on GNR-TiO<sub>2</sub> hybrid photoanodes of different content of GNR wt%. Among all DSSCs, the rate of V<sub>oc</sub> decay is observed to be faster in the case of DSSCs with GNR of 0.075 wt% and slowest in the case of DSSC with GNR content of 0.005 wt %, which are consistent for obtained PV performance of the respective DSSCs.

The electron lifetime ( $\tau_e$ ) (shown in Eqn (3-1) )was calculated from the V<sub>oc</sub> decay measurements by using the following equation (170)

$$\tau_e = \frac{k_B T}{e} \left( \frac{dV_{oc}}{dt} \right)^{-1} \quad (3-1)$$

where  $k_B$  is Boltzmann's constant, T is the absolute temperature, and e is the electronic charge.

**Figure 3-5** (c) shows that the calculated  $\tau$  is highest in the case of DSSC with 0.005 wt% GNR in GNR-TiO<sub>2</sub> photoanodes as compared to DSSCs based on other GNR content in TiO<sub>2</sub> as well as bare TiO<sub>2</sub> photoanodes. These increased values of  $\tau$  for the optimized GNR content confirms the reduced carrier recombination at TiO<sub>2</sub>/Dye/electrolyte interface due to improved carrier transport when GNRs are incorporated in the TiO<sub>2</sub> mesoporous film. With further increase of the GNR content (from 0.010 to 0.075 wt%), the value of  $\tau$  decreases due to the detrimental effects of a higher amount of GNRs in the TiO<sub>2</sub> mesoporous film on the structural and optical properties (crack formation and loss of film transparency) of GNR-TiO<sub>2</sub> hybrid photoanodes. At a particular  $V_{oc}$  ( $\sim$  0.350 V), the calculated  $\tau$  value is highest (0.62 s) for the DSSC with 0.005 wt% GNR among all other loadings (e.g. 0.34 s for 0.015 wt% and 0.13 s for 0.075 wt%) and 0.28 S for bare TiO<sub>2</sub>.  $\tau$  is directly related to the carrier recombination occurring at that interface, so the increased value of  $\tau$  for a DSSC with 0.005 wt% GNR confirms the reduced carrier recombination at the TiO<sub>2</sub>/Dye/electrolyte interface. The possible reasons behind the detrimental effects of large amounts of GNRs in TiO<sub>2</sub> would be the formation of cracks inside the TiO<sub>2</sub> matrix, and the formation of agglomerates of GNR which act as trapping sites for carrier recombination and also the absorption of a small portion of light in the UV-visible range that is then not available for exciton generation. Due to these factors, a large GNR content gives an overall PCE less than DSSCs based on bare TiO<sub>2</sub>. In addition, these findings are further supported by EIS measurements as discussed below.

EIS was applied under dark conditions. In particular, we focused on the recombination resistance  $R_{rec}$  and the chemical capacitance  $C_{\mu}$  (83, 185) associated to the photoanode. **Figure 3-7** (a), displays the systematic comparison of the  $R_{rec}$  for three representative samples: no GNR, with a 0.001 %wt GNR and with a 0.015 %wt GNRs. As previously observed for functionalized MWCNTs (186), the behaviour of the recombination resistance can be separated into two zones, one at low bias (below 500 mV) and the other at high bias (above 500 mV). The effect of the GNRs is clearly visible in the low bias region. In fact, at low bias, the main contribution to  $R_{rec}$  comes from the charge transfer from the uncovered FTO substrate at the bottom of the porous film (also called the back layer) (185, 187). As shown in **Figure 3-7** (a), in this region, the highest  $R_{rec}$  is observed for cells with a medium load of GNRs; these also exhibits also higher PCE and suggests a reduction of the back-reaction between the FTO, the TiO<sub>2</sub>/GNR composite and the electrolyte (83, 186, 185). Since the recombination resistance is inversely proportional to the electron recombination (186), the larger recombination resistance within the photoanode with 0.01 %wt, indicates a much slower back-reaction, confirming the beneficial effect of the addition of a proper amount of GNRs. Increasing further the amount of GNRs leads to a decrease of  $R_{rec}$  associated

with the back reaction. This kind of behaviour can be due to local agglomeration of GNRs that can create traps and surface defects and thus increase the probability to be in direct contact between the GNR agglomerate and the electrolyte, enhancing the recombination phenomena (186). **Figure 3-7** (b) reports the chemical capacitance of the three representative samples. As visible all the three cells present similar trends. The cell with the optimum amount of GNR presents a higher value of capacitance in the range 400–600 mV, that can be attributed to a higher specific surface area compared to the other two samples (74). A higher load of GNRs, as previously observed, can cause agglomeration that can instead reduce the surface area, boosting the recombination rate with a negative effect on the final PCE.

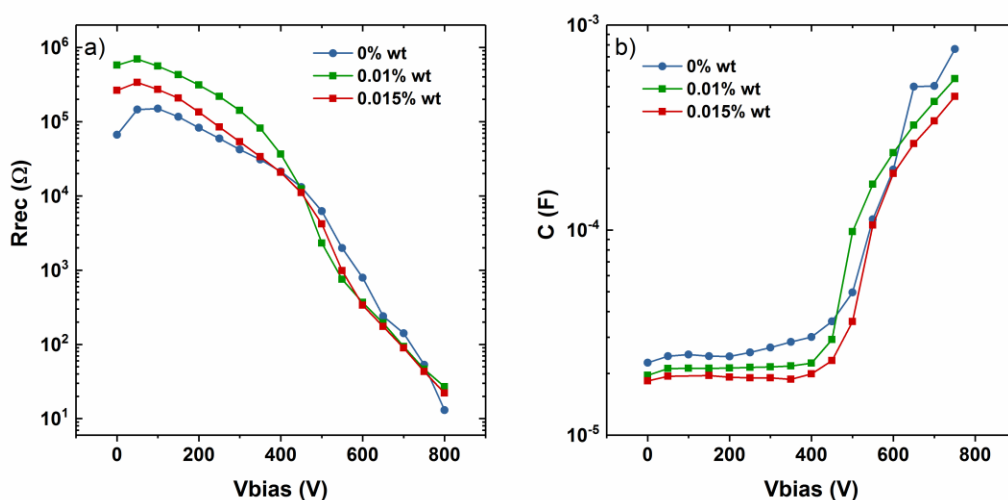


**Figure 3-7** EIS analysis of DSSCs at different GNR concentrations: (a) recombination resistance; (b) chemical capacitance from EIS measurements in the dark.

In addition to the high PV performance of the device, reproducibility of device fabrication is a really important factor. To highlight the reproducibility of fabrication and PV performance of the devices based on  $\text{TiO}_2$ -GNR hybrid photoanodes with different GNR concentrations, we fabricated three devices for each GNR concentration and their J-V curves were measured under one sun simulated sunlight (AM 1.5G,  $100 \text{ mW/cm}^2$ ). The J-V curves for each concentration are shown in **Figure S 3-1** and the corresponding functional parameters ( $J_{sc}$  ( $\text{mA/cm}^2$ ),  $V_{oc}$  (V),  $PCE$  (%) and  $FF$  (%)) values are reported in **Table S 3-1**. Each batch with a given GNR concentration shows remarkable reproducibility, as seen by the obtained functional PV performance.

### 3.3 Conclusions and perspectives

In summary, we demonstrated that a small amount of GNRs inserted in  $\text{TiO}_2$  nanoparticulate paste can significantly improve the functional performance of DSSCs. Our results show that an optimum GNR concentration in the  $\text{TiO}_2$  active layer improves the collection and transport of photogenerated electrons, which in turn improves the device functional performance. A further increase in GNR concentration results in decreased performance, due to the detrimental effect of higher amounts of GNR on optical and structural properties of GNR-  $\text{TiO}_2$  hybrid mesoporous film. At the optimum GNR concentration (0.005 wt%), the DSSCs yielding a PCE of 7.18%, which is 20% higher than bare  $\text{TiO}_2$  based DSSC. This improvement is mainly attributed to the beneficial role of GNRs in the photoanode in directing the transport of photogenerated electrons to the front contact thereby reducing carrier recombination. This is confirmed by the enhanced electron lifetime calculated with the help of transient photovoltage decay and EIS measurements. In addition, this improved PCE is also due to better dye uptake by GNR- $\text{TiO}_2$  hybrid mesoporous film as compared to the bare  $\text{TiO}_2$  mesoporous film. However, higher loadings of GNRs in the  $\text{TiO}_2$  nanoparticulate paste have detrimental effects on the PV performance of the DSSCs due to the formation of agglomerates that can induce electron recombination and cracks in the film. Moreover, high loads of GNR induce a considerably loss in optical transparency. Finally, the proposed approach offers a fast, low cost and highly reproducible way to boost the PCE of DSSCs.

## 4 CHAPTER 4 STRUCTURAL EFFECT OF LOW-DIMENSIONAL CARBON NANOSTRUCTURES ON LONG-TERM STABILITY OF DYE-SENSITIZED SOLAR CELLS

### 4.1 Introduction

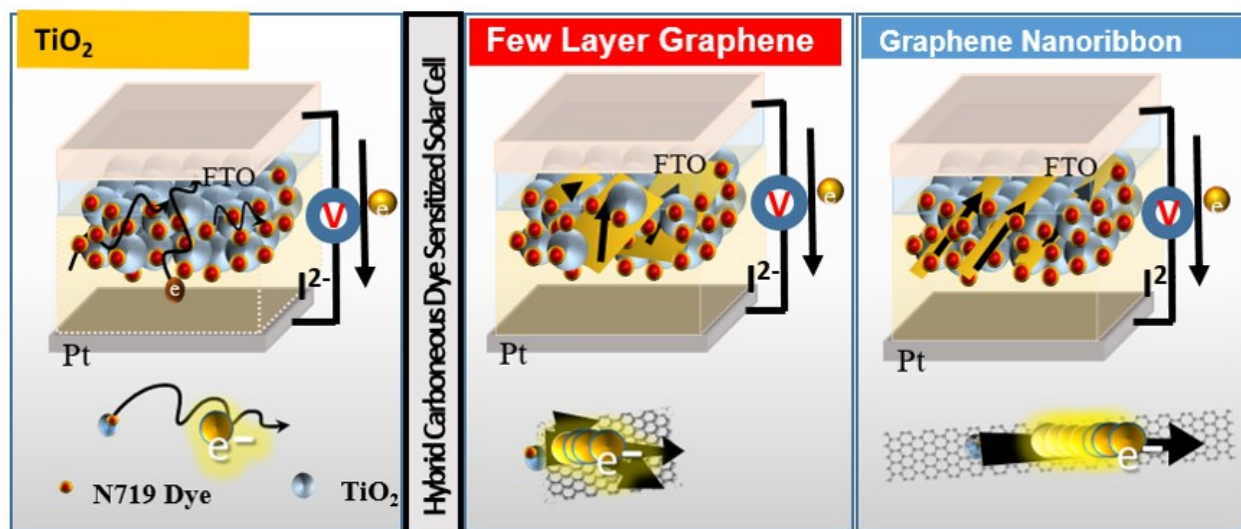


Figure 4-1. Schematic of DSSCs components with TiO<sub>2</sub>, TiO<sub>2</sub>-Graphene and TiO<sub>2</sub>-GNR hybrid photoanodes highlighting preferred electrons transport through FLG and GNR within mesoporous film toward FTO.

Herein, we incorporated optimal amounts of 0.01 wt% (141) and 0.005 wt% (188) of graphene and GNR in TiO<sub>2</sub> active layers respectively, and demonstrated how the presence of small amount of GNR provides a superior long-term stability in hybrid DSSCs. Given the high aspect ratio of GNR, general percolation theory confirms the down shift in concentration observed for GNR. To this end, GNR-TiO<sub>2</sub> hybrid photoanodes were compared with Few layer graphene (FLG)-TiO<sub>2</sub> hybrid photoanode and bare TiO<sub>2</sub> device for light illumination for 273 hours.

### 4.2 Results and discussions

#### 4.2.1 Structural characterization

SEM images of the FLG-TiO<sub>2</sub> and GNR-TiO<sub>2</sub> hybrid films are shown in **Figure 4-2** (b) and (c), respectively. The presence of FLG flakes and GNR within the TiO<sub>2</sub> matrix are highlighted in red.

Although the identification of these structures in the bulk of the film remains a challenge. Raman spectroscopy helped describe its embedded structure more accurately.

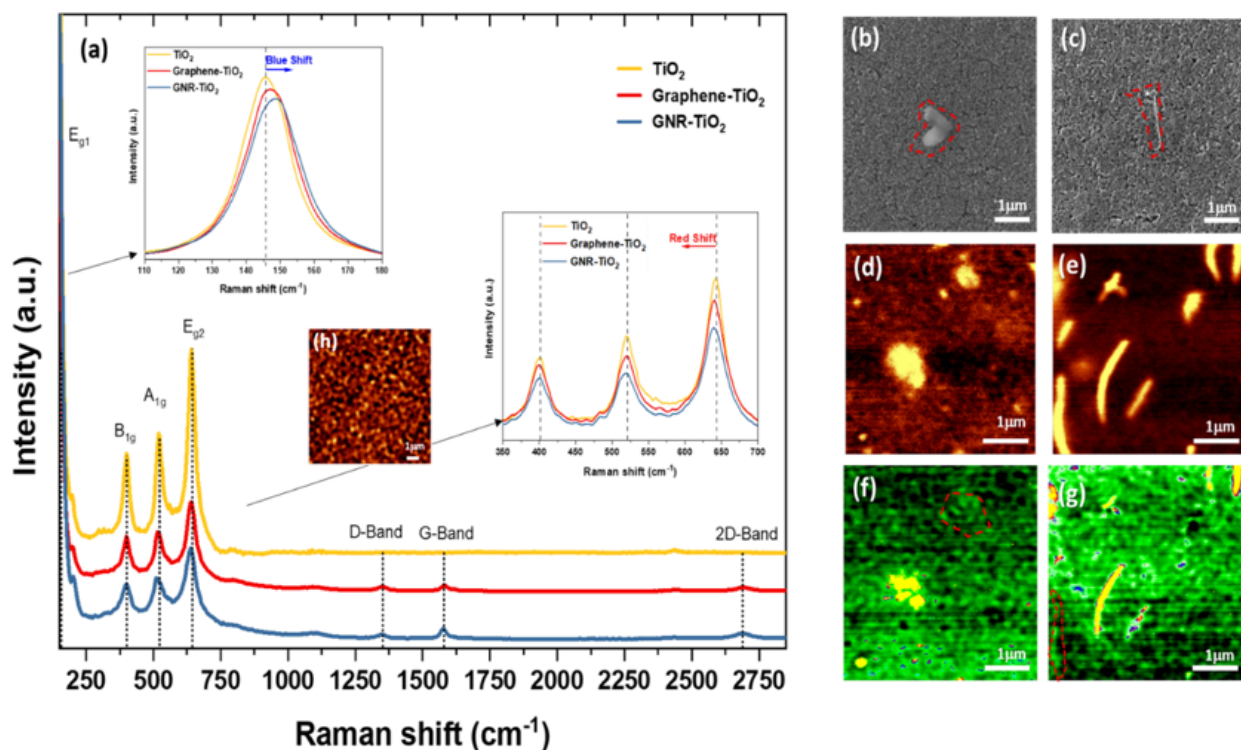


**Figure 4-2.** Raman spectra (a) of bare  $\text{TiO}_2$ , Graphene- $\text{TiO}_2$  and GNR- $\text{TiO}_2$  (0.010 and 0.005 wt % respectively) deposited on FTO. SEM images (b) of 0.075 wt% of graphene and (c) of 0.075 wt% of GNR in  $\text{TiO}_2$ , with dotted rectangle highlighting the presence of the nanocarbon structures. Raman maps of G-band (d)-(e) and D-band (f)-(g) intensities for the samples containing graphene, GNR respectively, and of (h)  $E_{g2}$  band of  $\text{TiO}_2$ .

Raman mapping was used in order to identify embedded nanocarbons within the mesoporous  $\text{TiO}_2$  films [Figure 4-2 (d)-(g)]. Images created from the intensities of the  $\text{TiO}_2$  specific  $E_{g2}$  band [shown in Figure 4-2 (a)], and the nanocarbon specific G-band are shown in Figure 4-2 (d) and (e) respectively. Similarly, intensity maps for the defect sensitive D-band of the nanocarbons are shown in Figure 4-2 (f) and (g) respectively. Compared with the SEM images, which only show surface features, these maps indicate the spatial distribution of the embedded nanocarbons in the  $\text{TiO}_2$  matrix. Moreover, as can be seen in Figure 4-2 (e) how the presence of GNR in  $\text{TiO}_2$  matrix provide with oriented scaffolds, which would allow for electrons to follow pathways through their  $\pi$ - $\pi$  bonds. This shows how similarly to Graphene sheets, GNR's morphologies can help the free-moving electrons to overcome the detrimental influences of grain boundaries in  $\text{TiO}_2$  films, which usually appears after degradation of  $\text{TiO}_2$  films due to long-term light soaking (189) In fact, compared to the FLG- $\text{TiO}_2$  structures, which boast uniform dispersion in the layer and show an

isotropic circular type of morphology, the GNR-TiO<sub>2</sub> structures show scaffolding structures that can easily contribute to the enhancement of the spatial extension of the layer from the bulk, as well as on the surface. This indicates that the mixing of GNR with TiO<sub>2</sub> yields a good dispersion and can provide orientated elongated bridges of approximately 1 μm into the structures.

In addition, the Raman spectra provide information on the nature of the interaction between the materials. Curve fitting for the Raman data were carried with multiple Lorentzian peak fit that allow more precision in their description. The nanocomposite films exhibit common trends in the region of the TiO<sub>2</sub> specific modes between 100 cm<sup>-1</sup> – 750 cm<sup>-1</sup>. The insets in **Figure 4-2** (a), show this spectral region with the TiO<sub>2</sub> anatase bands for the three samples (190): firstly both the GNR and FLG hybrids show a decrease in the intensities of the Eg1 (145 cm<sup>-1</sup>), B1g (399cm<sup>-1</sup>), A1g (520 cm<sup>-1</sup>) and Eg2 peaks (641.5 cm<sup>-1</sup>) and secondly the bands show a small blue shift in the Eg1 peak to higher frequencies (149 cm<sup>-1</sup> and 147.2 cm<sup>-1</sup> upon addition of GNR and FLG) and a small red shift for the Eg2 peak (639 cm<sup>-1</sup> and 640 cm<sup>-1</sup>).

In addition, the characteristic Raman modes of the nanocarbon materials exhibit frequency shifts, which can be attributed to contact doping resulting from interactions with the TiO<sub>2</sub> matrix (133, 191). **Figure 4-3** (a) shows the characteristics D and G bands of graphitic carbon structures (183), observed at 1342 and 1343 cm<sup>-1</sup> and at 1575 and 1570 cm<sup>-1</sup> for FLG and GNR respectively.

The D'-band is another defect related peak observed in graphitic carbons and manifests as a shoulder on the G-band as seen in **Figure 4-3** (a). Moreover, since the D'-band are largely independent of the edge structure their intensities can provide a way to compare the structural qualities of FLG and GNRs (192). Before mixing with TiO<sub>2</sub>, the intensity of D'-band is higher for the FLG as compared to GNR counterpart, suggesting that the FLG contains a significant number of defects within its structure (111, 193–195).



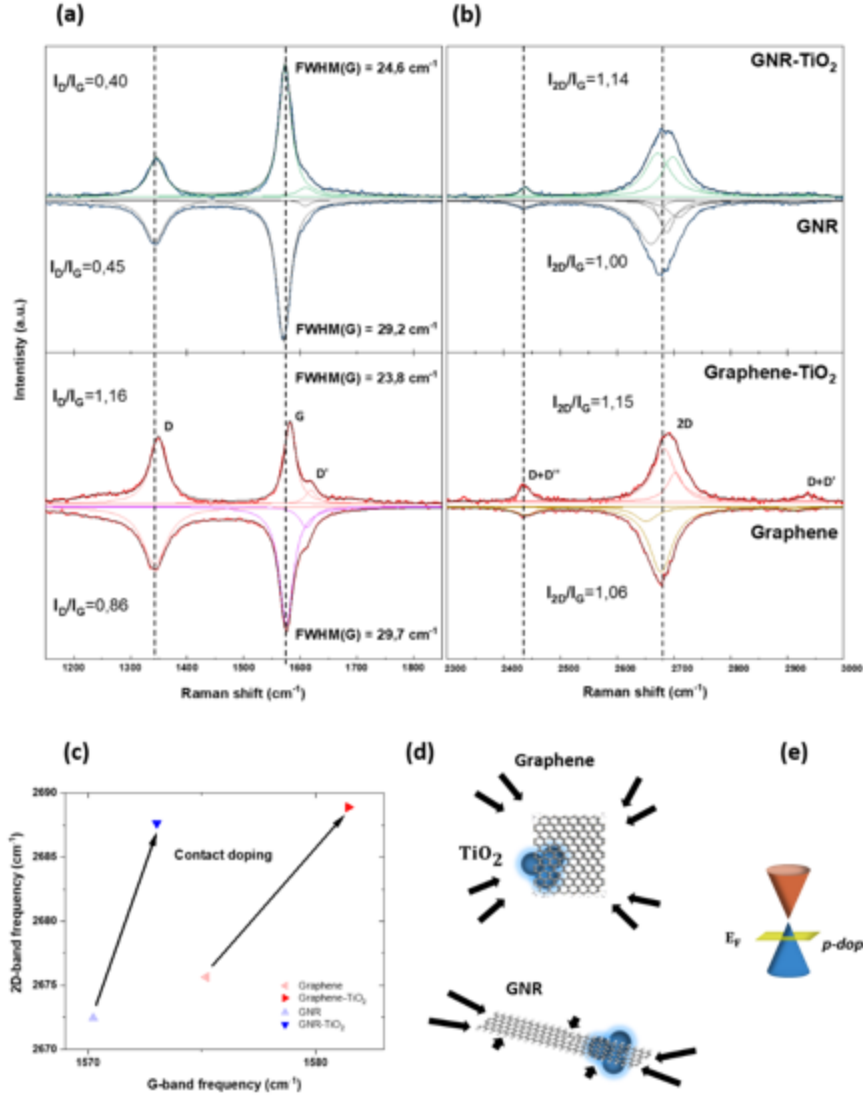


**Figure 4-3.** Raman spectra of the D, G and D'-bands (a) and the 2D and D+D'-bands (b) of GNR-TiO<sub>2</sub> and FLG-TiO<sub>2</sub> compared with pristine GNR and FLG spectra, under 532 nm laser. (c) G band and 2D band evolution by FLG and GNR incorporation in TiO<sub>2</sub>, (d) schematic of compressive strain forces applied to FLG and GNR, (e) schematic of Fermi energy position of energy at the Dirac K point of FLG type structures after p-doping

As mentioned above the D-band observed at  $\sim 1340$  cm<sup>-1</sup> is often used as an indicator of the number of defects present in nanocarbon samples. For high quality chemical vapour deposited (CVD) grown graphene, the D-band is not observed but for smaller and/or defective graphene flakes such as those used here, the D-band intensity is often comparable to that of the G-band. Using the ratio of the Raman intensities  $I_D/I_G$  as a measure of defectiveness of the nanocarbon materials shows that our FLG flakes have higher defects than that of the GNR samples ( $I_D/I_G = 0.86$  for FLG and 0.45 for GNR) in agreement with the conclusion based on the D' intensities.



Furthermore, the  $I_D/I_G$  ratio is seen to increase ( $I_D/I_G = 1.16$ ) for the FLG embedded in  $\text{TiO}_2$  while that of its GNR counterpart decreases ( $I_D/I_G = 0.40$ ). This suggests that overall the extent of GNR- $\text{TiO}_2$  defects is relatively smaller than that of FLG- $\text{TiO}_2$  (192).

The intensity ratio of G to D' represents the proportion of distorted FLG planes and amount of graphene edges provide similar information, whereas the intensity ratio of D to D' ( $I_D/I_{D'}$ ) determines the type of defects and thus are more useful for comparing our samples. This ratio in **Figure 4-3** (a) (b) suggests that GNR- $\text{TiO}_2$  ( $I_D/I_{D'} = 4.2$ ) has fewer vacancy defects than FLG- $\text{TiO}_2$  ( $I_D/I_{D'} = 7.1$ ) (196, 197). The GNRs, the 2D-band shown in **Figure 4-3** (b) reveals an asymmetric shape with a full width half maxima (FWHM) of  $\sim 52.8\text{-}57.5\text{ cm}^{-1}$  when embedded in the mesoporous film. This supports the hypothesis that the GNRs in the hybrid film are composed of few layers GNRs, as much as the pristine GNR (FWHM (2D) of  $61\text{ cm}^{-1}$ ) (198).

The positions of the G and 2D peaks of both FLG and GNR blue shift upon inclusion into the  $\text{TiO}_2$  matrix ( $6\text{ cm}^{-1}$  for FLG and  $3\text{ cm}^{-1}$  for GNR based structure). This may originate either from strains in graphene (phonon hardening-compressive strain or phonon softening-tensile strain) or from changes in the Fermi level of the nanocarbon structures (199, 200). Plotting the shift of the 2D-band against that of the G-band as in **Figure 4-3** (c) helps to determine the type of interactions that results from mixing of the materials. They are both seen to upshift, which can be attributed to a compressive strain or to a decrease of the Fermi level (*p*-doping) of the nanocarbon structures. The compressive strain could contribute positively to the film structural integrity as in **Figure 4-3** (d)), whereas the *p*-doping could help facilitate the charge transfer from the metal oxide to the nanocarbon material (see **Figure 4-4** (e)). Both effects could be occurring in a competitive way through phonon-electron and phonon-phonon interactions. Since the 2D band shows a larger shift than the G band, this suggests that the mechanical hardening effect dominates for both samples (200). Combined with the fact that the blue shift along G band direction, of the FLG counterpart is larger than that of GNR, we can suggest that inclusion of the nanocarbons gives GNR a stronger bridge-like compressive effect or reinforcement than FLG, which instead makes wrapping type of compressive effect, hence the different size of FLG can be seen in **Figure 4-2** (d). This result can also help to understand why FLG's defects are remarkably increasing upon inclusion in the  $\text{TiO}_2$  matrix.

Additionally, **Figure 4-3** (a) shows a decrease of the full-width at half-maximum (FWHM) of the G-band from  $29.2$  to  $4.6\text{ cm}^{-1}$  for GNR and  $29.7$  to  $5.9\text{ cm}^{-1}$  for FLG after the nanocarbon structures are introduced in the  $\text{TiO}_2$  films. Since, this stiffening of the G-band accounts for both electron

and hole doping (201, 202), However, we are not able to completely rule out that the interaction of the two moieties does not contribute in the modification of the carrier density.

Moreover, as the aging time under light exposure is prolonged, crack density in the electrode film have been shown to be increased. Thermal stress at high temperature induced by light exposure have also been shown to affect the photoelectrode film by expanding with heat and contracting with cold (113). The effects of these morphological changes can be further investigated through the photoelectrical characterization of the films.

#### 4.2.2 Photovoltaic characterization

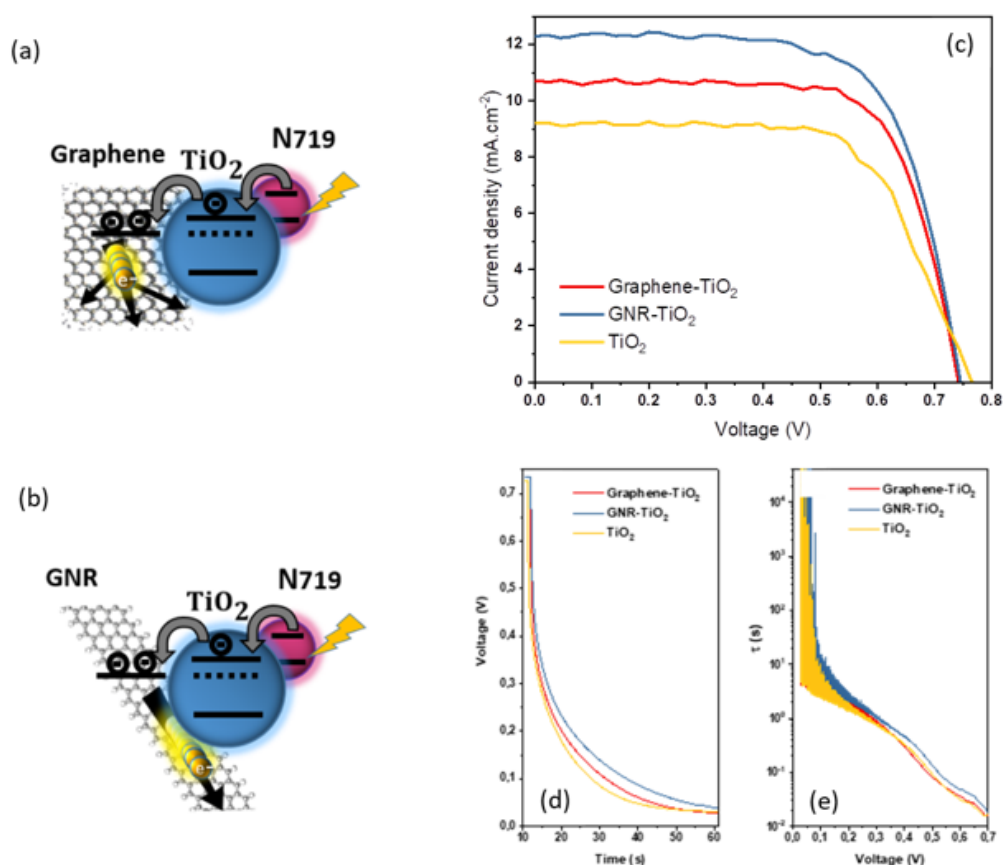


**Figure 4-4** Schematic of the band alignment and carrier dynamics within hybrid photoanodes: (a) FLG-TiO<sub>2</sub>; (b) GNR-TiO<sub>2</sub>. Photovoltaic characterizations of DSSCs based on hybrid photoanodes of FLG and GNR in TiO<sub>2</sub> and bare TiO<sub>2</sub>: (c) Current density–voltage curves under one sun illumination (AM1.5G irradiation (100 mW/cm<sup>2</sup>). Transient photovoltage decay measurements of the corresponding devices: (d) V<sub>oc</sub> decay; (e) electron lifetime.

The purpose of integrating nanocarbons into DSSCs is to enhance the performance and stability of the photoanode by bridging TiO<sub>2</sub> nanoparticles, as well as aiding in the transfer of electrons to

their collection sites (119, 203) (see **Figure 4-4** (a) (b)). The effect that these materials provide to the overall performance of cells are described in this section.

#### 4.2.2.1 Current density–voltage, Transient photovoltage decay and electron lifetime

The current-density vs voltage (J-V) curves of DSSCs are shown in **Figure 4-4** (c) and their corresponding functional parameters including the open circuit photovoltage ( $V_{oc}$ ), the short circuit current ( $J_{sc}$ ), the fill factor ( $FF$ ) and the PCE are reported in **Table 1**. The hybrid photoanodes, prepared with optimum FLG and GNR concentrations of 0.01 wt % and 0.005 wt % respectively, resulted in PCE enhancements of 21.3% and 23% with respect to bare  $TiO_2$ . Similar improved functional performance has been noted in previous studies from our group and attributed to enhanced dye loading and reduced charge recombination with addition of small quantities of FLG and GNR to the  $TiO_2$  based anodes (188). In addition, a set of DSSCs were fabricated by using different content of GNR and FLG in  $TiO_2$  mesoporous film and recorded their J-V curves [Figure S 4-1].

**Table 4-1 Functional properties of DSSCs with different FLG and GNR content.**

Sample	Carbonaceous content (wt%)	$V_{oc}$ (V)	$J_{sc}$ (mA/cm <sup>2</sup> )	$FF$ (%)	$PCE$ (%)
$TiO_2$	0.00	0.767	9.21	66	4.65
GNR- $TiO_2$	0.005	0.745	12.17	69	6.23
FLG- $TiO_2$	0.010	0.739	10.73	71	5.64

Transient photovoltage decay measurements have been carried out in order to understand the effect of the addition of nanocarbon materials on the carrier dynamics in the DSSCs. Results of these measurements provides information about the carrier recombination occurring at the  $TiO_2$ /dye/electrolyte interface. In this measurement, DSSCs were illuminated under one sun simulated sunlight (AM 1.5G, 100 mW/cm<sup>2</sup>) until a stable voltage ( $V_{oc}$ ) was reached. Then the simulator shutter was closed and the voltage decrease versus time was recorded under dark conditions. **Figure 4-4** (d) displays the  $V_{oc}$  decay curves versus time for DSSCs based on hybrid

nanocarbon-TiO<sub>2</sub> and bare TiO<sub>2</sub> photoanodes. The electron lifetime ( $\tau$ ) in **Figure 4-4 (e)** was calculated from the  $V_{oc}$  decay measurements by using the following equation (170),

$$\tau_e = \frac{k_B T}{e} \left( \frac{dV_{oc}}{dt} \right)^{-1}, \quad (4-1)$$

where  $k_B$  is Boltzmann's constant,  $T$  is the absolute temperature, and  $e$  is the elementary charge. It is observed that the rate of  $V_{oc}$  decay is faster for DSSCs based on bare TiO<sub>2</sub> than the DSSCs based on GNR-TiO<sub>2</sub> and FLG-TiO<sub>2</sub>. Similarly, at particular value of  $V_{oc}$  (0.7 V), the calculated  $\tau_e$  values of the DSSCs follows the trend GNR-TiO<sub>2</sub> > FLG-TiO<sub>2</sub> > TiO<sub>2</sub>, which is in agreement with obtained PV performance of the respective devices and previous studies (188).

#### 4.2.2.2 Long-term stability

The following section concern mechanisms related to stability of DSSCs due to aging of the photoelectrode film. Stability measurements were carried out on a set of bare TiO<sub>2</sub> DSSCs, as well as those incorporating FLG and GNRs. Changes occurring at the electrolyte components as well as degradation of the counter electrode of samples, were closely monitored. The evaporation of electrolytes usually being a restricting factor for this measurement. The results presented here are related to devices with strong liquid electrolyte conservation and do not consider those removed due to possible degradation. Four initial samples were prepared and monitored. For each series of measurements, only the data of the sample with prolonged electrolyte upholding was used to compare samples performance. **Figure 4-5 (a)-(d)** show the variation of PV parameters of the remaining DSSC samples under continuous one sun simulated sunlight at AM 1.5G (100 mW/cm<sup>2</sup>) at room temperature. All PV parameters are normalized to the initial value at the beginning of the test. These results demonstrates that the degradation rate of the PV parameters in hybrid cells with GNR was effectively suppressed as compared to their bare counterpart, while the FLG counterpart performs lower PV parameter preservation rate.

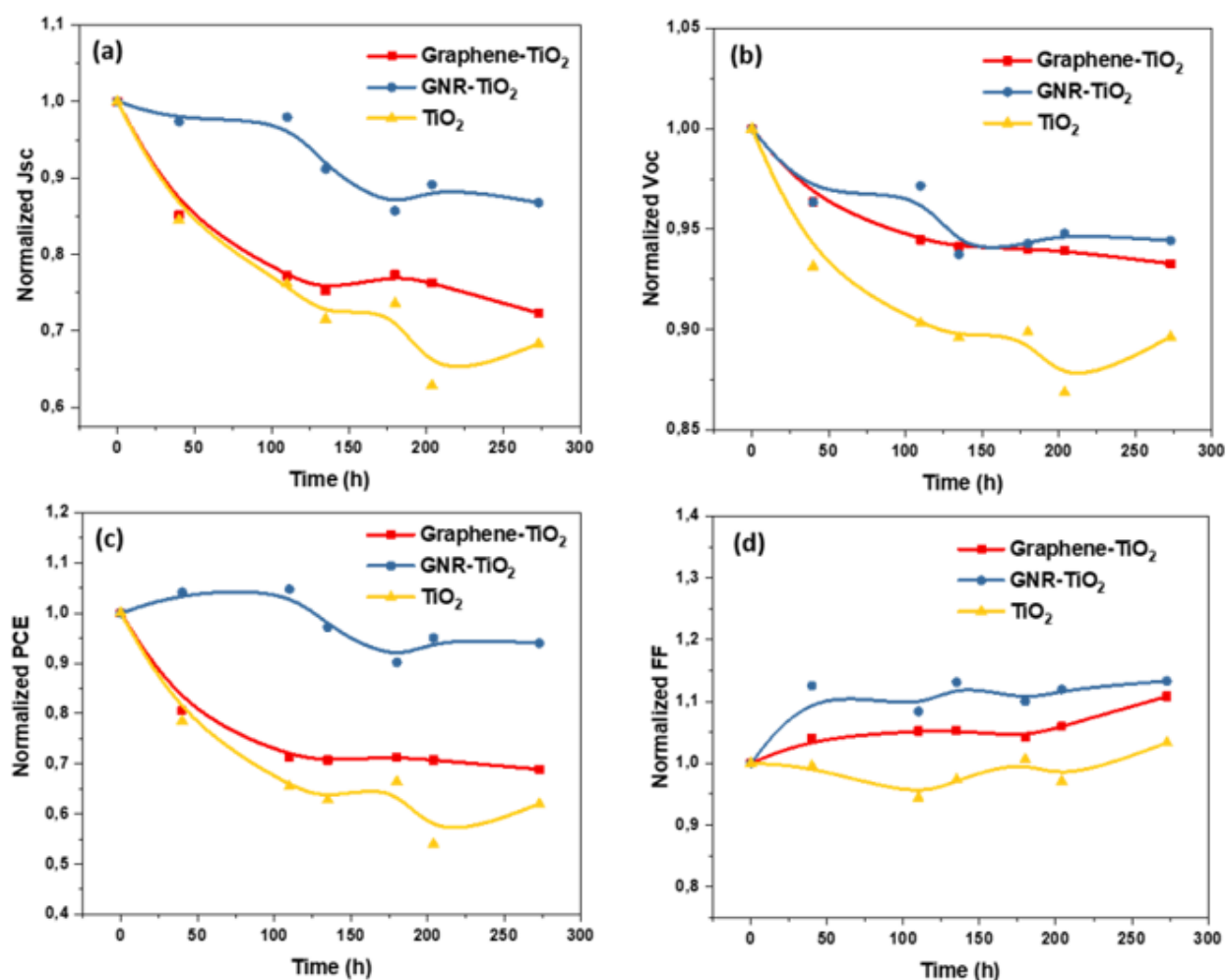


Figure 4-5. Normalized functional parameters of DSSCs with optimum concentration of FLG and GNR in TiO<sub>2</sub> and bare TiO<sub>2</sub> under a continuous light irradiation as a function of soaking time. (a)  $J_{sc}$ ; (b)  $V_{oc}$ ; (c) PCE; (d) FF.

As seen in **Figure 4-5 (a)** all the cells with bare TiO<sub>2</sub>, display a significant  $J_{sc}$  decline, however the cells with nanocarbon exhibited slower degradation, particularly in the case of those using the GNRs. Since, efficient electron transport and collection is related to the morphological quality of the mesoporous TiO<sub>2</sub> layers, any presence of bundles in nanocarbons and agglomeration between TiO<sub>2</sub> particles can be vectors for accelerated  $J_{sc}$  (mA/cm<sup>2</sup>) reduction rate (113). In fact, with time, the change of the electron transfer between the TiO<sub>2</sub>/dye/electrolyte interface (204) in DSSCs, are caused by aging of the photoelectrode film and UV light, which create detrimental electronic paths that adds recombination centers (168).

Although higher reduction is observed for  $V_{oc}$  in bare samples than in nanocarbon hybrid samples (**Figure 4-5 (b)**), these trends are considerably lower than that of  $J_{sc}$ , suggesting a minimal sensibility of the conduction band of composite also low degradation of this parameter for the devices with nanocarbons, and slow degradation for bare sample due to minimal sensibility of the conduction band over time.

**Figure 4-5 (d)** displays the systematic comparison of the variation of FF of DSSCs based on GNR-TiO<sub>2</sub>, FLG-TiO<sub>2</sub> and TiO<sub>2</sub>. The FF of all devices remain relatively stable throughout the study. This parameter is related to the charge transfer resistance at the counter electrode (ion exchange stability) and sheet resistance of the resistance of conducting glass substrate (i.e. FTO). Its stable values in these cases indicate that there are no apparent changes in the series connected resistances and degradation in both the transparent FTO and the Pt-catalyst layer. Hence, the overall drop of PCE in both types of cells with and without nanocarbon materials is mainly due to reduction trends of  $J_{sc}$ . However, in the composite device with GNRs the PCE is reduced more slowly (only 6%), as compared to the bare device (38%) and that with FLG (31.2%), suggesting an exclusive contribution of GNRs to maintain the parameters stability.

Although in DSSCs the rising temperature of the device could explain some heat related features of increased transport capability (205, 206), longer light soaking time usually lead to breaking the connections between TiO<sub>2</sub> particles in the mesoporous layer. Thus, by preserving better its structural integrity, both nanocarbons and especially GNR, not only help achieve an enhanced photoelectrical conductivity but they also support the mechanical strength of the host material, as can be seen with the p-doped compressive strain forces modifications in **Figure 4-3 (c)**. Moreover, with its contribution in the slowly decreasing  $J_{sc}$ , the elongated 1D strip of FLG help establishing reliable electron diffusion pathways for DSSC devices over time (189).

#### 4.2.3 EIS measurements

In addition, we carried out EIS measurements to investigate the effect of the addition of graphene flakes and GNRs to the TiO<sub>2</sub> photoanode. The main parameters (charge transfer resistance ( $R_{ct}$ ), chemical capacitance ( $C_{\mu}$ ) and electron lifetime ( $\tau_n$ ) of the mesoporous TiO<sub>2</sub> film), are extracted from the Nyquist plots according to an equivalent electrical model for the devices. The peak frequency of an arc in a Nyquist plot,  $\omega_{max}$ , is given as equal to the reaction rate constant for the recombination with tri-iodide, which can be easily determined through the Bode plot. Nyquist plots and Bode plots, taken at an intermediate potential of 650 mV, are shown in **Figure 4-6 (a) (b)** and highlight the shifts of each electrode after aging. In general, the Nyquist plots show 2-3 semicircles

in the frequency range of 0,1-100 kHz. The first semicircle,  $R_{CE}$ , is related to the charge transfer at the counter electrode measured in the kHz range. The second semicircle,  $R_{CT}$ , is related to the charge transfer resistance of the mesoporous layer of at the nanocomposite-TiO<sub>2</sub>/dye/electrolyte interface in the range of 1-100Hz. The third semicircle shows the Warburg diffusion process of iodide/tri-iodide in the electrolyte, measured in the mHz range. The Ohmic series resistance ( $R_s$ ), is associated with the series resistance of the electrolytes and electric contacts in the DSSC. As we reduce the potential, Constant Phase Elements (CPE) are used for chemical capacitor in order to fit the data accurately (207). The most remarkable feature in the Nyquist plots in **Figure 4-6** (a), is that at bias potential close to  $V_{OC}$  (700mV), the GNR-TiO<sub>2</sub> electrode leads to the smallest semicircle at mid-frequencies, related to  $R_{ct}$  at the TiO<sub>2</sub>/dye/electrolyte interface. This feature has been verified in previous studies (141) and are confirmed in this study where the diameter of the medium arc corresponds to the charge transfer resistance of the mesoporous layer. In contrast, the FLG-TiO<sub>2</sub> electrode, is seen to exhibit the largest arc, reflecting a  $R_{ct}$  which is larger than the bare device. Moreover, the respective frequencies for GNR-TiO<sub>2</sub>, FLG-TiO<sub>2</sub> and bare samples (15.9 Hz, 8 Hz, and 14 Hz), shown in **Table 4-2**, shows that GNR based nanocomposite devices exposes photogenerated electrons to slightly higher recombination rate than bare devices while FLG-TiO<sub>2</sub> samples, which exhibit low recombination rate ( $\omega_{max} = 8\text{Hz}$ ) and high  $R_{ct}$ , as shown in **Figure 4-6** (a) and (b). This suggests that FLG additives considerably reduces recombination processes while GNR manages to overcome it. In fact, J-V measurements shows how it has higher  $J_{SC}$  and higher PCE, which give the conduction capabilities of GNR high enough energy to increase electron collection efficiency (208). Comparatively, FLG-TiO<sub>2</sub>, help reduce recombination more efficiently while boasting good current density, thus suggesting the superior effect of GNR's aspect ratio on electron transport in the conduction band of the metal oxide.

**Figure 4-6** (e), shows the change in  $R_{ct}$  at different potentials before and after aging. For potentials between 500-800 mV, which corresponds to recombination processes at the TiO<sub>2</sub>/dye/electrolyte interface, both graphene and GNR samples show a large reduction in  $R_{ct}$  whereas the bare TiO<sub>2</sub> device shows a relatively small change. The general decrease can be attributed to the presence of increased cracks density in the film which engages loss in film extension and thus decrease of photocurrent density ( $J_{SC}$ ). However, the significant reductions of  $R_{ct}$  upon aging for the hybrid photoanodes can be attributed to the formation of bridges by GNR nanocarbons, enhancing its interfacial interaction with the electrolyte (to 70% and of 50% for FLG and GNR respectively). This can be attributed to higher  $J_{SC}$ , related with nanocarbon's high surface area, and high charge carrier mobility encouraging a sustained electron transport through nanoscale bridges despite cracks (135). At low potentials, in contrast the bare sample exhibits a

drastical decreases of  $R_{ct}$  upon aging to a low  $R_{ct}$  plateau (from up to 147 k $\Omega$  to 2 k $\Omega$ ), while FLG and GNR based electrode still behave like insulators (209) and therefore exhibit large charge transfer resistances (30 – 100 k $\Omega$ ) that remains mostly unchanged. GNR's  $R_{ct}$  even increases below 200mV before remaining constant in the 200-500 mV range, which suggest a well-kept cell integrity at the TCO at the bottom of the porous film or back layer (83). Thermal stress and light induced degradations, induces detrimental cracks in the back layer structure in bare cells (210) at the TCO/working electrode interface. Consequently, the addition of FLG and GNR help to preserve the integrity of the film, and working electrode performance by overcoming stresses at the mesoporous layer.(188)



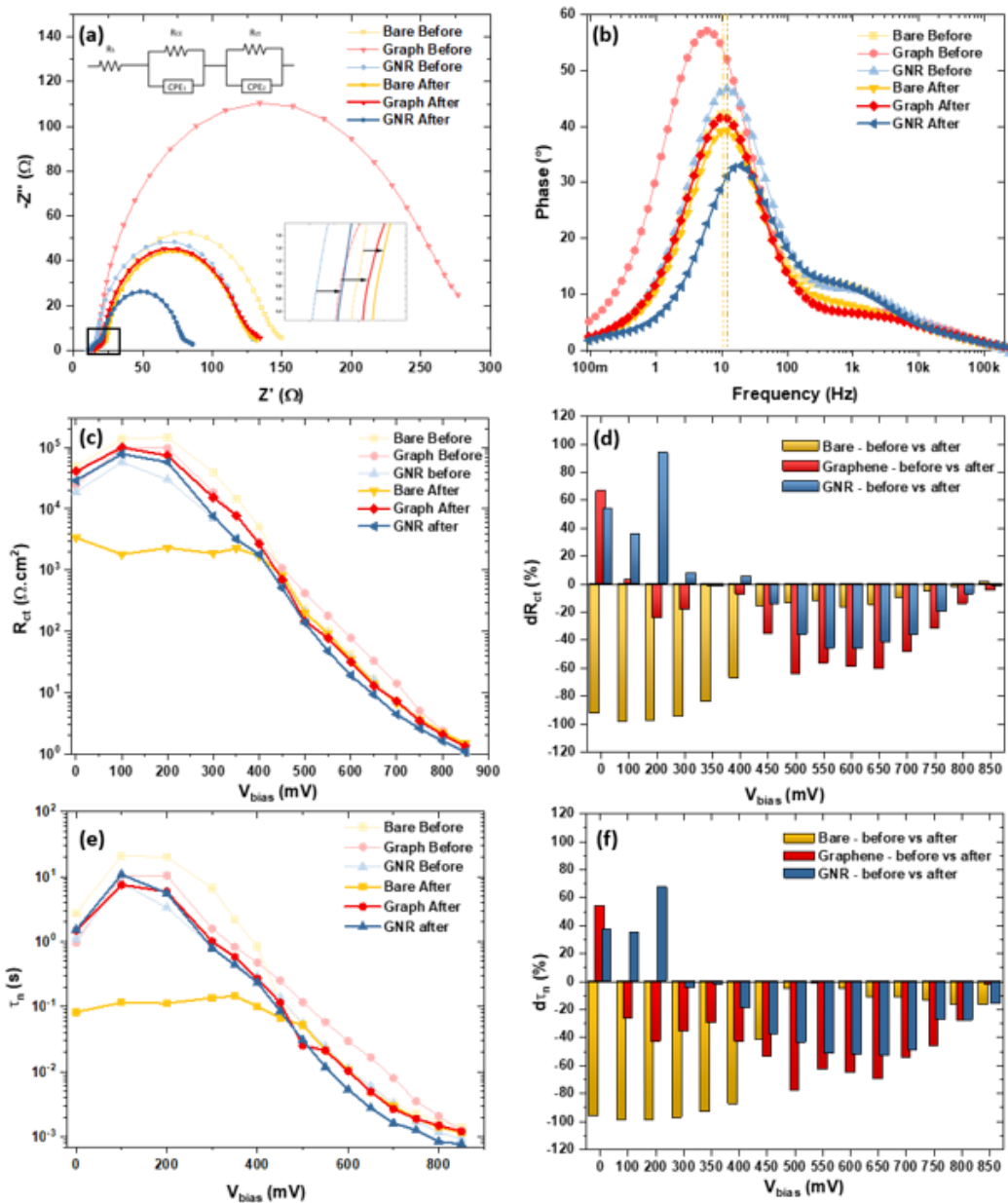


**Figure 4-6.** EIS analysis of bare DSSCs FLG-TiO<sub>2</sub> and GNR-TiO<sub>2</sub> hybrid DSSC before (lighter color) and after 270h (darker colours) simulated sun exposure under dark measurement: (a) Nyquist plot; (b) Bode plot at 750 mV and (c)  $R_{ct}$ , (e)  $\tau_n$ , (d) (f) histograms of changes in charge transfer resistance and electron lifetime after aging, at potentials between 0-850mV.

Subsequently, this trend can be correlated with the apparent electron lifetime  $\tau_n$  of the devices, calculated from  $R_{ct}$  and  $C_\mu$  through the expression ( $\tau_n = R_{ct} \times C_\mu$ ) and presented in **Figure 4-6** (d). The lifetime shows a similar overall trend as  $R_{ct}$  with a decrease as the bias voltage increases. The  $\tau_n$  in FLG-TiO<sub>2</sub> is larger than that of GNR-TiO<sub>2</sub> and TiO<sub>2</sub> samples at bias voltage 650 mV (16.6

ms, 5.9 ms and 5.5 ms respectively). **Figure 4-6** (f) shows the changes in apparent lifetime as the samples ages. The decrease of  $\tau_n$  at intermediate voltage is more important for FLG-TiO<sub>2</sub> than both GNR-TiO<sub>2</sub> and TiO<sub>2</sub> samples (70%, 53.7% and 11.9% respectively).

The electron lifetime ( $\tau_e$ ) obtained from the Bode plot in **Figure 4-6** (b) and from  $\tau_e = \frac{1}{\omega_{max}} = \frac{1}{2\pi f_{max}}$ , where  $f_{max}$  represents the maximum frequencies, exhibits similar trend at 600 mV as shown in **Table 4-2**, which confirms to the overall trend of each samples as the electron lifetimes  $\tau_n$  previously acquired.

**Table 4-2 EIS parameters evolution at 600mV before and after (bold) 273h of continuous one sun light soaking time for bare TiO<sub>2</sub>, FLG-TiO<sub>2</sub> and GNR-TiO<sub>2</sub> samples**

Sample	Carbonaceous content (wt%)	R <sub>CT</sub> (Ω.cm <sup>2</sup> )	ω <sub>max</sub> (Hz)	τ <sub>n</sub> (ms)	τ <sub>e</sub> (ms)
Bare	0.00	42.3 – <b>35.3</b>	7.2 – <b>7.3</b>	11.4 – <b>10.7</b>	22.0 – <b>21.9</b>
FLG-TiO <sub>2</sub>	0.010	77.8 – <b>31.7</b>	4.2 – <b>7.3</b>	29.6 – <b>10.3</b>	37.9 – <b>21.9</b>
GNR-TiO <sub>2</sub>	0.005	35.6 - <b>19</b>	8.1 – <b>12.5</b>	11,3 – <b>5.35</b>	19.7 – <b>12.7</b>

At low bias, dτ<sub>n</sub> displays a similar trend to dR<sub>ct</sub>, with a large decrease in the bare TiO<sub>2</sub> sample's electron lifetime (99% decrease at 200 mV and an average of 98.6% decrease), while the FLG based sample decreases mildly (43% at 200 mV and an average of 5.6% decrease) and the GNR-TiO<sub>2</sub> sample increases (67.2% at 200 mV and an average of 46.6% increase) (see **Figure 4-6** (f)).

These trends show that the devices incorporating GNR are more robust than those with FLG in terms of maintaining a stable charge transfer resistance at low bias voltage and contributing efficiently to isolating the anode. This can be firstly corroborated with the  $R_s$  of the GNR-TiO<sub>2</sub> sample in the inset of **Figure 4-6** (a), being smaller than both its FLG and bare counterparts while exhibiting a higher evolution rate after 273 h of aging (10.2 Ω with a 24% evolution vs 14.15 Ω with a 22% evolution vs 12.6 Ω with a 15.2% evolution for GNR-TiO<sub>2</sub>, Graphene-TiO<sub>2</sub> and TiO<sub>2</sub> samples respectively).

Moreover, since the capacitive response  $C_\mu$  of the  $\text{TiO}_2$  photoanode ( see **Figure S 4-2**), depends on the density of electronic state distribution below the conduction band edge ( $E_{\text{CB}}$ ) and the Fermi level (211), we can deduce that by embedding the nanocarbons with  $\text{TiO}_2$  we further induce a  $p$ -doping (see **Figure 4-3** (e)) by means of a shift in the position of the Fermi level overtime that is more significant for FLG- $\text{TiO}_2$  than for GNR- $\text{TiO}_2$ . This is shown in **Figure 4-3** (c) where the shift of the G-band of FLG is larger compared to that of GNR. This confirms that addition of FLG induces a larger change than GNR in the  $C_\mu$  change (see **Figure S 4-2** (b)). Charge separation relies on a good connectivity of the photoanode layer by extending spatially the structure. This is how GNR scaffolding provides sufficient driving force to maintain the integrity of the structure and improving charge transport in the layer, as can be witnessed by the increased  $J_{\text{SC}}$  and the decreased  $R_{\text{CT}}$ .

### 4.3 Conclusions and perspectives

In summary, we demonstrated that the addition of FLG and GNRs to  $\text{TiO}_2$  photoanodes can improve the PV performance and operational stability of DSSCs under continuous illumination. These 2D nanocarbon- $\text{TiO}_2$  composite anodes were assembled and characterized by different techniques to investigate differences in charge carrier mechanisms after extended light exposure. This study shows that after 273h of continuous one sun light soaking time, GNR- $\text{TiO}_2$  devices exhibit 51.6% more PCE stability compared to a bare  $\text{TiO}_2$  DSSC device, while FLG- $\text{TiO}_2$  devices only exhibited a 10% improvement in PCE stability under the same operating conditions and with 2 times more content. This increased stability is mainly due to a longer persistence of  $J_{\text{sc}}$  of GNR devices compared to FLG.

The Raman mapping of the films incorporating the nanocarbon materials highlighted how the elongated 1-D structure of the GNRs results in both vertical and horizontal pathways within the  $\text{TiO}_2$  matrix, reinforcing the composite in multiple directions compared to the planar FLG flakes. Analysis of the Raman spectra showed that compressive strain forces and  $p$ -doping were induced by the mixing of graphene and GNR inside the  $\text{TiO}_2$  matrix. The transient photovoltage decay and EIS measurements confirmed the higher  $\tau_e$ ,  $\tau_h$  and reduced recombination in both nanocarbon- $\text{TiO}_2$  nanocomposite network-based device in comparison to the device based on bare  $\text{TiO}_2$  nanoparticles. These results provide a straightforward way to improve long-term stability of the DSSC, which is crucial for this promising technology to move one step closer to commercialization. Such outstanding properties provided by GNR should stimulate the use of these nanomaterials in various photoelectronic systems.



## 5 CHAPTER 5 GRAPHENE NANORIBBON-TiO<sub>2</sub>-QUANTUM DOTS HYBRID PHOTOANODE TO BOOST THE PERFORMANCE OF PHOTOELECTROCHEMICAL FOR HYDROGEN GENERATION

### 5.1 Introduction

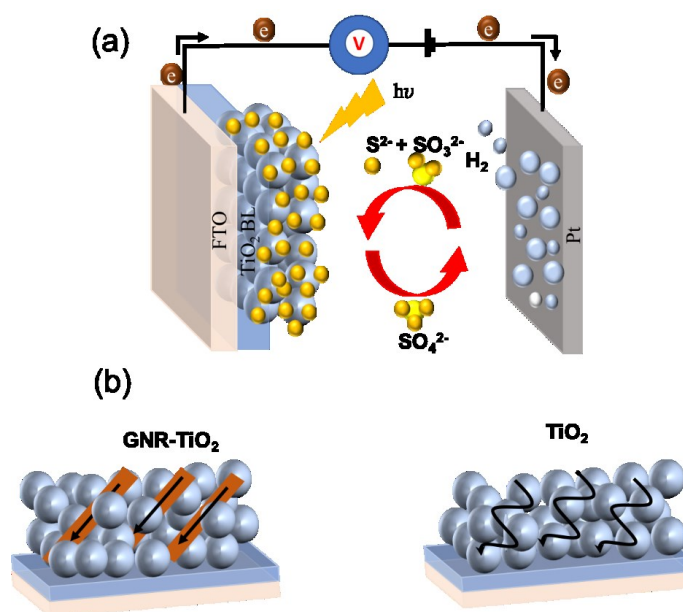


Figure 5-1 (a) Schematic illustration of the working principle of PEC device for hydrogen generation. (b) Electron transport process in mesoporous TiO<sub>2</sub> film with and without GNR. The arrows indicate the electron transfer process.

GNRs are capable of achieving high photocurrent and faster photoexcited electron transfer from the semiconductor to the liquid/solid interface through the 1D network of carbon, as in the case of hybrid GNRs-TiO<sub>2</sub> hybrid in DSSCs (188). Electrons follow random paths after entering into the semiconductor nanoparticles anode and thus have maximum probability to recombine due to intrinsic defects within the TiO<sub>2</sub> nanoparticle film, as shown in **Figure 5-1 (b)** (212). Therefore, by addition of a small amount of GNRs, we can achieve a unidirectional flow of electrons for increasing charge transport efficiency [see **Figure 5-1 (b)**].

Here we report a simple, fast and cost-effective approach for the fabrication of GNRs-TiO<sub>2</sub> hybrid anodes sensitized with colloidal heterostructured quantum dots (QDs), to improve the performance of PEC cells for H<sub>2</sub> generation. The highest saturated photocurrent density of the PEC device based on GNRs-TiO<sub>2</sub>/QDs hybrid photoanode reaches 5.51 mA/cm<sup>2</sup> (at 0.8 V RHE) under one sun illumination (AM 1.5 G, 100 mW/cm<sup>2</sup>), which is 30% higher than the PEC device

based on  $\text{TiO}_2/\text{QDs}$  photoanodes. This improvement is attributed to the enhanced electrons transport properties of GNRs- $\text{TiO}_2/\text{QDs}$  hybrid photoanode. In addition, the long-term stability of the PEC device based on GNRs- $\text{TiO}_2/\text{QDs}$  hybrid photoanode (0.02 wt%) is 15% better as compared to PEC based on  $\text{TiO}_2/\text{QDs}$  photoanode.

## 5.2 Results and discussion

### 5.2.1 Structural and morphological characterization of GNR- $\text{TiO}_2$ hybrid anode.

SEM images of the bare  $\text{TiO}_2$  and GNR- $\text{TiO}_2$  hybrid mesoporous anodes with different concentrations of GNRs at different magnification are shown in **Figure 5-2** (a)-(f). SEM images of bare  $\text{TiO}_2$  mesoporous film confirm the formation crack-free and porous film [see **Figure 5-2** (a)-(b)]. **Figure 5-2** (c)-(d) displays SEM images of GNR- $\text{TiO}_2$  hybrid mesoporous film with optimized concentration of GNR (0.02 wt%). However, it is very hard to identify the presence of GNRs in the hybrid mesoporous film due to low concentration of GNR and complete coverage of GNR by  $\text{TiO}_2$  nanoparticles as generally observed for similar carbonaceous- $\text{TiO}_2$  hybrid system (118, 123). SEM images of GNR- $\text{TiO}_2$  hybrid mesoporous film with the highest concentration of GNR (0.05 wt%) exhibits a series of deep cracks [**Figure 5-2** (e)-(f)], which are not observed in bare  $\text{TiO}_2$  and GNR- $\text{TiO}_2$  hybrid mesoporous film with optimized concentration of GNR (0.02 wt%).

The presence of these cracks with high loading of GNR (0.05 wt%) in the GNR- $\text{TiO}_2$  hybrid anode, hinder the efficient transport of electrons within the photoanode by trapping inside the anode. In addition, these cracks act as recombination sites for electrolyte and back transfer electrons (electrolyte/FTO). This may reduce the device's overall functional performance, confirmed also by photocurrent density measurements of PEC based on respective photoanodes (more details are reported in PEC measurement section).

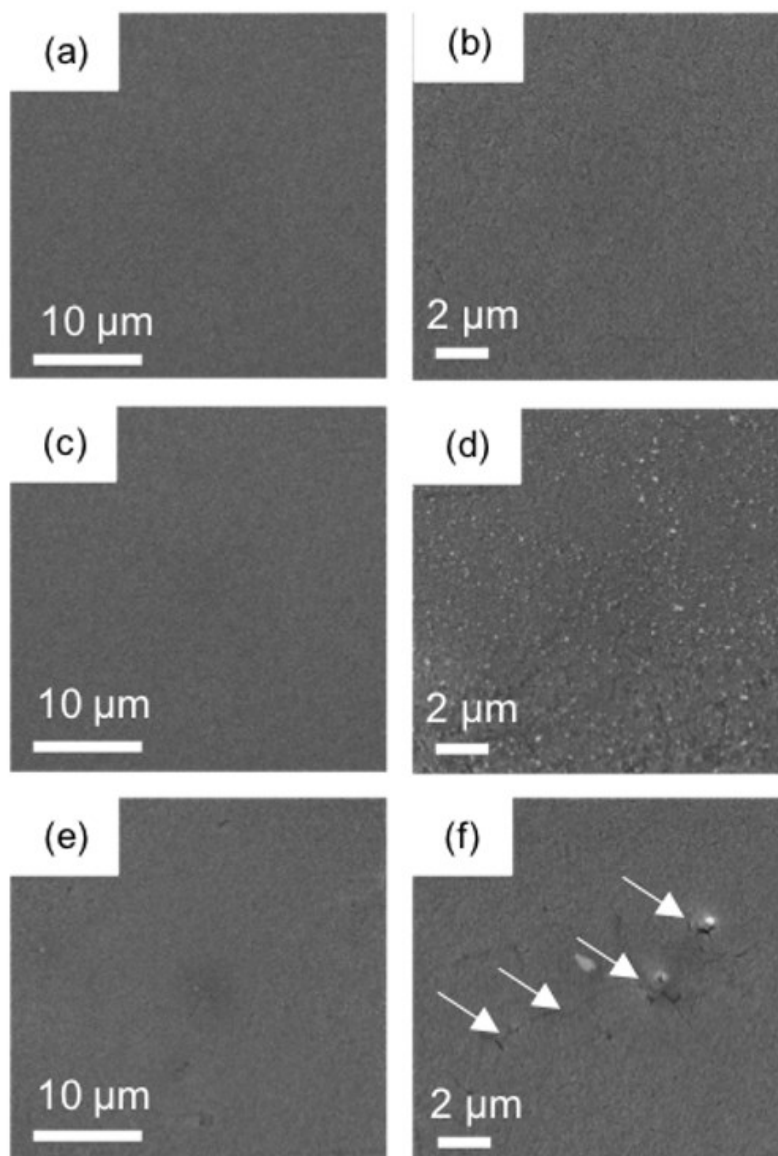


**Figure 5-2 SEM images of GNR-TiO<sub>2</sub> hybrid mesoporous films with different concentration of GNR: (a-b) 0.00 wt %; (c-d) 0.02 wt% and (e-f) 0.05 wt% at different magnifications. The presence of deep cracks at higher concentration of the GNR is highlighted in white**

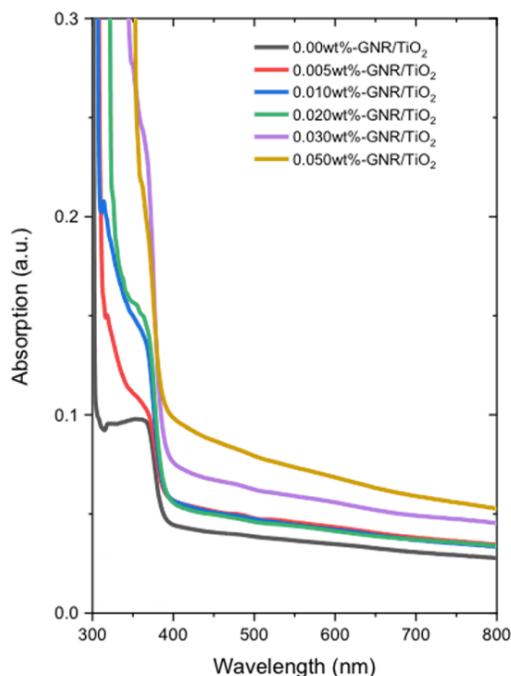


**Figure 5-3** A comparison of absorption spectra of GNR-TiO<sub>2</sub> hybrid mesoporous films deposited on transparent conducting oxide glass with different concentration of GNR (wt %)

The transparency of the GNR-TiO<sub>2</sub> hybrid mesoporous film in the UV-Vis region changes with different content of GNRs. **Figure 5-3** displays the variation of absorption spectra of GNR-TiO<sub>2</sub> hybrid mesoporous film with GNRs concentration. The transparency of GNR-TiO<sub>2</sub> hybrid mesoporous film with GNR content below 0.02 wt% is comparable to bare TiO<sub>2</sub> and absorption peak positions are close to each other, since they both show a drastic increased absorption intensity at 400 nm, corresponding to the intrinsic band gap of anatase TiO<sub>2</sub>. However, further increasing the content of GNR (0.03-0.05 wt%) in the hybrid film reduces its transparency. The UV-Vis spectrum of GNR-TiO<sub>2</sub> hybrid film (0.03-0.05 wt%) shows a stronger absorption in the range of 400-800 nm than bare TiO<sub>2</sub> and GNR-TiO<sub>2</sub> hybrid (GNR less than 0.02 wt%) and is consistent with reported literature on carbonaceous-TiO<sub>2</sub> hybrid film (116, 213–217). There is an obvious correlation between the GNRs content and the UV-Vis spectrum change, that can be attributed to the GNRs sheets on the surface of TiO<sub>2</sub>. The absorption of GNR-TiO<sub>2</sub> hybrid anode remains unaltered, when the mass amount of GNR is less than 0.02 wt%, may be due to the chemical monolayer adsorption. Once the monolayer coverage becomes saturated, further addition of GNRs tends to form multilayers, which will evolve into clusters that reduce the transparency (22, 218). Therefore, direct light absorption by the GNRs results in a loss of part of the radiation available for exciton generation, which in turn worsens the device's overall performance.



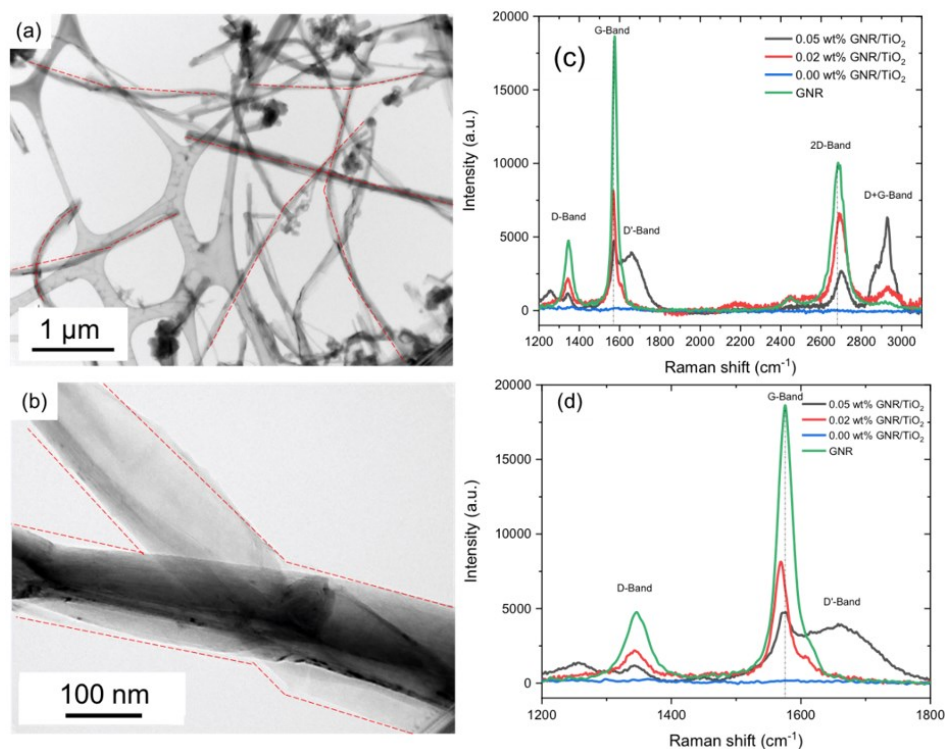


**Figure 5-4(a)-(b)** TEM images of GNRs (red-dotted) supported on Cu grid. Raman spectrum of the GNR (green), TiO<sub>2</sub> (blue), GNR-TiO<sub>2</sub> (red) composite photoanode with GNR = 0.02 wt% and GNR-TiO<sub>2</sub> (black) composite photoanode with GNR=0.05 wt%

TEM images of GNRs (highlighted by red-dotted lines) supported on a Cu grid are shown at different scales in **Figure 5-4 (a)-(b)**. The micrographs show that GNRs used in this work is a few-layers graphene, which is further confirmed by Raman spectroscopy measurements.

**Figure 5-4 (c)-(d)** displays the spectra of representative samples of GNR-TiO<sub>2</sub> hybrid mesoporous film at 0.02 and 0.05 wt%, and a Raman spectrum of GNR. The details in **Figure 5-4 (d)** consists of two dominant characteristic Raman features, the so-called D-band and G-band at 1346 cm<sup>-1</sup> and 1576 cm<sup>-1</sup> respectively for GNR, 1342 cm<sup>-1</sup> and 1569 cm<sup>-1</sup> respectively for 0.02 wt% hybrid GNR-TiO<sub>2</sub>, 1342 cm<sup>-1</sup> and 1575 cm<sup>-1</sup> respectively for 0.05 wt% hybrid GNR-TiO<sub>2</sub> (219). As the amount of GNRs is increased from 0.02 to 0.05 wt% ( $I_D/I_G = 0.28$  and  $I_D/I_G = 0.42$  respectively) into the TiO<sub>2</sub>, the  $I_D/I_G$  ratio increases as well by 0.14. This increased ratio confirms the higher amount of GNRs contributes to the more defects (195). In addition, the presence of the disorder-induced D'-band at the right side of the G-band can be also confirmed, which is activated by long-range defects such as charged impurities absorbed on the GNR sheets (220). This D'-band evolves from a small overlap into wider and more prominent and distinct peaks (from 1608 cm<sup>-1</sup> for 0.02 wt% to 1659 cm<sup>-1</sup> for 0.05 wt%).

Besides the overall decrease of the D-band and the 2D-band (195) (both only active in the vicinity of point defects) as we increase the amount of GNRs, the 2D-band shown in **Figure 5-4** (c) reveals a peak shift into higher wavenumbers as well as an asymmetric shape with a full width half maxima (FWHM) of  $\sim 52.8\text{--}57.5\text{ cm}^{-1}$  when embedded in the mesoporous film. This supports the hypothesis that the GNRs in the hybrid film are composed of few layers GNRs, as much as the pristine GNR (FWHM (2D) of  $61\text{ cm}^{-1}$ ) (198). The decrease in the intensity of the G-band with further increase in GNRs concentration (0.03-0.05 wt%), suggests that the quality of GNRs in the  $\text{TiO}_2$  matrix is diminished. A further confirmation of lower GNR quality can be seen in the defect activated D'-bands (221–223) and D+G-bands (193) whose intensities and FWHM steadily increases and the  $I_{\text{D}}/I_{\text{G}}$  ratio (indicating structural defects and disorder in the carbon network) also increases from 0.36 to 0.42 for bare and 0.05 wt% GNRs samples respectively. These trends show that the increased amount of GNRs gradually reduces the overall quality of the GNRs inside the  $\text{TiO}_2$  film.

### 5.2.2 Structural and optical characterization of QDs.

CdSe QDs were first synthesized via a hot injection approach as reported elsewhere (87). Then a CdS shell was further grown by SILAR (224) at  $240\text{ }^{\circ}\text{C}$  under  $\text{N}_2$  flow. The diameter of starting CdSe core QDs is around  $3.30 \pm 0.29\text{ nm}$  with uniform size distribution ( $<10\%$ ). The increased size of QDs after the six CdS shells growth, was confirmed by TEM analysis (see **Figure 5-5** (a)). The average size of CdSe/6CdS QDs is  $7.24 \pm 0.46\text{ nm}$  with an average shell thickness (H) of  $1.96\text{ nm}$  (estimated from TEM images). The high crystallinity of as-prepared QD is confirmed by High resolution transmission electron microscope (HRTEM) images, in which the lattice fringes of QDs are clearly visible (inset of **Figure 5-5** a).

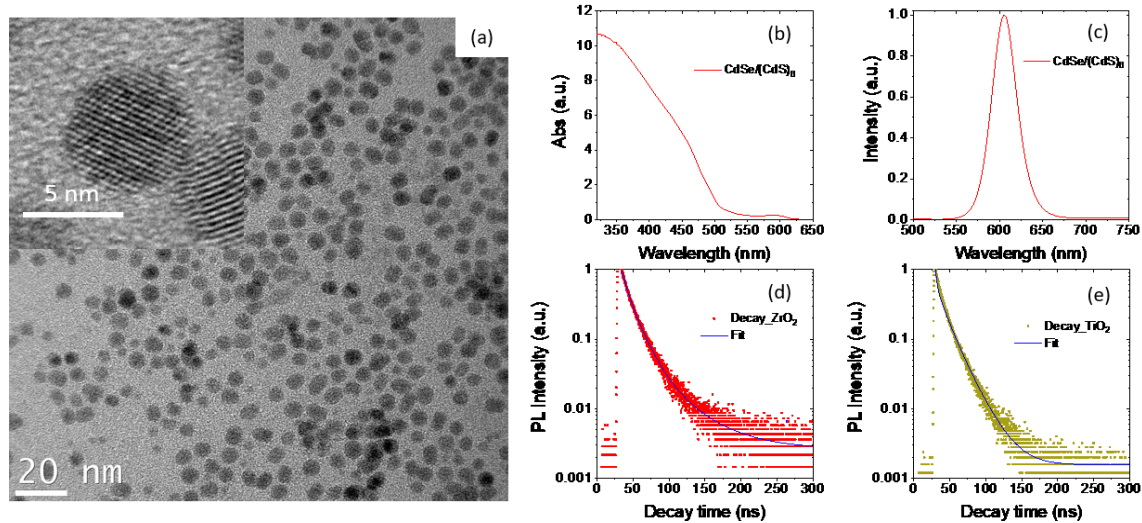


**Figure 5-5** (a) TEM image of CdSe/(CdS)<sub>6</sub> core/shell QDs, inset shows the HR-TEM image. Optical properties of QDs: (b) Absorption spectrum in UV-Visible region of as synthesized CdSe/(CdS)<sub>6</sub> core/shell QDs in toluene; (c) PL spectra of respective QDs in toluene. Transient PL curves of CdSe/(CdS)<sub>6</sub> core/shell QDs: (d) Deposited onto ZrO<sub>2</sub> mesoporous film; (e) Deposited onto TiO<sub>2</sub> mesoporous film. at 444 nm excitation wavelength

The optical properties of as-synthesized CdSe/(CdS)<sub>6</sub> core/shell QDs in toluene are shown in **Figure 5-5** (b)–(e). The first absorption excitonic peak is observed at 591 nm with broad absorption spectra range from UV to the visible region [see **Figure 5-5** (b)] (225). This broad absorption feature of the core/shell QDs may be due to carrier delocalization into the shell region. PL spectra of as synthesized CdSe/(CdS)<sub>6</sub> core/shell QDs in toluene are shown in **Figure 5-5** (c). The PL peak of CdSe/(CdS)<sub>6</sub> core/shell QDs is centered at 605 nm.

The carrier dynamic behavior of the CdSe/(CdS)<sub>6</sub> core/shell QDs after coupling with semiconductor metal oxide was studied by transient PL spectroscopy. The electron lifetime and electron transfer rate of QDs deposited on TiO<sub>2</sub> or ZrO<sub>2</sub> mesoporous films were measured under an excitation wavelength of  $\lambda = 444$  nm. All PL decay curves were well fitted using a three-stage exponential decay. The intensity-weighted average lifetime ( $\langle \tau \rangle$ ) (shown in Eqn.) is calculated by using the following equation:

$$\langle \tau \rangle = \frac{a_1\tau_1^2 + a_2\tau_2^2 + a_3\tau_3^2}{a_1\tau_1 + a_2\tau_2 + a_3\tau_3} \quad (5-1)$$

Where  $a_x$  ( $x = 1, 2, 3$ ) are the fitting coefficients of the PL decay and  $\tau_x$  ( $x = 1, 2, 3$ ) are the characteristic lifetimes, respectively. PL decay is faster in case of QDs anchored with TiO<sub>2</sub> than QDs with ZrO<sub>2</sub>, which confirms an efficient electron transfer from QDs to the TiO<sub>2</sub> (**Figure 5-5** (d)–(e)). This is mainly due to the difference in electronic band alignment of ZrO<sub>2</sub> (position of conduction band (CB) edge) and TiO<sub>2</sub>, which in case of ZrO<sub>2</sub> is not suitable for electron transfer

from QDs. The calculated average electron lifetime values for QDs anchored to the TiO<sub>2</sub> mesoporous film is 23±2 ns, whereas for QDs anchored to ZrO<sub>2</sub> mesoporous film is 25±1 ns, values comparable to the one in literatures (168). The difference between the average lifetime values gives electron transfer rate ( $K_{et}$ ), which is  $0.9\pm0.2\times10^7/s$ .

### 5.2.3 PEC measurements

We applied GNR-TiO<sub>2</sub> hybrid mesoporous films with different content of GNR sensitized with colloidal CdSe/(CdS)<sub>6</sub> core/shell QDs as working electrodes to fabricate a PEC device. A bare TiO<sub>2</sub> mesoporous film sensitized with colloidal CdSe/(CdS)<sub>6</sub> core/shell QDs was also applied as a working electrode and considered as a reference to highlight the effect of GNR. PEC measurements were performed under dark, continuous and chopped illumination (AM 1.5G, 100 mW·cm<sup>-2</sup>) by using a typical three-electrode configuration system. The current density vs applied potential curves of GNR-TiO<sub>2</sub>/QDs hybrid photoanode with different concentration of GNR and TiO<sub>2</sub>/QDs photoanode as a reference are shown in **Figure 5-6** (a)-(e).

The photocurrent density for all PEC devices varies with the different content of GNR in the TiO<sub>2</sub> mesoporous film. The variation of saturated photocurrent density values versus the concentrations of GNR in the hybrid photoanode at 0.8 V<sub>RHE</sub> is summarized in **Figure 5-6** (f) and corresponding values are reported in **Table 5-1**. In brief, at 0.8 V vs RHE, the highest saturated photocurrent density of PEC system based on bare TiO<sub>2</sub>/QDs photoanode is 4.21 mA/cm<sup>2</sup> under one sun illumination. With the addition 0.01 wt% of GNR in TiO<sub>2</sub>, the saturated photocurrent density increases to 4.51 mA/cm<sup>2</sup> under one sun illumination, then reaches the maximum value of 5.51 mA/cm<sup>2</sup> at 0.02 wt% of GNR content, which is 30% higher than that of a PEC system based on bare TiO<sub>2</sub>/QDs photoanodes. This improvement in photocurrent density with the addition of 0.02 wt% GNR in the hybrid photoanode based PEC cells is mainly attributed to enhanced electron transport and reduced charge transfer resistance (see more details in EIS section).

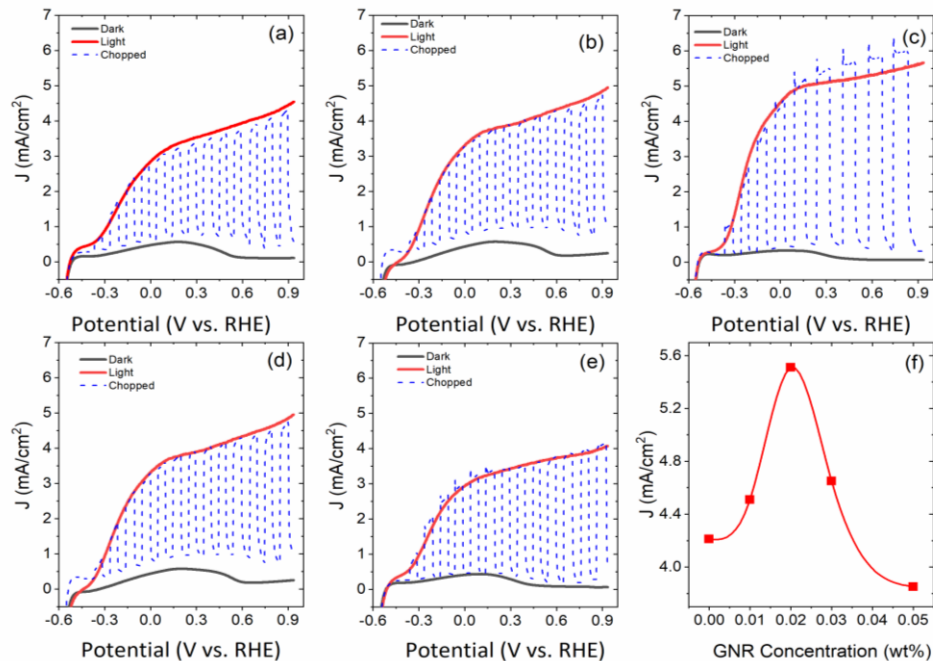


**Figure 5-6** Photocurrent density-potential curves of PEC devices based on QDs sensitized GNR-TiO<sub>2</sub> hybrid photoanodes under dark (black solid line), chopped (dotted blue line) and continuous illumination (AM 1.5 G, 100 mW/cm<sup>2</sup>) (red solid line) with different concentration of GNR: (a) 0.00 wt%; (b) 0.01 wt%; (c) 0.02 wt%; (d) 0.03 wt%; and (e) 0.05 wt%. (f) Variation of photocurrent density of PEC devices based on QDs sensitized GNR-TiO<sub>2</sub> hybrid photoanodes with different content of GNR at 0.8 V vs RHE under on sun illumination (AM 1.5 G, 100 mW/cm<sup>2</sup>).

For further increases in the concentration of GNRs, the photocurrent density reduces from 5.51 to 4.65 mA/cm<sup>2</sup> (0.03 wt%) and 3.85 mA/cm<sup>2</sup> (0.05 wt%) as mentioned previously. This is mainly due to the detrimental effect of the high concentration of GNRs such as crack formation, which act as recombination centers during carrier transport and also due to the reduced optical transparency of the hybrid photoanode.

**Table 5-1** Comparison of photocurrent density at 0.8V vs RHE under one sun illumination (AM 1.5 G, 100 mW·cm<sup>-2</sup>) of PEC devices based on GNR-TiO<sub>2</sub>/QDs hybrid photoanodes with different concentration of GNR (wt%).

GNR (wt %)	J (mA/cm <sup>2</sup> )
0	4.21
0.01	4.51
0.02	5.51
0.03	4.65
0.05	3.85

#### 5.2.4 Electrochemical impedance spectroscopy analysis

To fully understand the mechanism behind the improved performance for an optimal amount of GNRs and explore the electron transfer kinetic mechanism, we acquired EIS spectr (226). A three-electrode system was employed with the bare TiO<sub>2</sub> or GNR-TiO<sub>2</sub> photoanodes as working electrode, Ag/AgCl as reference electrode and a platinum foil as counter electrode.

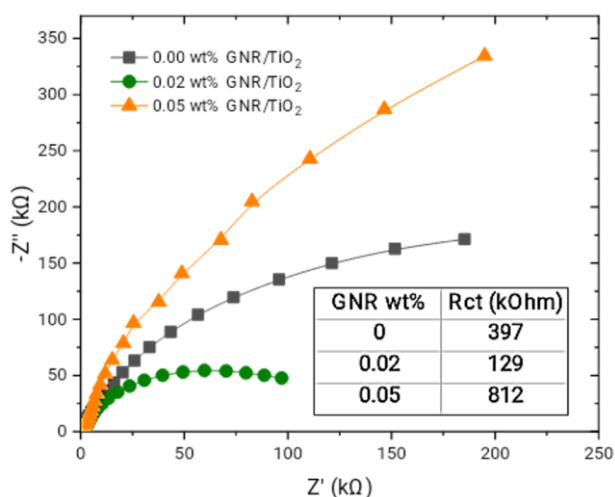


**Figure 5-7** The Nyquist plot of PEC devices based on GNR-TiO<sub>2</sub>/QDs hybrid photoanodes with different concentration of GNR: Black (0.0 wt%); Green (0.02 wt%) and Orange (0.05 wt%). Inset table displays the variation of charge transfer resistance with GNRs concentration

The Nyquist plot reported in **Figure 5-7** presents a small semicircle at high frequencies and a large one at low frequencies. The arc at low frequency corresponds to charge transfer resistance ( $R_{ct}$ ) and indicates the charge transfer is the dominant process at this stage (208, 227). A small  $R_{ct}$  indicates a higher charge transfer and an improved separation of electron/hole pairs (208). As visible in the Nyquist plot and in the table, the addition of an optimum amount of GNRs in the  $TiO_2$  matrix leads to a decrease in the  $R_{ct}$ , indicating an improved charge transfer for the best photoanode. Instead, when the GNR amount is increased, the charge transfer kinetics becomes slower, thereby reducing the current generated by the cell. This phenomenon can probably be attributed to the agglomeration of carbon nanostructures, as previously observed (123, 188).

### 5.2.5 Long-term stability measurements

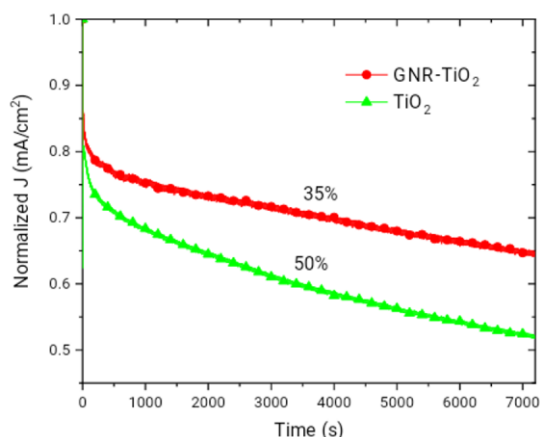


**Figure 5-8** Comparison of normalized current density ( $mW\cdot cm^{-2}$ ) versus time for PEC devices based on GNR-TiO<sub>2</sub>/QDs (red) and TiO<sub>2</sub>/QDs (green) photoanodes at 0.6 V (versus RHE) under one sun continuous illumination (AM 1.5 G, 100  $mW\cdot cm^{-2}$ ) for 7200 seconds

The long-term stability measurements were carried out under continuous one sun illumination (AM 1.5G, 100  $mW\cdot cm^{-2}$ ). We fabricated two types of PEC devices based on  $TiO_2$ /QDs and the best PEC performing hybrid GNRs- $TiO_2$ /QDs (0.02 wt%) to highlight the effect of GNRs addition on long-term stability. A systematic comparison of normalized photocurrent density of PEC devices based on  $TiO_2$ /QDs and GNR- $TiO_2$ /QDs (0.02 wt%) under continuous one sun illumination as a function of time is shown in **Figure 5-8**. The PEC device based on hybrid GNRs- $TiO_2$ /QDs maintains ~65% of the initial photocurrent density after 7200 seconds of continuous one sun illumination, whereas in case of the PEC device based on  $TiO_2$ /QDs photoanode maintains only ~50% of its initial photocurrent density. In both devices, all components are the same, so this difference in long-term stability of PEC devices with and without GNRs, is mainly attributed to the presence of GNRs in the  $TiO_2$  mesoporous film, which acts as UV light absorber



and simultaneously facilitates the removal of the charges, in turn improving long term stability (104, 228, 229).

### 5.3 Conclusions and perspectives

In summary, we prepared GNR-TiO<sub>2</sub> hybrid anodes with different concentrations (wt.%) of GNRs. The structural and optical properties of GNRs-TiO<sub>2</sub> hybrid anodes were characterized using UV-visible, SEM and Raman spectroscopy. GNRs-TiO<sub>2</sub> hybrid anodes were sensitized with a CdSe/(CdS)<sub>6</sub> colloidal core/shell QDs. The optimized concentration of GNRs (0.02 wt %) in the TiO<sub>2</sub> mesoporous film sensitized with CdSe/(CdS)<sub>6</sub> colloidal core/shell QDs, yielded the highest photocurrent density of 5.51 mA/cm<sup>2</sup> (at 0.08 V vs RHE) under one sun illumination (AM 1.5 G, 100 mW·cm<sup>-2</sup>), which is 30% higher than the control device. This demonstrates that a small amount of GNRs (0.02 wt%) dispersed in TiO<sub>2</sub> leads to improved electron transport (reducing the R<sub>ct</sub>) due to the directional path offered by GNRs to photoinjected electrons towards FTO. Furthermore, the PEC device based on TiO<sub>2</sub>-GNRs/QDs hybrid photoanode shows better long-term stability as compared to TiO<sub>2</sub>/QDs photoanode. Our results offer a simple and low-cost approach to improve the performance of PEC devices as well as the possibility to use other low dimensional carbonaceous materials to boost the efficiency of PEC devices. Future directions will focus on the application of functionalized GNRs in TiO<sub>2</sub> mesoporous films with best performing heterostructured colloidal QDs, to realize high efficiency and long-term stable PEC devices.



## 6 CHAPTER 6: CONCLUSIONS AND PERSPECTIVES

---

### 6.1 Conclusions

The general objective of this thesis was to develop stable, cost-effective, and high-performance nanocomposite photoanode designed by mixing GNR with  $\text{TiO}_2$  to be used in the field of photovoltaics and generation of clean chemical fuels. The overall strategy was to improve charge collection and charge injection efficiencies to enhance the performance of photovoltaic and solar-driven PEC devices. The long-term stability of these devices were also investigated to evaluate the beneficial contribution of GNR- $\text{TiO}_2$  nanocomposite. Consequently, in this thesis, the structural and optical properties of low dimensional (i.e. 1D) nanocarbon in  $\text{TiO}_2$  matrix was studied through UV-visible spectroscopy, SEM, TEM, Raman spectroscopy and carrier dynamics of fabricated devices via impedance spectroscopy, transient photovoltage decay and J-V measurements.

A direct straightforward, low cost and environmentally friendly approach was employed throughout this work in order to elaborate composite photoanode with low dimensional nanocarbons. The goals were to: (1) Elaborate DSSC and PEC devices with efficient GNR- $\text{TiO}_2$  composite photoanode to achieve high  $J_{sc}$  and PCE with lower carbonaceous content; (2) Compare the effect of GNR higher aspect-ratio on the percolation threshold of GNR- $\text{TiO}_2$  vs graphene- $\text{TiO}_2$  through photoelectrical performance and long-term stability of DSSCs ; (3) Fabricate highly efficient and durable solar-driven PEC device with colloidal core/shell QDs sensitized GNR- $\text{TiO}_2$  photoanode to improve  $\text{H}_2$  generation efficiency.

Therefore, based on these goals, the following conclusions have been drawn:

In chapter three, we demonstrated that DSSC with an optimum GNR concentration (0.005 wt%), below percolation threshold, was found to yield a PCE of 7.18%, which is 20% higher than bare DSSC. GNRs inserted in  $\text{TiO}_2$  nanoparticulate paste, can significantly improve the functional performance of DSSCs. The improvement is mainly attributed to the beneficial role of GNRs in the photoanode in directing the transport of photogenerated electrons to the collection site thereby reducing carrier recombination and increasing  $J_{sc}$ . This was confirmed from the enhanced electron lifetime calculated with the help of transient photovoltage decay and EIS measurements. Further incorporation of GNR resulted in detrimental effect on DSSCs performance, which decreased thereafter. This was found to be caused by the formation of agglomerates that can

induce cracks and electron recombination in the films as well as loss in optical transparency. Moreover, it was shown through that GNR embedded optimally within the grains can improve the charge separation efficiency and device stability due to good area to area interactions in nanocomposite.

Therefore, the results show how GNR-TiO<sub>2</sub> can be considered a valuable candidate for a hybrid photoanode in DSSC.

In chapter four, we used FLG-TiO<sub>2</sub> photoanode, with optimal concentrations of FLG obtained by DSSCs functional performance measurements and compared it with above mentioned GNR-TiO<sub>2</sub> photoanode with optimal concentration how the two nanocomposites revealed the effects of 1D dimensionalities of graphene sheets on overall performances and stability of DSSCs. Moreover, the presence of FLG and GNRs in TiO<sub>2</sub> nanoparticulate can improve the stability of DSSCs however in comparison the impedance spectroscopy investigation shows that the charge transfer stabilises better the GNR based device.

Structural analysis through Raman spectroscopy reveals that both carbonaceous nanocomposites showed compressive strain forces that contribute positively to mechanical toughening effects. However, GNR gives a stronger compressive effect than Graphene in comparison, which stabilises more effectively the integrity of the film. Combined with the functional parameters higher stability, this result suggests that GNR based photoanode are dispersed optimally along the grains boundaries, which may cause to improve the intergranular and transgranular network connectivity bridging and branching cracks in the composite photoanode film.

This helped understand the influence of GNR's 1D morphology for device performance and stability, providing GNR-TiO<sub>2</sub> devices an advantage over Graphene-TiO<sub>2</sub> devices, which has been corroborated by the better rate of change of charge transfer resistance  $R_{CT}$  and electron lifetime  $\tau_n$  over time. These results provide a straightforward way to improve long-term stability of the DSSC, which is crucial for this promising technology to move one step closer to commercialization.

These findings open up new avenues for investigating the size effect of graphene-based material in energy converting devices.

In chapter five, we modified the surface of GNR-TiO<sub>2</sub> by sensitizing the photoelectrode with colloidal CdSe/(CdS)<sub>6</sub> core/shell Quantum dots, and elaborated novel photoelectrochemical hybrid anodes to boost the efficiency of PEC devices.

The structural and optical properties of photoanode were characterized by UV-Visible, Raman and TEM, and showed that after the percolation threshold value of 0.02 wt% of GNR, the increased amount of GNRs gradually reduces the overall quality of the photoanode and also contributes to a loss of part of the radiation available for exciton generation, which in turn worsens the device's overall performance.

This optimized concentration of GNRs yielded the photocurrent density up to 30% higher than the control device.  $\text{TiO}_2$ -GNRs/QDs hybrid photoanode also showed better long-term stability as compared to  $\text{TiO}_2$ /QDs photoanode. This demonstrates that a small but different amount of GNRs dispersed in  $\text{TiO}_2$  leads to improved electron transport due to the directional path offered by GNRs to photoinjected electrons towards FTO. The same small amount contributes in reducing the charge transfer resistance which indicate a higher charge transfer and an improved separation of electron/hole pairs. Compared to DSSCs, in PEC the percolation threshold was shifted to higher concentrations of GNR than with DSSCs, this result suggests that, the percolation threshold is sensible to the host matrix and the type of application that it will be designed for.

The results obtained in the thesis, offers useful insight about the effect of low dimensional carbon nanostructures. As anticipated from the percolation theory, a higher aspect ratio for graphene sheets contributed in shifting to lower content the percolation threshold of GNR based photoanodes for their PCE and long-term stability in DSSCs. This may be attributed to their aspect ratio, which can form homogeneous network within matrix, rather than bundles, and thus improve the area to area contact with  $\text{TiO}_2$  nanoparticles. Moreover, the same optimal percolation threshold is found to be shifted to higher content when composite photoanode is used in a different application.

In conclusion, the fabrication of GNR- $\text{TiO}_2$  photoanodes constitute a very fast, and highly reproducible approach for incorporating low quantities of nanocarbons into the photoanodes of both DSSCs and PEC devices. We did not apply any surface treatment, which could significantly increase the functional properties of the devices, but which also are unlikely to be applied on a large scale for low cost and large scale production. Because of their 1D structure and excellent charge collection and conducting properties, GNRs are a natural choice as an additive to the photoactive layer in light harvesting devices, offering extraordinary pathways for low-resistance transport to the anode.

## 6.2 Perspectives

In addition to progress in the above-mentioned work, critical advances in the field are still required to improve the properties of GNRs to a satisfactory level. In depth research of new approaches will improve the photovoltaic performance of metal oxide carbonaceous composites and bring an understanding of these materials.

Furthermore, as this thesis shows a percolation threshold for  $V_{OC}$  is also present in the results. This feature was in fact absent in MWCNT, F-MWCNT and graphene nanocomposites, which suggests that the performances could have higher values if more precise investigation could be realised to improve the interfacial contact provided by GNR at the nanoscale with  $TiO_2$  nanocrystallites. Thus modifying the band structure of the nanocomposite.

Dispersion methods as well as processing routes for GNR composites (*in situ* crystallization, Layer-by-Layer assembly, chemical reduction or colloidal processing) are avenues to obtain novel nanocomposites.

Moreover, an investigation of the photoelectrical behavior of the GNR nanocomposites with other techniques can further reveal the mechanism of charge transport and charge transfer in  $TiO_2$  as well as the factors influencing the interfacial mechanical properties for stability.

Although up to now, there are no studies using selectively edges of GNR (between armchair and zigzag GNR) due to low availabilities, different type of GNR and other type of graphene such as graphdiyne, could be used to further investigate the size effect and aspect ratio of graphene allotropes which are synthesized from other methods.

Potential applications in biological photosystems can also be exploited to produce new class of dynamic solar energy harvesting cells, like it is the case of *Rhodobacter sphaeroides*. This material could be used as self-assembling hybrid materials to disassemble and replace damaged components with new ones faster and more efficiently with GNR..

With these new perspectives useful information about the structural and electronic changes can be obtained and bring further closer a fossil-fuel free era to humanity.

## 7 REFERENCES

---

1. , Fossil Fuels Still Supply 84 Percent Of World Energy — And Other Eye Openers From BP's Annual Review.
2. , International Energy Outlook 2019.
3. G. H. Bauer, "Global Energy Situation" in *Lecture Notes in Physics*, (Springer Verlag, 2015), pp. 5–8.
4. H. L. Tuller, Solar to fuels conversion technologies: a perspective. *Mater. Renew. Sustain. Energy* **6**, 3 (2017).
5. K. Basu, "Investigation of heterostructure photoanodes for solar energy conversion." (2018).
6. W. Shockley, H. J. Queisser, Detailed Balance Limit of Efficiency of p-n Junction Solar Cells. *J. Appl. Phys.* **32**, 510 (1961).
7. P. T. Landsberg, G. Tonge, Thermodynamic energy conversion efficiencies. *J. Appl. Phys.* **51**, R1–R20 (1980).
8. A. Polman, H. A. Atwater, Photonic design principles for ultrahigh-efficiency photovoltaics. *Nat. Mater.* **11**, 174–177 (2012).
9. , Top 10 Economic Benefits of Converting to Solar Energy (2019).
10. , "The Journey of Solar Energy: It's History and Modifications in Technologies Miss. Neha Kisan Kuber ME (EPS) student" (2017).
11. J. Szlufcik, S. Sivoththaman, J. F. Nlis, R. P. Mertens, R. Van Overstraeten, Low-cost industrial technologies of crystalline silicon solar cells. *Proc. IEEE* **85**, 711–730 (1997).
12. M. Grätzel, Photovoltaic and photoelectrochemical conversion of solar energy. *Philos. Trans. R. Soc. A Math. Phys. Eng. Sci.* **365**, 993–1005 (2007).
13. M. Henini, *Molecular beam epitaxy* (Elsevier, 2013) .
14. M. C. Scharber, N. S. Sariciftci, Efficiency of bulk-heterojunction organic solar cells. *Prog. Polym. Sci.* **38**, 1929–1940 (2013).
15. H. Tributsch, M. Calvin, Electrochemistry of excited molecules: Photo-electrochemical reactions of chlorophylls. *Photochem. Photobiol.* **14**, 95–112 (1971).
16. S. Shalini, R. Balasundara Prabhu, S. Prasanna, T. K. Mallick, S. Senthilarasu, Review on natural dye sensitized solar cells: Operation, materials and methods. *Renew. Sustain. Energy Rev.* **51**, 1306–

- 1325 (2015).
17. X. Yang, J. Loos, Toward high-performance polymer solar cells: The importance of morphology control. *Macromolecules* **40**, 1353–1362 (2007).
  18. Merck KGaA, Organic Photovoltaics (OPV) Tutorial | Sigma-Aldrich (2012).
  19. M. G. Walter, *et al.*, Solar water splitting cells. *Chem. Rev.* **110**, 6446–6473 (2010).
  20. K. Adachi, K. Ohta, T. Mizuno, Photocatalytic reduction of carbon dioxide to hydrocarbon using copper-loaded titanium dioxide. *Sol. Energy* **53**, 187–190 (1994).
  21. A. Fujishima, K. Honda, Electrochemical photolysis of water at a semiconductor electrode. *Nature* **238**, 37–38 (1972).
  22. M. Grätzel, A Low Cost, High Efficiency Solar Cell Based On Dye-Sensitized Colloidal TiO<sub>2</sub> Films. *Nature* **353**, 737–740 (1991).
  23. M. Matsumura, S. Matsudaira, H. Tsubomura, M. Takata, H. Yanagida, Dye Sensitization and Surface Structures of Semiconductor Electrodes. *Ind. Eng. Chem. Prod. Res. Dev.* **19**, 415–421 (1980).
  24. N. Mariotti, *et al.*, Recent advances in eco-friendly and cost-effective materials towards sustainable dye-sensitized solar cells. *Green Chem.* **22**, 7168–7218 (2020).
  25. N. A. Ludin, *et al.*, Prospects of life cycle assessment of renewable energy from solar photovoltaic technologies: A review. *Renew. Sustain. Energy Rev.* **96**, 11–28 (2018).
  26. K. Kakiage, *et al.*, Highly-efficient dye-sensitized solar cells with collaborative sensitization by silyl-anchor and carboxy-anchor dyes. *Chem. Commun.* **51**, 15894–15897 (2015).
  27. B. E. Hardin, J. Snaith, M. D. McGehee, The renaissance of dye-sensitized solar cells. *Nat. Photonics* **6**, 162–169 (2012).
  28. A. Hagfeldt, G. Boschloo, L. Sun, L. Kloo, H. Pettersson, Dye-Sensitized Solar Cells. *Chem. Rev.* **110**, 6595–6663 (2010).
  29. L. Stamenic, E. Smiley, K. Karim, Low light conditions modelling for building integrated photovoltaic (BIPV) systems. *Sol. Energy* **77**, 37–45 (2004).
  30. A. Herzog, EPFL's campus has the world's first solar window. *ÉCOLE Polytech. FÉDÉRALE LAUSANNE* (2013).
  31. M. Green, *et al.*, Solar cell efficiency tables (version 57). *Prog. Photovoltaics Res. Appl.* **29**, 3–15

- (2021).
32. V. Venkatraman, R. Raju, S. P. Oikonomopoulos, B. K. Alsberg, The dye-sensitized solar cell database. *J. Cheminform.* **10**, 18 (2018).
  33. K. Kakiage, *et al.*, Highly-efficient dye-sensitized solar cells with collaborative sensitization by silyl-anchor and carboxy-anchor dyes. *Chem. Commun.* **51**, 15894–15897 (2015).
  34. A. Polman, M. Knight, E. C. Garnett, B. Ehrler, W. C. Sinke, Photovoltaic materials: Present efficiencies and future challenges. *Science (80)*. **352**, (2016).
  35. M. Hao, *et al.*, Ligand-assisted cation-exchange engineering for high-efficiency colloidal Cs<sub>1-x</sub>FaxPbI<sub>3</sub> quantum dot solar cells with reduced phase segregation. *Nat. Energy* **5**, 79–88 (2020).
  36. S. Shalini, R. Balasundara Prabhu, S. Prasanna, T. K. Mallick, S. Senthilarasu, Review on natural dye sensitized solar cells: Operation, materials and methods. *Renew. Sustain. Energy Rev.* **51**, 1306–1325 (2015).
  37. M. A. M. Al-Alwani, A. B. Mohamad, N. A. Ludin, A. A. H. Kadhum, K. Sopian, Dye-sensitised solar cells: Development, structure, operation principles, electron kinetics, characterisation, synthesis materials and natural photosensitisers. *Renew. Sustain. Energy Rev.* **65**, 183–213 (2016).
  38. S. Z. Siddick, C. W. Lai, J. C. Juan, S. B. Hamid, Reduced Graphene Oxide - Titania Nanocomposite Film for Improving Dye-Sensitized Solar Cell (DSSCs) Performance. *Curr. Nanosci.* **13** (2017).
  39. R. Jose, V. Thavasi, S. Ramakrishna, Metal oxides for dye-sensitized solar cells. *J. Am. Ceram. Soc.* **92**, 289–301 (2009).
  40. U. Mehmood, S. Rahman, K. Harrabi, I. A. Hussein, B. V. S. Reddy, Recent Advances in Dye Sensitized Solar Cells. *Adv. Mater. Sci. Eng.* **2014**, 1–12 (2014).
  41. C. Sima, C. Grigoriu, S. Antohe, Comparison of the dye-sensitized solar cells performances based on transparent conductive ITO and FTO. *Thin Solid Films* **519**, 595–597 (2010).
  42. S. Ito, *et al.*, High-efficiency (7.2%) flexible dye-sensitized solar cells with Ti-metal substrate for nanocrystalline-TiO<sub>2</sub> photoanode. *Chem. Commun.*, 4004–4006 (2006).
  43. T. N. Murakami, Y. Kijitori, N. Kawashima, T. Miyasaka, Low temperature preparation of mesoporous TiO<sub>2</sub> films for efficient dye-sensitized photoelectrode by chemical vapor deposition combined with UV light irradiation. *J. Photochem. Photobiol. A Chem.* **164**, 187–191 (2004).
  44. P. J. Cameron, L. M. Peter, Characterization of Titanium Dioxide Blocking Layers in Dye-

- Sensitized Nanocrystalline Solar Cells. *J. Phys. Chem. B* **107**, 14394–14400 (2003).
45. Y. Hua, “Design and synthesis of new organic dyes for highly efficient dye-sensitized solar cells.” (2014).
  46. E. Galoppini, Linkers for anchoring sensitizers to semiconductor nanoparticles. *Coord. Chem. Rev.* **248**, 1283–1297 (2004).
  47. M. K. Nazeeruddin, R. Humphry-Baker, P. Liska, M. Grätzel, Investigation of sensitizer adsorption and the influence of protons on current and voltage of a dye-sensitized nanocrystalline TiO<sub>2</sub> solar cell. *J. Phys. Chem. B* **107**, 8981–8987 (2003).
  48. A. S. Polo, M. K. Itokazu, N. Y. Murakami Iha, Metal complex sensitizers in dye-sensitized solar cells. *Coord. Chem. Rev.* **248**, 1343–1361 (2004).
  49. K. E. Jasim, Dye sensitized solar cells-working principles, challenges and opportunities. *Dye Sensitized Sol. Cells - Work. Princ. Challenges*, 171–204 (2007).
  50. A. Mishra, M. K. R. Fischer, P. Büuerle, Metal-Free organic dyes for dye-Sensitized solar cells: From structure: Property relationships to design rules. *Angew. Chemie - Int. Ed.* **48**, 2474–2499 (2009).
  51. S. Ananthakumar, J. Ramkumar, S. M. Babu, Semiconductor nanoparticles sensitized TiO<sub>2</sub> nanotubes for high efficiency solar cell devices. *Renew. Sustain. Energy Rev.* **57**, 1307–1321 (2016).
  52. H.-H. Wang, *et al.*, Preparation of Nanoporous TiO<sub>2</sub> Electrodes for Dye-Sensitized Solar Cells. *J. Nanomater.* **2011**, 1–7 (2011).
  53. N. Memarian, *et al.*, Hierarchically assembled ZnO nanocrystallites for high-efficiency dye-sensitized solar cells. *Angew. Chemie - Int. Ed.* **50**, 12321–12325 (2011).
  54. Z. Tebby, *et al.*, Low-temperature UV processing of nanoporous SnO<sub>2</sub> layers for dye-sensitized solar cells. *ACS Appl. Mater. Interfaces* **3**, 1485–1491 (2011).
  55. , Titanium | Ti (Element) - PubChem.
  56. , Titanium dioxide | TiO<sub>2</sub> - PubChem.
  57. A. Niilisk, *et al.*, Structural study of TiO<sub>2</sub> thin films by micro-Raman spectroscopy. *Cent. Eur. J. Phys.* **4**, 105–116 (2006).
  58. Y. Mi, Y. Weng, Band Alignment and Controllable Electron Migration between Rutile and Anatase TiO<sub>2</sub>. *Sci. Rep.* **5**, 1–10 (2015).



59. B. Liu, E. S. Aydil, Growth of oriented single-crystalline rutile TiO<sub>2</sub> nanorods on transparent conducting substrates for dye-sensitized solar cells. *J. Am. Chem. Soc.* **131**, 3985–3990 (2009).
60. V. T. Tiong, H. Wang, “Photon-responsive nanomaterials for solar cells” in *Springer Series in Materials Science*, (Springer, 2020), pp. 1–63.
61. T. P. Chou, Q. Zhang, B. Russo, G. E. Fryxell, G. Cao, Titania particle size effect on the overall performance of dye-sensitized solar cells. *J. Phys. Chem. C* **111**, 6296–6302 (2007).
62. A. Luque, S. Hegedus, *Handbook of Photovoltaic Science and Engineering* (2011)
63. B. A. Gregg, Interfacial processes in the dye-sensitized solar cell. *Coord. Chem. Rev.* **248**, 1215–1224 (2004).
64. M. Ye, *et al.*, Recent advances in dye-sensitized solar cells: From photoanodes, sensitizers and electrolytes to counter electrodes. *Mater. Today* **18**, 155–162 (2015).
65. S. Bose, V. Soni, K. R. Genwa, Recent Advances and Future Prospects for Dye Sensitized Solar Cells: A Review. *Int. J. Sci. Res. Publ.* **5** (2015).
66. S. Galliano, *et al.*, Photoanode/Electrolyte Interface Stability in Aqueous Dye-Sensitized Solar Cells. *Energy Technol.* **5**, 300–311 (2017).
67. K. G. Reddy, *et al.*, On global energy scenario, dye-sensitized solar cells and the promise of nanotechnology. *Phys. Chem. Chem. Phys.* **16**, 6838 (2014).
68. F. Bella, S. Galliano, C. Gerbaldi, G. Viscardi, Cobalt-based electrolytes for dye-sensitized solar cells: Recent advances towards stable devices. *Energies* **9**, 1–22 (2016).
69. H. Jeong, *et al.*, Enhancing the Charge Transfer of the Counter Electrode in Dye-Sensitized Solar Cells Using Periodically Aligned Platinum Nanocups. *Small* **8**, 3757–3761 (2012).
70. R. H. Atkinson, Electrodeposition of Platinum from Chloroplatinic Acid. *Trans. IMF* **36**, 7–16 (1959).
71. J. Wu, *et al.*, Counter electrodes in dye-sensitized solar cells. *Chem. Soc. Rev.* **46**, 5975–6023 (2017).
72. P. V. Kamat, J. Bisquert, Solar fuels. Photocatalytic hydrogen generation. *J. Phys. Chem. C* **117**, 14873–14875 (2013).
73. V. D. Dao, Y. Choi, K. Yong, L. L. Larina, H. S. Choi, Graphene-based nanohybrid materials as the counter electrode for highly efficient quantum-dot-sensitized solar cells. *Carbon N. Y.* **84**, 383–389 (2015).

74. I. Mora-Seró, J. Bisquert, Fermi level of surface states in TiO<sub>2</sub> nanoparticles. *Nano Lett.* **3**, 945–949 (2003).
75. K. D. Benkstein, N. Kopidakis, J. Van de Lagemaat, A. J. Frank, Influence of the percolation network geometry on electron transport in dye-sensitized titanium dioxide solar cells. *J. Phys. Chem. B* **107**, 7759–7767 (2003).
76. R. Könenkamp, R. Henninger, P. Hoyer, Photocarrier transport in colloidal TiO<sub>2</sub> films. *J. Phys. Chem.* **97**, 7328–7330 (1993).
77. K. Schwarzburg, F. Willig, Influence of trap filling on photocurrent transients in polycrystalline TiO<sub>2</sub>. *Appl. Phys. Lett.* **58**, 2520–2522 (1991).
78. J. Bisquert, A. Zaban, M. Greenshtein, I. Mora-Seró, Determination of rate constants for charge transfer and the distribution of semiconductor and electrolyte electronic energy levels in dye-sensitized solar cells by open-circuit photovoltage decay method. *J. Am. Chem. Soc.* **126**, 13550–13559 (2004).
79. K. Park, Q. Zhang, D. Myers, G. Cao, Charge transport properties in TiO<sub>2</sub> network with different particle sizes for dye sensitized solar cells. *ACS Appl. Mater. Interfaces* **5**, 1044–1052 (2013).
80. M. M. Maitani, K. Tanaka, Q. Shen, T. Toyoda, Y. Wada, Electron transport properties in dye-sensitized solar cells with {001} facet-dominant TiO<sub>2</sub> nanoparticles. *Phys. Chem. Chem. Phys.* **19**, 22129–22140 (2017).
81. A. Baghbany Oskouei, M. R. Banaei, M. Sabahi, Hybrid PV/wind system with quinary asymmetric inverter without increasing DC-link number. *Ain Shams Eng. J.* **7**, 579–592 (2016).
82. N. Yang, J. Zhai, D. Wang, Y. Chen, L. Jiang, Two-dimensional graphene bridges enhanced photoinduced charge transport in dye-sensitized solar cells in *ACS Nano*, ( American Chemical Society, 2010), pp. 887–894.
83. F. Fabregat-Santiago, *et al.*, Correlation between photovoltaic performance and impedance spectroscopy of dye-sensitized solar cells based on ionic liquids. *J. Phys. Chem. C* **111**, 6550–6560 (2007).
84. M. Mahbubur Rahman, N. Chandra Deb Nath, J.-J. Lee, Electrochemical Impedance Spectroscopic Analysis of Sensitization-Based Solar Cells. *Isr. J. Chem.* **55**, 990–1001 (2015).
85. X. Chen, S. Shen, L. Guo, S. S. Mao, Semiconductor-based Photocatalytic Hydrogen Generation. *Chem. Rev.* **110**, 6503–6570 (2010).

86. H. Ahmad, S. K. Kamarudin, L. J. Minggu, M. Kassim, Hydrogen from photo-catalytic water splitting process: A review. *Renew. Sustain. Energy Rev.* **43**, 599–610 (2015).
87. L. Jin, *et al.*, Near-Infrared Colloidal Quantum Dots for Efficient and Durable Photoelectrochemical Solar-Driven Hydrogen Production. *Adv. Sci.* **3**, 1500345 (2016).
88. R. Adhikari, *et al.*, Heterostructured quantum dot architectures for efficient and stable photoelectrochemical hydrogen production. *J. Mater. Chem. A* **6**, 6822–6829 (2018).
89. Q. Zhang, T. P. Chou, B. Russo, S. A. Jenekhe, G. Cao, Aggregation of ZnO nanocrystallites for high conversion efficiency in dye-sensitized solar cells. *Angew. Chemie - Int. Ed.* **47**, 2402–2406 (2008).
90. S. K. Saraswat, D. D. Rodene, R. B. Gupta, Recent advancements in semiconductor materials for photoelectrochemical water splitting for hydrogen production using visible light. *Renew. Sustain. Energy Rev.* **89**, 228–248 (2018).
91. H. Y. Chen, D. Bin Kuang, C. Y. Su, Hierarchically micro/nanostructured photoanode materials for dye-sensitized solar cells. *J. Mater. Chem.* **22**, 15475–15489 (2012).
92. M. Samadpour, N. Taghavinia, A. Iraj-Zad, M. Marandi, F. Tajabadi, Charge transport properties in nanocomposite photoanodes of DSSCs: Crucial role of electronic structure. *EPJ Appl. Phys.* **57**, 20401 (2012).
93. T.-S. Kang, A. P. Smith, B. E. Taylor, M. F. Durstock, Fabrication of Highly-Ordered TiO<sub>2</sub> Nanotube Arrays and Their Use in Dye-Sensitized Solar Cells. *Nano Lett.* **9**, 601–606 (2009).
94. G. K. Mor, O. K. Varghese, M. Paulose, K. Shankar, C. A. Grimes, A review on highly ordered, vertically oriented TiO<sub>2</sub> nanotube arrays: Fabrication, material properties, and solar energy applications. *Sol. Energy Mater. Sol. Cells* **90**, 2011–2075 (2006).
95. K. Zhu, N. R. Neale, A. Miedaner, A. J. Frank, Enhanced charge-collection efficiencies and light scattering in dye-sensitized solar cells using oriented TiO<sub>2</sub> nanotubes arrays. *Nano Lett.* **7**, 69–74 (2007).
96. J. R. Jennings, A. Ghicov, L. M. Peter, P. Schmuki, A. B. Walker, Dye-sensitized solar cells based on oriented TiO<sub>2</sub> nanotube arrays: Transport, trapping, and transfer of electrons. *J. Am. Chem. Soc.* **130**, 13364–13372 (2008).
97. P. Roy, D. Kim, K. Lee, E. Spiecker, P. Schmuki, TiO<sub>2</sub> nanotubes and their application in dye-sensitized solar cells. *Nanoscale* **2**, 45–59 (2010).

98. S. V Nair, *et al.*, “Effect of TiO<sub>2</sub> nanotube length and lateral tubular spacing on photovoltaic properties of back illuminated dye sensitized solar cell” (2012).
99. N. A. Ilahi, R. Suryana, F. Nurrosyid, N. T. Linda Kusuma, Electrospinning Titanium Dioxide (TiO<sub>2</sub>) nanofiber for dye sensitized solar cells based on Bryophyta as a sensitizer in *Journal of Physics: Conference Series*, (Institute of Physics Publishing, 2017), p. 12033.
100. S. Chuangchote, T. Sagawa, S. Yoshikawa, Efficient dye-sensitized solar cells using electrospun TiO<sub>2</sub> nanofibers as a light harvesting layer. *Appl. Phys. Lett.* **93**, 33310 (2008).
101. M. Adachi, *et al.*, Highly efficient dye-sensitized solar cells with a titania thin-film electrode composed of a network structure of single-crystal-like TiO<sub>2</sub> nanowires made by the “oriented attachment” mechanism. *J. Am. Chem. Soc.* **126**, 14943–14949 (2004).
102. J. B. Baxter, E. S. Aydil, Nanowire-based dye-sensitized solar cells. *Appl. Phys. Lett.* **86**, 1–3 (2005).
103. J. B. Baxter, E. S. Aydil, Dye-sensitized solar cells based on semiconductor morphologies with ZnO nanowires. *Sol. Energy Mater. Sol. Cells* **90**, 607–622 (2006).
104. W. Wang, P. Serp, P. Kalck, J. L. Faria, Visible light photodegradation of phenol on MWNT-TiO<sub>2</sub> composite catalysts prepared by a modified sol-gel method. *J. Mol. Catal. A Chem.* **235**, 194–199 (2005).
105. A. K. Geim, K. S. Novoselov, The rise of graphene. *Nat. Mater.* **6**, 183–191 (2007).
106. C. Shen, S. O. Oyadiji, The Processing and Analysis of Graphene and the Strength Enhancement Effect of Graphene-based Filler Materials: A Review. *Mater. Today Phys.*, 100257 (2020).
107. C. B. Song, *et al.*, Dye-sensitized solar cells based on graphene-TiO<sub>2</sub> nanoparticles/TiO<sub>2</sub> nanotubes composite films. *Int. J. Electrochem. Sci.* **9**, 8090–8096 (2014).
108. Z. Yazdi, Doped Graphene Nanoribbons: Synthesis, Characterization and Application. 179 (2015).
109. B. Aïssa, N. K. Memon, A. Ali, M. K. Khraisheh, Recent Progress in the Growth and Applications of Graphene as a Smart Material: A Review. *Front. Mater.* **2**, 1–19 (2015).
110. H. Terrones, R. Lv, M. Terrones, M. S. Dresselhaus, The role of defects and doping in 2D graphene sheets and 1D nanoribbons. *Reports Prog. Phys.* **75**, 62501 (2012).
111. D. V. Kosynkin, *et al.*, Highly conductive graphene nanoribbons by longitudinal splitting of carbon nanotubes using potassium vapor. *ACS Nano* **5**, 968–974 (2011).
112. L. Jiao, L. Zhang, X. Wang, G. Diankov, H. Dai, Narrow graphene nanoribbons from carbon nanotubes. *Nature* **458**, 877–880 (2009).

113. G. Xue, *et al.*, Degradation Mechanisms Investigation for Long-term Thermal Stability of Dye-Sensitized Solar Cells. *Int. J. Electrochem. Sci* **7**, 1496–1511 (2012).
114. V. Etacheri, C. Di Valentin, J. Schneider, D. Bahnemann, S. C. Pillai, Visible-light activation of TiO<sub>2</sub> photocatalysts: Advances in theory and experiments. *J. Photochem. Photobiol. C Photochem. Rev.* **25**, 1–29 (2015).
115. C. Wang, Y. S. Li, J. Jiang, W. H. Chiang, Controllable Tailoring Graphene Nanoribbons with Tunable Surface Functionalities: An Effective Strategy toward High-Performance Lithium-Ion Batteries. *ACS Appl. Mater. Interfaces* **7**, 17441–17449 (2015).
116. Z. Peining, *et al.*, Rice grain-shaped TiO<sub>2</sub>–CNT composite—A functional material with a novel morphology for dye-sensitized solar cells. *J. Photochem. Photobiol. A Chem.* **231**, 9–18 (2012).
117. L. Wang, J. Han, D. Kong, Y. Tao, Q. H. Yang, Enhanced Roles of Carbon Architectures in High-Performance Lithium-Ion Batteries. *Nano-Micro Lett.* **11**, 1–23 (2019).
118. K. T. Dembele, *et al.*, Effect of multi-walled carbon nanotubes on the stability of dye sensitized solar cells. *J. Power Sources* **233**, 93–97 (2013).
119. M. Batmunkh, M. J. Biggs, J. G. Shapter, Carbonaceous Dye-Sensitized Solar Cell Photoelectrodes. *Adv. Sci.* **2**, 1400025 (2015).
120. A. Kongkanand, R. M. Domínguez, P. V. Kamat, Single wall carbon nanotube scaffolds for photoelectrochemical solar cells. Capture and transport of photogenerated electrons in *Nano Letters*, ( American Chemical Society , 2007), pp. 676–680.
121. U. Mehmood, I. A. Hussein, A. Al-ahmed, S. Ahmed, Enhancing Power Conversion Efficiency of Dye-Sensitized Solar Cell Using TiO<sub>2</sub> -MWCNT Composite Photoanodes. **6**, 486–490 (2016).
122. P. Du, *et al.*, Dye-sensitized solar cells based on anatase TiO<sub>2</sub>/multi-walled carbon nanotubes composite nanofibers photoanode. *Electrochim. Acta* **87**, 651–656 (2013).
123. D. Benetti, *et al.*, Functionalized multi-wall carbon nanotubes/TiO<sub>2</sub> composites as efficient photoanodes for dye sensitized solar cells. *J. Mater. Chem. C* **4**, 3555–3562 (2016).
124. W. Xie, *et al.*, Utilizing carbon nanotube electrodes to improve charge injection and transport in bis(trifluoromethyl)-dimethyl-rubrene ambipolar single crystal transistors. *ACS Nano* **7**, 10245–10256 (2013).
125. M. R. Golobostanfard, H. Abdizadeh, Comparing incorporation of carbon nanotubes in hierarchical porous photoanodes of quantum dot and dye sensitized solar cells. *Ceram. Int.* **41**, 497–504 (2015).

126. P. Brown, K. Takechi, P. V. Kamat, Single-walled carbon nanotube scaffolds for dye-sensitized solar cells. *J. Phys. Chem. C* **112**, 4776–4782 (2008).
127. D. S. Hecht, L. Hu, G. Irvin, Emerging transparent electrodes based on thin films of carbon nanotubes, graphene, and metallic nanostructures. *Adv. Mater.* **23**, 1482–1513 (2011).
128. L. Q. Wang, J. M. Feng, Improved energy conversion efficiency of CdS quantum dots sensitised solar cells using TiO<sub>2</sub>/carbon nanotube nanocomposite photoanodes in *Materials Research Innovations*, (Maney Publishing, 2015), pp. S541–S546.
129. G. H. Guai, Y. Li, C. M. Ng, C. M. Li, M. B. Chan-Park, TiO<sub>2</sub> Composing with Pristine, Metallic or Semiconducting Single-Walled Carbon Nanotubes: Which Gives the Best Performance for a Dye-Sensitized Solar Cell. *ChemPhysChem* **13**, 2566–2572 (2012).
130. D. S. Su, G. Centi, A perspective on carbon materials for future energy application. *J. Energy Chem.* **22**, 151–173 (2013).
131. D. S. Su, S. Perathoner, G. Centi, Nanocarbons for the development of advanced catalysts. *Chem. Rev.* **113**, 5782–5816 (2013).
132. L. J. Brennan, M. T. Byrne, M. Bari, Y. K. Gun'ko, Carbon Nanomaterials for Dye-Sensitized Solar Cell Applications: A Bright Future. *Adv. Energy Mater.* **1**, 472–485 (2011).
133. Y. C. Wang, C. P. Cho, Application of TiO<sub>2</sub>-graphene nanocomposites to photoanode of dye-sensitized solar cell. *J. Photochem. Photobiol. A Chem.* **332**, 1–9 (2017).
134. Y. Zhang, H. Li, L. Kuo, P. Dong, F. Yan, Recent Applications of Graphene in Dye-sensitized Solar Cells. *Curr. Opin. Colloid Interface Sci.* **20**, 406–415 (2015).
135. X. Guo, G. Lu, J. Chen, Graphene-Based Materials for Photoanodes in Dye-Sensitized Solar Cells. *Front. Energy Res.* **3**, 1–15 (2015).
136. J. D. Roy-Mayhew, I. A. Aksay, Graphene Materials and Their Use in Dye-Sensitized Solar Cells. *Chem. Rev.* **114**, 6323–6348 (2014).
137. T. Chen, W. Hu, J. Song, G. H. Guai, C. M. Li, Interface functionalization of photoelectrodes with graphene for high performance dye-sensitized solar cells. *Adv. Funct. Mater.* **22**, 5245–5250 (2012).
138. Y. B. Tang, *et al.*, Incorporation of graphenes in nanostructured TiO<sub>2</sub> films via molecular grafting for dye-sensitized solar cell application. *ACS Nano* **4**, 3482–3488 (2010).
139. H. Wang, S. L. Leonard, Y. H. Hu, Promoting effect of graphene on dye-sensitized solar cells. *Ind. Eng. Chem. Res.* **51**, 10613–10620 (2012).

140. N. Yang, J. Zhai, D. Wang, Y. Chen, L. Jiang, Two-dimensional graphene bridges enhanced photoinduced charge transport in dye-sensitized solar cells in *ACS Nano*, (American Chemical Society, 2010), pp. 887–894.
141. K. T. Dembele, *et al.*, Graphene below the percolation threshold in TiO<sub>2</sub> for dye-sensitized solar cells. *J. Mater. Chem. A* **3**, 2580–2588 (2014).
142. K. T. Dembele, *et al.*, Graphene below the percolation threshold in TiO<sub>2</sub> for dye-sensitized solar cells. *J. Mater. Chem. A* **3**, 2580–2588 (2014).
143. K. T. Dembele, G. S. Selopal, C. Soldano, R. Nechache, A. Vomiero, Hybrid Carbon Nanotubes – TiO<sub>2</sub> Photoanodes for High Efficiency Dye-Sensitized Solar Cells (2013).
144. P. Blake, *et al.*, Graphene-Based Liquid Crystal Device. *Nano Lett.* **8**, 1704–1708 (2008).
145. Z. Liu, S. P. Lau, F. Yan, Functionalized graphene and other two-dimensional materials for photovoltaic devices: device design and processing. *Chem. Soc. Rev.* **44**, 5638–5679 (2015).
146. A. Fasolino, J. H. Los, M. I. Katsnelson, Intrinsic ripples in graphene. *Nat. Mater.* **6**, 858–861 (2007).
147. F. Guinea, B. Horovitz, P. Le Doussal, Gauge fields, ripples and wrinkles in graphene layers. *Solid State Commun.* **149**, 1140–1143 (2009).
148. W. Zhu, *et al.*, Structure and electronic transport in graphene wrinkles. *Nano Lett.* **12**, 3431–3436 (2012).
149. Y. S. No, J. H. Lee, B. H. Park, J. S. Choi, Ripples, Wrinkles, and Crumples in Folded Graphene. *J. Korean Phys. Soc.* **76**, 985–990 (2020).
150. E. Castillo-Martínez, *et al.*, High temperature structural transformations of few layer graphene nanoribbons obtained by unzipping carbon nanotubes. *J. Mater. Chem. A* **2**, 221–228 (2014).
151. S. V. Morozov, *et al.*, Giant intrinsic carrier mobilities in graphene and its bilayer. *Phys. Rev. Lett.* **100**, 16602 (2008).
152. I. Patsora, S. Hillmann, H. Heuer, B. C. Foos, J. G. Calzada, High-frequency eddy current based impedance spectroscopy for characterization of the percolation process of wet conductive coatings in *AIP Conference Proceedings*, (American Institute of Physics Inc., 2015), pp. 414–423.
153. K. Markandan, J. K. Chin, M. T. T. Tan, Recent progress in graphene based ceramic composites: A review. *J. Mater. Res.* **32**, 84–106 (2017).
154. L. Kvetková, *et al.*, Fracture toughness and toughening mechanisms in graphene platelet reinforced

- Si 3N 4 composites. *Scr. Mater.* **66**, 793–796 (2012).
155. J. Dusza, *et al.*, Microstructure and fracture toughness of Si 3N 4+graphene platelet composites. *J. Eur. Ceram. Soc.* **32**, 3389–3397 (2012).
  156. L. S. Walker, V. R. Marotto, M. A. Rafiee, N. Koratkar, E. L. Corral, Toughening in graphene ceramic composites. *ACS Nano* **5**, 3182–3190 (2011).
  157. K. S. Novoselov, *et al.*, Electric field in atomically thin carbon films. *Science* (80-. ). **306**, 666–669 (2004).
  158. J. W. Essam, Percolation theory. *Reports Prog. Phys.* **43**, 833–912 (1980).
  159. A. Nogales, *et al.*, Low Percolation Threshold in Nanocomposites Based on Oxidized Single Wall Carbon Nanotubes and Poly(butylene terephthalate). *Macromolecules* **37**, 7669–7672 (2004).
  160. Z. Sun, *et al.*, Quantitative evaluation of surfactant-stabilized single-walled carbon nanotubes: Dispersion quality and its correlation with zeta potential. *J. Phys. Chem. C* **112**, 10692–10699 (2008).
  161. J. Dai, R. M. F. Fernandes, O. Regev, E. F. Marques, I. Furó, Dispersing Carbon Nanotubes in Water with Amphiphiles: Dispersant Adsorption, Kinetics, and Bundle Size Distribution as Defining Factors. *J. Phys. Chem. C* **122**, 24386–24393 (2018).
  162. B. Munkhbayar, *et al.*, Influence of dry and wet ball milling on dispersion characteristics of the multi-walled carbon nanotubes in aqueous solution with and without surfactant. *Powder Technol.* **234**, 132–140 (2013).
  163. M. Quintana, M. Prato, Supramolecular aggregation of functionalized carbon nanotubes. *Chem. Commun.* **0**, 6005 (2009).
  164. P. M. Sommeling, *et al.*, Influence of a TiCl<sub>4</sub> post-treatment on nanocrystalline TiO<sub>2</sub> films in dye-sensitized solar cells. *J. Phys. Chem. B* **110**, 19191–19197 (2006).
  165. K. Basu, *et al.*, Enhanced photovoltaic properties in dye sensitized solar cells by surface treatment of SnO<sub>2</sub> photoanodes. *Sci. Rep.* **6**, 23312 (2016).
  166. R. Adhikari, *et al.*, High efficiency, Pt-free photoelectrochemical cells for solar hydrogen generation based on “giant” quantum dots. *Nano Energy* **27**, 265–274 (2016).
  167. B. O. Dabbousi, *et al.*, (CdSe)ZnS core-shell quantum dots: Synthesis and characterization of a size series of highly luminescent nanocrystallites. *J. Phys. Chem. B* **101**, 9463–9475 (1997).
  168. G. S. Selopal, *et al.*, Highly Stable Colloidal “Giant” Quantum Dots Sensitized Solar Cells. *Adv.*



- Funct. Mater.* **27**, 1701468 (2017).
169. Y. Ghosh, *et al.*, New insights into the complexities of shell growth and the strong influence of particle volume in nonblinking “giant” core/shell nanocrystal quantum dots. *J. Am. Chem. Soc.* **134**, 9634–9643 (2012).
  170. A. Zaban, M. Greenshtein, J. Bisquert, Determination of the electron lifetime in nanocrystalline dye solar cells by open-circuit voltage decay measurements. *ChemPhysChem* **4**, 859–864 (2003).
  171. M. Sajedi Alvar, M. Javadi, Y. Abdi, E. Arzi, Enhancing the electron lifetime and diffusion coefficient in dye-sensitized solar cells by patterning the layer of TiO<sub>2</sub> nanoparticles. *J. Appl. Phys.* **119**, 114302 (2016).
  172. , Gamry Potentiostat Difference - Top 10.
  173. Jonathan Atteberry, The Key Components of a Scanning Electron Microscope | HowStuffWorks. *HowStuffWorks* (2018)
  174. S. Gelin, “Dépôt de films d’oxyde de silicium par vaporisation sous vide : dynamique moléculaire et expériences.” (2016)
  175. Shiu-Sing T, Atomic World - Transmission electron microscope(TEM) - Principle of TEM (2020).
  176. V. Zólyomi, J. Koltai, J. Kürti, Resonance Raman spectroscopy of graphite and graphene. *Phys. Status Solidi Basic Res.* **248**, 2435–2444 (2011).
  177. F. Hardcastle, Raman Spectroscopy of Titania (TiO<sub>2</sub>) Nanotubular Water-Splitting Catalysts. *J. Ark. Acad. Sci.* **65**, 43–48 (2011).
  178. C. Ozkan, *Handbook of Graphene, Volume 4: Composites* | Wiley (Wiley, 2019).
  179. K. T. Dembele, *et al.*, Hybrid Carbon Nanotubes–TiO<sub>2</sub> Photoanodes for High Efficiency Dye-Sensitized Solar Cells. *J. Phys. Chem. C* **117**, 14510–14517 (2013).
  180. G. S. Selopal, *et al.*, Graphene as transparent front contact for dye sensitized solar cells. *Sol. Energy Mater. Sol. Cells* **135**, 99–105 (2015).
  181. J. Fan, *et al.*, Enhanced photovoltaic performance of dye-sensitized solar cells based on TiO<sub>2</sub> nanosheets/graphene composite films. *J. Mater. Chem.* **22**, 17027 (2012).
  182. J. Chen, B. Yao, C. Li, G. Shi, An improved Hummers method for eco-friendly synthesis of graphene oxide. *Carbon N. Y.* **64**, 225–229 (2013).
  183. S. Jovanović, *et al.*, Raman spectroscopy of graphene nanoribbons synthesized by longitudinal

- unzipping of multiwall carbon nanotubes. *Phys. Scr.* **T162**, 14023 (2014).
184. R. C. Nelson, Energy Transfers between Sensitizer and Substrate IV Energy Levels in Solid Dyes. *J. Opt. Soc. Am.* **51**, 1186 (1961).
  185. J. Bisquert, I. Mora-Sero, F. Fabregat-Santiago, Diffusion-recombination impedance model for solar cells with disorder and nonlinear recombination. *ChemElectroChem* **1**, 289–296 (2014).
  186. D. Benetti, *et al.*, Functionalized multi-wall carbon nanotubes/TiO<sub>2</sub> composites as efficient photoanodes for dye sensitized solar cells. *J. Mater. Chem. C* **4**, 3555–3562 (2016).
  187. L. M. Peter, N. W. Duffy, R. L. Wang, K. G. U. Wijayantha, Transport and interfacial charge transfer of electrons in dye-sensitized nanocrystalline solar cells. *J. Electroanal. Chem.* **524–525**, 127–136 (2002).
  188. R. Akilimali, *et al.*, Hybrid TiO<sub>2</sub>-Graphene nanoribbon photoanodes to improve the photoconversion efficiency of dye sensitized solar cells. *J. Power Sources* **396**, 566–573 (2018).
  189. M. Mohammadnezhad, *et al.*, Towards Long-Term Thermal Stability of Dye-Sensitized Solar Cells Using Multiwalled Carbon Nanotubes. *Chempluschem* **83**, 682–690 (2018).
  190. Q. Xiang, J. Yu, M. Jaroniec, Enhanced photocatalytic H<sub>2</sub>-production activity of graphene-modified titania nanosheets. *Nanoscale* **3**, 3670–3678 (2011).
  191. R. Rahimi, S. Zargari, Z. Sadat Shojaei, Photoelectrochemical Investigation of TiO<sub>2</sub>-Graphene Nanocomposites in *Proceedings of The 18th International Electronic Conference on Synthetic Organic Chemistry*, (MDPI, 2014), p. a044.
  192. M. A. Pimenta, *et al.*, Studying disorder in graphite-based systems by Raman spectroscopy. *Phys. Chem. Chem. Phys.* **9**, 1276–91 (2007).
  193. P. T. Araujo, M. Terrones, M. S. Dresselhaus, Defects and impurities in graphene-like materials. *Mater. Today* **15**, 98–109 (2012).
  194. L. G. Cançado, *et al.*, Quantifying defects in graphene via Raman spectroscopy at different excitation energies. *Nano Lett.* **11**, 3190–6 (2011).
  195. M. S. Dresselhaus, A. Jorio, A. G. Souza Filho, A. R. Saito, R. Saito, Defect characterization in graphene and carbon nanotubes using Raman spectroscopy. *Philos. Trans. A. Math. Phys. Eng. Sci.* **368**, 5355–5377 (2010).
  196. R. Lv, *et al.*, Nitrogen-doped graphene: Beyond single substitution and enhanced molecular sensing. *Sci. Rep.* **2**, 2980–2982 (2012).

197. E. Sandoz-Rosado, *et al.*, Vertical graphene by plasma-enhanced chemical vapor deposition: Correlation of plasma conditions and growth characteristics. *J. Mater. Res.* **29**, 417–425 (2014).
198. A. C. Ferrari, D. M. Basko, Raman spectroscopy as a versatile tool for studying the properties of graphene. *Nat. Nanotechnol.* **8**, 235–46 (2013).
199. A. Das, *et al.*, Monitoring dopants by Raman scattering in an electrochemically top-gated graphene transistor. *Nat. Nanotechnol.* **3**, 210–215 (2008).
200. L. Chong, H. Guo, Y. Y. Zhang, Y. Hu, Y. Y. Zhang, Raman study of strain relaxation from grain boundaries in epitaxial graphene grown by chemical vapor deposition on SiC. *Nanomaterials* **9**, 372 (2019).
201. W. X. Wang, *et al.*, The study of interaction between graphene and metals by Raman spectroscopy in *Journal of Applied Physics*, (2011).
202. T. Yu, *et al.*, Raman Mapping Investigation of Graphene on Transparent Flexible Substrate: The Strain Effect. *J. Phys. Chem. C* **112**, 12602–12605 (2008).
203. E. Singh, H. S. Nalwa, Singh, E. and Nalwa, H.S., 2015. Graphene-based dye-sensitized solar cells: a review. *Science of Advanced Materials*, 7(10), pp.1863-1912. *Sci. Adv. Mater.* **7**, 1863–1912 (2015).
204. A. Hinsch, *et al.*, Long-term stability of dye-sensitised solar cells. *Prog. Photovoltaics Res. Appl.* **9**, 425–438 (2001).
205. D. H. Cha, Y. S. Kim, J. H. Pan, Y. H. Lee, W. I. Lee, “Synthesis of the mesoporous TiO<sub>2</sub> films and their application to dye-sensitized solar cells” in *Studies in Surface Science and Catalysis*, (Elsevier Inc., 2007), pp. 625–628.
206. W. Pervez, S. R. Ali, Photoanode annealing effect on charge transport in dye-sensitized solar cell. *J. Mater. Sci. Mater. Electron.* **31**, 779–784 (2019).
207. J. Bisquert, *et al.*, Doubling Exponent Models for the Analysis of Porous Film Electrodes by Impedance. Relaxation of TiO<sub>2</sub> Nanoporous in Aqueous Solution. *J. Phys. Chem. B* **104**, 2287–2298 (2000).
208. M. Adachi, M. Sakamoto, J. Jiu, Y. Ogata, S. Isoda, Determination of parameters of electron transport in dye-sensitized solar cells using electrochemical impedance spectroscopy. *J. Phys. Chem. B* **110**, 13872–13880 (2006).
209. Q. Wang, *et al.*, Characteristics of High Efficiency Dye-Sensitized Solar Cells <sup>†</sup>. *J. Phys. Chem. B*

- 110**, 25210–25221 (2006).
210. M. Mohammadnezhad, *et al.*, Role of Carbon Nanotubes to Enhance the Long-Term Stability of Dye-Sensitized Solar Cells. *ACS Photonics* **7**, 653–664 (2020).
  211. J. Bisquert, Chemical capacitance of nanostructured semiconductors: Its origin and significance for nanocomposite solar cells. *Phys. Chem. Chem. Phys.* **5**, 5360–5364 (2003).
  212. P. V. Kamat, Meeting the clean energy demand: Nanostructure Architectures for Solar Energy Conversion. *Phys. Chem.* **392**, 2834–2860 (2007).
  213. L. Zhang, Y. Wang, T. Xu, S. Zhu, Y. Zhu, Surface hybridization effect of C60 molecules on TiO<sub>2</sub> and enhancement of the photocatalytic activity. *J. Mol. Catal. A Chem.* **331**, 7–14 (2010).
  214. S. Hu, F. Li, Z. Fan, The Property and Photocatalytic Performance Comparison of Graphene, Carbon Nanotube, and C 60 Modified TiO<sub>2</sub> Nanocomposite Photocatalysts. *Bull. Korean Chem. Soc.* **34**, 3671–3676 (2013).
  215. S. Mu, Y. Long, S.-Z. Kang, J. Mu, Surface modification of TiO<sub>2</sub> nanoparticles with a C60 derivative and enhanced photocatalytic activity for the reduction of aqueous Cr(VI) ions. *Catal. Commun.* **11**, 741–744 (2010).
  216. W. Wang, P. Serp, P. Kalck, J. L. Faria, Photocatalytic degradation of phenol on MWNT and titania composite catalysts prepared by a modified sol–gel method. *Appl. Catal. B Environ.* **56**, 305–312 (2005).
  217. M. S. A. Sher Shah, A. R. Park, K. Zhang, J. H. Park, P. J. Yoo, Green synthesis of biphasic TiO<sub>2</sub>-reduced graphene oxide nanocomposites with highly enhanced photocatalytic activity. *ACS Appl. Mater. Interfaces* **4**, 3893–3901 (2012).
  218. W. Fan, Q. Lai, Q. Zhang, Y. Wang, Nanocomposites of TiO<sub>2</sub> and reduced graphene oxide as efficient photocatalysts for hydrogen evolution. *J. Phys. Chem. C* **115**, 10694–10701 (2011).
  219. R. Nishinakagawa, K. Matsuda, T. Arai, A. Sawada, T. Terashima, Raman spectroscopy investigations of chemically derived zigzag edge graphene nanoribbons. *AIP Adv.* **3**, 92111 (2013).
  220. A. Jorio, *et al.*, Measuring disorder in graphene with the G and D bands. *Phys. status solidi* **247**, 2980–2982 (2010).
  221. L. M. Malard, M. A. Pimenta, G. Dresselhaus, M. S. Dresselhaus, Raman spectroscopy in graphene. *Phys. Rep.* **473**, 51–87 (2009).
  222. A. C. Ferrari, Raman spectroscopy of graphene and graphite: Disorder, electron–phonon coupling,

- doping and nonadiabatic effects. *Solid State Commun.* **143**, 47–57 (2007).
223. M. S. Dresselhaus, G. Dresselhaus, R. Saito, A. Jorio, Raman spectroscopy of carbon nanotubes. *Phys. Rep.* **409**, 47–99 (2005).
  224. J.-W. Lee, S. Makuta, S. Sukarasep, J. Bo, T. Suzuki, Electron Injection from a CdS Quantum Dot to a TiO<sub>2</sub> Conduction Band as an Efficiency Limiting Process : Comparison of QD Depositions between SILAR and Linker Assisted Attachment. *J. Photopolym. Sci. Technol.* **29**, 357–362 (2016).
  225. W. Nan, *et al.*, Crystal structure control of zinc-blende CdSe/CdS core/shell nanocrystals: Synthesis and structure-dependent optical properties. *J. Am. Chem. Soc.* **134**, 19685–19693 (2012).
  226. J. Bisquert, A. Zaban, P. Salvador, Analysis of the mechanisms of electron recombination in nanoporous TiO<sub>2</sub> dye-sensitized solar cells. Nonequilibrium steady-state statistics and interfacial electron transfer via surface states. *J. Phys. Chem. B* **106**, 8774–8782 (2002).
  227. W. H. Leng, Z. Zhang, J. Q. Zhang, C. N. Cao, Investigation of the kinetics of a TiO<sub>2</sub> photoelectrocatalytic reaction involving charge transfer and recombination through surface states by electrochemical impedance spectroscopy. *J. Phys. Chem. B* **109**, 15008–15023 (2005).
  228. R. Asahi, T. Morikawa, T. Ohwaki, K. Aoki, Y. Taga, Visible-light photocatalysis in nitrogen-doped titanium oxides. *Science (80-. )*. **293**, 269–271 (2001).
  229. S. Zhang, *et al.*, Synthesis of TiO<sub>2</sub> Nanoparticles on Plasma-Treated Carbon Nanotubes and Its Application in Photoanodes of Dye-Sensitized Solar Cells. *J. Phys. Chem. C* **115**, 22025–22034 (2011).

## 8 LIST OF PUBLICATIONS

---

### Published:

**R. Akilimali**, G.S. Selopal, D. Benetti, M. Mohammadnezhad, H. Zhao, Z.M. Wang, B.Stansfield, F. Rosei, Catal. Today **340**, 161–169 (2020).

**R. Akilimali**, G.S. Selopal, D. Benetti, I. Serrano-Esparza, P.A. Algarabel, J.M. De Teresa, H. Zhao, Z.M. Wang, B.Stansfield, F. Rosei. *J. Power Sources* **396**, 566–573 (2018).

K. Basu G.S. Selopal, D. Benetti, M. Mohammadnezhad, **R. Akilimali**, H. Zhao, Z.M. Wang, F. Vetrone, F. Rosei, Hybrid graphene/metal oxide anodes for efficient and stable dye sensitized solar cell. *Electrochim. Acta* **349**, 136409 (2020).

M. Mohammadnezhad, G.S.Selopal, N. Alsayyari, **R. Akilimali**, F. Navarro-Pardo, H. Zhao, Z.M. Wang, B.Stansfield, F. Rosei., CuS/Graphene Nanocomposite as a Transparent Conducting Oxide and Pt-Free Counter Electrode for Dye-Sensitized Solar Cells. *J. Electrochem. Soc.* **166**, H3065–H3073 (2019).

### In preparation :

**R. Akilimali**, G.S. Selopal, M. Mohammadnezhad, I. Ka, ,Z.M. Wang, R. Nechache, G.P. Lopinsky, H. Zhao, F. Rosei, Structural effect of low-dimensional carbon nanostructures on long-term stability of dye sensitized solar cells



## 9 ANNEXE I : SOMMAIRE RÉCAPITULATIF

---

La découverte en 1991 des cellules solaires à pigment photosensible par O'Regan and Grätzel (22) a ouvert de nouvelles perspectives dans le domaine photovoltaïque (PV). Inspiré par la photosynthèse végétale (15), ces cellules utilisent des pigments photosensibles dénommés chromophores (16).

Bien que ces pigments, qui sont greffés sur les oxydes métalliques à grande bande, ne permettent pas une performance élevée des cellules, elles présentent néanmoins l'avantage de pouvoir produire de l'énergie dans condition d'ensoleillement faible et indirect, comme dans les espaces intérieurs ou les journées ennuagées (28, 45). Ceci les rend très attractives pour les applications à grande échelle et les positionne de ce fait comme technologie les plus prometteuses pour le PV (29).

Par ailleurs, leurs méthodes de production ne demandent pas des conditions coûteuses et ultra-propres comme pour les cellules solaires à silicium qui dominent actuellement le marché. Par conséquent plusieurs études ont été menées afin de pouvoir améliorer leur rendement et ainsi contribuer à une transition énergétique moins onéreuse (27).

Leur faible efficacité est principalement liée aux faibles conductivités électriques et aux effets de recombinaison présente au sein de leurs composants (37). D'autre part, pour répondre à la demande croissante des énergies renouvelables, des technologies durables sont privilégiées afin de minimiser les coûts d'investissements (25).

Les cellules de Grätzel, présentent en effet, quelques inconvénients concernant la stabilité de ses composants qui doivent être résolus afin que la technologie puisse effectivement contribuer à offrir de l'énergie à bas coût (56).

Par ailleurs, à travers l'utilisation d'un composant important des cellules de Grätzel, la photoanode, il est possible de réaliser des dispositifs qui permettent la production d'hydrogène. Ce dernier, est une énergie renouvelable qui s'obtient en utilisant les mêmes oxydes métalliques que les cellules de Grätzel et ont la particularité de produire l'hydrogène par scission de la molécule d'eau (86).

En effet, Fujishima et Honda (21) ont découvert une variante de l'électrolyse de l'eau qui est la photo-électrolyse. La photo-électrolyse se fait à la surface d'une électrode activée par la lumière. Cette activation génère un photo-courant qui permet de diminuer l'alimentation électrique extérieure nécessaire pour atteindre le potentiel de dissociation de l'eau. L'énergie de la bande



interdite du semi-conducteur constitutif de la photoanode doit être relativement élevée, de part et d'autre du couple d'oxydation ( $O_2/H_2O$ ) et de réduction ( $H^+ /H_2$ ) de l'eau. Cette caractéristique est au détriment de son absorption dans le visible, domaine majoritaire du spectre solaire (85).

## Les composants

Une cellule de Grätzel typique est constituée d'un substrat d'oxyde conducteur transparent, un film mince de semi-conducteur mésoporeux à large bande interdite (également appelé photoanode), un photosensibilisateur (des molécules de colorant adsorbées sur la photoanode mésoporeuse) (52), un électrolyte en couple redox, et enfin une contre-électrode (CE) pour compléter la cellule. La photoanode est le composant le plus important d'une cellule de Grätzel, qui joue un rôle crucial dans la maximisation du rendement d'une cellule de Grätzel (79). La photoanode nécessite une grande surface pour pouvoir ancrer une grande quantité de molécules de colorant et ainsi générer suffisamment de photoélectrons pour contribuer à la densité de photocourant et donc augmenter le rendement global du dispositif (92).

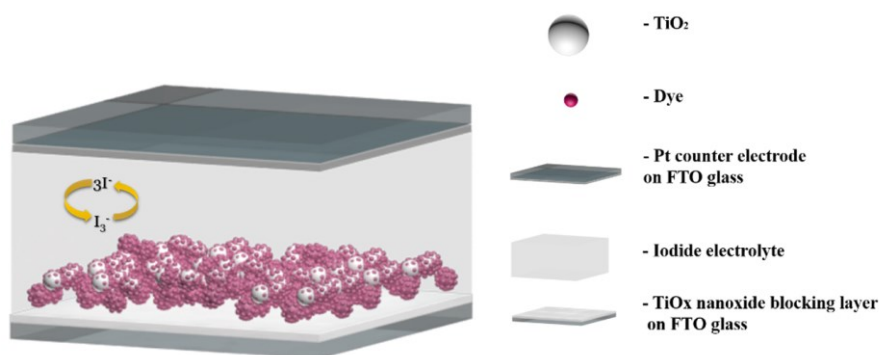


Figure 1 : Schéma de la structure d'une Cellule de Grätzel

La bande de conduction (CB) du matériau photoanode doit être énergétiquement à une position légèrement inférieure à la plus basse orbitale moléculaire inoccupée (LUMO) du colorant pour minimiser les pertes potentielles énergétiques (140, 141). La photoanode doit également posséder une grande mobilité d'électrons pour assurer un transport d'électrons efficace puisque le transport de charge dans une cellule de Grätzel se produit via un procédé de diffusion lente caractérisée par des pièges à électrons. Les cellules de Grätzel basées sur des photoanodes de TiO<sub>2</sub> ont atteint les rendements les plus élevés à ce jour (26), essentiellement en raison de la

faible surtension par rapport aux colorants couramment utilisés et du rapport surface / volume élevé.

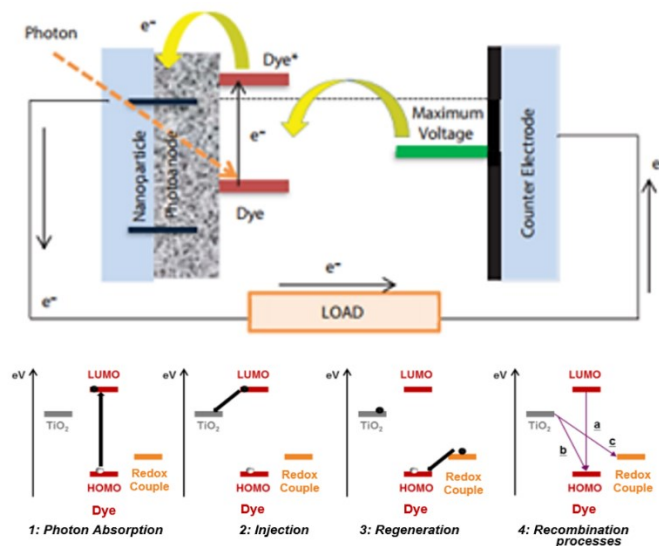
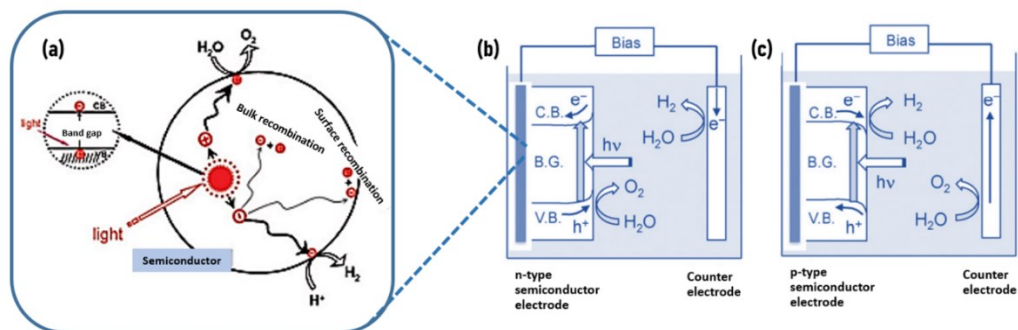


Figure 2 : Fonctionnement des cellules de Grätzel (37)

La division photocatalyse de l'eau est l'un des processus les plus importants pour la conversion du carburant solaire en fournissant un vecteur d'énergie propre, stockable et durable tel que l'hydrogène directement à partir de la lumière du soleil, de l'eau et du CO<sub>2</sub>.

La première cellule a été construite par les scientifiques Fujishima et Honda en 1972 avec l'utilisation de photoanode TiO<sub>2</sub> immergée dans l'eau et de platine comme cathode éclairée par la lumière UV (18). L'eau a ensuite été décomposée en dégagement d'oxygène à la photoanode et H<sub>2</sub> à la cathode (76).



**Figure 3 (a) Principaux procédés de transport de charge et de recombinaison dans la division photocatalytique de l'eau. Systèmes de séparation d'eau à base de PEC mettant en œuvre (b) une photoanode à semi-conducteur de type n, et (c) une photocathode à semi-conducteur de type p (76).**

En raison de leur capacité à diviser sa bande électronique en niveaux électroniques discrets, les Boîtes quantiques (QD) ont été proposés comme des nanomatériaux prometteurs capables d'ajuster leur bande passante en contrôlant sa taille et sa morphologie. Le diamètre de l'exciton Bohr du  $\text{TiO}_2$  est de 1,5 nm, en dessous duquel  $\text{TiO}_2$  présente des effets de taille quantique. Les particules de  $\text{TiO}_2$  considérées pour le Cellules de Grätzel sont généralement au-dessus de la plage de 20 nm, c'est-à-dire beaucoup plus élevées que son rayon de Bohr d'exciton de 1,5 nm. Ils sont donc considérés comme un réseau de nanocristaux massifs absorbant la lumière uniquement dans le domaine des UV. Afin de pallier ces inconvénients, les photoanodes sensibilisés QD ont depuis été promus pour étendre la plage d'absorption de la lumière et ainsi améliorer les efficacités de génération de  $\text{H}_2$  (78, 79).

Dans cette thèse, un nouveau type de structure core-shell CdS / CdSe Giant avec un QD de coiffage ZnS avec une structure de bande adéquate a été utilisé.

Le semi-conducteur nanocristallin représente le composant central dans la réalisation des mécanismes Cellules de Grätzel. Avec le photosensibilisateur, ils sont appelés photoanode. Sa porosité offre des sites de greffage pour l'absorption de la lumière qui contrôlent les performances. Il sépare les charges via sa configuration électronique et assure la diffusion des charges à travers les réseaux de transport et de recombinaison des particules percolantes.

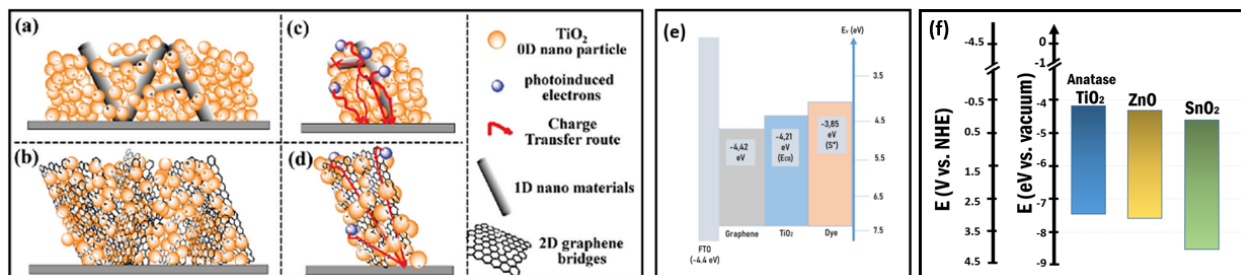


**Figure 3 : Différence entre a, c) 1D et b, d) électrodes composites de nanomatériaux 2D. Dans les électrodes composites de nanomatériaux 2D (ponts de graphène) (140), le diagramme du niveau d'énergie des CELLULE DE GRÄTZEL à base de (e)  $\text{TiO}_2$ -graphène et d'autres oxydes métalliques.**

En raison de leur bande interdite accordable, de leur grande surface spécifique et de leur grande mobilité électronique, les feuilles de graphène et à base de graphène ont été signalées comme des composants efficaces pour diverses parties des Cellules de Grätzel (123–125). Introduit comme additif dans le photoanode nanocristallin des Cellules de Grätzel, la structure 2D profite de la séparation des charges car elle a non seulement une excellente conductivité, mais aussi un bon contact de zone à zone avec le  $\text{TiO}_2$ , par rapport au contact point à point présenté par le nanocomposite intégré aux CNT (126) .

De nombreuses études montrent que les photoanodes hybrides  $\text{TiO}_2$  à base de graphène fournissent un meilleur rendement électronique par rapport aux CNT (127–130). En fait, contrairement à son homologue 1D, la feuille unique de graphène offre un meilleur contact avec les nanoparticules sphériques de  $\text{TiO}_2$  à l'échelle nanométrique, pontant ainsi plus efficacement la structure mésoporeuse. Cela a un impact sur l'efficacité globale des Cellules de Grätzel en raison d'une plus faible recombinaison de charge avec l'électrolyte par rapport aux CNT.

De plus, le graphène a une fonction de travail (-4,42 eV) (128) qui se situe précisément entre l'ECB du  $\text{TiO}_2$  (-4,4 eV) (25) et le substrat en verre conducteur FTO (-4,7 eV) (25). Cet alignement de bande approprié facilite à son tour le transport échafaudé d'électrons photo-injectés de la bande de conduction  $\text{TiO}_2$  au substrat FTO (130, 131).

De plus, plusieurs facteurs tels que le rapport du graphène, la taille et l'épaisseur du film de graphène, qui déterminent en outre l'efficacité de la cellule solaire. De petites quantités de 0,6% en poids de graphène ont conduit à un transport d'électrons plus rapide et à une recombinaison plus faible, ainsi qu'à une diffusion de la lumière plus élevée. Cependant, une teneur excessive en graphène est impliquée dans les processus de recombinaison avec  $\text{TiO}_2$ .

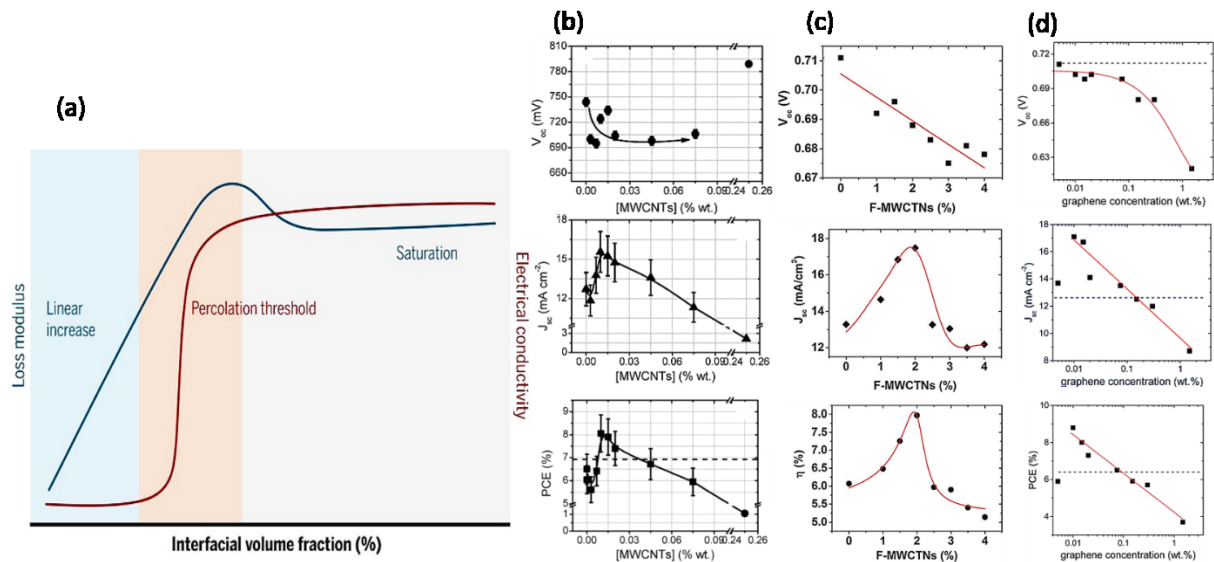


**Figure 4** (a) Seuil de percolation avec module de perte et évolution de la conductivité électrique en fraction volumique interfaciale. Paramètres I-V du nanocomposite  $\text{TiO}_2$  avec (b) MWCNT (113) (c) F-MWCNT (133) (d) et graphène (131)

Bien que les GNR présentent les mêmes caractéristiques anisotropes que leurs homologues NTC d'origine, ils ont cependant tendance à se comporter chimiquement comme des feuilles de graphène, offrant une dispersion améliorée dans le solvant. Comme le montre la **Figure 4**, globalement en tant qu'additifs, les nanocarbones décrivent un seuil de percolation après une augmentation linéaire, puis suivi d'une dimide référenciation des performances. La même tendance doit donc être observée pour GNR.

De plus, selon la théorie de la percolation (68), le rapport d'aspect plus élevé du GNR par rapport aux feuilles de graphène devrait abaisser le seuil de percolation à la fois pour la trempe et la conductivité électrique.

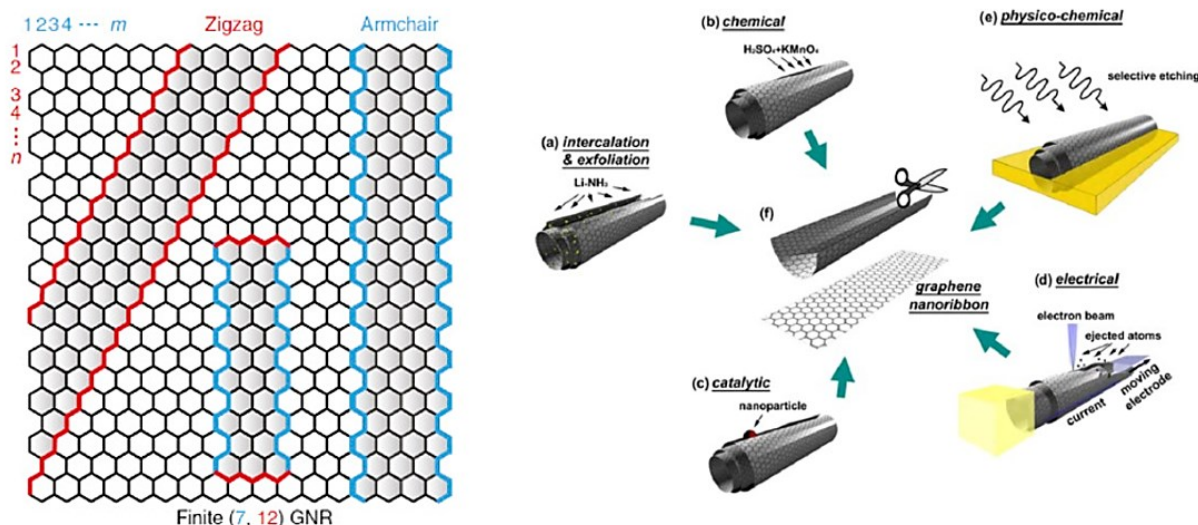


**Figure 5** Schéma de la forme des bords et de la nomenclature des GNR en fauteuil et en zigzag et différentes manières de décompresser les CNT pour la production de GNR: (a) Exfoliation par intercalation, (b) oxydation chimique, (c) approche catalytique, (d) méthode électrique, et (f) gravure sélective par plasma Ar (100)

Étant donné que l'intensité des effets de renforcement dépend de manière significative de la liaison interfaciale du matériau hôte et de la dispersion des GNR dans la matrice, les mécanismes de renforcement peuvent probablement contribuer positivement aux problèmes de dégradation du film de TiO<sub>2</sub> en comblant les fissures formées par le vieillissement et les arrachements de graphène. Ils pourraient ainsi être utilisés pour obtenir des résistances mécaniques plus élevées, favorisant une résistance à la flexion et une élasticité plus élevées (142–145), et augmenter la stabilité à long terme des Cellule de Grätzel.

Les atomes de carbone plans liés au sp<sup>2</sup> avec une transparence monocouche élevée (97,3%), une surface spécifique élevée (2630 m<sup>2</sup> / g), une conductivité électrique élevée de 106 S / m et une conductivité thermique de 5300 W / mK (146) de nanocarbons de faible dimension tels que le graphène et le GNR a motivé notre étude pour permettre des conductivités électriques plus élevées d'un nouveau film de composites de nanocarbone pour les dispositifs photoélectriques.

La théorie de la percolation (147) se référant à une charge critique de charge consiste à augmenter le comportement de conductivité électrique des films à plusieurs ordres de grandeur du fait de la formation d'électrons contide références et de chemins conducteurs. Les chemins

d'électrons ne se formeront pas en dessous de la plage de transition de percolation. La concentration de GNR doit donc être supérieure au seuil de percolation pour qu'un réseau conducteur puisse être réalisé dans la photoanode.

Même à de faibles concentrations d'additifs, le GNR peut profiter de leurs rapports d'aspect élevés pour être en contact intime avec l'électrolyte  $\text{TiO}_2$  et se rapprocher de chaque ruban en flocons créant des voies conductrices à travers la masse (131, 142, 148).

La théorie de la percolation prédit que le début du seuil de percolation devrait dimide référencer avec l'augmentation du rapport d'aspect (longueur / largeur) ( $L / l$ ) du graphène.

Pour obtenir des valeurs optimales pour les renforts et la conductivité du film, un nanocomposite GNR et  $\text{GNR-TiO}_2$  de bonne qualité avec une concentration de défauts plus faible doit être élaboré. Ces caractéristiques critiques dépendent des voies et des conditions de traitement (142). Ainsi, la fonctionnalité du graphène joue un rôle critique dans la réduction du taux de chargement, de la dispersion et de l'organisation des feuilles dans la matrice hôte pour améliorer les performances globales des composites. En effet, le rendement électronique des Cellules de Grätzel est fortement affecté par la dispersion des nanocarbones dans le fluide de base (68, 148-150), comme l'eau, l'éthanol etc., en raison du manque de groupements hydrophiles (109, 151).

Par conséquent, dans cette thèse, des méthodes de production faciles, peu coûteuses et peu agressives ont été privilégiées.

### **Les objectifs**

Dans ce contexte, ma thèse porte sur le développement de nouveaux nanocomposite en utilisant l'incorporation des nanorubans de graphène (GNR) à l'intérieur de la couche photoactive de dioxyde de titane ( $\text{TiO}_2$ ) des dispositifs de cellules de Grätzel et de photoélectrochimie solaire (PEC), afin d'en augmenter la conductivité et la stabilité à long-terme.

De fait, en raison des propriétés morphologiques, électriques et mécaniques exceptionnelles que possède le GNR, nous pouvons former par une méthode de mélange simple une interaction interfaciale attrayante à l'échelle nanométrique qui peut améliorer efficacement la direction du flux d'électrons et empêcher le  $\text{TiO}_2$  de s'agglomérer au fil du temps en renforçant les grains à

travers van der Waals force et améliore l'efficacité de la collecte de charge des électrons photogénérés grâce à son rapport hauteur / largeur unidimensionnel plus élevé.

Plus précisément, les objectifs de la thèse sont:

(1) Élaborer des Cellules de Grätzel avec photoanode composite GNR-TiO<sub>2</sub> efficace pour obtenir des J<sub>sc</sub> et des rendements énergétique plus élevés avec une teneur en carbone inférieure, par densité de courant-tension (J-V), désintégration photovoltaïque transitoire et spectroscopie d'impédance électrochimique (EIS)

(2) Comparez l'effet d'un rapport hauteur / largeur plus élevé de GNR sur le seuil de percolation de GNR-TiO<sub>2</sub> par rapport au graphène-TiO<sub>2</sub> grâce à la performance photoélectrique et à la stabilité à long terme des Cellules de Grätzel, en utilisant la spectroscopie Raman et l'EIS pour étudier l'effet des morphologies comparatives sur le transport mécanismes

(3) Fabriquer un dispositif PEC hautement efficace et durable avec une photoanode GNR-TiO<sub>2</sub> sensibilisée aux points quantiques pour améliorer l'efficacité de la génération d'hydrogène, en utilisant UV-visible pour surveiller les effets négatifs du nanocomposite sur l'absorption, la spectroscopie SEM et Raman et pour optimiser la concentration de GNR dans le dispositif pour J<sub>sc</sub> élevé.

La thèse est organisée en six chapitres comme suit :

**Chapitre 1** Introduction des concepts fondamentaux de l'arrière-plan sont brièvement présentés ici, suivis de l'objectif et du but de la thèse sont présentés.

**Chapitre 2** Matériel et méthodes. Dans ce chapitre, nous présentons la description des techniques de fabrication et de caractérisation utilisées tout au long de ce travail.

**Chapitre 3** Photoanodes hybrides TiO<sub>2</sub>-Nanorubans de graphène pour augmenter l'efficacité de photoconversion des cellules solaires à colorant. Nous démontrons la fabrication de cellules de Grätzel avec des concentrations optimales de GNR dans le photoanode et comment il améliore l'efficacité globale.

**Chapitre 4** Effet structurel des nanostructures de carbone de faible dimension sur la stabilité à long terme des cellules solaires à colorant. Nous discutons et comparons l'effet de l'incorporation



de feuilles de graphène avec différents rapports d'aspect sur l'évolution des paramètres de densité photovoltaïque J-V et des paramètres d'impédance, et la capacité de ces matériaux à stabiliser efficacement les dispositifs.

**Chapitre 5** Photoanode hybride nanoribbon-TiO<sub>2</sub>-points quantiques (QD) de graphène pour booster les performances de la photoélectrochimie pour la production d'hydrogène. Nous démontrons comment la fabrication de cellules PEC avec des concentrations optimales de GNR dans le photoanode peut améliorer l'efficacité globale de la génération d'hydrogène

**Chapitre 6** Conclusions et recommandations basées sur l'analyse des résultats et la proposition d'études complémentaires.

Cette thèse impliquait l'utilisation de nouveaux nanocomposites hybrides dans les cellules de Grätzel et le PEC. La conclusion générale reprendra les principaux résultats présentés dans ce document et s'ouvrira sur des perspectives scientifiques et technologiques liées au dispositifs.

## Chapitre 2 : Partie expérimentale

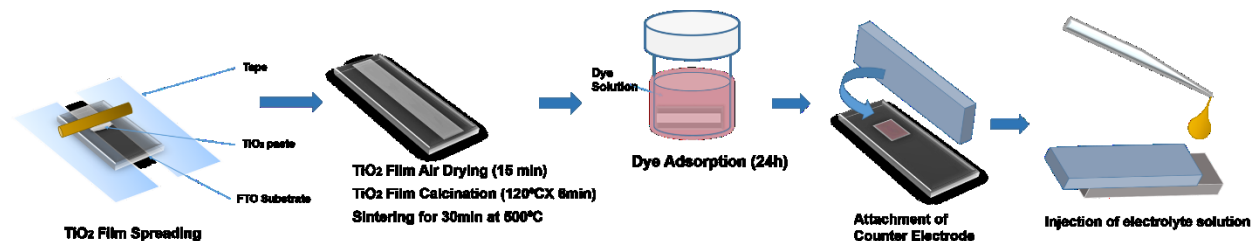


Figure 5 Schéma des étapes de fabrication du dispositif de Cellules de Grätzel. Image d'une électrode après sensibilisation au colorant N719

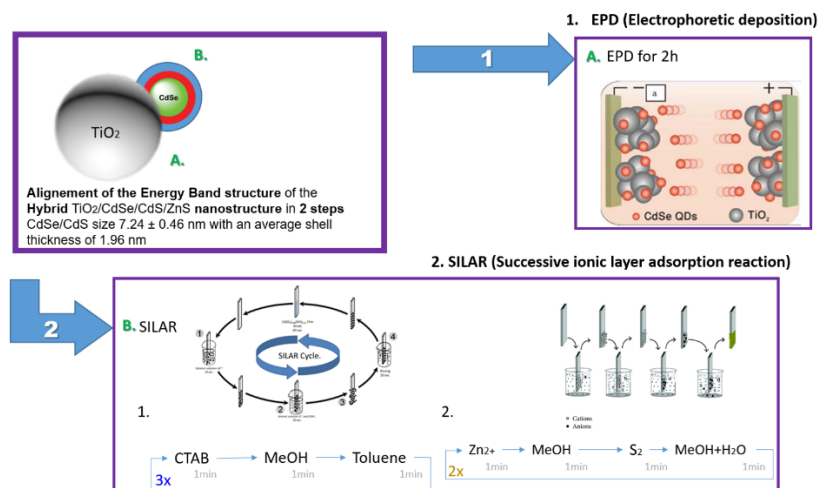


Figure 5 Schéma reprenant la formation des cellules PEC

### CHAPITRE 3 : PHOTOANODES HYBRIDES $\text{TiO}_2$ -NANORUBAN DE GRAPHÈNE POUR BOOSTER L'EFFICACITÉ DE PHOTOCONVERSION DES CELLULES SOLAIRES SENSIBLES AUX COLORANTS

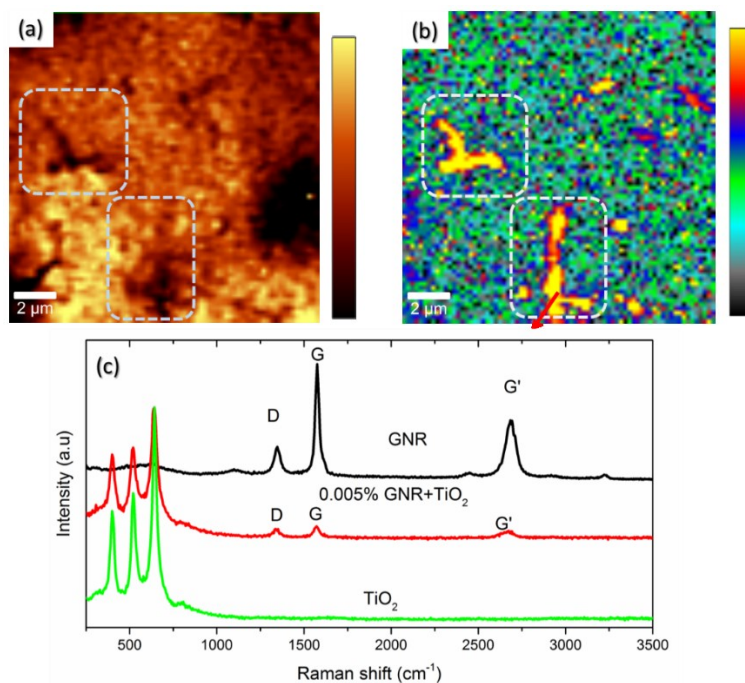


Figure 6 Cartographie Raman de la photoanode composite filtrée pour: (a)  $\text{TiO}_2$ ; (b) GNR respectivement. (c) Spectres Raman de film mésoporeux de  $\text{TiO}_2$  de référence (ligne verte), film mésoporeux hybride  $\text{TiO}_2$ -GNR (ligne rouge) et poudre GNR (ligne noire).

GNR ( wt %)	$V_{oc}$ (V)	$J_{sc}$ (mA/cm <sup>2</sup> )	FF (%)	PCE (%)
0	0.705	13.13	65	5.99
0.0025	0.692	13.60	69	6.49
0.0050	0.724	14.22	70	7.18
0.010	0.724	13.01	68	6.39
0.015	0.726	11.59	60	5.07
0.075	0.696	10.50	68	4.99

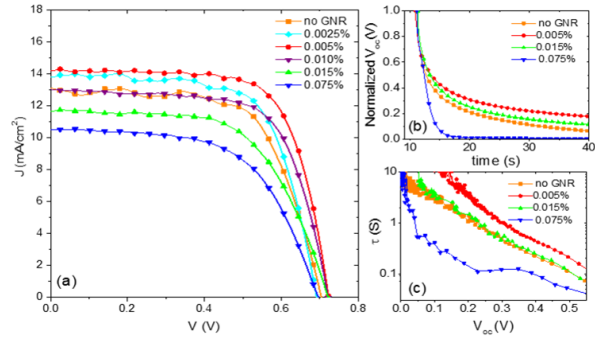


Figure 7 Tableau des propriétés fonctionnelles des Cellules de Grätzel avec un contede référence GNR différent. Courbes de densité de courant-tension de l'appareil avec différentes concentrations de GNR dans  $\text{TiO}_2$  sous un éclairage solaire (rayonnement AM1.5G (100 mW / cm<sup>2</sup>), (b) Mesures de la décroissance de la tension photovoltaïque transitoire des dispositifs correspondants. Décroissance normalisée des  $V_{oc}$  avec le temps; (c) Calcul des valeurs de durée de vie des électrons à partir de la désintégration  $V_{oc}$ .

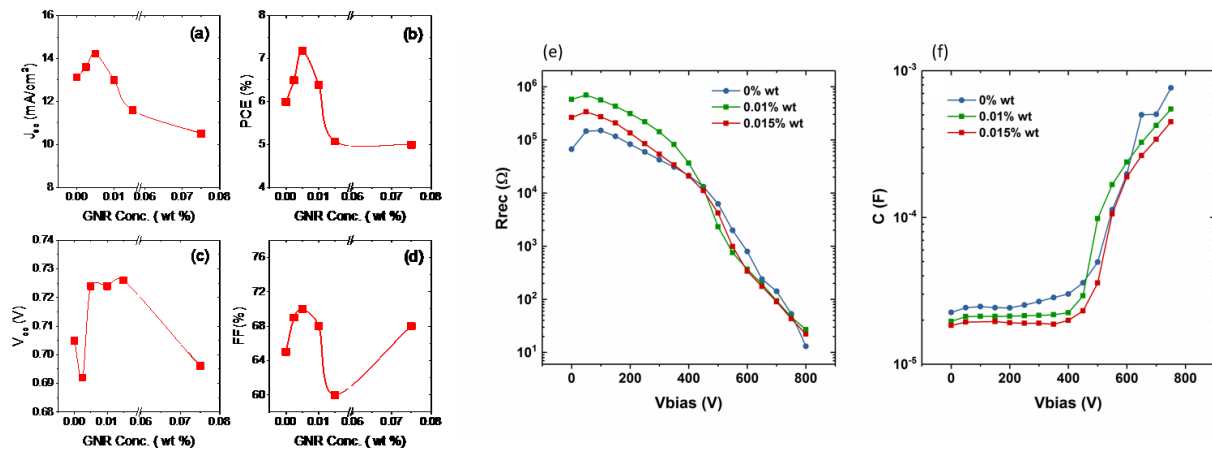


Figure 8. Variation des paramètres fonctionnels du dispositif sous un éclairage solaire (irradiation AM1.5G, 100 mW cm<sup>-2</sup>) avec concentration de GNR en  $\text{TiO}_2$ : (a)  $J_{sc}$ ; (b) rendement électronique; (c)  $V_{oc}$ ; (d) FF. Analyse EIS des Cellules de Grätzel à différentes concentrations de GNR: (e) résistance à la recombinaison; (f) capacité chimique des mesures EIS dans l'obscurité

En résumé, nous avons démontré qu'une petite quantité de GNR insérés dans la pâte nanoparticulaire  $\text{TiO}_2$  peut améliorer considérablement les performances fonctionnelles des Cellules de Grätzel. Nos résultats montrent qu'une concentration optimale de GNR dans la couche active de  $\text{TiO}_2$  améliore la collecte et le transport des électrons photogénérés, ce qui à son tour améliore les performances fonctionnelles du dispositif. Une augmentation supplémentaire de la concentration de GNR entraîne une diminue des performances, en raison de l'effet néfaste de quantités plus élevées de GNR sur les propriétés optiques et structurales du film mésoporeux hybride GNR- $\text{TiO}_2$ . À la concentration optimale de GNR (0,005% en poids), les Cellules de Grätzel donnent un rendement électronique de 7,18%, ce qui est 20% plus élevé que les Cellules de Grätzel à base de  $\text{TiO}_2$  de référence. Cette amélioration est principalement attribuée au rôle bénéfique des GNR dans la photoanode en dirigeant le transport des électrons photogénérés vers le contact avant, réduisant ainsi la recombinaison des porteurs. Ceci est confirmé par la durée de vie améliorée des électrons calculée à l'aide de la décroissance photovoltaïque transitoire et des mesures EIS. En outre, ce rendement électronique amélioré est également dû à une meilleure absorption de colorant par le film mésoporeux hybride GNR- $\text{TiO}_2$  par rapport au film mésoporeux  $\text{TiO}_2$  de référence. Cependant, des charges plus élevées de GNR dans la pâte nanoparticulaire de  $\text{TiO}_2$  ont des effets néfastes sur les performances PV des Cellules de Grätzel en raison de la formation d'agglomérats qui peuvent induire une recombinaison électronique et une fissure dans le film. De plus, une charge élevée de GNR induit une perte considérable de transparence optique. Enfin, l'approche proposée offre un moyen rapide, peu coûteux et hautement reproductible de booster le rendement électronique des Cellules de Grätzel.

#### **CHAPITRE 4 : EFFET STRUCTUREL DES NANOSTRUCTURES DE CARBONE DE FAIBLE DIMENSION SUR LA STABILITÉ À LONG TERME DES CELLULES SOLAIRES SENSIBLES AUX COLORANTS**

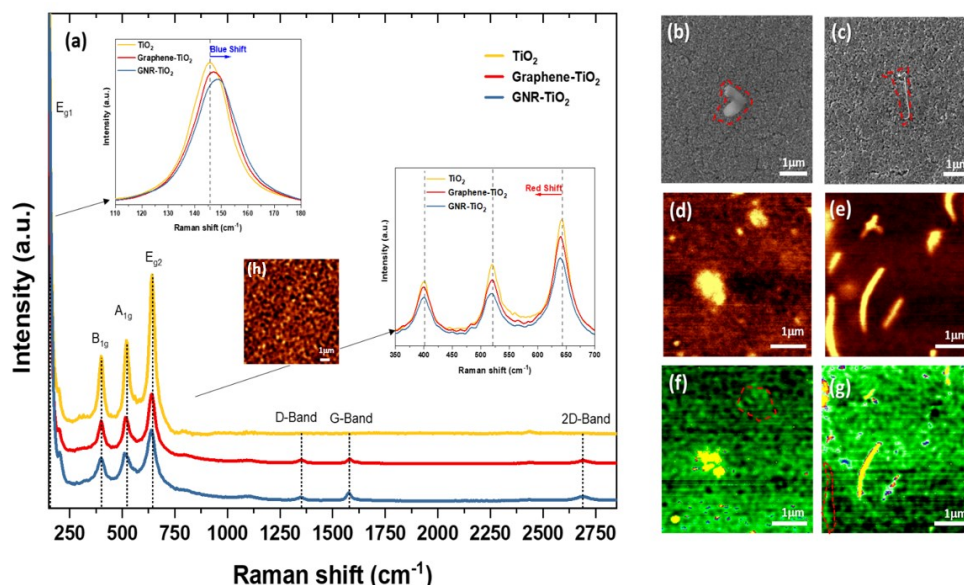


Figure 9. Spectres Raman (a) de  $\text{TiO}_2$  de référence, Graphène- $\text{TiO}_2$  et GNR- $\text{TiO}_2$  (0,010 et 0,005% en poids respectivement) déposés sur FTO. Images MEB (b) de 0,075% en poids de graphène et (c) de 0,075% en poids de GNR dans  $\text{TiO}_2$ , avec un rectangle en pointillé soulignant la présence des structures nanocarbonées. Cartes Raman des intensités des bandes G (d) - (e) et D (f) - (g) pour les échantillons contenant du graphène, respectivement GNR, et de la bande (h)  $E_{g2}$  de  $\text{TiO}_2$ .

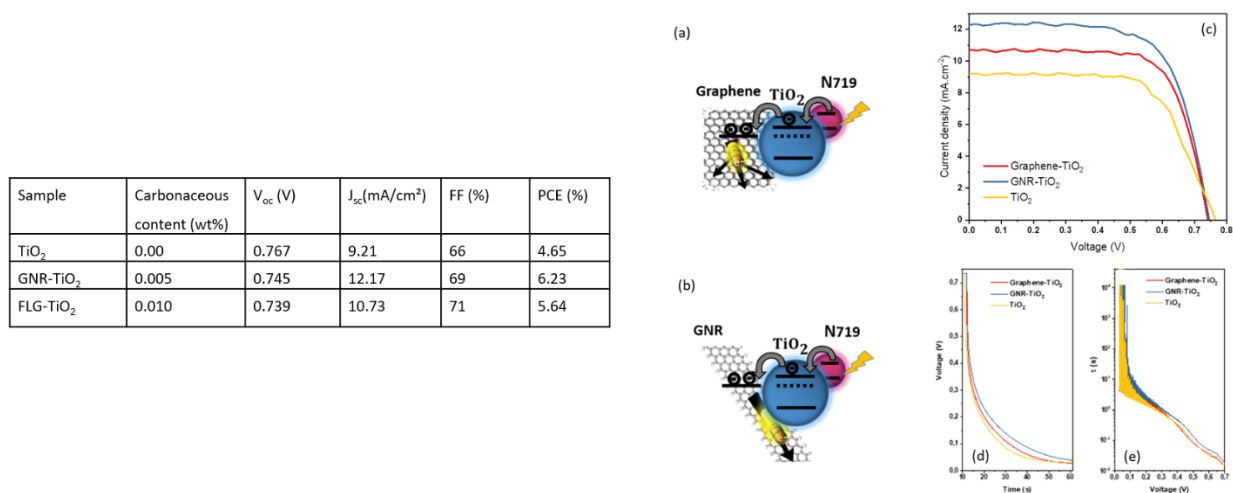


Figure 10 : Tableau des propriétés fonctionnelles des Cellules de Grätzel avec différents contede références FLG et GNR. Schéma de l'alignement de bande et de la dynamique des porteurs dans les photoanodes hybrides: (a) FLG- $\text{TiO}_2$ ; (b) GNR- $\text{TiO}_2$ . Caractérisations photovoltaïques des Cellules de Grätzel basées sur des photoanodes hybrides de graphène et GNR dans  $\text{TiO}_2$  et  $\text{TiO}_2$  de référence: (c) Courbes de densité de courant-tension sous un éclairage solaire (irradiation AM1.5G (100 mW / cm<sup>2</sup>). Mesures de décroissance

photovoltaïque transitoire des dispositifs correspondants : (d) désintégration des Voc; (e) durée de vie des électrons.

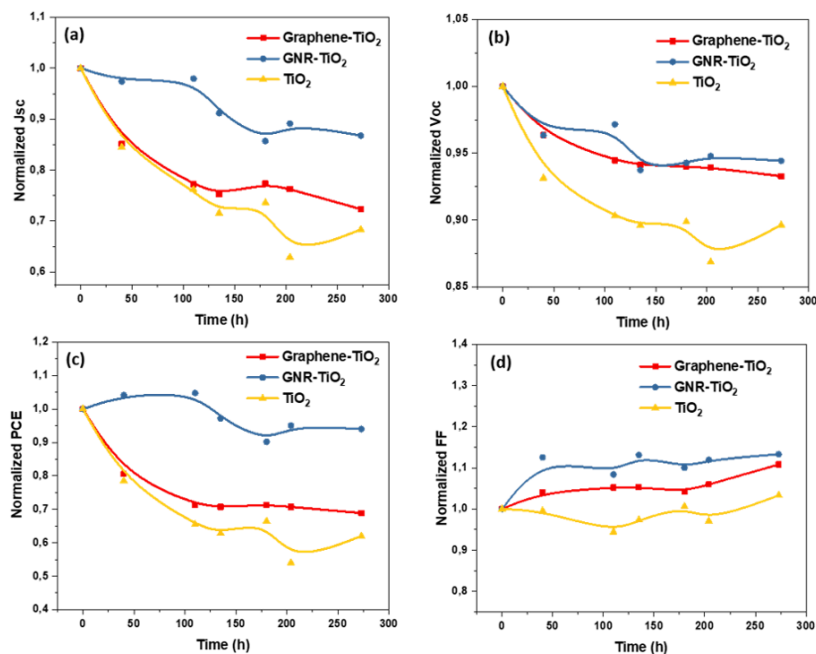
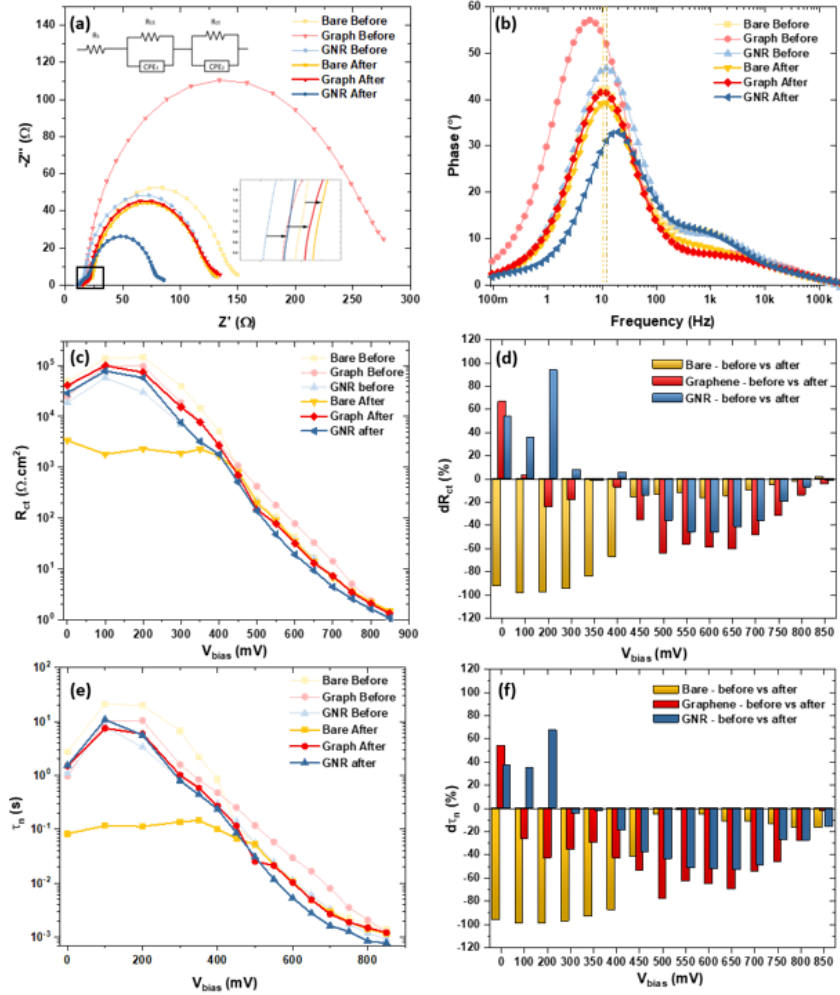


Figure 11. Propriétés fonctionnelles des Cellules de Grätzel avec une concentration optimale de graphène et de GNR dans TiO<sub>2</sub> et TiO<sub>2</sub> de référence sous une irradiation lumineuse contide référencée en fonction du temps de trempage. (a) Jsc (mA / cm<sup>2</sup>); (b) Voc (V); (c) rendement électronique (%), (d) FF (%), mesures de désintégration photovoltaïque transitoire après 273 h de temps de trempage (e) désintégration de Voc et (f) durée de vie électronique de l'appareil.



**Figure 12.** Analyse EIS des Cellules de Grätzel de références Cellules hybride graphène-TiO<sub>2</sub> et GNR-TiO<sub>2</sub> avant (couleur plus claire) et après 270 h (couleurs plus foncées) exposition au soleil simulée dans l'obscurité: (a) Rct; (b) C<sub>p</sub> à 750 mV et (c) Rct, (d)  $\tau_n$ , (e), (f) histogrammes des changements de la résistance de transfert de charge et de la durée de vie des électrons après vieillissement, à des potentiels entre 0 et 850 mV.

En résumé, nous avons démontré que l'ajout de graphène et de GNR aux photoanodes TiO<sub>2</sub> peut améliorer la stabilité des Cellules de Grätzel. Ces anodes composites 2D nanocarbone-TiO<sub>2</sub> ont été assemblées et caractérisées par différentes techniques pour étudier les différences dans les mécanismes des porteurs de charge après une exposition prolongée à la lumière. Cette étude montre qu'après 273h de temps d'immersion dans la lumière, les dispositifs GNR-TiO<sub>2</sub> présentent 51,6% de stabilité du rendement électronique en plus par rapport à un dispositif de Cellule de Grätzel TiO<sub>2</sub> de référence, tandis que les dispositifs graphène-TiO<sub>2</sub> ne présentent qu'une amélioration de 10% de la stabilité du rendement électronique dans les mêmes conditions et avec

2 fois plus de teneur en nanocarbone. Cette stabilité accrue est principalement due à une persistance plus longue de  $J_{sc}$  des dispositifs GNR-TiO<sub>2</sub> par rapport au graphène-TiO<sub>2</sub>.

La cartographie Raman des films incorporant les matériaux nanocarbonés a mis en évidence comment la structure 1-D allongée des GNR se traduit par des voies à la fois verticales et horizontales dans la matrice TiO<sub>2</sub>, renforçant le composite dans plusieurs directions par rapport aux flocons de graphène plans. L'analyse du spectre Raman a montré que les forces de déformation de compression et le dopage p étaient induits par le mélange de graphène et de GNR à l'intérieur de la matrice TiO<sub>2</sub>. Les mesures EIS ont confirmé un processus électrochimique différent, bien qu'une augmentation de  $J_{sc}$  et PCE pour les deux dispositifs à base de nanocarbone se font aussi observer. En effet, alors que le FLG-TiO<sub>2</sub> réduit sa recombinaison, le nanocomposite GNR-TiO<sub>2</sub> surmonte celle-ci en pontant la couche active avec des réseaux inférieurs à la percolation, malgré un taux de recombinaison plus élevé et un  $R_{CT}$  plus faible qu'il produit. Néanmoins, les deux dispositifs nanocomposites conduisent finalement à une plus grande stabilité et rendement des DSSC. Ces résultats montrent non seulement l'effet du rapport longueur / largeur 1D élevé du GNR, mais fournissent également un moyen simple d'améliorer l'efficacité et la stabilité à long terme du DSSC, ce qui est crucial pour que cette technologie prometteuse se rapproche de la commercialisation. Ces propriétés exceptionnelles fournies par GNR devraient stimuler l'utilisation de ces nanomatériaux dans divers systèmes photoélectroniques.

## **CHAPITRE 5 GRAPHENE NANORIBBON-TIO2-QUANTUM DOTS HYBRID PHOTOANODE POUR AMÉLIORER LES PERFORMANCES DE LA PHOTOÉLECTROCHIMIE POUR LA GÉNÉRATION D'HYDROGÈNE**



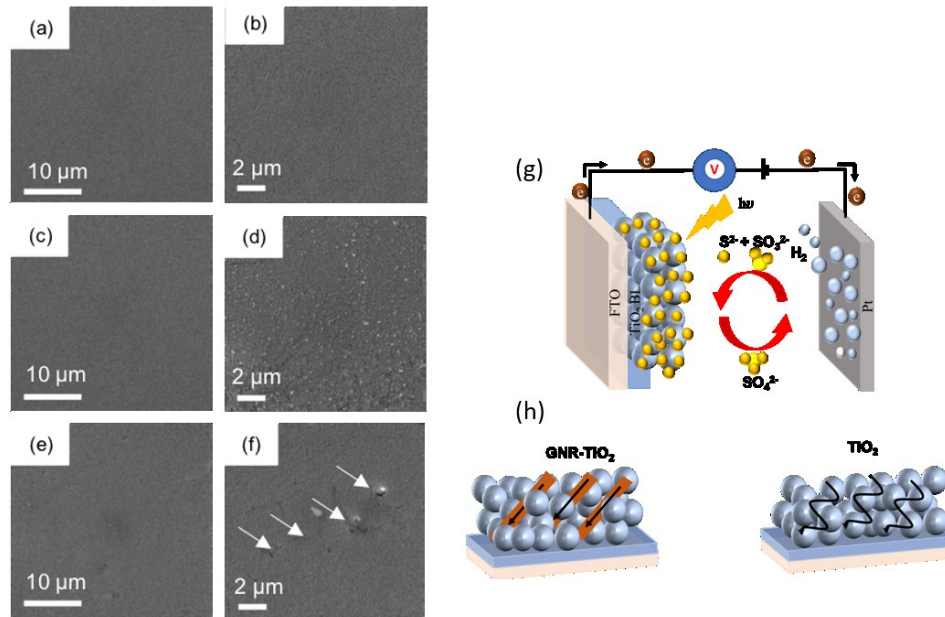


Figure 13 Images SEM de films mésoporeux hybrides GNR-TiO<sub>2</sub> avec différentes concentrations de GNR: (a-b) 0,00% en poids; (c-d) 0,02% en poids et (e-f) 0,05% en poids à différents grossissements. La présence de fissures profondes à une concentration plus élevée du GNR est mise en évidence en blanc. Illustration schématique du principe de fonctionnement du (g) dispositif PEC pour la production d'hydrogène. (h) Processus de transport d'électrons dans un film de TiO<sub>2</sub> mésoporeux avec et sans GNR. Les flèches indiquent le processus de transfert d'électrons.

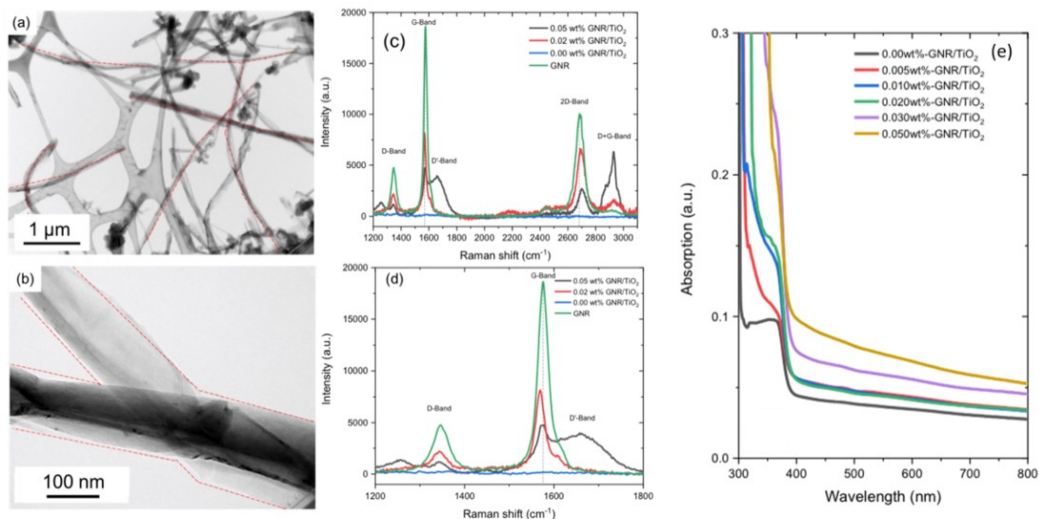
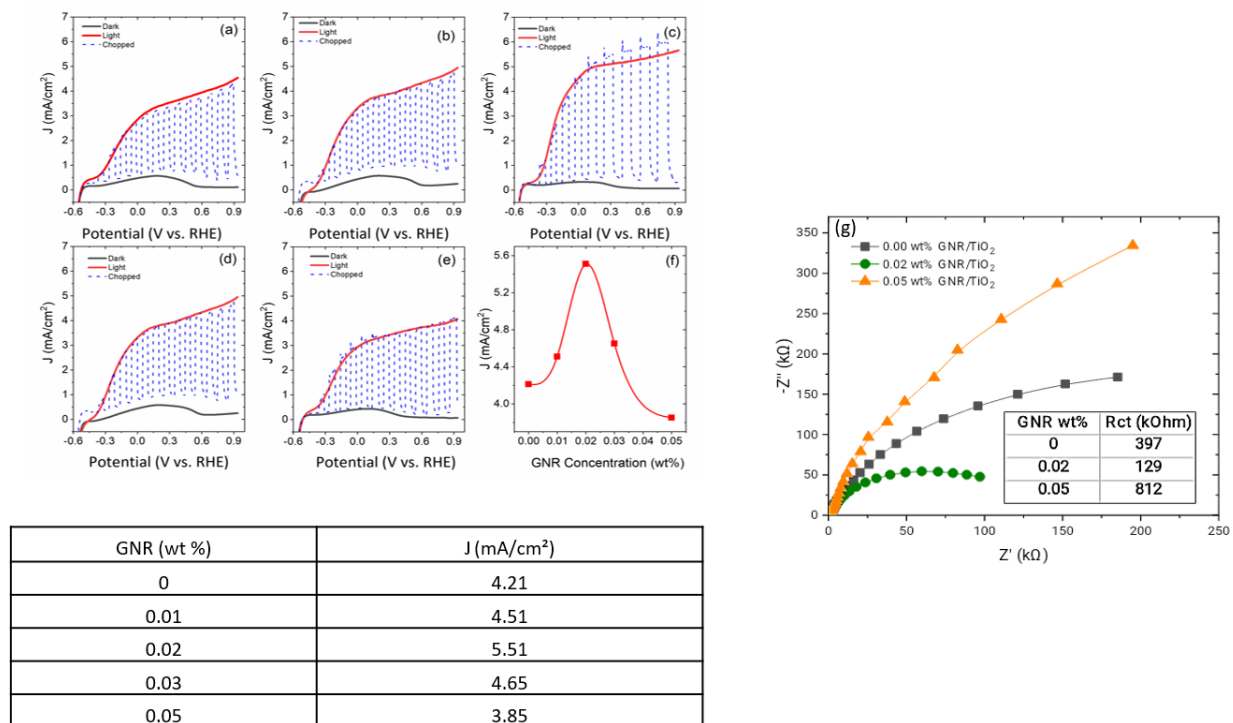


Figure 14 (a) - (b) Images TEM de GNR (pointillés rouges) supportés sur la grille Cu. Spectre Raman de la photoanode composite GNR (vert), TiO<sub>2</sub> (bleu), GNR-TiO<sub>2</sub> (rouge) avec GNR = 0,02% en poids et photoanode composite GNR-TiO<sub>2</sub> (noir) avec GNR = 0,05% en concentration. (e) Comparaison des spectres d'absorption

de films mésoporeux hybrides GNR-TiO<sub>2</sub> déposés sur un verre d'oxyde conducteur transparent avec différentes concentrations de GNR (% en concentration)



**Figure 15** Courbes de densité-potential de photocourant des dispositifs PEC basés sur des photoanodes hybrides GNR-TiO<sub>2</sub> sensibilisés par QD sous un éclairage sombre (trait plein noir), haché (ligne bleue pointillée) et contide référence (AM 1,5 G, 100 mW / cm<sup>2</sup>) (contide référence rouge ligne) avec une concentration différente de GNR: (a) 0,00% en poids; (b) 0,01% en poids; (c) 0,02% en poids; (d) 0,03% en poids; et (e) 0,05% en poids. (f) Variation de la densité de photocourant des dispositifs PEC sur la base de photoanodes hybrides GNR-TiO<sub>2</sub> sensibilisés par QD avec une teneur différente en GNR à 0,8 V par rapport à RHE sous un éclairage solaire (AM 1,5 G, 100 mW / cm<sup>2</sup>). (g) Le graphique de Nyquist des dispositifs PEC basés sur des photoanodes hybrides GNR-TiO<sub>2</sub> / QD avec différentes concentrations de GNR: noir (0,0% en poids); Vert (0,02% en poids) et orange (0,05% en poids). La courbe de Nyquist affiche la variation de la résistance de transfert de charge avec la concentration de GNR. Comparaison de la densité de photocourant à 0,8 V vs RHE sous un éclairage solaire (AM 1,5 G, 100 mW cm<sup>-2</sup>) de dispositifs PEC basés sur des photoanodes hybrides GNR-TiO<sub>2</sub> / QDs avec différentes concentrations de GNR (% en poids).

En résumé, nous avons préparé des anodes hybrides GNR-TiO<sub>2</sub> avec différentes concentrations (% en poids) de GNR. Les propriétés structurales et optiques des anodes hybrides GNRs-TiO<sub>2</sub> ont été caractérisées par spectroscopie UV-visible, SEM et Raman. Les anodes hybrides GNRs-TiO<sub>2</sub> ont été sensibilisées avec un noyau colloïdal / enveloppe QD CdSe / (CdS)<sub>6</sub>. La

concentration optimisée de GNR (0,02% en poids) dans le film mésoporeux  $\text{TiO}_2$  sensibilisé avec  $\text{CdSe} / (\text{CdS})_6$  noyau colloïdal / coquille QDs, a donné la densité de photocourant la plus élevée de 5,51 mA /  $\text{cm}^2$  (à 0,08 V vs RHE) sous un éclairage solaire. (AM 1,5 G, 100  $\text{mW} \cdot \text{cm}^{-2}$ ), ce qui est 30% plus élevé que l'appareil de contrôle. Cela démontre qu'une petite quantité de GNR (0,02% en poids) dispersés dans  $\text{TiO}_2$  conduit à un transport d'électrons amélioré (réduisant le  $R_{\text{ct}}$ ) en raison du chemin directionnel offert par les GNR aux électrons photo-injectés vers FTO. En outre, le dispositif PEC basé sur la photoanode hybride  $\text{TiO}_2$ -GNRs / QDs montre une meilleure stabilité à long terme par rapport au photoanode  $\text{TiO}_2$  / QDs. Nos résultats offrent une approche simple et peu coûteuse pour améliorer les performances des dispositifs PEC ainsi que la possibilité d'utiliser d'autres matériaux carbonés de faible dimension pour augmenter l'efficacité des dispositifs PEC. Les orientations futures se concentreront sur l'application de GNR fonctionnalisés dans des films mésoporeux de  $\text{TiO}_2$  avec les QD colloïdaux hétérostructurés les plus performants, pour réaliser des dispositifs PEC stables à haut rendement et à long terme.

## Chapitre 6: Conclusion générale

L'objectif général de cette thèse était de développer des photoanodes composites stables, rentables et hautes performances conçues en mélangeant GNR avec  $\text{TiO}_2$  à utiliser dans le domaine du photovoltaïque et de la production de combustibles chimiques propres. La stratégie globale consistait à améliorer l'efficacité de la collecte de charge et de l'injection de charge pour avoir un impact sur les dispositifs PEC photovoltaïques et solaires. La stabilité à long terme de ces dispositifs a également été étudiée pour évaluer la contribution bénéfique du nanocomposite GNR- $\text{TiO}_2$ . Par conséquent, dans cette thèse, l'effet structurel et optique du nanocarbone 1D de faible dimension dans la matrice  $\text{TiO}_2$  a été étudié par spectroscopie UV-visible, MEB, MET, spectroscopie Raman et dynamique des porteurs via la spectroscopie d'impédance, la désintégration photovoltaïque transitoire et les mesures I-V.

Une approche directe, simple, peu coûteuse et respectueuse de l'environnement a été utilisée tout au long de ce travail afin d'élaborer des photoanodes composites avec des nanocarbones 1D de faible dimension. Les objectifs étaient les suivants: (1) Élaborer des dispositifs Cellules de Grätzel et des dispositifs PEC avec des photoanodes composites GNR- $\text{TiO}_2$  efficaces pour obtenir des  $J_{\text{sc}}$  et des rendement électronique à faible teneur en carbone; (2) Comparer l'effet d'un rapport hauteur / largeur plus élevé de GNR sur le seuil de percolation de GNR- $\text{TiO}_2$  par rapport au FLG- $\text{TiO}_2$  grâce aux performances photoélectriques et à la stabilité à long terme des Cellules de Grätzel; (3) Fabriquer un appareil photoélectrochimique (PEC) hautement efficace et

durable avec une photoanode GNR-TiO<sub>2</sub> sensibilisée par points quantiques pour améliorer l'efficacité de la génération d'hydrogène.

Par conséquent, sur la base de ces objectifs, les conclusions suivantes ont été tirées:

Dans le chapitre trois, nous avons démontré qu'une concentration optimale de GNR (0,005% en poids), inférieure au seuil de percolation, s'est avérée 20% plus élevée que les Cellules de Grätzel de référence jusqu'à 7,18%, le rendement électronique des Cellules de Grätzel nanocomposites GNR-TiO<sub>2</sub>. Insérés dans une pâte nanoparticulaire TiO<sub>2</sub>, les GNR peuvent améliorer considérablement les performances fonctionnelles des Cellules de Grätzel. L'amélioration est principalement attribuée au rôle bénéfique des GNR dans la photoanode en dirigeant le transport d'électrons photogénérés vers le site de collecte, réduisant ainsi la recombinaison des porteurs et augmentant la J<sub>SC</sub>. Cela a été confirmé par la durée de vie améliorée des électrons calculée à l'aide de la décroissance photovoltaïque transitoire et des mesures EIS. Une nouvelle incorporation de GNR a eu un effet néfaste sur les performances des Cellules de Grätzel, qui a dimidié la référence par la suite. Cela s'est avéré être causé par la formation d'agglomérats qui peuvent induire des fissures et une recombinaison électronique dans les films ainsi qu'une perte de transparence optique. De plus, il a été démontré que le GNR intégré de manière optimale dans les grains peut améliorer l'efficacité de la séparation des charges et la stabilité du dispositif en raison de bonnes interactions de zone à zone dans le nanocomposite.

Par conséquent, les résultats montrent comment GNR-TiO<sub>2</sub> peut être considéré comme un candidat précieux pour un photoanode hybride dans les Cellules de Grätzel.

Dans le chapitre quatre, nous avons utilisé le photoanode graphène-TiO<sub>2</sub>, avec des concentrations optimales de graphène obtenues de référence par les mesures de performances fonctionnelles des Cellules de Grätzel et l'avons comparé avec le photoanode GNR-TiO<sub>2</sub> mentionné ci-dessus avec une concentration optimale comment les deux nanocomposites ont révélé les effets des dimensionnalités 1D des feuilles de graphène sur l'ensemble performances et stabilité des Cellules de Grätzel. De plus, la présence de graphène et de GNR dans des nanoparticules de TiO<sub>2</sub> peut améliorer la stabilité des Cellules de Grätzel, mais en comparaison, l'enquête par spectroscopie d'impédance montre que le transfert de charge stabilise mieux le dispositif basé sur GNR.

L'analyse structurale par spectroscopie Raman révèle que les deux nanocomposites carbonés ont montré des forces de déformation de compression qui contribuent positivement aux effets de trempe mécanique. Cependant, GNR donne un effet de compression plus fort que le graphène

en comparaison, ce qui stabilise plus efficacement l'intégrité du film. Combiné à une stabilité des paramètres fonctionnels plus élevée, ce résultat suggère que les photoanodes à base de GNR sont dispersées de manière optimale le long des limites des grains, ce qui peut améliorer les fissures de pontage et de ramification de la connectivité intergrade référencellaire et transgrade référencellaire dans le film de photoanode composite.

Cela a permis de comprendre l'influence de la morphologie 1D de GNR sur les performances et la stabilité des appareils, offrant aux appareils GNR-TiO<sub>2</sub> un avantage par rapport aux appareils Graphène-TiO<sub>2</sub>, ce qui a été corroboré par le meilleur taux de changement de la résistance de transfert de charge  $R_{CT}$  et la durée de vie des électrons  $\tau_n$  au fil du temps. Ces résultats fournissent un moyen simple d'améliorer la stabilité à long terme des Cellules de Grätzel, ce qui est crucial pour que cette technologie prometteuse se rapproche d'un pas de la commercialisation.

Ces découvertes ouvrent de nouvelles voies pour étudier l'effet de taille des matériaux à base de graphène dans les dispositifs de conversion d'énergie.

Dans le chapitre cinq, nous avons modifié la surface de GNR-TiO<sub>2</sub> en sensibilisant la photoélectrode avec des points quantiques à noyau / coquille colloïdal CdSe / (CdS)<sub>6</sub> et élaboré de nouvelles anodes hybrides photoélectrochimiques pour augmenter l'efficacité des dispositifs PEC.

Les propriétés structurelles et optiques du photoanode ont été caractérisées par UV-Visible, Raman et MET, et ont montré qu'après la valeur du seuil de percolation de 0,02% en poids de GNR, une quantité accrue de GNR réduit progressivement la qualité globale du photoanode et contribue également à la perte d'une partie du rayonnement disponible pour la génération d'excitons, ce qui à son tour aggrave les performances globales de l'appareil.

Cette concentration optimisée de GNR a donné une densité de photocourant jusqu'à 30% supérieure à celle du dispositif de contrôle. La photoanode hybride TiO<sub>2</sub>-GNRs / QDs a également montré une meilleure stabilité à long terme par rapport à la photoanode TiO<sub>2</sub> / QDs. Cela démontre qu'une petite mais différente quantité de GNR dispersés dans TiO<sub>2</sub> conduit à un transport d'électrons amélioré en raison du chemin directionnel offert par les GNR aux électrons photo-injectés vers FTO. La même petite quantité contribue à réduire la résistance de transfert de charge qui indique un transfert de charge plus élevé et une séparation améliorée des paires électrons / trous. Bien que, par rapport au PEC, le seuil de percolation ait été déplacé vers des concentrations plus élevées de GNR qu'avec les Cellules de Grätzel, ce résultat suggère que le

seuil de percolation est sensible à la matrice hôte et au type d'application pour laquelle il sera conçu.

Les résultats obtenus de références dans la thèse offrent un aperçu utile de l'effet des nanostructures de carbone de faible dimension. Comme prévu à partir de la théorie de la percolation, un rapport hauteur / largeur plus élevé pour les feuilles de graphène a contribué à déplacer vers un seuil de percolation inférieur le seuil de percolation des photoanodes basés sur GNR pour leur rendement électronique et la stabilité à long terme dans les Cellules de Grätzel. Cela peut être attribué à leur rapport d'aspect, qui peut former un réseau homogène dans la matrice, plutôt que des faisceaux, et ainsi améliorer le contact de zone à zone avec les nanoparticules de  $\text{TiO}_2$ . De plus, le même seuil de percolation optimal se trouve décalé vers un seuil de percolation plus élevé lorsque la photoanode composite est utilisée dans une application différente.

En conclusion, l'élaboration de photoanodes GNR- $\text{TiO}_2$  constitue une approche très rapide et hautement reproductible pour l'incorporation de faibles quantités de nanocarbones dans les photoanodes des Cellules de Grätzel et des dispositifs PEC. Nous n'avons appliqué aucun traitement de surface, ce qui pourrait augmenter considérablement les propriétés fonctionnelles des appareils, mais il est également peu probable qu'il soit appliqué à grande échelle pour une production bon marché et massive. En raison de leur structure 1D et de leurs excellentes propriétés de collecte de charges et de conduction, les GNR sont un choix naturel en tant qu'additif à la couche photoactive dans les dispositifs de collecte de lumière, offrant des voies extraordinaires pour un transport à faible résistance vers l'anode.

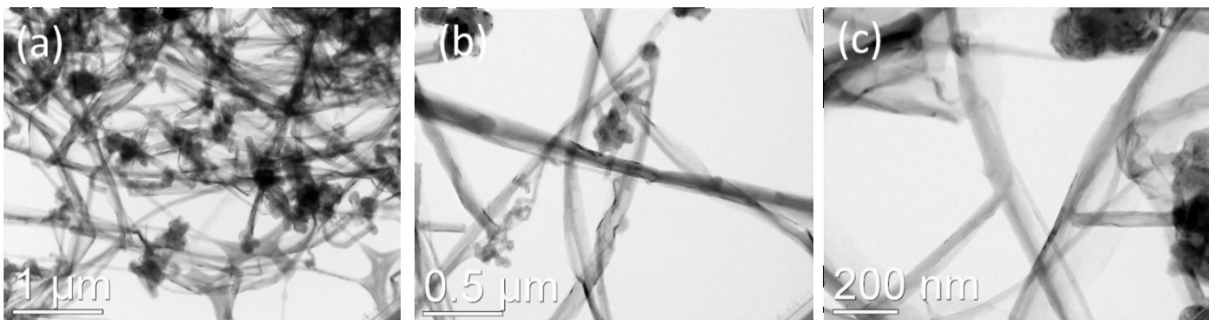


**Figure S 3-1. TEM images of GNR at different magnifications**

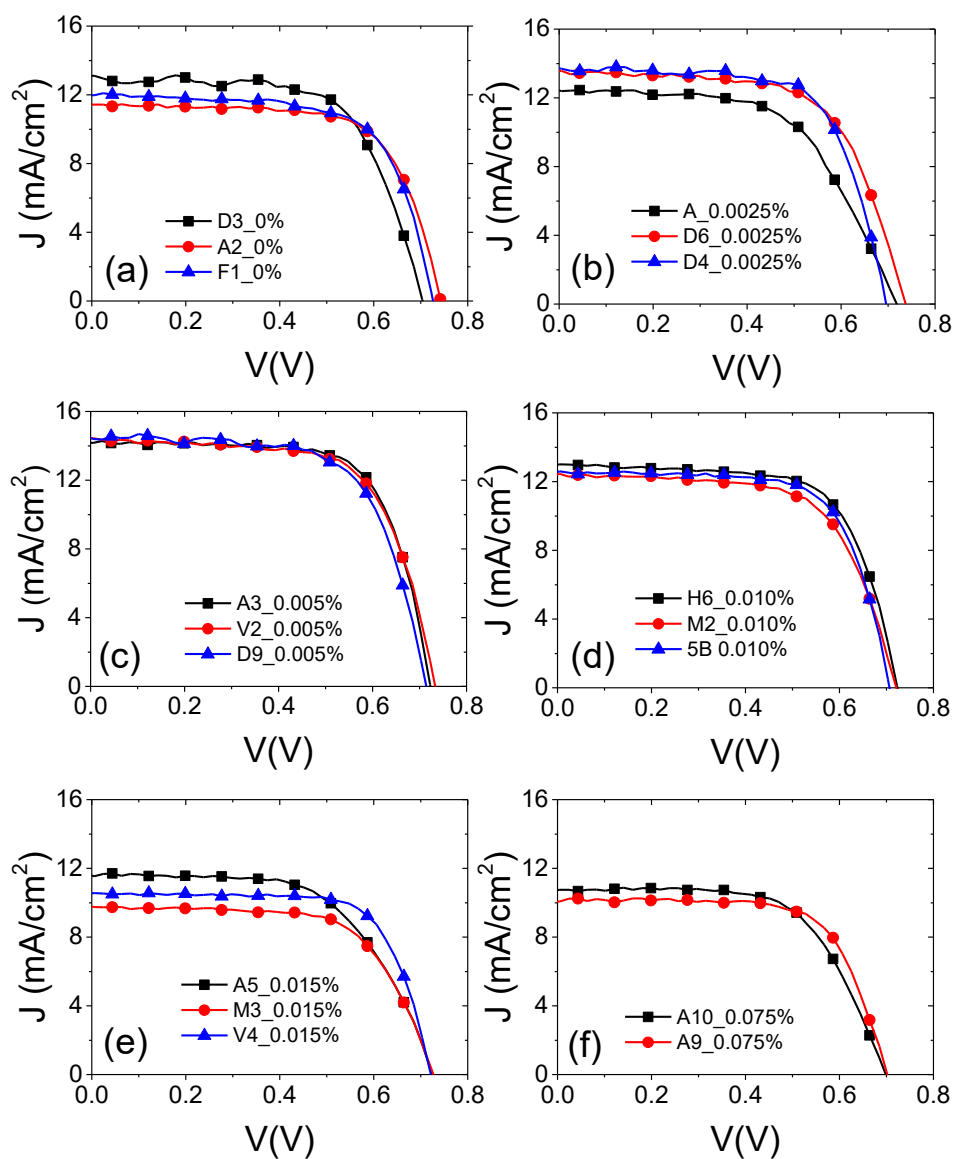


**Figure S 3-2. Current density–voltage curves reproducibility of device with different concentration of GNR in  $\text{TiO}_2$  under one sun illumination (AM1.5G irradiation ( $100 \text{ mW/cm}^2$ )): (a) without GNR; (b) 0.0025 wt%; (c) 0.0050 wt%; (d) 0.010 wt%; (e) 0.015 wt%; and (f) 0.075 wt%.**

**Table S 3-1. Functional parameters statics of DSSCs with different GNR content.**



<b>GNR (%wt)</b>	<b>V<sub>oc</sub> (V)</b>	<b>J<sub>sc</sub> (mA/cm<sup>2</sup>)</b>	<b>FF (%)</b>	<b>PCE (%)</b>
<b>0</b>	0.705	13.13	0.65	5.99
	0.726	11.99	0.69	5.96
	0.744	11.44	0.69	5.82
<b>0.0025</b>	0.692	13.60	0.69	6.49
	0.717	12.43	0.59	5.25
	0.734	13.54	0.64	6.38
<b>0.005</b>	0.713	14.51	0.66	6.85
	0.724	14.22	0.70	7.18
	0.733	14.43	0.66	7.03
<b>0.010</b>	0.709	12.58	0.69	6.16
	0.720	12.48	0.66	5.84
	0.724	13.01	0.68	6.39
<b>0.015</b>	0.721	10.54	0.72	5.48
	0.726	11.59	0.60	5.07
	0.727	9.79	0.65	4.65
<b>0.075</b>	0.696	10.50	68	4.99
	0.696	9.96	71	4.96

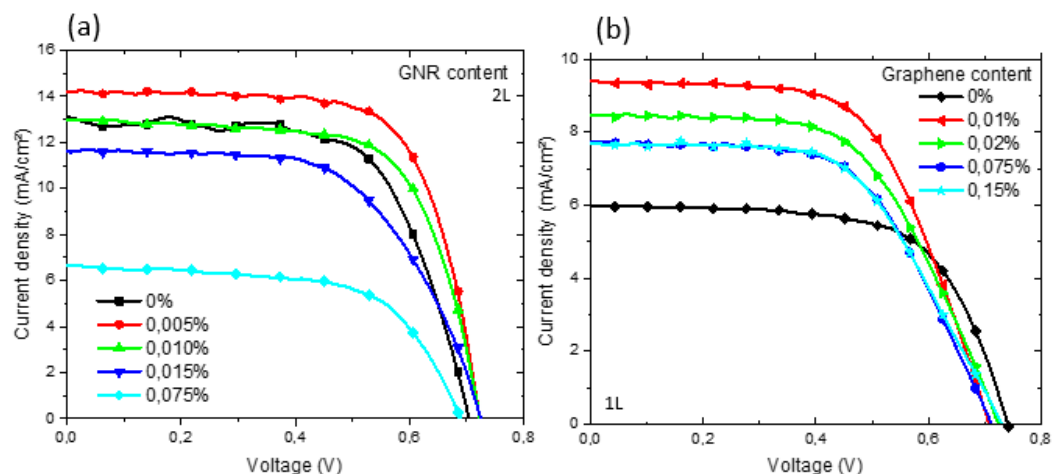


Figure S 4-1 Current density–voltage curves under one sun illumination (AM1.5G irradiation (100 mW/cm<sup>2</sup>) for (a) graphene nanoribbon (GNR)-TiO<sub>2</sub> and (b) few layer graphene (FLG)-TiO<sub>2</sub> of increasing content

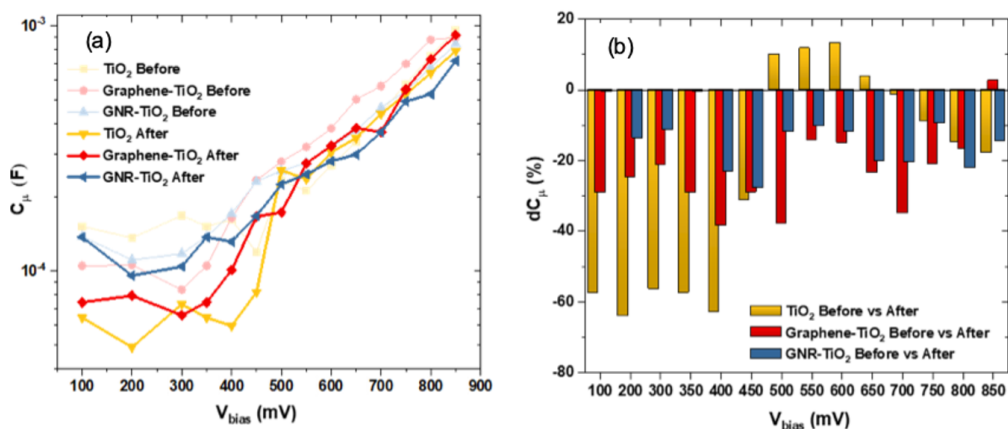


Figure S 4-2 Electrochemical impedance spectroscopy (EIS) analysis of Dye sensitized solar cells (DSSCs) based on TiO<sub>2</sub>, Graphene-TiO<sub>2</sub> and GNR-TiO<sub>2</sub> hybrid photoanodes before (lighter color) and after 270h (darker colours) simulated sun exposure under dark measurement: (a) chemical capacitance  $C_{\mu}$ ; (b) chemical capacitance variations  $dC_{\mu}$

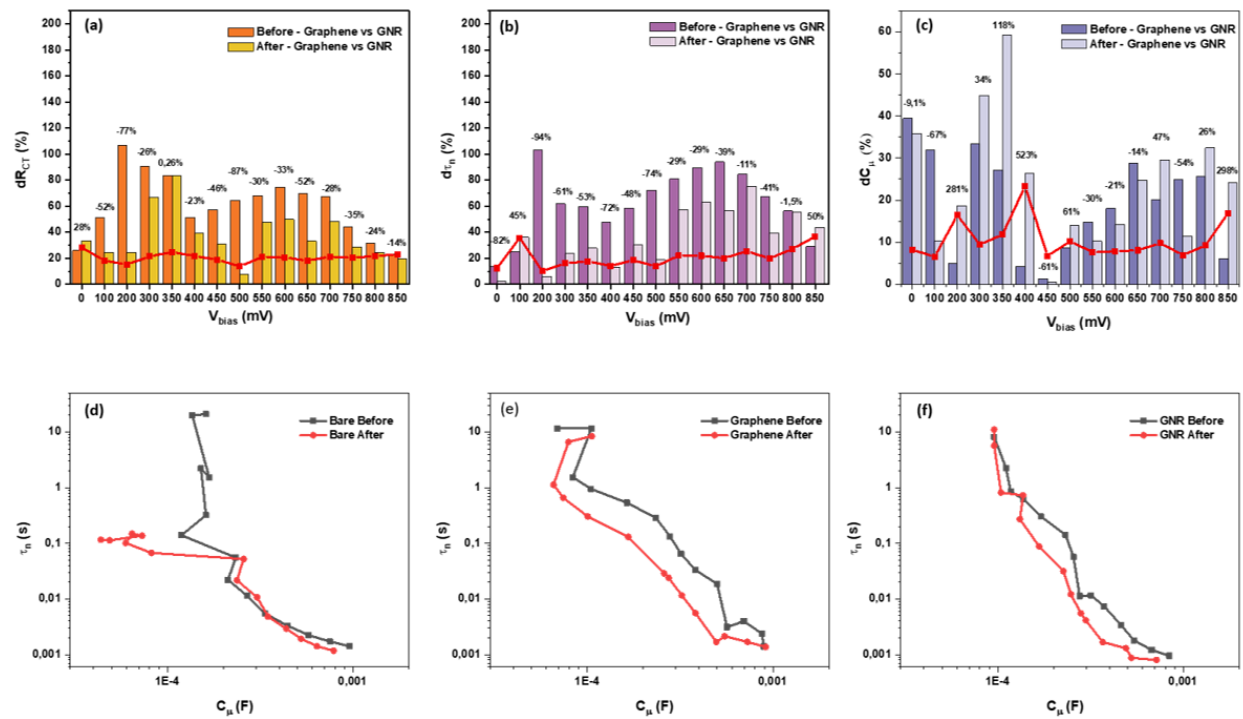


Figure S 4-3. Histograms of evolution of the percentage change between Graphene and GNR, before and after light soaking for  $R_{CT}$  (a),  $\tau_n$  (b) and  $C_{\mu}$  (c). Evolution of  $\tau_n$  as a function of  $C_{\mu}$  before and after light soaking for Bare sample (d), Graphene (e) and GNR based sample (f).